THÈSE

En vue de l'obtention du

DOCTORAT DE L'UNIVERSITÉ DE TOULOUSE

Délivré par :

Institut National Polytechnique de Toulouse (INP Toulouse)

Discipline ou spécialité :

Dynamique des fluides

Présentée et soutenue par :

M. CHRISTOPHE GUY COREIXAS

le jeudi 22 février 2018

Titre :

High-order extension of the recursive regularized lattice Boltzmann method

---

Ecole doctorale :

Mécanique, Energétique, Génie civil, Procédés (MEGeP)

Unité de recherche :

Centre Européen de Recherche et Formation Avancées en Calcul Scientifique (CERFACS)

Directeur(s) de Thèse :

M. GUILLAUME PUIGT

M. JEAN-FRANCOIS BOUSSUGE

Rapporteurs :

M. FLORIAN DE VUYST, UNIVERSITE DE TECHNOLOGIE DE COMPIEGNE

M. FRANCOIS DUBOIS, CNAM PARIS

Membre(s) du jury :

M. NICOLAS GOURDAIN, ISAE-SUPAERO, Président

M. GUILLAUME PUIGT, CERFACS, Membre

M. IRINA GINZBURG, IRSTEA, Membre

M. JONAS LATT, UNIVERSITE DE GENEVE, Membre

Résumé

Au cours des deux dernières décennies, la méthode Lattice Boltzmann (LB) a connu un essor remarquable, et notamment, en mécanique des fluides numérique. Cependant, les méthodes LB standards sont toujours sujettes à des problèmes de stabilité lors de la simulation d'écoulements: (1) isothermes et faiblement compressibles à nombre de Reynolds élevés, ou (2) compressibles et comprenant des discontinuités telles que des ondes de choc. Alors que plusieurs solutions ont été proposées pour répondre au premier problème, les schémas numériques développés pour la simulation d'écoulements complètement compressibles sont bien trop coûteux pour être viables dans un contexte industriel. Afin d'apporter une première pierre à l'édifice, la pertinence de l'utilisation de méthodes LB d'ordre élevé est investiguée. Ce travail s'effectue alors en trois étapes.

Tout d'abord, un nouveau modèle LB, compatible avec un grand nombre de discrétisations en vitesses, est proposé pour contourner les problèmes rencontrés pour des nombres de Reynolds élevés. Ses gains en stabilité et précision sont liés au nouveau modèle de collision basé sur l'étape de régularisation. Ce dernier inclut désormais un calcul par récurrence des coefficients hors-équilibre du développement en polynômes d'Hermite. Ces formules de récurrence sont directement issues du développement de Chapman-Enskog, et permettent de correctement filtrer les contributions non-hydrodynamiques émergeant lors de l'utilisation de maillages sous-résolus.

Ensuite, la capacité du nouveau modèle de collision à gérer les discontinuités est étudiée. Les résultats montrent que ce dernier permet bel et bien de réduire l'amplitude des oscillations parasites, mais des problèmes persistent lorsque les coefficients de diffusion sont trop faibles. Il est alors proposé de coupler le modèle de collision avec une méthode de capture de choc afin d'améliorer sa robustesse. L'ajout de viscosité artificielle, à l'aide d'un senseur de choc de type Jameson, permet au final de lisser les oscillations près des chocs. Ainsi, le couplage avec la nouvelle méthode LB permet de grandement améliorer le domaine de stabilité du schéma de base, tout en conservant l'efficacité de l'algorithme 'Collision & Propagation'.

Finalement, des études de stabilité linéaires sont menées sur les équations de Boltzmann discrétisées en vitesses, ainsi que sur le modèle LB correspondant. Restreintes au cas isotherme, ces dernières sont dédiées à une meilleur compréhension de l'origine des instabilités rencontrées pour des nombres de Reynolds et de Mach élevés. L'analyse de stabilité linéaire sur l'équation discrétisée en vitesses confirme que cette dernière peut être utilisée en tant qu'alternative au développement de Chapman-Enskog. En ce qui concerne le cas des modèles discrétisés en espace et en temps, il est montré que toutes les méthodes LB ont des propriétés spéctrales différentes, et ce, quelque soit: leur nombre de vitesses discrètes, et la valeur de leur constante d'adimensionnement. Cette étude se conclut par la confirmation du gain en stabilité, induit par la nouvelle étape de régularisation, pour l'intégralité des modèles LB considérés lors de ce travail.

Abstract

Over the past two decades, the lattice Boltzmann method (LBM) has emerged as an interesting candidate for computational fluid dynamics and beyond. Despite a wide range of validity of standard LBMs, the simulation of certain flows remains a tedious task for: (1) isothermal and weakly compressible flows at high Reynolds numbers, and (2) fully compressible flows including discontinuities such as shock waves. While several solutions have been proposed to tackle the simulation of isothermal flows in the zero-viscosity limit, numerical schemes that were developed for the simulation of fully compressible flows are not affordable in the industrial context. To pave the way for the extension of LBMs to industry-oriented simulations of fully compressible flows, the present work focuses on the use of high-order LBMs. This is done through three major investigations.

First, the issue of high-Reynolds number flow simulations is tackled thanks to a new LBM with enhanced stability and accuracy, and compatible with a large number of velocity sets. Its collision operator relies on a regularization step, which is here improved through a recursive computation of nonequilibrium Hermite polynomial coefficients. Recursive formulas directly derive from the Chapman-Enskog expansion, and allow to properly filter out second- (and higher-) order nonhydrodynamic contributions in underresolved conditions.

Then, it is proposed to study the impact of the new stabilization approach on spurious oscillations induced by discontinuities. The latter is shown to drastically reduce their amplitude, but not enough to ensure the stability and accuracy of the scheme for small values of the viscosity. To further improve their stability in the zero-viscosity limit, and to be able to properly handle discontinuities, a simple coupling with a shock-capturing technique is presented. It results in a specific injection of second-order artificial viscosity near discontinuities through the use of a Jameson-like shock-sensor. Final results confirm the drastic improvement induced by the coupling between the recursive regularized LBM and a shock-capturing technique, while keeping the efficiency of the 'Collide & Stream' algorithm.

Finally, linear stability analysis (LSA) of both the lattice Boltzmann equation (LBE), and its related LBM, are conducted in the isothermal case to further understand stability issues encountered with high-Reynolds and high-Mach number flows. The LSA of the LBE confirms that it can be used as an alternative to the Chapman-Enskog expansion to determine its macroscopic behavior. Regarding the LSA of the LBM, it highlights the fact that all lattices have very different spectral properties, whatever the number of discrete velocities or the value of their lattice constant. Furthermore, the filtering behavior of the recursive approach is shown to drastically increase their stability domains. Being observed for all the proposed velocity sets, this last result seems quite general.

Remerciements

Tout d'abord, je tiens à remercier les membres du jury qui ont accepté d'évaluer mon travail de thèse, et avec lesquels j'ai pu avoir des échanges passionnants sur les méthodes lattice Boltzmann.

J'aimerais aussi remercier mes encadrants de thèse Guillaume Puigt et Jean-François Boussuge pour leur soutien au cours de ces trois années de thèse, et sans qui ce travail de thèse n'aurait jamais pu aboutir. Je tiens tout particulièrement à te remercier Guillaume de m'avoir aidé à mieux comprendre les bases de l'analyse de stabilité linéaire, et Jean-François de m'avoir toujours poussé à rendre mes travaux accessibles aux personnes non-initiées aux méthodes lattice Boltzmann.

Je suis également ravi d'avoir eu la chance de pouvoir travailler avec Alois Sengissen, Jean-Christophe Giret, Denis Ricot et Romain Cuidard dans le cadre de mon stage de fin d'études et tout au long du projet CLIMB. Je te remercie tout particulièrement Alois pour ton soutien dans les moments difficiles, ainsi que pour ton enthousiasme envers mon travail. De même, je te suis vraiment reconnaissant Denis pour les nombreux échanges que nous avons pu avoir sur la théorie et l'implémentation des méthodes lattice Boltzmann.

J'ai été très heureux de pouvoir faire partie de l'équipe CFD du CERFACS, au sein de laquelle j'ai pu participer à un très grand nombre de formations de qualité, ce qui m'a permis d'améliorer ma culture scientifique de façon non négligeable. De plus, je tiens à remercier les permanents pour leur intérêt envers mon travail, ainsi que pour leurs remarques constructives qui m'ont permis de mieux replacer la LBM dans le contexte de la CFD plus traditionnelle.

De même, je remercie tous les stagiaires, doctorants et post-doctorants avec qui j'ai pu passer d'excellents moments que ce soit à la pause-café, ou autour d'un petit verre. Je remercie notamment Julien, Thibault, François, Majd, Mélissa, Carlos, Romain, César, Dario, Maxime, Valentin, Bastien, Pamphile et Robin pour les très bons moments passés ensemble !

Une mention spéciale est de rigueur pour la 'team LBM' composée de Gauthier Wissocq, Thomas Astoul, Florian Renard, Jean-François Parmentier et 'Danny Boy' (bien malgré lui...). Je les remercie tous pour les conversations passionnantes que nous avons pu avoir sur diverses notions en lien (ou non) avec la LBM. Plus particulièrement, je remercie chaleureusement Gauthier sans qui le nouveau modèle de collision régularisé et le travail sur l'analyse de stabilité linéaire n'auraient jamais pu voir le jour. Merci égale-

Acronyms & Abbreviations

BE	**B**oltzmann **E**quation
BGK	**B**hatnagar-**G**ross-**Kr**ook
CAA	**C**omputational **A**ero**A**coustics
CE	**C**hapman-**E**nskog
CFD	**C**omputational **F**luid **D**ynamics
DDF	**D**ouble **D**istribution **F**unction
DoF	**D**egree **o**f **F**reedom
EDF	**E**quilibrium **D**istribution **F**unction
ELBM	**E**ntropic **L**attice **B**oltzmann **M**ethod
FHP	**F**risch, **H**asslacher and **P**omeau
HPP	**H**ardy, **P**omeau and **P**azzis
KTG	**K**inetic **T**heory of **G**ases
KT	**K**ataoka and **T**sutahara
LBE	**L**attice **B**oltzmann **E**quation
LBM	**L**attice **B**oltzmann **M**ethod
LGCA	**L**attice **G**as **C**ellular **A**utomata
LHS	**L**eft-**H**and **S**ide
LSA	**L**inear **S**tability **A**nalysis
MOOC	**M**assive **O**pen **O**nline **C**ourse
MRT	**M**ulti-**R**elaxation **T**ime
MS	**M**ulti**S**peed

NSF	Navier-Stokes-Fourier
ODE	Ordinary Differential Equation
PDE	Partial Differential Equation
PR	Projection based Regularization
RHS	Right-Hand Side
RLBM	Regularized Lattice Boltzmann Method
RR	Recursive Regularization
SDF	Single Distribution Function
SGS	SubGrid Scale
SPOC	Small Private Online Course
TRT	Two-Relaxation Time
VDF	Velocity Distribution Function
WT	Watari and Tsutahara

Contents

Chapter 1

Introduction

Over the past two decades, the lattice Boltzmann method (LBM) has emerged as an interesting candidate for computational fluid dynamics (CFD) and beyond. Despite a first restriction to isothermal and weakly compressible flows, its range of applicability in both physics and engineering has grown in such a way that it is now possible to simulate very complex phenomena including turbulence [1, 2], combustion [3–5], multiphase interactions [6–9], hemodynamics [10], magnetohydrodynamics [11–14], relativistic flows [15, 16] and even quantum systems [17, 18].

From the numerical point of view, the LBM requires a strong coupling between discretizations of the velocity and the physical spaces. This is usually done using a Cartesian grid coupled with an octree based refinement technique [19–21]. Combining these numerical tools with the kinetic nature and the local dynamics of the LBM, the simulation of complex phenomena around realistic geometries is greatly eased [22–25]. Moreover, the method is simple to implement, induces a very low computational cost per degree of freedom, and presents a compact stencil, all of which contribute to its intrinsic advantage for parallel computations [26]. All these key points make the LBM of great interest for both academic and industry groups. More precisely, a strong interest in these methods has rapidly grown in the automotive industry [22] in the 2000's, before they caught the attention of aerospace industry and research groups [24, 27] in the 2010's.

More specifically, the LBM derives from the Boltzmann equation (BE), the milestone of the kinetic theory of gases [28]. The BE describes the balance between the transport and the collision of packets of particles through the evolution of the velocity distribution function (VDF). The latter, usually written $f(\boldsymbol{x}, \boldsymbol{\xi}, t)$, can be seen as the probability density of finding *fictive* particles at a given point $(\boldsymbol{x}, t)$ and with a given velocity $\boldsymbol{\xi}$. Hydrodynamic variables (such as density ρ, momentum $\rho\boldsymbol{u}$ and total energy ρE) are then recovered through the computation of the average, over the velocity space, of their mesoscopic counterparts. The lattice Boltzmann equation (LBE) results from a velocity discretization of the BE, meaning that the degrees of freedom allowed to the transport phenomenon are restricted to a finite set of velocities (directions and norms are fixed). The standard numerical discretization of the LBE relies on the successive resolution of both collision and advection of particles through the famous 'Collide & Stream' algorithm.

The present work is part of the **CLIMB** (**C**omputationa**L** methods with **I**ntensive **M**ultiphysics **B**oltzmann solver) project, which results from a consortium of industrial companies (Renault, Airbus, CS), academic laboratories (Aix-Marseille University, École Centrale de Lyon, Laboratoire de Mathématiques d'Orsay) and strong partnerships with others entities (CERFACS, ONERA, Alstom, GANTHA, Matelys, Kalray). Part of the project focuses on the derivation of new LBMs for the simulation, in the industrial context, of several types of physical phenomena: (1) aeroacoustics, (2) heat exchanges, (2) pollutant spreading, and (3) fully compressible flows including discontinuities.

This manuscript is dedicated to the last point, which remains an open question due to stability issues encountered during the simulation of high-Reynolds and high-Mach numbers flows using standard LBMs. As a first step towards the full understanding of these stability issues, a new regularized LBM (RLBM) [29] is derived aiming at ensuring the compliance with industrial requirements as best as possible. These requirements mainly includes: (a) **robust, accurate and efficient** numerical scheme, (b) **curved boundary conditions** to simulate flows around realistic geometries, (c) **octree based refinement techniques** to adapt the grid cell size to the physics of interest, and (d) **subgrid scale models** to take into account the contribution of underresolved turbulent scales. More specifically, the current work focuses on the first point with a particular emphasis placed on both accuracy and robustness of the proposed approach in underresolved conditions.

This work is organized as follows. After a brief literature review (Chap. 2), the successive derivations of both the LBE and the LBM are reminded in the framework of Hermite polynomials (Chap. 3). As one of the possible cure to stability issues encountered with high-Reynolds number flows, the concept of RLBM is then recalled in Chap. 4, with a particular emphasis placed on the new extension to thermal and compressible RLBMs. The coupling between the regularization step and a standard shock-capturing technique is also studied in this chapter. A linear stability analysis (LSA) is then conducted on several sets of LBE (Chap. 5) to understand the spectral behavior of both hydrodynamic and nonhydrodynamic modes in the Fourier space. Applying the same analysis to the associated LBMs, linear stability domains are further obtained using BGK and regularized collision models for a very large number of velocity sets (Chap. 6). General conclusions regarding the present work, and perspectives for further improvement, are proposed in Chap. 7. Finally, several appendices gather all the necessary material to derive and code the proposed RLBMs.

How to read this manuscript

The author's main concern was not to overwhelm the reader with unnecessary mathematical derivations. Hence, the present manuscript is written in such a way that it contains the very essence of this PhD work and nothing more. Nonetheless, several appendices are provided to help the interested reader with all the tedious algebra.

In addition, it has been chosen to only briefly present the fundamentals of LBMs. The reason for this is twofold. First, the LBM is a well established numerical tool in the statistical physics community. Second, a more extensive presentation would only have

been a paraphrasing of reference books/articles.

Nevertheless, the interested reader can find insightful information regarding both theoretical and practical aspects of standard LBMs in Krüger *et al.*'s book [30]. This recently published book (end-2016) contains all the necessary material to properly (1) introduce fundamentals of the LBM to beginners, and (2) implement a solver from scratch. Furthermore, a section is dedicated to frequently ask questions, and allows to deal with standard misconceptions about the LBM. Finally, complete code examples are available to help the reader to quickly and easily implement its own lattice Boltzmann solver.

Mathematical notations

Throughout this manuscript, it has been chosen to note both vectors and higher order tensors using a bold text notation, whereas their index notation relies on Greek letters. As an example, the tensor notation of the velocity is $\boldsymbol{u}$, with its index notation being u_α, where α stands for Cartesian coordinates (x, y and z in 3D). To avoid any confusions concerning vector and tensor operations, they are recalled in Tab. 1.1. Finally, while Greek letters are used for Cartesian indexes x, y and z, Roman letters are employed for non-Cartesian indexes. More specifically, i is used as the velocity space index.

Operation	Tensor notation	Index notation	Shorthand notation
Scalar product (1st order)	$\lambda = \boldsymbol{a} \cdot \boldsymbol{b}$	$\lambda = \sum_\alpha a_\alpha b_\alpha$	$\lambda = a_\alpha b_\alpha$
Scalar product (2nd order)	$\boldsymbol{a} = \boldsymbol{A} \cdot \boldsymbol{b}$	$a_\alpha = \sum_\beta A_{\alpha\beta} b_\beta$	$a_\alpha = A_{\alpha\beta} b_\beta$
Tensor contraction	$\lambda = \boldsymbol{A} : \boldsymbol{B}$	$\lambda = \sum_\alpha \sum_\beta A_{\alpha\beta} B_{\alpha\beta}$	$\lambda = A_{\alpha\beta} B_{\alpha\beta}$
Gradient (physical space)	$\boldsymbol{a} = \boldsymbol{\nabla} \lambda$	$a_\alpha = \partial\lambda/\partial\alpha$	$a_\alpha = \partial_\alpha \lambda$
Gradient (velocity space)	$\boldsymbol{a} = \boldsymbol{\nabla}_\xi \lambda$	$a_\alpha = \partial\lambda/\partial\xi_\alpha$	$a_\alpha = \partial_{\xi_\alpha} \lambda$
Divergence (1st order)	$\lambda = \boldsymbol{\nabla} \cdot \boldsymbol{a}$	$\lambda = \sum_\alpha \partial a_\alpha/\partial\alpha$	$\lambda = \partial a_\alpha/\partial\alpha$
Divergence (2nd order)	$\boldsymbol{a} = \boldsymbol{\nabla} \cdot \boldsymbol{A}$	$a_\alpha = \sum_\beta \partial A_{\alpha\beta}/\partial\beta$	$a_\alpha = \partial A_{\alpha\beta}/\partial\beta$

Table 1.1 – Examples of standard operations using tensor and index notations. Einstein's summation rule is used to further simplify notations (shorthand notation). Greek letters stand for x, y or z in 3D.

Chapter 2

Literature Review

Contents

This chapter gathers in a first part all the historical steps that led to the advent of the lattice Boltzmann method (LBM) as it is known today. Starting with the derivation of the set of governing equations of fluid mechanics (Navier-Stokes-Fourier equations), the milestone of kinetic theory of gases, namely, the Boltzmann equation (BE), is presented. Origins of the LBM are then traced back to lattice gas cellular automata (LGCA) before it is introduced as a method in its own rights. The second part of this chapter is dedicated to the review of thermal and compressible LBMs. After presenting the standard extensions of LBMs, the attention is focused on two particular LBMs. This allows to identify the key points for the derivation of thermal and compressible LBMs in an industrial context.

2.1   Macroscopic definition of fluid flows

Let us start introducing all the different steps that historically led to the governing equations of fluid mechanics.

2.1.1   Inviscid flows

Equations describing the motion of fluids are the result of extensive works conducted by many scientists between the 18th and the 19th centuries. Euler (1755) was one of the first to derive a macroscopic set of equations in the particular case of *inviscid* fluid flows [31]. The latter was based on two fundamental principles:

- Conservation of mass

$$\frac{\partial \rho}{\partial t} + \boldsymbol{\nabla} \cdot (\rho \boldsymbol{u}) = 0, \tag{2.1.1}$$

- Conservation of momentum

$$\frac{\partial \rho \boldsymbol{u}}{\partial t} + \boldsymbol{\nabla} \cdot (\rho \boldsymbol{u}^2) = \rho \boldsymbol{g} - \boldsymbol{\nabla} p, \tag{2.1.2}$$

where $\boldsymbol{\nabla}$ is the gradient operator of the physical space, ρ the density, $\rho \boldsymbol{u}$ the momentum, $\rho \boldsymbol{g}$ an external force, p the pressure, and $\rho \boldsymbol{u}^2$ the second-order tensor associated to the convection of momentum.

Assuming the external force $\rho \boldsymbol{g}$ is known, the above set of two equations contains three unknowns: ρ, $\rho \boldsymbol{u}$ and p. Hence this system of equations is open. Apart of boundary and initial conditions, the system can be closed giving a constitutive law of evolution for the pressure. Euler then proposed [31] that pressure should only depends on density (barotropic fluid), i.e,

$$p = p(\rho), \tag{2.1.3}$$

to obtain a well posed set of equations. Nevertheless, his work only described the motion of non-viscous (inviscid) and non-heat-conducting flows. The former restriction is linked

to the lack of shear stresses in the momentum conservation equation (2.1.2), while the latter limitation flows from the fact that: (a) the energy conservation principle is not taken into account in the above set of equations, and (b) pressure is not related to temperature T through a proper equations of state.

2.1.2 Navier-Stokes equation

A first correction to Euler momentum equation was proposed by Navier in 1821 [32] for *incompressible* flows[1]. Its purpose was to take into account viscous forces applying to an object moving at constant speed in this kind of flow. A more general derivation of the momentum equation for compressible flows was later given by Cauchy in 1829. In his work [33], Cauchy derived a general equation of motion that included non normal (shear) deformations based on continuum mechanic theory. In 1845, Stokes rederived the compressible momentum equation in the fluid mechanics framework [34], leading to the modern form of the Navier-Stokes equation:

$$\frac{\partial \rho \boldsymbol{u}}{\partial t} + \boldsymbol{\nabla} \cdot (\rho \boldsymbol{u}^2) = \rho \boldsymbol{g} - \nabla p + \boldsymbol{\nabla} \cdot \boldsymbol{\Pi}, \qquad (2.1.4)$$

with $\boldsymbol{\Pi} = \mu[\boldsymbol{\nabla} \boldsymbol{u} + (\boldsymbol{\nabla} \boldsymbol{u})^T - (2/D)(\boldsymbol{\nabla} \cdot \boldsymbol{u})\boldsymbol{\delta}] + \mu_b(\boldsymbol{\nabla} \cdot \boldsymbol{u})\boldsymbol{\delta}$ the viscous stress tensor, μ the dynamic viscosity, μ_b the bulk viscosity, D the number of physical dimensions, $\boldsymbol{\delta}$ the identity matrix, and the superscript T being the transpose operator. Eventually, combining the Euler continuity equation (2.1.1) with the above momentum equation (2.1.4) leads to the so called *Navier-Stokes equations*.

Despite this further extension of fluid flow modeling, some shortcomings still remain since several phenomena, such as conversion of mechanical energy into heat by viscosity, are still not taken into account. Furthermore, the barotropic pressure evolution equation is still oversimplified.

2.1.3 Viscous, compressible and thermal flows

Fourier was among the first to be interested in temperature fluctuations inside an *inviscid* and *incompressible* flow [35]. In 1833, he proposed to take into account these fluctuations through an energy equation. Kirschoff (1868) further included the impact of small viscous effects, and properly introduced the equation of state for the pressure[2] in the fluid mechanics framework [36]. While the authorship of the total energy equation is not really known[3], the hydrodynamic and thermodynamic behavior of *compressible* flows are most

---

[1]As a reminder, an incompressible fluid implies that density does not change along characteristic lines: $D_t\rho \equiv \partial_t\rho + \boldsymbol{u} \cdot \boldsymbol{\nabla}\rho = 0$. Thus, incompressible Euler equations read as $\boldsymbol{\nabla} \cdot \boldsymbol{u} = 0$ and $\rho\partial_t\boldsymbol{u} + \rho\boldsymbol{u} \cdot \boldsymbol{\nabla}\boldsymbol{u} = \rho\boldsymbol{g} - \nabla p$.

[2]It originated from thermodynamics, and was defined as $p = \rho r T$ with T the temperature, and r the gas constant.

[3]Truesdell claimed a compressible internal energy equation was first proposed by Neumann (1894) in the framework of fluid mechanics [37], but to the best of the author's knowledge, it still remains an open question.

commonly governed by the so called *Navier-Stokes-Fourier equations*:

$$\begin{aligned}
\partial_t(\rho) + \boldsymbol{\nabla} \cdot (\rho\boldsymbol{u}) &= 0, \\
\partial_t(\rho\boldsymbol{u}) + \boldsymbol{\nabla} \cdot (\rho\boldsymbol{u}^2) &= -\boldsymbol{\nabla}p + \boldsymbol{\nabla} \cdot \boldsymbol{\Pi}, \\
\partial_t(\rho E) + \boldsymbol{\nabla} \cdot [(\rho E + p)\boldsymbol{u}] &= -\boldsymbol{\nabla} \cdot \boldsymbol{q} + \boldsymbol{\nabla} \cdot (\boldsymbol{\Pi} \cdot \boldsymbol{u}),
\end{aligned} \tag{2.1.5}$$

supplemented with the following equation of state (ideal gas)

$$p = \rho r T, \tag{2.1.6}$$

and Fourier's law for the heat flux

$$\boldsymbol{q} = -\lambda\boldsymbol{\nabla}T. \tag{2.1.7}$$

The total energy E is defined as $E = e + u^2/2$, with $e = c_v T$ the internal energy, $c_v = c_p - r$ the heat capacity at constant volume, c_p the heat capacity at constant pressure, and r the gas constant. Finally, λ is the thermal conductivity coefficient.

In this manuscript, the above Navier-Stokes-Fourier (NSF) equations (2.1.5), (2.1.6) and (2.1.7), will be considered as the reference set of equations for the macroscopic definition of fluid flows[4]. Hence, evolution equations of multiphase and multicomponent flows will not be addressed. In the particular case of isothermal flows, only mass and momentum conservation equations will be used, and they will be supplemented with the isothermal equation of state for an ideal gas, i.e,

$$p = \rho r T_0, \tag{2.1.8}$$

with T_0 a reference temperature.

2.2   Behind the scenes of the Boltzmann equation

Since all the historical steps that led to the modern macroscopic description of fluid flows have been presented, let us now introduce the main events behind the derivation of the Boltzmann-BGK equation, and of its numerical resolution through the lattice Boltzmann method.

2.2.1   Kinetic theory of gases

In the second half of the 19$^\text{th}$ century, the works of Maxwell (1867) [38] and Boltzmann (1872) [28] greatly contributed to the advent of kinetic theory of gases (KTG) as it is known today. KTG describes the evolution of probability density functions, also called

---

[4]The name 'compressible Navier-Stokes equations' may also be encountered in the literature. In the author's opinion, this appellation is not sufficiently precise since it does not give any information on either an energy equation is taken into account or not. Hence, the name 'Navier-Stokes-Fourier equations' is preferred here.
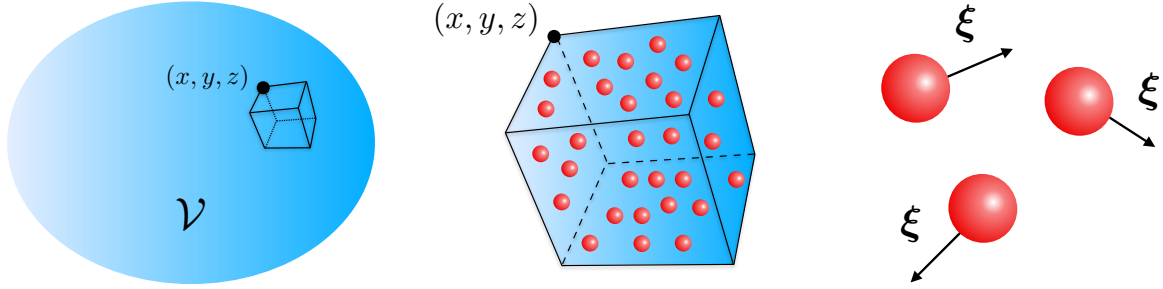
Figure 2.1 − Illustration of all the different scales used to describe matter. From left to right: macroscopic, mesoscopic and microscopic scales. $\mathcal{V}$ is the macroscopic control volume which contains a very large number of imperceptible particles. The mesoscopic approach relies on a control volume restricted to the vicinity of $\boldsymbol{x} = (x, y, z)$, and contains fewer particles. Eventually, the microscopic scale is based on the description of each particle.

hereafter velocity distribution function (VDF)[5], instead of classical macroscopic quantities, such as density ρ, velocity $\boldsymbol{u}$ and temperature T. The milestone of KTG is the Boltzmann equation (BE) which governs the evolution of the VDF $f(\boldsymbol{x}, \boldsymbol{\xi}, t)$. In a nutshell, this VDF corresponds to the probability density of finding particles at a point $(\boldsymbol{x}, t)$, and with a given velocity $\boldsymbol{\xi}$. Hence, the present *mesoscopic* description of matter lies in between microscopic and macroscopic worlds, where for the former the evolution of each particle is tracked, while the latter describes the evolution of large number of particles, averaging their perceptible quantities over a control volume $\mathcal{V}$. All three scales are illustrated in Fig. 2.1.

The transport of packets of particles, whose velocity distribution is described by f, is affected by either external forces $\boldsymbol{F}$ or collisions. Thus, the evolution of f is governed by an advection-collision equation, the BE:

$$\frac{\partial f}{\partial t} + \boldsymbol{\xi} \cdot \boldsymbol{\nabla} f + \boldsymbol{F} \cdot \boldsymbol{\nabla}_{\boldsymbol{\xi}} f = \Omega_f, \tag{2.2.1}$$

where $\boldsymbol{\nabla}(= \boldsymbol{\partial}/\boldsymbol{\partial x})$ and $\boldsymbol{\nabla}_{\boldsymbol{\xi}}(= \boldsymbol{\partial}/\boldsymbol{\partial \xi})$ are gradient operators with respect to geometrical and velocity spaces. The left-hand side (LHS) term corresponds to the advective part in both geometrical ($\boldsymbol{\xi} \cdot \boldsymbol{\nabla} f$) and velocity ($\boldsymbol{F} \cdot \boldsymbol{\nabla}_{\boldsymbol{\xi}} f$) spaces, whereas the right-hand side (RHS) term is linked to the rate of change of f originating from collisions. The main difficulty lies in the definition of the collision term Ω_f, which contains all the underlying physics. It is interesting to note that Boltzmann itself only had a rough idea on how to model collision processes. He then proposed to assimilate Ω_f with a binary collision operator.

Despite the beauty and the meaningfulness of the results flowing from the work of Boltzmann [28][6], it remained misunderstood by the scientific community for quite a long time. It is only after his death that experiments confirmed the validity of his work in

---

[5]This appellation is preferred in this manuscript since the distribution of particles is done with respect to their velocity.

[6]The H-theorem is the most famous one, and it constitutes the very first derivation of the second law of thermodynamics, which says the total entropy of a closed system cannot decrease over time.

1906. It would not be before 1920 for a new collision model to be proposed by Chapman and Enskog. Their work [39] allowed to link NSF and Boltzmann equations. The only blot on the picture was the complexity of their collision model.

In 1954, Bhatnagar, Gross and Krook proposed a new collision model, named after them (BGK) [40], to circumvent the complexity of the previous one, and to include the physics of dense fluids[7]. This collision operator relies on a very simple idea: *collisions induce a deviation with respect to their local equilibrium state, which is recovered after a time τ called relaxation time.* Hence the mathematical expression of their collision term reads as

$$\Omega_f^{\mathrm{BGK}} = -\frac{1}{\tau}\left(f - f^{(eq)}\right), \tag{2.2.2}$$

with the Maxwellian (or Maxwell-Boltzmann) equilibrium state expressed as

$$f^{(eq)} = \frac{\rho}{(2\pi r T)^{D/2}} \exp\left[-\frac{(\boldsymbol{\xi}-\boldsymbol{u})^2}{2rT}\right], \tag{2.2.3}$$

in D-dimensional space.

A numerical resolution of the Boltzmann-BGK equation could have then readily be derived thanks to all the above derivations. Nevertheless, tools necessary to the numerical solving of the BE were not yet available.

2.2.2 Lattice gas cellular automata

It is not until the second half of the 20th century that the notion of numerical (space and time) discretization was introduced. Von Neumann [41] developed one of the first cellular automata using boolean operators. Parallel activities led Broadwell [42] in 1964, and Gatignol [43] in 1975, to propose a velocity discretization of the BE, namely, the lattice Boltzmann equation (LBE). Of course, the numerical discretization was still lacking in their model to make it of any use from the numerical simulation point of view.

In 1973, lattice gas cellular automata (LGCA) arised from the numerical simulation of the LBE using cellular automata. One of the first model was developed by Hardy, Pomeau & Pazzis, hence its name the 'HPP model' [44]. This LGCA was based on a Fermi-Dirac distribution function for the modeling of the equilibrium state $f^{(eq)}$ toward which collisions make f to relax. Nevertheless, the HPP model was not able to recover the macroscopic behavior of the NSF equations. Improvements were then proposed by Frisch, Hasslacher & Pomeau (2D FHP model [45]), and d'Humière (3D face centered hypercube [46]) to recover the proper macroscopic behavior through better symmetry properties of the underlying velocity discretization. Eventually, these models quickly declined due to: (1) numerical noise induced by boolean operators, and (2) Galilean invariance issues originating from the use of Fermi-Dirac distribution functions.

Despite its flaws, LGCA were shown to be a first attempt allowing the recovery of the NSF equations, through the numerical resolution of the LBE using cellular automata.

---

[7]The BE supplemented with this BGK collision model is most commonly known as the *Boltzmann-BGK equation.*

2.2.3   Lattice Boltzmann method

To improve LGCA, it was then proposed to use: (1) floating operations to suppress the numerical noise, and (2) the Maxwell-Boltzmann equilibrium state to recover the Galilean invariance principle. In 1988, McNamara & Zanetti [47] created one of the first lattice Boltzmann method (LBM) which was based of the above improvements of LGCA, but their model suffered from a complex collision model. This deficiency was quickly overcome by Higuera & Jiménez (1989) linearizing the collision operator [48]. A further improvement was then proposed by Chen [49] and Qian [50] in 1992. Their model were based on the use of a simple collision modeling: the BGK collision operator. This eventually led to the LBM-BGK as it is known today.

One last point needed to be clarified. Indeed, the LBM was shown to allow the recovery of the NSF macroscopic behavior in an *a posteriori* way through LGCA. Hence no direct link was known between the LBM and the BE until the work of He & Luo [51] in 1997. It is only after that, the LBM was shown to derive in an *a priori* way from the BE, and thus to be able to recover the macroscopic behavior of NSF equations without resorting to LGCA.

2.3   Review on thermal and compressible LBMs

For the last 25 years, LBMs have gained attention as a numerical tool for multiphysics simulations [52]. Nevertheless, LBMs suffer from stability issues when dealing with high-Reynolds and/or moderate to high-Mach number flow simulations. In the present section, the most common attempts to derive thermal and compressible LBMs are presented.

2.3.1   The big picture

In the past two decades, two major lines of research have been explored. The first one consists in increasing the number of free parameters modifying the velocity discretization and the discrete equilibrium state, keeping the standard 'Collide & Stream' algorithm. This method is inherited from the *a posteriori* way of deriving LGCA. The second solution focuses on the numerical discretization of the LBE comparing several numerical schemes. It relies on a purely numerical viewpoint of stability limitations. With this approach, it is assumed the way the LBE is obtained only plays a minor role on stability issues. Of course, the most accurate and robust approaches combine the two above solutions.

Other non-numerical limitations encountered with standard LBMs are the fixed values for both the Prandlt number ($\text{Pr} = 1$) [8], and the heat capacity ratio ($\gamma = 1 + (2/D)$). The first limitation implies that when the dynamic viscosity is fixed, then the thermal diffusivity coefficient cannot be chosen freely, and vice versa. The second restriction is directly linked to the number of internal degrees of freedom (DoFs) of gas molecules. Indeed, $\gamma = 1 + 2/b$ with b the number of internal DoFs. When $b = D$, only translational DoFs are taken into account, which restricts the corresponding LBM to the simulation of

---

[8]As a reminder, the Prandtl number is the ratio between dynamic and thermal diffusivity coefficients, i.e, $\text{Pr} = \mu/\alpha$ with $\alpha = \lambda/(\rho c_p)$.

monatomic gas flows. In order to simulate realistic flows, such as air, at least rotational DoFs need to be included in the definition of either the internal energy or the total energy.

This eventually led to the derivation of three kinds of LBMs for the simulation of thermal and fully compressible flows with variable Prandtl number and heat capacity ratio: (1) multispeed (or high-order), (2) double distribution function, and (3) hybrid LBMs. The multispeed (MS) approach is a direct extension of standard (second-order) isothermal and weakly compressible LBMs. It consists in adding discrete velocities in the LBE, and taking into account high-order velocity terms in the definition of the discrete equilibrium state. The double distribution function (DDF) approach aims at introducing the notion of temperature fluctuations through the evolution of a second (energy) distribution function. Hence both aerodynamic and thermodynamic relaxation processes can be decoupled with this type of LBM, which eventually allows to independently choose both dynamic and thermal diffusivity coefficients. Regarding the hybrid LBM, it is based on a two-equation approach, as for the DDF-LBM, but the energy equation is now solved using standard numerical schemes (finite volume, finite difference, etc.).

In what follows, the main characteristics, strengths and flaws of compressible LBMs will be emphasized. Eventually, their ability to deal with the above restrictions will also be discussed.

2.3.2   Moment-matching equilibrium states

Most LBMs below are constructed modifying either the velocity discretization or the equilibrium distribution function (EDF) $f^{(eq)}$. First LBMs dedicated to the simulation of thermal and compressible are no exception to these rules. All of them follow the path of LGCA in the sense that they can all be shown to lead to the physics of interest in an *a posteriori* way. These models relies on 'moment-matching' techniques whose aim is to recover the macroscopic behavior of interest enforcing the EDF expansion coefficients to match certain values, eventually allowing an *a posteriori* recovery of the physics of interest.

This kind of approaches was notably proposed by Alexander *et al.* (1993) to derive thermal and weakly compressible LBMs using a single distribution function (SDF). In their work [53], they added four discrete speeds to the standard D2Q9 LBM, and used the 'moment-matching' technique to derive the proper form of their EDF using the new D2Q13 MS-LBM. Due to the use of a BGK collision model which only includes one relaxation time[9], their model was restricted to the simulation of thermal flows with $Pr = 1/2$ and $\gamma = 1 + 2/D$. The same year, Qian and his coworkers [56] further extended this approach to 3D MS-LBMs. Nevertheless, these models encountered severe stability issues. That is why Chen *et al.* (1994) proposed to include both $\mathcal{O}(u^4)$ terms in the definition of $f^{(eq)}$, and symmetry conditions that must be followed by the lattice of discrete velocities [57, 58]. This eventually led to a more stable numerical scheme with respect

---

[9]At least two relaxation times are required to correctly decouple aerodynamic and thermodynamic relaxation processes. In the context of SDF LBM, one way to deal with the Prandtl number limitation is to use a matrix form of the collision model [54], as originally proposed by d'Humière [55] in the isothermal context.

to previous models. Nonetheless, severe stability issues were still present for moderate temperature fluctuations with this kind of models [59].

At this point, all proposed models were based on extensions of standard LBMs. This means all discrete velocities were pointing towards grid nodes, which allowed the use of the *most efficient and accurate* numerical discretization, namely, the 'Collide & Stream' algorithm. For most authors, this was why all above approaches were encountering severe stability limitations. To deal with this issue, they proposed to use the so called 'off-lattice' LBMs. The latter are based on particular lattice of velocities, which do not point towards grid nodes. They are two main advantages to these models: (1) less discrete velocities are required to recover the physics of interest, and (2) interpolation techniques are used to obtain VDFs values at grid nodes, hence introducing some numerical dissipation. Pavlo *et al.* (1998) were among the first to try this kind of approach for the stabilization of MS-LBMs [60]. Watari & Tsutahara (2003) improved the numerical stability of their model using a new numerical discretization of the collision term [61]. This WT model was eventually extended to compressible flows with a variable heat capacity ratio [62].

Another famous MS-LBM dedicated to the simulation of compressible flows with variable heat capacity ratio was proposed by Kataoka & Tsutahara in 2004. Their KT model included further constraints on internal DoFs for the derivation of the EDF. When coupled with the 'Collide & Stream' algorithm, severe stability issues were encountered, and this was overcome using a more robust, and *a fortiori* less accurate, numerical discretization of the LBE, namely, the Crank Nicolson numerical scheme [63]. Nevertheless, the Prandlt number was still fixed in their approach. This is why Li *et al.* (2007) used a double distribution function (DDF) MS-LBM [64, 65]. Hence the second relaxation time could be adjusted in order to obtain the correct Prandtl number. Furthermore, they proposed to replace the 'Collide & Stream' algorithm with rather complex space and time discretizations[10] to increase the numerical stability of their model.

Other LBMs based on either the WT or the KT models can be found in the literature [67–70], but they only try to either increase the stability testing new numerical discretization, or reduce the number of discrete velocities.

In sum, LBMs based on the 'moment-matching' construction of the EDF definitely follow the path of LGCA. They suffer from severe stability issues whose origin is considered to be linked to the numerical discretization by the above authors. Hence solutions which do not rely on the kinetic theory are, most of the time, proposed to stabilize their MS-LBMs. Nevertheless, these high-order LBMs succeed in simulating compressible flows with variable Prandtl number and heat capacity ratio, with about 50 discrete velocities for the most demanding models in 3D. Of course, the CPU time needed to solve each of the discrete BE is much higher than for the 'Collide & Stream' algorithm.

---

[10]For the space discretization, a fifth-order weighted essentially nonoscillatory (WENO) scheme, and a the total variation diminishing (TVD) scheme, were used to capture the discontinuities. Furthermore an implicit-explicit (IMEX) Runge-Kutta was used for the time-marching approach [66]. It consists in using an explicit time discretization of the advective part of the LBE while the collision part is discretized using an implicit time discretization, both belonging to the family of Runge-Kutta numerical schemes.

2.3.3   Non-Maxwellian equilibrium states

Due to the severe aforementioned stability issues encountered with the discrete EDF, which is based on the continuous Maxwellian EDF (2.2.3), some authors tried to use a different type of EDF. This was motivated by the fact that one has to expand the Maxwellian EDF in a polynomial series to derive the EDF associated to the LBE. The truncation of the polynomial series, at an order N, eventually led to the omission of $\mathcal{O}(u^{n>N})$ terms, hence the common limitation to weakly compressible flow of standard LBM. Two types of new EDFs were then proposed using: (1) delta (Kronecker), and (2) circular functions.

The delta-function based MS-LBM was proposed by Sun in 1998. It relied on a local adaptive velocity discretization of the BE, where discrete velocities were related to the local macroscopic velocity and internal energy [71–73], and consequently needed to be computed at each grid point and at each time step. Furthermore, even if the 'Collide & Stream' algorithm was used in his approach, complex reconstruction techniques were required to get values of the VDF at the current node. Finally, the relaxation time linked to the dynamic viscosity could not be chosen freely to avoid huge memory and CPU consumption. Although this model was originally derived for the simulation of the 2D compressible Euler equations, supplemented with an energy equation, several extensions were proposed shortly after by Sun & Hsu (2003, 2004) to recover the behavior of the 3D NSF equations [74, 75]. Nevertheless, they were not able to improve memory and CPU consumptions.

Later, Qu *et al.* (2007) proposed to replace the Maxwellian EDF (2.2.3) by a circular function [76, 77]. Using these kind of functions, it was possible to replace integrals over the whole velocity space by line integrals over a circle, within which all the mass, momentum and energy were supposed to be contained. Furthermore, standard polynomial series expansions were replaced with third-order Lagrange interpolated polynomials, in order to satisfy quadrature constraints derived from line integrals. Finally, energy levels were associated to each VDFs in order to capture temperature fluctuations. This MS-LBM was shown to properly recover the compressible Euler equations supplemented with an inviscid energy equation. Nevertheless, the extension to the compressible NSF equations seemed complicated since one of the constraint (linked to the fourth-order moments of the VDF, i.e, heat flux) could not be recovered using circular functions. To deal with this issue, two types of circular functions were used by Qu [78]. Nevertheless, the resulting model was not able to simulate compressible flows with $\mathrm{Pr} \neq 1$ due to the use of a single BGK collision model. Several extensions to this model were also proposed to circumvent the Prandtl number limitation [64, 79].

To summarize, two ways of building new EDFs were proposed in order to increase the stability range of compressible LBMs. Even though strong improvements were shown using the above models, the accurate and efficient 'Collide & Stream' algorithm was, most of the time, changed for more robust and less efficient numerical schemes. Hence the superiority of the above LBMs over Maxwellian EDF based LBMs is generally not clear.

2.3.4 Partial conclusions

All in all, both aforementioned Maxwellian and non-Maxwellian EDF based compressible LBMs have been built using *non-systematic* approaches. This is a huge flaw in the perspective of possible extensions to any kind of dimensions (1D, 2D, 3D), or physics (multiphase, multicomponent, etc.). Furthermore, the use of complex numerical schemes drastically deteriorates the efficiency of the method, with respect to standard LBMs, in two ways: (1) the time needed to update all VDFs at a grid node becomes close or even higher than for standard CFD methods, and (2) the accuracy/simplicity induced by the use of non-body-fitted Cartesian-type grids is lost. Thus the simulation of flows around complex geometries starts getting complicated again. Consequently, all the above models do not fall within the scope of this PhD work.

Nevertheless, some interesting facts need to be remembered from this brief literature review. First, a MS-LBM is mandatory to recover either the isothermal behavior of the compressible Navier-Stokes equations, or the behavior of the NSF equations. Second, when a SDF-LBM is used, the BGK collision model is not sufficient to simulate flows with $\Pr \neq 1$. Both a DDF-LBM or a more complex collision model can be used to deal with this issue. Third, a shock-capturing technique is compulsory to handle discontinuities in realistic conditions (low dynamic and thermal diffusivity coefficients). Instead of using complex time/space discretization of the LBE, a local modification of diffusivity coefficients through the use of a shock sensor may bring enough numerical stability without drastically deteriorating the efficiency of the whole method.

Two compressible LBMs compliant with these three requirements were recently published in the literature. They are respectively based on: (1) an entropic LBM (ELBM), and (2) an hybrid LBM. While the compressible DDF-ELBM can be classified as an academic model, the compressible hybrid LBM implemented in PowerFLOW software definitely belongs to the family of industry-oriented solvers.

Before moving to their description, it should be noted that another kind of numerical solver of the LBE, originating from gas kinetic schemes and called discrete unified gas kinetic scheme (DUGKS), could also be used for the simulation of thermal and compressible flows [80, 81]. These DUGKS are nothing more than finite volume based numerical solvers of the LBE. Hence they are far less accurate and efficient than LBMs based on the 'Collide & Stream' algorithm [82]. Nevertheless, they are particularly interesting for flows including large variations of the Knudsen number[11]. This is clearly out of the scope of the present PhD work. Thus these DUGKS will not be considered in the rest of the manuscript.

2.3.5 State of the art

The basic features of two remarkable types of compressible MS-LBM are now presented. Particular emphasis will be placed on their strengths, flaws, and applicability ranges.

---

[11]As a reminder, the Knudsen number is the ratio between the mean free path l (mean distance between two successive collisions) and a characteristic length L.

2.3.5.a Entropic LBM for compressible flows

Starting with the compressible MS-ELBM [83], it was proposed by Frapolli and his coworkers in end-2015. Their model relies on several extensions of the standard ELBM. Before reviewing them, let us recall the basic feature of ELBM.

These models ensure the H-theorem to be valid after the velocity discretization of the BE. This is done solving a minimization problem at each grid point and time step. This leads to a variable relaxation time that locally self-adjusts to the flow. Hence a non-constant dynamic viscosity is obtained with ELBMs, especially when underresolved mesh grids are used for the simulation of high-Reynolds (turbulent) flows. This particular feature of ELBMs led to several criticisms from part of the lattice Boltzmann community [84–86]. Nevertheless, it is a well known fact among the CFD community that underresolved turbulent scales must be accounted for through the use of a subgrid scale (SGS) model [2, 87]. Furthermore, the behavior of the ELBM was shown to share similarities with the standard Smagorinsky SGS model such as: (1) the form of the additional eddy viscosity which scales as the strain rate tensor, and (2) whose value tends towards zero when the resolution of the mesh grid is increased [88]. Hence the numerical behavior of the ELBM seems pretty sound, in the author's opinion. Nevertheless, it should be noted that solving the minimization problem induces a nonnegligible extra CPU cost, that is why one may prefer to use approximations to the minimization problem [88–92]. In the context of this compressible ELBM, the variable relaxation time seems also to act as a shock-capturing technique since it automatically adjusts itself to strong local gradients without deteriorating the accuracy of smooth regions [83, 93].

Concretely, the compressible ELBM relies on the derivation of admissible 1D high-order lattices to recover the macroscopic behavior of interest [94]. The extension to higher physical dimensions is then straightforwardly obtained using the tensor product of these 1D velocity sets. Hence lattices proposed by Frapolli *et al.* have the form DdQq^d, with q^d being the number of discrete velocities in d-dimensions[12]. This way of building LBMs is not the most efficient regarding the number of discrete velocities, but it allows to drastically ease the overall process since only 1D calculations are required to impose the correct physics in any physical dimensions (see Sec. 3.3.3 for more details). In their model, the D1Q7 and its extensions are used to simulate both academic and industrial test cases [93].

Another interesting feature of this model concerns its discrete EDF. While all the above compressible LBMs are based on *polynomial approximations* of the continuous EDF, this model keeps the Gaussian shape of the continuous EDF where equilibrium density, velocity and temperature are now obtained through the resolution of another minimization problem. This non-polynomial form of the EDF allows to deal with the two major flaws of the polynomial form, i.e, bounded positivity domain and inaccuracy for large velocity/temperature variations. One may wonder if the computation of such an EDF, solving a minimization problem at each grid point and time step, may or not be

---

[12]Standard LBMs such as the D2Q9 and the D3Q27 lattices also result from this way of building lattices. They are respectively 2D and 3D tensor products of the D1Q3 lattice which is a velocity discretization allowing the recovery of isothermal and weakly compressible Navier-Stokes equations.

affordable. In fact, this particular evaluation was shown to be no more than two times the computational time required for the evaluation of a fourth-order[13] polynomial EDF [93].

The last interesting property introduced in this compressible ELBM concerns the 'shifting method'. The latter corresponds to a velocity-shift of the previously introduced lattice of velocities in order to widen the Mach number stability range [83]. Indeed, the accuracy of the velocity discretization is directly linked to the deviation of the local Mach number with respect to the traditional reference at rest. In order to increase the stability range of the compressible ELBM, the velocity discretization is done in a comoving reference frame. The use of such a comoving reference frame to increase the numerical stability of LBM was already introduced by Geier et al. [95, 96] a decade ago (2006). In their 'cascaded' (central moment) approach, they proposed to relax moments in a comoving reference frame to increase the numerical stability of LBM for the simulation of high-Reynolds number flows in underresolved conditions. Nevertheless, all steps of the ELBM are done in the comoving reference frame here, which sort of extends Geier's model to the whole 'Collide & Stream' algorithm.

Regarding boundary conditions [97], a multi-layer version of the Tamm-Mott-Smith boundary condition was developed for this compressible ELBM [97,98]. One of the main advantage of this kind of boundary conditions is its relative simplicity, and its straight-forward extension to curved walls. Indeed, once missing populations are identified at boundary condition nodes, they are computed using Grad's representation of the VDFs, which is also encountered in regularized boundary conditions [99]. This representation allows to decompose missing populations into equilibrium and nonequilibrium parts, which are then computed using local macroscopic quantities and their gradients. Target values used for the reconstruction are finally defined through a simple interpolation based on wall and adjacent fluid node values.

The inclusion of internal DoFs allowing the simulation of polyatomic flows is done in the same spirit as in Refs. [100, 101]. Hence a second population is used to track the evolution of rotational and vibrational (internal) DoFs [97]. This means this compressible MS-ELBM is based on the DDF formalism.

This ELBM was successfully combined with the octree based mesh refinement technique by Dorschner, Frapolli *et al.* in 2016. To the best of the author's knowledge, this is the first and only work dealing with industrial-type refinement technique for the simulation of high-Reynolds and high-Mach number flows in underresolved conditions [102].

Finally, Frapolli's model is able to simulate thermal and fully compressible flows up to a freestream Mach number $M_0 \approx 3$ and a temperature ratio $T_{\max}/T_{\min} \approx 4.5$. With the exception of flows encountered in aeronautical burners, the validity range of this LBM is within the scope of transonic and slightly supersonic flows of interest for aeronautical industry groups.

The above characteristics perfectly fit all the requirements of the present PhD work – strong mathematical background, validity domain, ability to handle complex geometries, 'Collide & Stream' algorithm, octree based refinement technique – with one exception. The above DDF-MS-ELBM relies on two D3Q7³ (D3Q343) lattices which makes it un-

---

[13]This is the minimal order required for the recovery of the NSF equations using a fourth-order MS-LBM.

affordable from the industry point of view. Nevertheless, all notions introduced by this model make it the most interesting compressible LBM from the academic point of view.

2.3.5.b   Hybrid LBM for compressible flows

The last compressible LBM studied in this review belongs to the commercial software 'PowerFLOW'. Even if this model is considered to be a **black box**, some information are available in the literature. Hence its consistency is analysed below.

This hybrid MS-LBM would have never seen the light of day without the pioneer work of Grad [103, 104]. Indeed, Grad proposed in 1949 a new derivation of fluid models as approximations of the BE. In his work, the VDF was expanded using Hermite polynomials. This allowed a straightforward computation of polynomial coefficients through the definition of the VDF moments. Projecting the BE on the basis of Hermite polynomials, equations linked to Hermite coefficients were then obtained. Successive approximations of these coefficients, with respect to the Knudsen number, eventually led to several fluid models of increasing complexity, namely, thermal Euler equations, NSF equations, Burnett equations, etc.

In 1998, Shan & He proposed to use the work of Grad to build a direct relationship between the BE and its velocity discretization through the Gauss-Hermite quadrature rule [105]. Shan *et al.* (2006) further took advantage of the Hermite polynomial framework to build lattices in a *systematic way*, and proposed a 39-velocity discretization of the BE to construct a LBM able of simulating 3D isothermal flows without any Mach number restriction [106]. In the meantime, a stabilization technique dedicated to the standard (second-order) LBM was proposed by Latt & Chopard (2005, 2006) for the simulation of high-Reynolds number flows [107, 108]. It was based on the Hermite polynomial expansion of the VDF including up to first-order Knudsen terms (Navier-Stokes level). Shortly after (2006), this so called 'regularization step' was extended to third-order LBMs, such as the D3Q39, for the simulation of finite Knudsen number flows by Zhang, Shan and Chen [109].

Further results about thermal and compressible LBMs were presented by Nie, Shan and Chen in 2008. In a first paper, they improved the previous *systematic way* of building lattices [106] by including symmetry properties to ensure the Galilean invariance of high-order LBMs. Both dynamic and thermal diffusivity coefficients of the fourth-order D3Q121 lattice were then shown to be Galilean invariant [110]. They also introduced a simple way to include rotational and vibrational DoFs for the simulation of polyatomic gases [101]. Finally, they proposed in 2009 an hybrid high-order LBM based on the coupling of the D3Q39 and a finite difference discretization of the entropy equation [111]. In their paper, they used a Lax-Wendroff scheme to discretize the entropy equation. Furthermore, a shock sensor was used to locally increase the heat diffusion in the entropy equation. Even if it is not specified in their paper, one can suppose that another shock sensor is also employed to locally add artificial dynamic viscosity through the D3Q39 LBM. Even if it is not known for sure that the proposed model is part of PowerFLOW software, the appellation 'PowerFLOW-Sup' is visible on the legend of Fig. 4 in Ref. [111].

To the best of the author's knowledge, the first official paper about the PowerFLOW

compressible LBM is based on the works of Fares and his coworkers [112], and was presented at the 52$^{\text{nd}}$ AIAA Aerospace Sciences Meeting held in 2014. In their paper, they demonstrated the viability of hybrid MS-LBM as a numerical tool for the simulation of compressible flows in an industrial context. Their model is based on an isothermal MS-LBM composed of 39 velocities, which is coupled with the entropy equation, the latter being solved using standard numerical discretization techniques. The MS-LBM is used to properly recover the isothermal behavior of Navier-Stokes equations without any restriction on the Mach number. This model was shown to give accurate results up to $M_0 \approx 2$.

Since then, a lot of papers have shown the viability of the coupling between this hybrid MS-LBM and the regularization step. The latter can now be considered as a well established stabilization technique for the simulation of thermal and fully compressible flows around realistic geometries [25, 113].

2.4 Conclusions

Starting with the macroscopic description of fluid flows, a thorough historical review of the Euler, Navier-Stokes-Fourier and the lattice Boltzmann equations has been proposed in this chapter. The LBM was shown to derive from two successive discretizations (velocity and numerical) of the Boltzmann equation, even if it was originally derived via LGCA.

A review of thermal and compressible LBMs was then proposed. The main strengths and flaws of the most popular compressible LBMs were presented, allowing to extract minimal requirements for the derivation of such models in the context of the present PhD work. More attention was paid to two particular compressible LBMs: Frapolli's DDF-MS-ELBM, and the compressible hybrid MS-LBM implemented in PowerFLOW software. While the first was shown to include new paradigms of uttermost interest, this ELBM is not yet affordable from the industrial point of view. On the contrary, the hybrid model is based on the coupling of a isothermal D3Q39 LBM and the finite difference discretization of the entropy equation. It is shown to lead to accurate results up to a freestream Mach number of 2 for both academic and industrial oriented test cases. With 'only' 40 equations to be solved (39 lattice Boltzmann equations and the entropy equation), this model is definitely the most efficient compressible LBM available in the literature.

Based on the foregoing, and to be compliant with requirements from the industry, the present work will first focus on regularized collision models as stabilization techniques for the simulation of thermal and compressible flows. Furthermore, this will be done using SDF-MS-LBMs based on the 'Collide & Stream' algorithm. Due to its versatility, the regularization step will be studied in depth for a large number of velocity sets. Possible improvements will be proposed and validated against numerical test cases (Chap. 4). A linear stability analysis of the proposed extension will study the stability property of the new regularization step (Chap. 6). Finally, few elements about 3D DDF-MS-LBMs are also provided in App. A. For the sake of completeness, the macroscopic behavior deriving from DDF models is recalled in App. C.

Chapter 3

Lattice Boltzmann Method

Contents

This chapter describes the basic features of the lattice Boltzmann method (LBM). Starting from the Boltzmann equation (BE), all the different steps leading to the lattice Boltzmann equation (LBE) are first considered. The most common LBM is then obtained through a particular space and time discretization of the LBE, namely, the 'Collide & Stream' algorithm. Finally, a simple way to construct velocity sets compliant with this numerical scheme is presented. All of these are introduced in the context of the Hermite polynomial framework.

3.1   From BE to LBE

Hereafter, all quantities are defined in the D-dimensional Cartesian space $\mathbb{R}^D$. Properties concerning tensor products and Hermite polynomials in $\mathbb{R}^D$ are based on the works of Grad and Shan [104, 106]. For the sake of completeness, all the necessary material for the proper understanding of all derivations related to the Hermite polynomial framework are recalled in App. B.

3.1.1   Boltzmann equation

In kinetic theory, gases are modeled by the velocity distribution function (VDF) $f(\boldsymbol{x}, \boldsymbol{\xi}, t)$ describing the probability density of finding a *fictive* particle at position $\boldsymbol{x}$, time t and with a mesoscopic velocity $\boldsymbol{\xi}$. When no external accelerations are considered, this VDF evolves through time and space in accordance to the force-free form of the BE:

$$\partial_t f + \boldsymbol{\xi} \cdot \boldsymbol{\nabla} f = \Omega_f, \tag{3.1.1}$$

where the center dot denotes the scalar product over $\mathbb{R}^D$, $\boldsymbol{\nabla}$ is the gradient operator associated to the physical space and Ω_f is the collision operator. The macroscopic quantities of interest (density ρ, momentum $\rho\boldsymbol{u}$, and total energy ρE) are recovered summing up their mesoscopic counterparts over the velocity space:

$$\begin{cases} \rho = \displaystyle\int f \, \mathrm{d}\boldsymbol{\xi}, \\ \rho\boldsymbol{u} = \displaystyle\int f \boldsymbol{\xi} \, \mathrm{d}\boldsymbol{\xi}, \\ 2\rho E = \displaystyle\int f \xi^2 \, \mathrm{d}\boldsymbol{\xi}, \end{cases} \tag{3.1.2}$$

with integrals computed over $\mathbb{R}^D$. Hereafter, integration bounds will be omitted for the sake of clarity.

Regarding the collision model Ω_f, it must satisfy the conservation of mass, momentum and total energy:

$$\int \Omega_f \, \Phi(\boldsymbol{\xi}) \, \mathrm{d}\boldsymbol{\xi} = \boldsymbol{0}, \tag{3.1.3}$$

with $\Phi(\boldsymbol{\xi}) = (1, \boldsymbol{\xi}, \xi^2/2)$. This collision process induces a relaxation of the VDF to the local thermodynamic equilibrium

$$f^{(eq)} = \frac{\rho}{(2\pi rT)^{D/2}} \exp\left(-\frac{c^2}{2rT}\right), \tag{3.1.4}$$

where $\boldsymbol{c} = \boldsymbol{\xi} - \boldsymbol{u}$, r is the gas constant and T the thermodynamic temperature. Most common collision models are based on linearized ones, such as the single relaxation time (SRT) collision term of Bhatnagar-Gross-Krook (BGK) [40]

$$\Omega_f^{\mathrm{BGK}} = -\frac{1}{\tau}\left(f - f^{(eq)}\right). \tag{3.1.5}$$

Their simplicity makes these collision operators very appealing as a first step to model the collision process outcomes. Nevertheless, only one parameter, the relaxation time τ, is included in SRT collision models, which limit their scope of applications as explained in the end of Sec. 3.1.3.

3.1.2   Projection onto the Hermite polynomial basis

In the present context, solutions of Eq. (3.1.1) are sought in the form of Hermite polynomials [105],

$$f(\boldsymbol{x}, \boldsymbol{\xi}, t) = \omega(\boldsymbol{\xi}) \sum_{n=0}^{\infty} \frac{1}{n!(rT_0)^n} \boldsymbol{a}^{(n)}(\boldsymbol{x}, t) : \boldsymbol{\mathcal{H}}^{(n)}(\boldsymbol{\xi}), \tag{3.1.6}$$

where ":" stands for the full contraction of indexes, T_0 is a reference temperature, $\boldsymbol{a}^{(n)}$ is the (tensor of) coefficient(s) related to the Hermite tensor $\boldsymbol{\mathcal{H}}^{(n)}$, both being $n-$rank tensors, and $\omega(\boldsymbol{\xi})$ is the weight function. They are defined as follows:

$$\boldsymbol{a}^{(n)}(\boldsymbol{x}, t) = \int f(\boldsymbol{x}, \boldsymbol{\xi}, t) \boldsymbol{\mathcal{H}}^{(n)}(\boldsymbol{\xi}) \, \mathrm{d}\boldsymbol{\xi}, \tag{3.1.7}$$

where

$$\boldsymbol{\mathcal{H}}^{(n)} = \frac{(-rT_0)^n}{\omega(\boldsymbol{\xi})} \boldsymbol{\nabla}_{\boldsymbol{\xi}}^n \omega(\boldsymbol{\xi}) \tag{3.1.8}$$

with

$$\omega(\boldsymbol{\xi}) = \frac{1}{(2\pi rT_0)^{D/2}} \exp\left(-\frac{\xi^2}{2rT_0}\right), \tag{3.1.9}$$

$\boldsymbol{\nabla}_{\boldsymbol{\xi}}^n$ being the n-th derivative with respect to the velocity space. It should be noted that Eq. (3.1.8) is not the standard definition of Hermite polynomials. Here, the coefficient rT_0 is taken into account in order to keep the very same definition of these polynomials for both isothermal and thermal LBMs. It allows to have temperature-independent weights even in the thermal case (the curious reader may refer to App. B for more information).

   The polynomial expansion (3.1.6) can be seen as the decomposition of f onto an orthogonal polynomial basis, since Hermite tensors are orthogonal with respect to the following scalar product:

$$\langle g|h \rangle \equiv \int \omega(\boldsymbol{\xi}) g(\boldsymbol{\xi}) h(\boldsymbol{\xi}) \mathrm{d}\boldsymbol{\xi}. \tag{3.1.10}$$

Thus $\boldsymbol{a}^{(n)}$ can simply be obtained as a projection of f onto this orthogonal basis $\boldsymbol{a}^{(n)} = \langle \boldsymbol{\mathcal{H}}^{(n)} | f/\omega \rangle$. For the sake of clarity, the list of function variables will be omitted throughout the rest of this chapter, except in Sec. 3.2, where the space/time discretization of the LBE is presented.

By construction, $\boldsymbol{a}^{(n)}$ can be linked to the familiar hydrodynamic moments [106,114]:

$$\begin{cases} \boldsymbol{a}^{(0)} = \rho, \\ \boldsymbol{a}^{(1)} = \rho \boldsymbol{u}, \\ \boldsymbol{a}^{(2)} = \boldsymbol{\Pi} + \rho(\boldsymbol{u}^2 - \boldsymbol{\delta}), \\ \boldsymbol{a}^{(3)} = \boldsymbol{Q} + \boldsymbol{u}\boldsymbol{a}^{(2)} + (1 - D)\rho\boldsymbol{u}^3, \\ \boldsymbol{a}^{(4)} = \boldsymbol{R} - \boldsymbol{P}\boldsymbol{\delta} + \boldsymbol{\delta}^2, \end{cases} \tag{3.1.11}$$

where $\boldsymbol{\delta}$ is the identity matrix, $\boldsymbol{\delta}^2$ is the fourth-order identity tensor, and

$$\boldsymbol{\Pi} = \int f\boldsymbol{c}^2 \, \mathrm{d}\boldsymbol{\xi}, \quad \boldsymbol{Q} = \int f\boldsymbol{c}^3 \, \mathrm{d}\boldsymbol{\xi}, \quad \boldsymbol{R} = \int f\boldsymbol{c}^4 \, \mathrm{d}\boldsymbol{\xi}. \tag{3.1.12}$$

In order to create a *systematic* link between the BE and its macroscopic counterpart, Eq. (3.1.1) is projected onto the Hermite tensor basis using the projection operator $\langle \ldots | \ldots \rangle$ defined in Eq. (3.1.10):

$$\partial_t \left(\boldsymbol{a}^{(n)} \right) + \boldsymbol{\nabla} \cdot \left(\boldsymbol{a}^{(n+1)} \right) + rT_0 \boldsymbol{\nabla} \boldsymbol{a}^{(n-1)} = \Omega^{\mathrm{BGK}}. \tag{3.1.13}$$

Here the BGK approximation (3.1.5) is adopted for the computation of the collision term, i.e., $\Omega^{\mathrm{BGK}} = -(\boldsymbol{a}^{(n)} - \boldsymbol{a}_{eq}^{(n)})/\tau$, where $\boldsymbol{a}_{eq}^{(n)} = \langle \boldsymbol{\mathcal{H}}^{(n)} | f^{(eq)}/\omega \rangle$. The computation of these coefficients is straightforward since the expression of $f^{(eq)}$ is known. Up to the fourth order, one obtains (App. B.3)

$$\begin{cases} \boldsymbol{a}_{eq}^{(0)} = \rho, \\ \boldsymbol{a}_{eq}^{(1)} = \rho \boldsymbol{u}, \\ \boldsymbol{a}_{eq}^{(2)} = \rho \Big[\boldsymbol{u}^2 + rT_0 \left(\theta - 1 \right) \boldsymbol{\delta} \Big], \\ \boldsymbol{a}_{eq}^{(3)} = \rho \Big[\boldsymbol{u}^3 + rT_0 \left(\theta - 1 \right) \boldsymbol{u}\boldsymbol{\delta} \Big], \\ \boldsymbol{a}_{eq}^{(4)} = \rho \Big[\boldsymbol{u}^4 + rT_0 \left(\theta - 1 \right) \boldsymbol{u}^2 \boldsymbol{\delta} + (rT_0)^2 \left(\theta - 1 \right)^2 \boldsymbol{\delta}^2 \Big], \end{cases} \tag{3.1.14}$$

with $\theta = T/T_0$, T_0 being a reference temperature.

3.1.3   Chapman-Enskog expansion

After expressing the BE in the Hermite tensor basis and defining the related coefficients $\boldsymbol{a}^{(n)}$, the macroscopic behavior linked to Eq. (3.1.13) is recovered by applying a separation of scales through the Chapman-Enskog (CE) expansion [39]. For this purpose, both time and space derivatives are expanded in powers of the Knudsen number ϵ as in Ref. [39]:

$$\partial_t = \epsilon \partial_{t_1} + \epsilon^2 \partial_{t_2}, \quad \boldsymbol{\nabla} = \epsilon \boldsymbol{\nabla}_1. \tag{3.1.15}$$

First, let us assume that f and $\boldsymbol{a}^{(n)}$ are at equilibrium. Injecting Eq. (3.1.15) into Eq. (3.1.13), this separation of scales leads to

$\underline{\epsilon^0}$:

$$\boldsymbol{a}_0^{(n)} = \boldsymbol{a}_{eq}^{(n)}, \tag{3.1.16}$$

$\underline{\epsilon^1}$:

$$\partial_{t_1}\boldsymbol{a}_0^{(n)} + \boldsymbol{\nabla}_1 \cdot \left(\boldsymbol{a}_0^{(n+1)}\right) + rT_0\boldsymbol{\nabla}_1\boldsymbol{a}_0^{(n-1)} = 0, \tag{3.1.17}$$

$\underline{\epsilon^2}$:

$$\partial_{t_2}\boldsymbol{a}_0^{(n)} = 0. \tag{3.1.18}$$

Adding all contributions, the macroscopic equations corresponding to the conservation of mass, momentum and total energy are finally recovered, using Eq. (3.1.14) for $n = 0$, $n = 1$ and $n = 2$ respectively,

$$\begin{aligned} \partial_t(\rho) + \boldsymbol{\nabla} \cdot (\rho\boldsymbol{u}) &= 0, \\ \partial_t(\rho\boldsymbol{u}) + \boldsymbol{\nabla} \cdot (\rho\boldsymbol{u}^2 + p\boldsymbol{\delta}) &= 0, \\ \partial_t(\rho E) + \boldsymbol{\nabla} \cdot [(\rho E + p)\boldsymbol{u}] &= 0, \end{aligned} \tag{3.1.19}$$

where $p = \rho rT$ is the thermodynamic pressure. Hence, assuming f and $\boldsymbol{a}^{(n)}$ are at equilibrium leads to thermal and compressible Euler equations.

In a second step, the contributions of order $\mathcal{O}(\epsilon)$ are taken into account in the definition of f and $\boldsymbol{a}^{(n)}$

$$\begin{aligned} f &= f^{(0)} + f^{(1)} \quad , f^{(0)} \gg f^{(1)} \sim \mathcal{O}(\epsilon), \\ \boldsymbol{a}^{(n)} &= \boldsymbol{a}_0^{(n)} + \boldsymbol{a}_1^{(n)}, \boldsymbol{a}_0^{(n)} \gg \boldsymbol{a}_1^{(n)} \sim \mathcal{O}(\epsilon), \end{aligned} \tag{3.1.20}$$

assuming the continuum limit $\epsilon \ll 1$. Applying the same multiscale analysis leads to
$\underline{\epsilon^1}$:

$$\partial_{t_1}\boldsymbol{a}_0^{(n)} + \boldsymbol{\nabla}_1 \cdot \left(\boldsymbol{a}_0^{(n+1)}\right) + rT_0\boldsymbol{\nabla}_1\boldsymbol{a}_0^{(n-1)} = -\frac{\boldsymbol{a}_1^{(n)}}{\tau}, \tag{3.1.21}$$

$\underline{\epsilon^2}$:

$$\partial_{t_2}\boldsymbol{a}_0^{(n)} + \partial_{t_1}\boldsymbol{a}_1^{(n)} + \boldsymbol{\nabla}_1 \cdot \left(\boldsymbol{a}_1^{(n+1)}\right) + rT_0\boldsymbol{\nabla}_1\boldsymbol{a}_1^{(n-1)} = 0. \tag{3.1.22}$$

Therefore the set of macroscopic equations (3.1.19) becomes

$$\begin{aligned} \partial_t(\rho) + \boldsymbol{\nabla} \cdot (\rho\boldsymbol{u}) &= 0, \\ \partial_t(\rho\boldsymbol{u}) + \boldsymbol{\nabla} \cdot (\rho\boldsymbol{u}^2 + p\boldsymbol{\delta}) &= -\boldsymbol{\nabla} \cdot \boldsymbol{a}_1^{(2)}, \\ \partial_t(\rho E) + \boldsymbol{\nabla} \cdot [(\rho E + p)\boldsymbol{u}] &= -\frac{1}{2}\mathrm{Tr}\left(\boldsymbol{\nabla} \cdot \boldsymbol{a}_1^{(3)}\right), \end{aligned} \tag{3.1.23}$$

since the collision model must satisfy Eq. (3.1.3) or equivalently,

$$\boldsymbol{a}_1^{(0)} = \boldsymbol{a}_1^{(1)} = \mathrm{Tr}\left(\boldsymbol{a}_1^{(2)}\right) = \boldsymbol{0}. \tag{3.1.24}$$

Now, only $a^{(2)}_{1,\alpha\beta}$ and $a^{(3)}_{1,\alpha\beta\beta}$ remain to be computed. They can either be computed thanks to Eq. (3.1.13) or noticing that,

$$\begin{aligned}
\mathbf{\Pi}^{(1)} &= \int f^{(1)} \boldsymbol{c}^2 \mathrm{d}\boldsymbol{\xi} = \int f^{(1)} \boldsymbol{\xi}^2 \mathrm{d}\boldsymbol{\xi} + 0 \equiv \boldsymbol{a}^{(2)}_1, \\
\boldsymbol{Q}^{(1)} &= \int f^{(1)} \boldsymbol{c}^3 \mathrm{d}\boldsymbol{\xi} = \int f^{(1)} \boldsymbol{\xi}^3 \mathrm{d}\boldsymbol{\xi} + 0 \equiv \boldsymbol{a}^{(3)}_1,
\end{aligned} \tag{3.1.25}$$

where $\mathbf{\Pi}^{(1)}$ and $\boldsymbol{q}^{(1)} = \mathrm{Tr}(\boldsymbol{Q}^{(1)})/2$ are the standard second- and third-order nonequilibrium moments at the Navier-Stokes level [114],

$$\begin{cases} \mathbf{\Pi}^{(1)} = -\tau p \left[\boldsymbol{S} - \left(\frac{2}{D} \boldsymbol{\nabla} \cdot \boldsymbol{u} \right) \boldsymbol{\delta} \right], \\ \boldsymbol{q}^{(1)} = -\tau p c_p \boldsymbol{\nabla} T + \boldsymbol{u} \cdot \mathbf{\Pi}^{(1)}, \end{cases} \tag{3.1.26}$$

with $\boldsymbol{S} = \boldsymbol{\nabla}\boldsymbol{u} + (\boldsymbol{\nabla}\boldsymbol{u})^T$, and the superscript T standing for the transpose operator. $c_p = (1 + D/2)r$ is the heat capacity at constant pressure. The interested reader can refer to App. C for a detailed derivation of both second- and third-order nonequilibrium coefficients (3.1.26).

Finally, injecting Eq. (3.1.26) in Eq. (3.1.23) allows to link the Hermite formulation of the BE (3.1.13) to the following macroscopic set of equations, namely, Navier-Stokes-Fourier (NSF) equations,

$$\begin{aligned}
\partial_t(\rho) + \boldsymbol{\nabla} \cdot (\rho\boldsymbol{u}) &= 0, \\
\partial_t(\rho\boldsymbol{u}) + \boldsymbol{\nabla} \cdot (\rho\boldsymbol{u}^2) &= \boldsymbol{\nabla} \cdot (\boldsymbol{\sigma}), \\
\partial_t(\rho E) + \boldsymbol{\nabla} \cdot [\rho E\boldsymbol{u}] &= \boldsymbol{\nabla} \cdot (\lambda' \boldsymbol{\nabla} T) + \boldsymbol{\nabla} \cdot (\boldsymbol{\sigma} \cdot \boldsymbol{u}),
\end{aligned} \tag{3.1.27}$$

where $\boldsymbol{\sigma} = \overline{\mathbf{\Pi}} - p\boldsymbol{\delta}$ is the stress tensor, $\overline{\mathbf{\Pi}} = \mu \left[\boldsymbol{S} - \left(\frac{2}{D} \boldsymbol{\nabla} \cdot \boldsymbol{u} \right) \boldsymbol{\delta} \right]$ is the traceless viscous stress tensor, $\mu = \tau p$ and $\lambda' = \tau p c_p$ being the dynamic viscosity and the thermal conductivity coefficients.

Before proceeding any further, several remarks concerning the above approach and its limitations can be pointed out.
First, only coefficients $\boldsymbol{a}^{(n)}_0$ ($\boldsymbol{a}^{(n)}_1$) up to the fourth order (third order) are needed to recover the NSF equations. And more generally, the CE expansion of the BE at order k needs coefficients of the Hermite expansion to include terms at order $n + k$. This is mandatory to properly recover the hydrodynamic behavior of the BE [106].
Second, a strong assumption is made by using the BGK collision operator, which allows only one parameter to represent the physical behavior of the fluid: the single relaxation time τ. This choice induces a coupling between the momentum and the energy relaxation processes since the Prandtl number is fixed at $Pr = \mu c_p / \lambda' = 1$. To overcome this deficiency, a more sophisticated collision operator may be employed, such as the general multirelaxation time (MRT) collision term expressed in the Hermite tensor basis [115]. The latter reads

$$\Omega^{MRT} = -\sum_{n=0}^{\infty} \frac{1}{\tau_n} \frac{1}{n!(rT_0)^n} \boldsymbol{a}^{(n)} : \boldsymbol{\mathcal{H}}^{(n)}. \tag{3.1.28}$$

Here choosing $\tau_2 = \mu/p$ and $\tau_3 = \lambda/pc_p$ allows to tune the Prandtl number which now equals $Pr = \tau_2/\tau_3$. A double distribution function (DDF) LBM could also be used to

overcome this difficulty (see for example [116]).

Third, as depicted in Eq. (3.1.27), the computed viscous stress tensor is traceless, which means that only fluids without bulk viscosity can be simulated. This is another consequence of the BGK approximation, and again this can be avoided by using a more sophisticated collision operator belonging to the Hermite polynomial expansion framework [30]. Concretely, it consists in decoupling the dissipation rate of $a_{1,\alpha\alpha}$ from the one of $a_{1,\alpha\beta}$

Last, the specific heat ratio has a fixed value $\gamma = (D+2)/D$. To overcome this issue, one can employ a second distribution function to take into account the energy evolution linked to internal degrees of freedom (rotational and vibrational) of molecules [97, 100, 101].

The interested reader can refer to App. C for a detailed derivation of DDF compatible solutions. In the rest of the manuscript, only SDF-LBMs coupled with the single-relaxation-time approximation are considered.

3.1.4   Truncation of the VDF

As briefly discussed in Sec. 3.1.3, a finite expansion of the VDF in Hermite tensors, up to the fourth order, is sufficient to recover the macroscopic behavior of the NSF equations from the BE. Here particular attention is paid to error terms arising, at the macroscopic level, from a wrong truncation of the VDF. From now on, let f^N denote the truncation of f, to the order N, of the Hermite polynomial development

$$f^N = \omega \sum_{n=0}^{N} \frac{1}{n!(rT_0)^n} \boldsymbol{a}^{(n)} : \boldsymbol{\mathcal{H}}^{(n)}. \tag{3.1.29}$$

The key element is to ensure that this truncation still allows the proper conservation of the macroscopic moment of the VDF. Introducing $\boldsymbol{a}^{(M)}$ as the Mth-order moment of f:

$$\boldsymbol{a}^{(M)} = \int \boldsymbol{\mathcal{H}}^{(M)} f \, \mathrm{d}\boldsymbol{\xi}, \tag{3.1.30}$$

orthogonality properties of the Hermite polynomials lead to [106]

$$\int \boldsymbol{\mathcal{H}}^{(M)} f \, \mathrm{d}\boldsymbol{\xi} = \int \boldsymbol{\mathcal{H}}^{(M)} f^N \, \mathrm{d}\boldsymbol{\xi}, \text{ if } N \geq M. \tag{3.1.31}$$

This means that f and f^N share the same moments up to the order M, if the truncation order N is at least equal to the highest moment M that we need to conserve.

As mentioned in Sec. 3.1.3, moments of $f^{(0)}$ up to the fourth order are sufficient to recover the proper macroscopic behavior of the BE. Consequently, truncation errors appear at the macroscopic level when the equilibrium VDF is truncated to an order lower than $N = 4$. These error terms can be evaluated quite easily using Eq. (3.1.13). For $N = 3$, the only term that cannot be used for the computation of $\boldsymbol{a}_1^{(3)}$ is $\boldsymbol{\nabla} \cdot \boldsymbol{a}_0^{(4)}$. Hence, the error term introduced by a third-order truncation modifies the heat flux $\boldsymbol{q} = \mathrm{Tr}(\mathbf{Q})/2$:

$$\boldsymbol{q}' = \boldsymbol{q}^{(1)} - \frac{\tau}{2} \mathrm{Tr} \left[\boldsymbol{\nabla} \cdot \boldsymbol{a}_0^{(4)} \right]$$

$$= \boldsymbol{q}^{(1)} - \frac{\tau}{2} \boldsymbol{\nabla} \cdot \left\{ \rho u^2 \boldsymbol{u}^2 + \rho(\theta - 1) \left[(4 + D)\boldsymbol{u}^2 + u^2 \boldsymbol{\delta} \right] \right.$$

$$\left. + \rho(\theta - 1)^2 (2 + D)\boldsymbol{\delta} \right\}$$

$$= \boldsymbol{q} + \mathcal{O}\left(\mathrm{Ma}^4, \mathrm{Ma}^2 \theta, \theta^2 \right). \tag{3.1.32}$$

For $N = 2$, too many error terms are introduced in the energy equation and the concept of temperature should not be used. This is why this truncation is restricted to isothermal, or more precisely athermal[1] LBMs ($\theta = 1$). Furthermore, the computation of $\boldsymbol{a}_1^{(2)}$ is also affected by the truncation. As for the heat flux when $N = 3$, the deviation also comes from the divergence term $\boldsymbol{\nabla} \cdot (\boldsymbol{a}_0^{(3)})$ which cannot be used anymore for the computation of $\boldsymbol{a}_1^{(2)}$. The viscous stress tensor is thus modified:

$$\boldsymbol{\Pi}' = \boldsymbol{\Pi}^{(1)} - \tau \boldsymbol{\nabla} \cdot \left(\boldsymbol{a}_0^{(3)} \right)$$

$$= \boldsymbol{\Pi}^{(1)} - \tau \boldsymbol{\nabla} \cdot \left(\rho \boldsymbol{u}^3 \right)$$

$$\approx \boldsymbol{\Pi}^{(1)} + \mathcal{O}(\mathrm{Ma}^3). \tag{3.1.33}$$

The famous $\mathcal{O}(\mathrm{Ma}^3)$ error term is then recovered from the above procedure, explaining why second-order truncation of the VDF are restricted to the simulation of weakly compressible flows [50].

In the most general case, the truncation criterium (3.1.31) becomes [106]

$$\forall k \in \mathbb{N}, \ \int \boldsymbol{\mathcal{H}}^{(M)} f^{(k)} \, \mathrm{d}\boldsymbol{\xi} = \int \boldsymbol{\mathcal{H}}^{(M)} f^{(k),N} \, \mathrm{d}\boldsymbol{\xi} \tag{3.1.34}$$

if $N + k \geq M$. Here, we recover the fact that the NSF macroscopic behavior is achieved if $N = 4$ at equilibrium ($k = 0$), while $N = 3$ is sufficient for the nonequilibrium VDF $f^{(1),N}$. From the macroscopic point of view, there is no reason why $f^{(0),N}$ and $f^{(1),N}$ should be truncated at the same order N. But it will be shown hereafter (Sec. 4.3) that keeping the same order N for both $f^{(0),N}$ and $f^{(1),N}$ is possible thanks to a recursive computation of these coefficients.

3.1.5   Discretization of the velocity space

In order to numerically solve the BE, a discretization of the velocity space is necessary. It consists in keeping only a discrete set of V velocities $\boldsymbol{\xi}_i$, $i \in [\![1, V]\!]$, ensuring the preservation of f_i moments, from the continuum velocity space to the discrete one. To do so, a Gauss-Hermite quadrature is applied [106, 110]:

$$\int \boldsymbol{\mathcal{H}}^{(M)} f^{(0),N} \mathrm{d}\boldsymbol{\xi} = \sum_{i=1}^{V} \boldsymbol{\mathcal{H}}_i^{(M)} f_i^{(0),N} \ \text{if} \ M + N \leq Q. \tag{3.1.35}$$

---

[1]This word originates from the lattice Boltzmann community, and was introduced to describe a system for which the concept of temperature does not have any meaning.

Here $\boldsymbol{\mathcal{H}}_i^{(M)} = \boldsymbol{\mathcal{H}}^{(M)}(\boldsymbol{\xi}_i)$, $f_i^{(0),N} = \frac{\omega_i}{\omega(\boldsymbol{\xi}_i)} f^{(0),N}(\boldsymbol{\xi}_i)$, ω_i are the Gaussian weights of the quadrature, and Q is the order of accuracy of the quadrature. The resolution of this quadrature problem aims at finding lattices, i.e., discrete weights ω_i associated with discrete velocities $\boldsymbol{\xi}_i$, allowing the conservation of Hermite polynomials orthogonality properties up to a requested order M. Then, the Mth-order moment can be exactly recovered if the equilibrium function is truncated to the order $N \geq M$, and if the quadrature order is greater than $2N - 1$. The particular case of the D1Q3 lattice is presented in Sec. 3.3 for pedagogical purposes. Besides, some two- and three-dimensional lattices, satisfying Eq. (3.1.35) for several N, are also detailed in App. D.

3.2 From LBE to LBM

In this section, the key points on the space/time discretization of the LBE are recalled. For the sake of clarity, the previous truncation notation (superscript N) is now dropped.

Let us start from the force-free LBE with a general collision operator,

$$\partial_t f_i + \boldsymbol{\xi}_i \cdot \boldsymbol{\nabla} f_i = \Omega_i. \tag{3.2.1}$$

This equation is a first-order partial differential equation. The left-hand side (LHS) term is *linear* and corresponds to the advection of the discrete VDFs f_i at *constant* velocity $\boldsymbol{\xi}_i$, while the right-hand side (RHS) term is *non-linear* and translates the rate of change of f_i induced by collisions. Since these two contributions behave differently from the mathematical point of view, two different time integrations are used: (a) the method of characteristics allows to *exactly* integrate the LHS term between t and $t + \Delta t$, whereas (b) the trapezoidal rule ensures a *second-order* accuracy in time for the integration of the RHS term. These techniques lead to

$$f_i\left(\boldsymbol{x} + \boldsymbol{\xi}_i\Delta t, t + \Delta t\right) - f_i\left(\boldsymbol{x}, t\right) = \frac{\Omega_i\left(t + \Delta t\right) + \Omega_i(t)}{2}\Delta t + \mathcal{O}(\Delta t^2, \Delta x^2), \tag{3.2.2}$$

where the space discretization error $\mathcal{O}(\Delta x^2)$ comes from (a): $\Delta \boldsymbol{x} = \boldsymbol{\xi}_i \Delta t$. This space/time discretization results in an implicit formulation since $\Omega_i\left(t + \Delta t\right)$ depends on $f_i\left(\boldsymbol{x} + \boldsymbol{\xi}_i\Delta t, t + \Delta t\right)$. Nevertheless, a change of variables $\overline{f_i}$ compliant with the conservation of mass, momentum and total energy allows to get around it [117, 118]

$$\overline{f_i}\left(\boldsymbol{x}, t\right) = f_i\left(\boldsymbol{x}, t\right) - \frac{\Delta t}{2}\Omega_i(t), \tag{3.2.3}$$

and leads to an explicit numerical scheme,

$$\overline{f_i}\left(\boldsymbol{x} + \boldsymbol{\xi}_i\Delta t, t + \Delta t\right) - \overline{f_i}\left(\boldsymbol{x}, t\right) = \Delta t\, \Omega_i(t). \tag{3.2.4}$$

To be fully consistent with the new set of VDFs $\overline{f_i}$, the collision operator needs to be slightly modified. For the BGK collision model,

$$\Delta t\, \Omega_i(t) = -\frac{\Delta t}{\tau}\left[f_i\left(\boldsymbol{x}, t\right) - f_i^{(0)}\left(\boldsymbol{x}, t\right)\right]$$

$$= -\frac{\Delta t}{\tau} \left[\overline{f}_i\left(\boldsymbol{x},t\right) + \frac{\Delta t}{2}\Omega_i(t) - f_i^{(0)}\left(\boldsymbol{x},t\right) \right]$$

$$= \frac{-\Delta t}{\tau + \Delta t/2} \left[\overline{f}_i\left(\boldsymbol{x},t\right) - f_i^{(0)}\left(\boldsymbol{x},t\right) \right]. \tag{3.2.5}$$

Adopting the shorthand notation $\Delta x = \Delta t = 1$, we end up with the famous 'Collide & Stream' algorithm which is a **second-order accurate and explicit numerical scheme**

$$\overline{f}_i\left(\boldsymbol{x}+1,t+1\right) = \overline{f}_i\left(\boldsymbol{x},t\right) - \frac{1}{\tau+1/2} \left[\overline{f}_i\left(\boldsymbol{x},t\right) - f_i^{(0)}\left(\boldsymbol{x},t\right) \right] \tag{3.2.6}$$

To achieve the full potential of this numerical scheme, specific discretizations of the velocity space are required to ensure the method of characteristics to be used without introducing numerical errors. These velocity sets are built using an on-grid condition (see for example the works of Philippi *et al.* [119] and Shan [120]),

$$\boldsymbol{\xi}_i \longrightarrow \frac{1}{c_s}\boldsymbol{\xi}_i, \quad ||\boldsymbol{\xi}_i|| \in \mathbb{N}, \tag{3.2.7}$$

meaning these discrete velocities are chosen in a way to exactly point toward grid nodes. Hence the advection of VDFs is done without introducing any numerical error. The renormalization constant (or lattice constant) c_s, in Eq. (3.2.7), can further be identified as the isothermal lattice speed of sound, i.e., $c_s = \sqrt{rT_0}\Delta t/\Delta x$ [121]. Its value is recalled for a large number of lattices in App. D.

3.3 Greatest strength of LBMs

Now that both the velocity and the numerical discretizations of the BE have been introduced, let us come back on their bond which results in one of the most efficient kinetic based numerical solver for CFD: the 'Collide & Stream' algorithm (3.2.6).

3.3.1 1D quadrature solutions

As a starting point let us consider the D1Q3 lattice, which is a one-dimensional discretization of the velocity space composed of three velocities ξ_{-1}, ξ_0 and ξ_{+1} (see Fig. 3.1). The link between both numerical and velocity discretizations lies in the lattice constant c_s defined in such a way that $||\boldsymbol{\xi}_i||/c_s$ have positive integer values (*on-grid* condition). The quadrature problem (3.1.35) then corresponds to finding ω_i and c_s to ensure the preservation of Hermite polynomials orthogonality properties during the velocity space discretization. The latter condition on c_s allows to ensure the validity of the numerical discretization of the streaming step by the method of characteristics. Since the D1Q3 lattice only has three degrees of freedom, this velocity set will only be required to conserve the orthogonality properties of the first three one-dimensional Hermite polynomials,

namely, $\mathcal{H}^{(0)}$, $\mathcal{H}_x^{(1)}$ and $\mathcal{H}_{xx}^{(2)}$. In this context, the preservation rule (3.1.35) becomes

$$\mathbb{I}\left(\mathcal{H}^{(n)}\mathcal{H}^{(m)}\right) \equiv \frac{1}{\sqrt{2\pi c_s^2}}\int_{\mathbb{R}} \mathcal{H}^{(n)}\mathcal{H}^{(m)} e^{-\xi_x^2/2c_s^2}\,\mathrm{d}\boldsymbol{\xi}_x = \sum_{i=1}^{3} \omega_i \mathcal{H}_i^{(m)}\mathcal{H}_i^{(n)}. \tag{3.3.1}$$

This leads to the following two sets of equations

$$\begin{cases} \mathbb{I}\left(\mathcal{H}^{(0)}\mathcal{H}^{(0)}\right) = \omega_{-1}(1)^2 & + \omega_0(1)^2 & + \omega_{+1}(1)^2 \\ \mathbb{I}\left(\mathcal{H}_x^{(1)}\mathcal{H}_x^{(1)}\right) = \omega_{-1}(\xi_{-1,x})^2 & + \omega_0(\xi_{0,x})^2 & + \omega_{+1}(\xi_{+1,x})^2 \\ \mathbb{I}\left(\mathcal{H}_{xx}^{(2)}\mathcal{H}_{xx}^{(2)}\right) = \omega_{-1}(\xi_{-1,x}^2 - c_s^2)^2 & + \omega_0(\xi_{0,x}^2 - c_s^2)^2 & + \omega_{+1}(\xi_{+1,x}^2 - c_s^2)^2 \end{cases} \tag{3.3.2}$$

and

$$\begin{cases} \mathbb{I}\left(\mathcal{H}^{(0)}\mathcal{H}_x^{(1)}\right) = \omega_{-1}\xi_{-1,x} & + \omega_0\xi_{0,x} & + \omega_{+1}\xi_{+1,x} \\ \mathbb{I}\left(\mathcal{H}^{(0)}\mathcal{H}_{xx}^{(2)}\right) = \omega_{-1}(\xi_{-1,x}^2 - c_s^2) & + \omega_0(\xi_{0,x}^2 - c_s^2) & + \omega_{+1}(\xi_{+1,x}^2 - c_s^2) \\ \mathbb{I}\left(\mathcal{H}_x^{(1)}\mathcal{H}_{xx}^{(2)}\right) = \omega_{-1}\xi_{-1,x}(\xi_{-1,x}^2 - c_s^2) + \omega_0\xi_{0,x}(\xi_{0,x}^2 - c_s^2) + \omega_{+1}\xi_{+1,x}(\xi_{+1,x}^2 - c_s^2) \end{cases} \tag{3.3.3}$$

where Eqs. (3.3.2) and (3.3.3) respectively correspond to the conservation of the norm and orthogonality of $\mathcal{H}^{(0)}$, $\mathcal{H}_x^{(1)}$ and $\mathcal{H}_{xx}^{(2)}$. Rearranging these constraints in a matrix form, we obtain

$$\begin{bmatrix} 1 \\ c_s^2 \\ 2c_s^4 \\ 0 \\ 0 \\ 0 \end{bmatrix} = \begin{bmatrix} 1 & 1 & 1 \\ 1 & 0 & 1 \\ A^2 & c_s^4 & A^2 \\ -1 & 0 & 1 \\ A & -c_s^2 & A \\ -A & 0 & A \end{bmatrix} \begin{bmatrix} \omega_{-1} \\ \omega_0 \\ \omega_{+1} \end{bmatrix} \tag{3.3.4}$$

with $A = 1 - c_s^2$, and where integrals $\mathbb{I}(\ldots)$ have been computed using the recursive formula (see App. E for its derivation), $\forall p \in \mathbb{N}$,

$$\int_{\mathbb{R}} x^n e^{-x^2/2\beta}\,\mathrm{d}x = \left(\frac{\beta}{2}\right)^p \frac{(2p)!}{p!}\sqrt{2\pi\beta} \qquad \text{if } n = 2p, \tag{3.3.5}$$

$$= 0 \qquad \text{otherwise.}$$

At first sight, this system seems to be overdetermined (6 equations and only 4 unknowns). Nevertheless, it can easily be seen that several constraints are redundant. Numbering lines of the 6×3 matrix in Eq. (3.3.4) using L_a, $a \in [1,6]$, then it is clear that $\mathrm{L}_6 = A\mathrm{L}_4$, and $\mathrm{L}_5/c_s^2 + \mathrm{L}_1 = (A/c_s^2 + 1)\mathrm{L}_2$. Keeping only constraints imposed by the first four lines of the 6×3 matrix, the solution of the quadrature problem (3.3.1) reads as

$$\begin{cases} c_s & = & 1/\sqrt{3} \\ \omega_0 & = & 2/3 \\ \omega_{\pm 1} & = & 1/6 \end{cases} . \tag{3.3.6}$$

Here, the common characteristics of the D1Q3 lattice are recovered [30]. Since this lattice only conserve up to second-order moments of the VDF, it is restricted to the simulation of isothermal and weakly compressible flows.

With the aim of getting the macroscopic behavior related to $\mathcal{H}^{(3)}_{xxx}$, more degrees of freedom are needed for the velocity space discretization. Furthermore, velocities with higher norm values need to be incorporated into the velocity space discretization to avoid any aliasing issues, such as $\xi_i^3 = \xi_i$, encountered when $\xi_i \in \{0, \pm 1\}$. A naive choice would be to use the original D1Q5 which includes $\xi_{\pm 2} = \pm 2$. Unfortunately, it is not sufficient to conserve the properties of $\mathcal{H}^{(3)}_{xxx}$ during the velocity discretization. Nonetheless, there is a way to get around this issue without further increasing the number of discrete velocities [94, 120, 122]. It consists in using the zero-one-three (ZOT) version of the D1Q5, which is composed of $\xi_i \in \{0, \pm 1, \pm 3\}$.

Finally, to recover the macroscopic behavior of NSF equations, properties of $\mathcal{H}^{(4)}_{xxxx}$ need to be conserved. This last constraint requires at least seven velocities (D1Q7 lattice with $\xi_i \in \{0, \pm 1, \pm 2, \pm 3\}$ [94, 120, 122]).

3.3.2 Further extension to 2D and 3D velocity sets

The previous quadrature resolution has been extended to 2D and 3D by several authors [94, 119, 120]. They showed that the standard way to add velocities to low-order velocity sets, i.e, by successively adding higher level of velocity groups only in horizontal, vertical and diagonal directions, is not necessary the best way to end up with compact lattices – in the sense of lowest maximal value of their norm. The most striking example is the inability of the D2Q13 and the D2Q17 to conserve the norm of $\mathcal{H}^{(3)}_{xxx}$, which led to the use of the D2Q21 [119] to get rid of $\mathcal{O}(\text{Ma}^3)$ error terms in the definition of the viscous stress tensor. Instead, 'space-filling' lattices have been proposed to: (1) concentrate all degrees of freedom in successive shells of neighbor nodes (2) using as less shells as possible. The contrast between 'standard' and 'space-filling' lattices is even more striking for lattices dedicated to the simulation of fully compressible NSF equations, as shown in Fig. 3.2. In this PhD work, the numerical behavior of several 2D third- (D2V17a/b/c/d and D2Q21 lattices) and fourth-order (D2V37a/b/c/d) LBMs will be thoroughly studied. All of their characteristics are summarized in App. D.

For the 3D extension, D3Q39 lattices seem to be the most compact ones to recover a proper isothermal behavior [120]. Regarding fully compressible flows, the D3Q103 lattice seems to be the best candidate. Their characteristics are also recalled in App. D for the sake of completeness.

$$
\begin{array}{ccc}
\underset{\xi_{-1} \quad \xi_0 \quad \xi_1}{\overleftrightarrow{}} & \longrightarrow & \begin{aligned} \mathcal{H}^{(0)}_i &= 1 \\ \mathcal{H}^{(1)}_{i,x} &= \xi_{i,x} \\ \mathcal{H}^{(2)}_{i,xx} &= \xi_{i,x}{}^2 - c_s^2 \end{aligned} \\
D1Q3 & &
\end{array}
$$

Figure 3.1 – Illustration of the D1Q3 velocity set (left), and its associated Hermite polynomial basis (right), where $i \in \{0, \pm 1\}$.
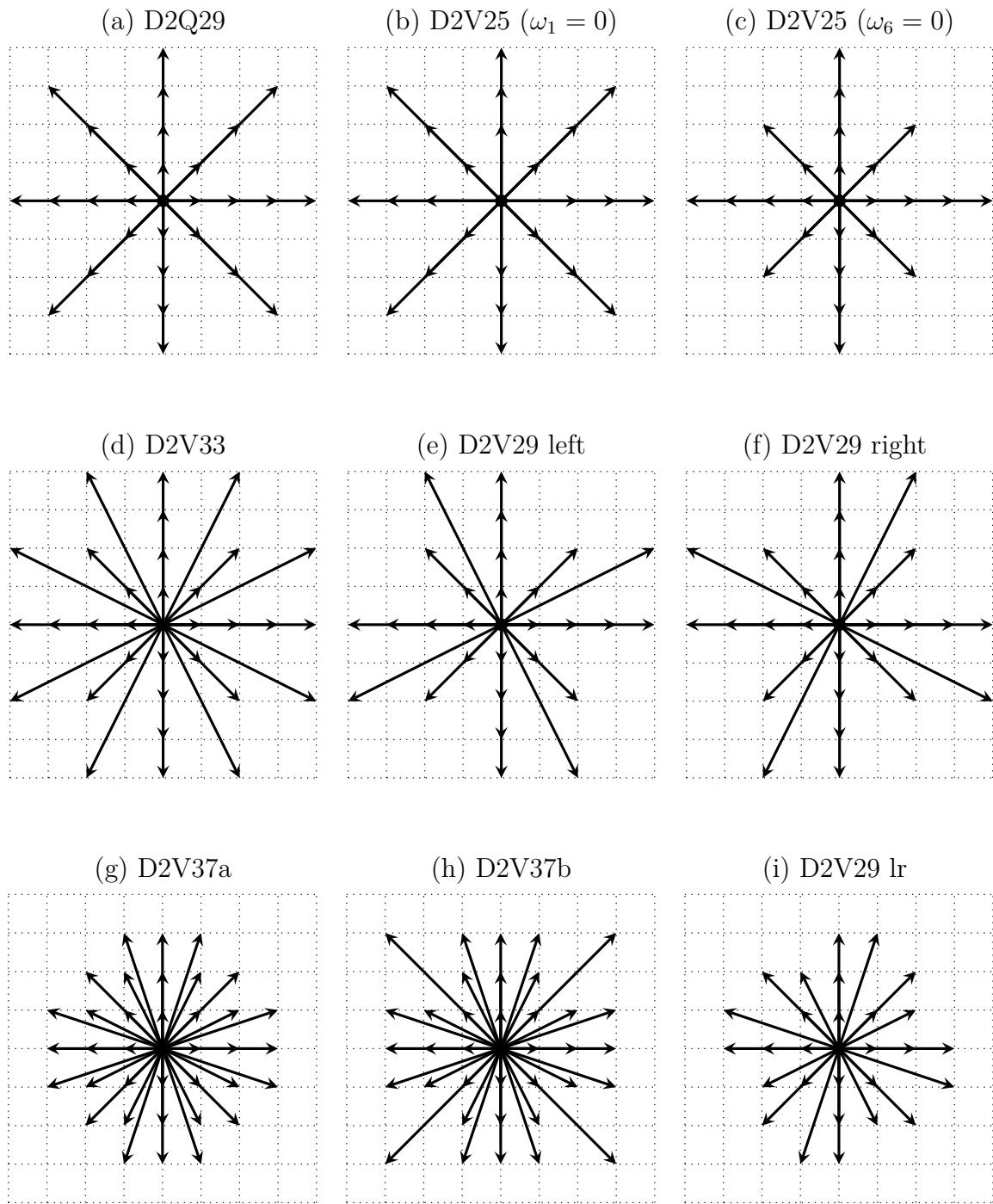
Figure 3.2 – Illustration of the contrast between 'standard' [(a) - (c)] and 'space-filling' [(d)-(i)] lattices. The top row is composed of lattices allowing the recovery of the Navier-Stokes-Fourier equations and nothing more, i.e, up to $\mathcal{H}^{(3)}$ and the trace of $\mathcal{H}^{(4)}$ ($\mathcal{H}^{(4)}_{\alpha\alpha\beta\gamma}$ polynomials). Second and third rows are composed of lattices allowing to conservation all Hermite polynomials up to the fourth order. (b) and (c) are obtained through pruning of (a) assuming the weight of the shell of velocities with a norm of 1 and $3\sqrt{2}$ are respectively null [119]. (e) and (f) result from (d) removing four velocities [123]. (g) and (h) are two among the four available D2V37 lattices [120]. Eventually, (i) is obtained through partial pruning of (g).

3.3.3 Quadrature solutions based on tensor products

Another way of extending the 1D quadrature resolution to 2D and 3D lattices exists. It is based on the fact that 2D and 3D lattices can be built through tensor products of lower order velocity sets. This idea originates from the 3D derivation of the Maxwell Boltzmann equilibrium states, which is constructed through the product of three 1D equilibrium state,

$$f_{3D}^{(0)}(x, y, z) = f_{1D}^{(0)}(x) f_{1D}^{(0)}(y) f_{1D}^{(0)}(z), \tag{3.3.7}$$

with the above derivation assuming the isotropy, or independence with respect to the direction, of $f_{3D}^{(0)}$ [122].

Even if in most cases this way of extending 1D velocity sets to 2D or 3D does not lead to the most compact lattices, it allows to learn a lot of things regarding properties of the resulting velocity discretization, and especially about the polynomial space in which their associated VDFs evolve. As an example, the D2Q9 (D3Q27) lattices can be built through the tensor product of two (three) D1Q3. To ease their definition, the standard velocity subscript i is here replaced by (x_i, y_i) and (x_i, y_i, z_i) which indicate the coordinates in the 2D and 3D cases of ξ_i. The rules regarding the definition of discrete velocities and their associated weights are

1. Velocities: $\boldsymbol{\xi}_{(x_i, y_i)}^{Q9} = \left(\xi_{x_i}^{Q3}, \xi_{y_i}^{Q3}\right)$ & $\boldsymbol{\xi}_{(x_i, y_i, z_i)}^{Q27} = \left(\xi_{x_i}^{Q3}, \xi_{y_i}^{Q3}, \xi_{z_i}^{Q3}\right)$

2. Weights: $\omega_{(x_i, y_i)}^{Q9} = \omega_{x_i}^{Q3} \omega_{y_i}^{Q3}$ & $\omega_{(x_i, y_i, z_i)}^{Q27} = \omega_{x_i}^{Q3} \omega_{y_i}^{Q3} \omega_{z_i}^{Q3}$

where $(x_i, y_i, z_i) \in \{0, \pm 1\}^3$, and the lattice constant being unchanged, i.e. $c_s^{Q27} = c_s^{Q9} = c_s^{Q3}$. Furthermore, the above 'product' rules can also be applied to the polynomial basis on which the VDF is expanded. Hence, the polynomial basis of the D2Q9 ($\mathcal{B}_{Q9}$) and the D3Q27 ($\mathcal{B}_{Q27}$) lattices read as

$$\mathcal{B}_{Q9} = \left(\mathcal{H}_i^{(0)}, \mathcal{H}_{i,x}^{(1)}, \mathcal{H}_{i,y}^{(1)}, \mathcal{H}_{i,xx}^{(2)}, \mathcal{H}_{i,xy}^{(2)}, \mathcal{H}_{i,yy}^{(2)}, \mathcal{H}_{i,xxy}^{(3)}, \mathcal{H}_{i,xyy}^{(3)}, \mathcal{H}_{i,xxyy}^{(4)}\right) \tag{3.3.8}$$

$$\begin{aligned}
\mathcal{B}_{Q27} = \Big(&\mathcal{H}_i^{(0)}, \mathcal{H}_{i,x}^{(1)}, \mathcal{H}_{i,y}^{(1)}, \mathcal{H}_{i,z}^{(1)}, \mathcal{H}_{i,xx}^{(2)}, \mathcal{H}_{i,yy}^{(2)}, \mathcal{H}_{i,zz}^{(2)}, \mathcal{H}_{i,xy}^{(2)}, \mathcal{H}_{i,xz}^{(2)}, \mathcal{H}_{i,yz}^{(2)}, \\
&\mathcal{H}_{i,xxy}^{(3)}, \mathcal{H}_{i,xxz}^{(3)}, \mathcal{H}_{i,xyy}^{(3)}, \mathcal{H}_{i,xzz}^{(3)}, \mathcal{H}_{i,yzz}^{(3)}, \mathcal{H}_{i,zyy}^{(3)}, \mathcal{H}_{i,xyz}^{(3)}, \\
&\mathcal{H}_{i,xxyy}^{(4)}, \mathcal{H}_{i,xxzz}^{(4)}, \mathcal{H}_{i,yyzz}^{(4)}, \mathcal{H}_{i,xxyz}^{(4)}, \mathcal{H}_{i,xyyz}^{(4)}, \mathcal{H}_{i,xyzz}^{(4)}, \\
&\mathcal{H}_{i,xxyyz}^{(5)}, \mathcal{H}_{i,xxyzz}^{(5)}, \mathcal{H}_{i,xyyzz}^{(5)}, \mathcal{H}_{i,xxyyzz}^{(6)}\Big) \tag{3.3.9}
\end{aligned}$$

where **standard polynomial basis only includes up to second-order Hermite polynomials**. Here, third- and higher-order Hermite polynomials are obtained through tensor product since

$$\begin{aligned}
\mathcal{H}_{i,x...xy...yz...z}^{(nx+ny+nz)} &= \frac{(-rT_0)^{nx+ny+nz}}{\omega(\boldsymbol{\xi})} \boldsymbol{\nabla}_{\boldsymbol{\xi}}^{nx+ny+nz} \omega(\boldsymbol{\xi}) \\
&= \left[\frac{(-rT_0)^{nx}}{\omega'(\xi_x)} \nabla_{\xi_x}^{nx} \omega'(\xi_x)\right] \left[\frac{(-rT_0)^{ny}}{\omega'(\xi_y)} \nabla_{\xi_y}^{ny} \omega'(\xi_y)\right] \left[\frac{(-rT_0)^{nz}}{\omega'(\xi_z)} \nabla_{\xi_z}^{nz} \omega'(\xi_z)\right] \\
&= \mathcal{H}_{i,x...x}^{(nx)} \mathcal{H}_{i,y...y}^{(ny)} \mathcal{H}_{i,z...z}^{(nz)} \tag{3.3.10}
\end{aligned}$$

where ω' is the one-dimensional version of the Gaussian weight (3.1.9), and (nx, ny, nz) are the number of occurrences of indexes (x, y, z). This means that the degree of each Hermite polynomial is at most *two per direction*. It will be shown in Chap. 4 that the D2Q9 and D3Q27 lattices are of particular interest since their polynomial basis are *entirely* spanned by Hermite polynomials, leading to a proper stabilization of the resulting LBMs.

3.3.4 The million-dollar question

Still one question remains regarding velocity sets which were designed to recover the very same macroscopic behavior: Do they share similar numerical stability ranges?

This question is of uttermost interest since most of researchers have tried to built lattices including as less velocities as possible to recover a macroscopic behavior of interest. Of course, applying a CE expansion to them leads to the correct set of equations. Nevertheless, it has been shown that this way of designing lattices for the simulation of compressible flows leads to very unstable numerical schemes [119]. Most of the time, this is circumvented by changing the numerical discretization of the LBE (see for example [61, 63, 81]). We shall prove in this manuscript that stability issues are induced by a misconception about their origin, and that a simple solution, based on the filtering of nonhydrodynamic contributions to the lattice Boltzmann dynamics, allows to greatly improve the numerical stability of existing lattices without changing what is definitely the greatest strength of LBMs: the coupling between velocity and numerical discretizations. While the previous assumption will first be assessed through numerical simulations (Chap. 4), further confirmations will be given through the linear stability analysis of the LBM in Chap. 6.

Chapter 4

Recursive Regularized LBM

Contents

This chapter presents the derivation of stabilization techniques based on the Hermite polynomial expansion framework for both standard and high-order LBMs. Starting with a recall on stability issues commonly encountered with LBMs, a short review of stabilization techniques for LBMs is then provided. The theoretical background of regularized LBMs (RLBMs) is further recalled in the standard case (isothermal LBMs). The extension to the most general case of thermal and fully compressible LBMs is derived. Improved stability ranges are obtained through the conception of these recursive RLBMs. Eventually, the coupling of the proposed collision model with a shock-capturing technique is studied and validated using a high-order LBM.

4.1   LBM limitations

Before moving to the derivation of stabilization techniques for LBMs, let us present the main stability issues encountered with the physics of interest, i.e, high-Reynolds and high-Mach numbers flows. Descriptions of velocity sets used hereafter are summarized in App. D.

4.1.1   Zero viscosity mirage

Coming back to the LBE with the BGK collision model (3.1.5), recovering the behavior of high-Reynolds number flows seems quite complicated since the collision term is directly proportional to $1/\tau$, and $\tau \propto \nu$. Hence making the kinematic viscosity tends towards zero would lead to a predominant collision term. This kind of equation requires particular care to be numerically solved. From this point of view, the 'Collide & Stream' algorithm (3.2.6) is particularly interesting since the change of variables it introduced allows to circumvent the issue of a stiff collision term. Historically, this numerical scheme was thought to be able to reach the zero-viscosity limit without encountering any numerical issues since $\nu \to 0$ would lead to $\tau + 1/2 \to 1/2$ [124].

Let us see if the above assessment is verified on a very simple test: the doubly periodic shear layer. It is a well known test case which allows to quantify the stability of numerical schemes as a first step [125]. This flow is composed of two longitudinal shear layers, located at $y = L/4$ and $y = 3L/4$, in a 2D doubly periodic domain with $(x,y) \in [0,L]^2$. A transverse perturbation is superimposed to the flow, leading to the roll-up of the shear layers, and the generation of two counter-rotating vortices by the Kelvin-Helmholtz instability mechanism. In addition, any numerically induced disturbances may lead to the formation of further spurious vortices, or in the worst case, make the simulation reach its stability threshold. This is why this test case is an excellent candidate to evaluate the stability of numerical schemes. The initial state is defined by,

$$u_x = \begin{cases} u_0 \tanh[k^*(y^* - 1/4)], & y^* \le 1/2 \\ u_0 \tanh[k^*(3/4 - y^*)], & y^* > 1/2 \end{cases} \tag{4.1.1}$$
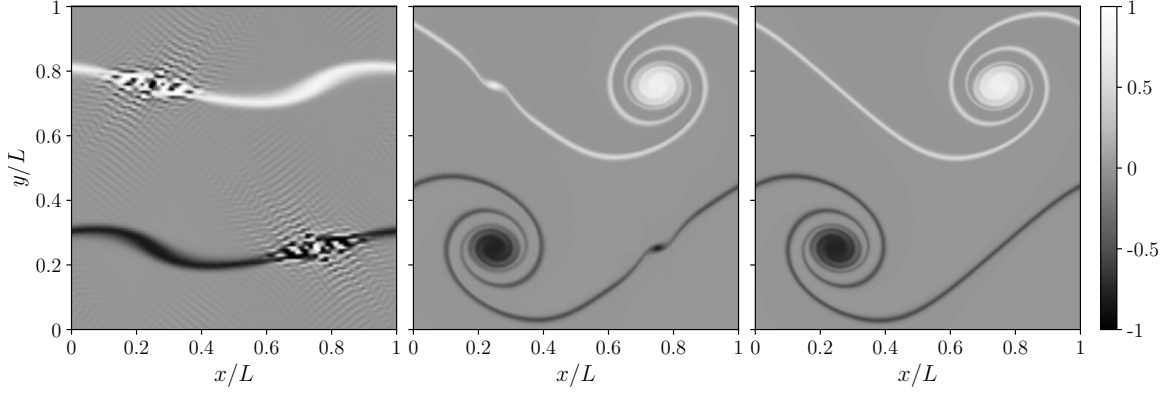
Figure 4.1 − Rollup of the double shear layer at $M_0 = 0.2$ and $\mathrm{Re} = 3 \times 10^4$. Visualization of the dimensionless vorticity field using (from left to right) $L = 128$, 256 and 512 grid points in each directions, with the D2Q9 and the BGK collision model. Instantaneous snapshots are taken at time $t_c = L/u_0 = 1$ expect for the case $L = 128$ where $t_c = L/u_0 = 0.5$.

and

$$u_y = u_0 \delta^* \sin[2\pi(x^* + 1/4)], \qquad (4.1.2)$$

where $(x^*, y^*) = (x/L, y/L)$, and u_0 is the characteristic speed. k is related to the width of the shear layers while δ controls the amplitude of the transverse perturbation. The critical parameters of this test case are the width of the shear layers, and the Reynolds number which is the ratio between convective and diffusive phenomena. Here the case of thin shear layers is considered, i.e, $(k^*, \delta^*) = (80, 0.05)$. The Reynolds number is here fixed to a moderate value of $\mathrm{Re} = u_0 L/\nu = 3 \times 10^4$. A freestream Mach number of $M_0 = u_0/c = 0.2$ is used to further highlight the stability issues encountered at moderate Reynolds number.

The dimensionless vorticity field[1] $\omega_z/|\omega_z^{\max}|$ obtained with the D2Q9-BGK is presented in Fig. 4.1. Starting from the finest mesh grid, it does not show any premise of stability issues. On the contrary, two spurious vortices are observed for the intermediate case ($L = 256$). They are generated by Gibbs oscillations appearing when shear layers are stretched. Regarding the coarsest mesh grid, Gibbs oscillations are too important for the simulation to remain stable.

This simple test case clearly shows that the LBM encounters numerical stability issues when moderate to high-Reynolds number flows are simulated using underresolved mesh grids. The case of high-order LBMs based on the D2V17a and the D2V37a have also been studied, and they show similar behaviors, but for higher values of M_0 (see Fig. 4.5 and Fig. 4.6 for more details). As a conclusion, even if the zero-viscosity limit seems to be achievable with the 'Collide & Stream' algorithm, it still encounters stability issues in underresolved conditions. This is why, the simulation of high-Reynolds number flows still remains an active research topic of the lattice Boltzmann community [2, 20, 91, 126].

---

[1] As a reminder, the vorticity field is defined as $\omega_z = \partial_x u_y - \partial_y u_x$.

4.1.2   Flow including discontinuities

To evaluate the ability of LBMs to simulate highly compressible flows, the Sod shock tube is considered here. In order to capture all the mechanisms of this test case, a velocity discretization allowing the recovery of the Navier-Stokes-Fourier (NSF) macroscopic behavior is required. In what follows the D2V37a lattice is employed.

This 1D Riemann problem consists in a closed tube divided into two regions by a thin membrane. Each region is filled with the same gas but has different thermodynamic properties (density ρ, temperature T, pressure P and velocity u). At the initialization, the breakdown of the membrane induces a strong acceleration of the flow, from the high-pressure side to the low-pressure one, whose purpose is to equalize the pressure inside the tube. This leads to the generation and the propagation of three characteristic waves: (1) the compression of the gas creates a *shock* wave which propagates towards the low-pressure side, (2) the expansion of the gas towards the high-pressure side induces the propagation of the *expansion* or *rarefaction* wave, and (3) the separation between the two waves, namely, the *contact discontinuity*. The latter can be seen as a fictitious diaphragm traveling at a constant speed towards the low-pressure side.

With the aim of evaluating the ability of high-order LBMs to recover the physics of flows including discontinuities, the following configuration is considered :

$$(P_L, \rho_L, u_L) = (4, 4, 0), \quad (P_R, \rho_R, u_R) = (1, 1, 0), \tag{4.1.3}$$

where subscripts L and R stand for the left and the right states respectively. Furthermore, two values of the kinematic viscosity are considered: $\nu = 1$ and $0.2 \ [m^2/s]$[2]. To avoid the contribution of the boundary conditions, the computation takes place in a periodic domain of length $2L_x$ centered around the location $x = L_x/2$ where the discontinuity between the two states belongs. Results are compiled in Fig. 4.2. They confirm that a fourth-order LBMs can be used to recover the generation and propagation of shock waves.

Nevertheless, stability issues arise even for high values of the kinematic viscosity. This seems to come from the initial discontinuity imposed at $t = 0$. To further investigate this last point, a parametric study has been conducted on the initial density profile. The latter is now defined as

$$\forall \, x \in [0, L_x], \quad \rho(x) = \frac{\rho_L + \rho_R}{2} + \frac{\rho_L - \rho_R}{2} \tan\left[a\left(\frac{x}{L_x} - \frac{1}{2}\right)\right] \tag{4.1.4}$$

where a controls the 'width' of the discontinuity. Imposing small values of a then allows to 'smooth' the discontinuity, which eventually leads to more stable simulations as illustrated in Fig. 4.3. This confirms that spurious oscillations originates from the initial discontinuity. This kind of behavior is encountered for all kind of numerical schemes that are not specifically designed to handle discontinuities. Nevertheless, several approaches are available to improve their robustness. Among them, one may find [127]: flux limiters, artificial viscosity, spatial filtering, etc. One of these propositions will be evaluated in Sec. 4.4 as a shock-capturing technique for compressible LBMs.

---

[2]Dimensional units are used here since several mesh grids are employed. Furthermore, the acoustic scaling is used for the computation of the time step ($\Delta t \propto \Delta x$). The interested reader can refer to Ref. [30] (Chap. 7) for more details about the relationship between physical and lattice units.
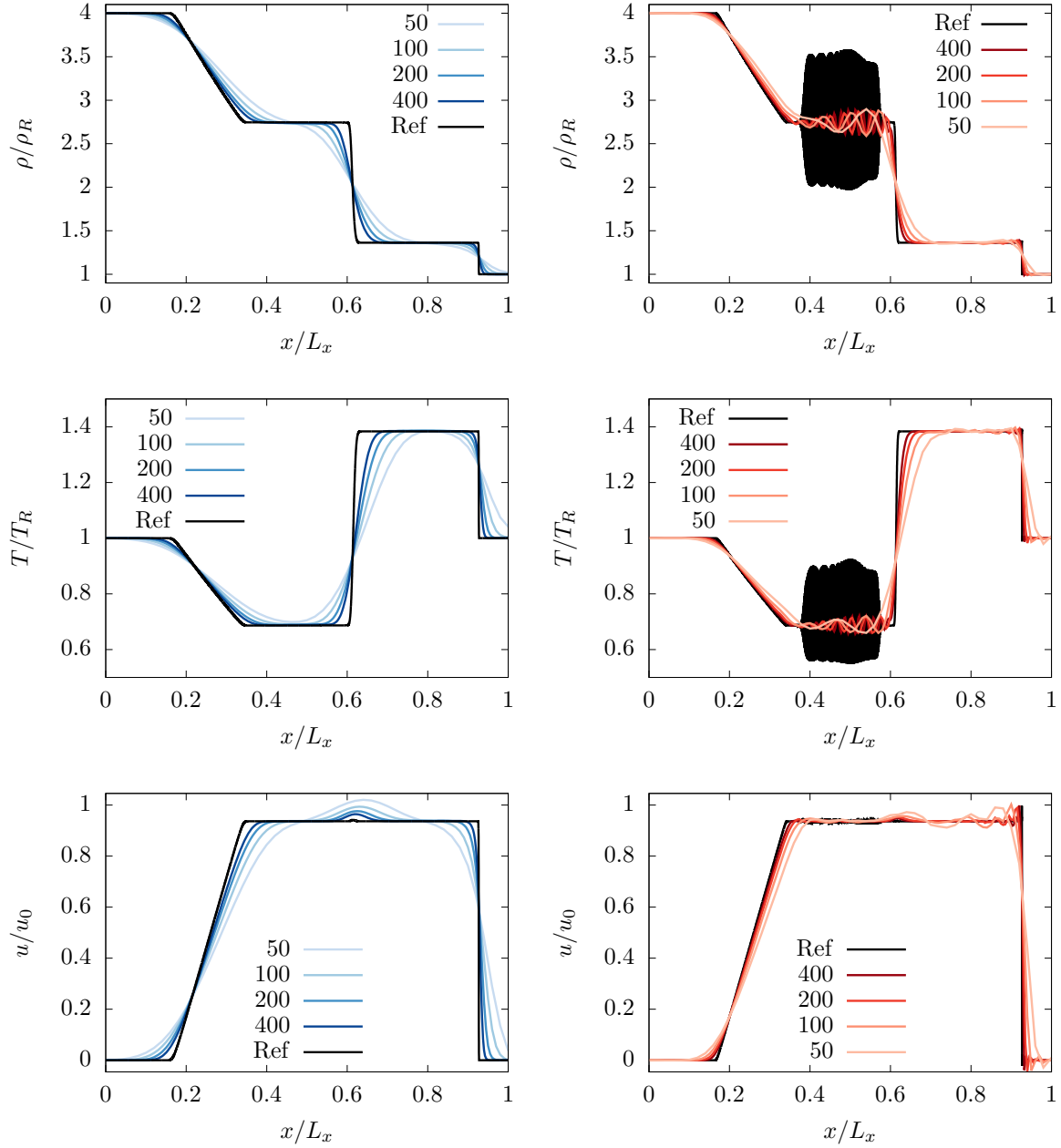
Figure 4.2 – Illustration of the 1D Riemann problem: $[P_L/P_R, \rho_L/\rho_R] = [4, 4]$ with a kinematic viscosity of $\nu = 1$ (left) and 0.2 $[m^2/s]$ (right). From top to bottom: dimensionless density, temperature and velocity profiles. The mesh refinement is done using $L_x = 50, 100, 200, 400$ and $10\,000$ grid points, where the last mesh grid is considered to be the reference solution. Stability issues are encountered for $\nu = 0.2 \ [m^2/s]$.
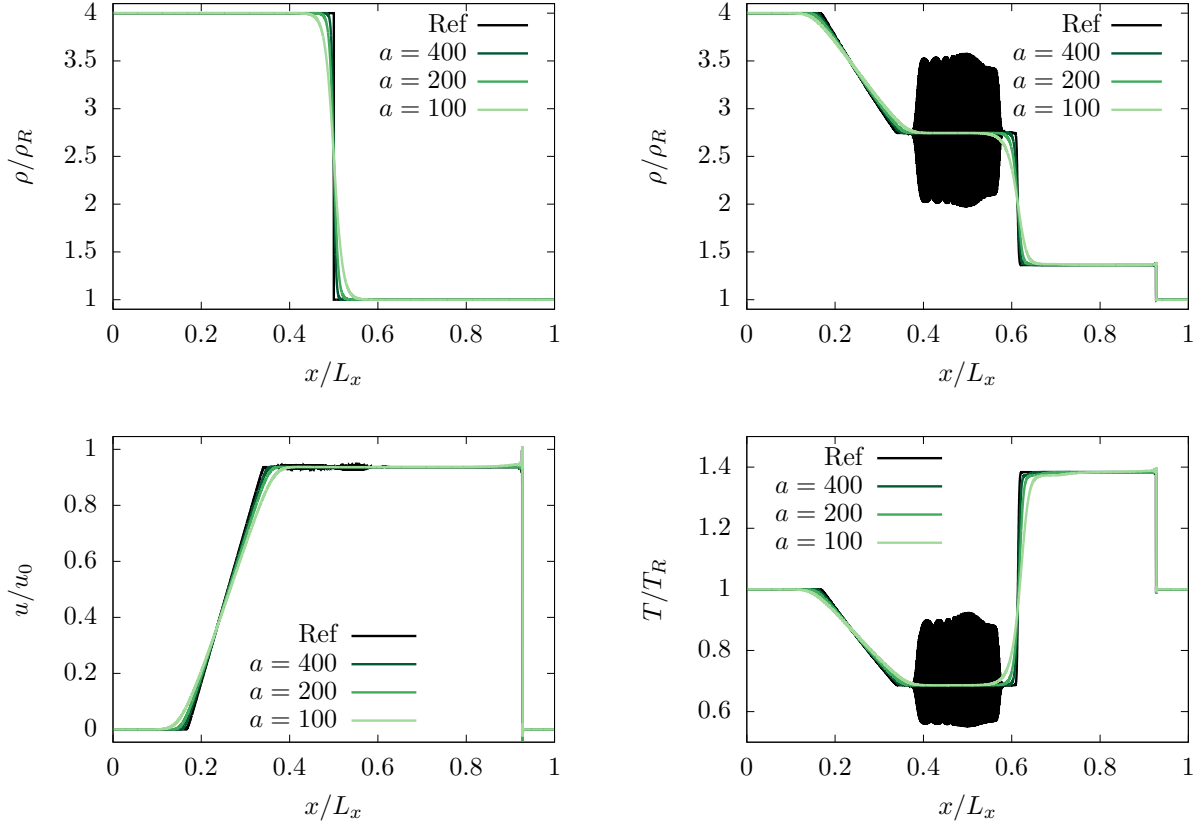
Figure 4.3 – 1D Riemann problem: $[P_L/P_R, \rho_L/\rho_R] = [4, 4]$. Impact of the initial density profile for the finest mesh ($L_x = 10\,000$) with the critical kinematic viscosity $\nu = 0.2\ [m^2/s]$, and $a = 100, 200$ and 400. The reference computation corresponds to $a \to \infty$, i.e, a 'true' discontinuity. The top left figure illustrates the impact of the parameter a on the initial discontinuity, while other figures show its impact on all three characteristic waves after their formation and propagation.

4.2   Brief review of stabilization techniques for LBMs

The lattice Boltzmann method has become more and more appealing due to its ability to simulate various kinds of phenomena, at relatively small turnover times with respect to standard NSF solvers. Nonetheless, some difficulties remain for the simulation of (1) weakly compressible flows at high Reynolds numbers, and (2) fully compressible flows including discontinuities, as previously demonstrated.

Most of the time, more sophisticated collision operators, than the standard BGK approach, are employed to overcome these issues. Among them, particular attention has been paid to: (a) multirelaxation time (MRT) [95, 128, 129], (b) entropic [89, 130, 131] and (c) regularized [108, 132, 133] approaches. The present work focuses on the latter, and more precisely on the recursive regularization (RR) step recently introduced by Malaspinas [134]. As a reminder, the purpose of the regularized collision model is to filter out nonhydrodynamic contributions, of the lattice Boltzmann dynamics, to stabilize numerical computations. In the isothermal case, it was first proposed to discard contribu-

tions from third- and higher-order Hermite polynomials [108, 133]. Since Hermite tensors form an orthogonal basis, it was thought that a simple projection onto second- and lower-order Hermite tensors would be sufficient to eliminate nonhydrodynamic contributions. This method is referred as the projection based regularized LBM or simply PR approach. Nevertheless, it has been shown that the only way to properly filter out high-order contributions is to recompute the first-order nonequilibrium part of Hermite coefficients $a_1^{(n)}$, with $n \geq 3$ in the isothermal case, via the Chapman-Enskog (CE) expansion [134].

Hereafter, the differences between PR and RR approaches are properly highlighted by studying the impact of nonequilibrium Hermite coefficients on the stability range of both standard and high-order LBMs. Furthermore, our extension of the RR procedure to thermal and fully compressible flows [29] is also presented.

4.3   Regularized collision operator

Let us start with the truncated velocity distribution function (VDF) at order N. At the Navier-Stokes level, f^N is of the form

$$f^N = f^{(0),N} + f^{(1),N}.$$

The reason for this decomposition lies in the definition of the regularization step [107, 108, 133]. This collision operator is based on the reconstruction of the nonequilibrium part of precollision distribution functions, and aims at filtering out nonhydrodynamic sources. To do so, f^N is reconstructed before the collision step discarding $\mathcal{O}(\epsilon^k)$ contributions ($k \geq 2$):

$$f^{reg,N} \equiv f^{(0),N} + f^{(1),N}, \tag{4.3.1}$$

with

$$f^{(1),N} = \omega \sum_{n=2}^{N} \frac{1}{n!(rT_0)^n} \boldsymbol{a}_1^{(n)} : \boldsymbol{\mathcal{H}}^{(n)}, \tag{4.3.2}$$

and where the sum begins at $n = 2$ due to mass and momentum conservation (3.1.24). The post-collision VDF is then defined as follows,

$$f^{coll,N} = f^{(0),N} + \left(1 - \frac{1}{\tau}\right) f^{(1),N} \tag{4.3.3}$$

$$= \omega \sum_{n=0}^{N} \frac{1}{n!(rT_0)^n} \left[\boldsymbol{a}_0^{(n)} + \left(1 - \frac{1}{\tau}\right) \boldsymbol{a}_1^{(n)} \right] : \boldsymbol{\mathcal{H}}^{(n)}.$$

Here coefficients $\boldsymbol{a}_1^{(n)}$ are the only missing information required to reconstruct $f^{(1),N}$. Originally, this stabilization technique was used for the simulation of isothermal and weakly compressible flows for which only second-order terms were kept [107, 108]. Nonequilibrium coefficients $\boldsymbol{a}_1^{(2)}$ were then computed projecting the VDFs onto the second-order Hermite polynomials

$$\boldsymbol{a}_1^{(2)} \approx \int \boldsymbol{\mathcal{H}}^{(2)} \left(f^N - f^{(0),N} \right) \mathrm{d}\boldsymbol{\xi}, \tag{4.3.4}$$

assuming that $f^N - f^{(0),N} \approx f^{(1),N}$. But doing so, only contributions belonging to the Hilbert space that were not taken into account are filtered, while some nonhydrodynamic contributions are still hidden in $\boldsymbol{a}_1^{(2)}$. Hereafter, this method will be referred as to the projection based regularization (PR) process.

Later, Malaspinas [134] proposed a *complete* regularization procedure based on *recursive* properties of the nonequilibrium coefficients, allowing an enhancement of accuracy and stability compared to BGK and standard MRT models. Regarding the *recursive* property of this stabilization procedure, it comes from the fact that nonequilibrium coefficients $\boldsymbol{a}_1^{(n)}$ are computed using a recursive formula flowing from the CE expansion. This step provides a proper way to filter out nonhydrodynamic sources.

It must be understood that this recursive regularization (RR) approach was introduced in the context of **isothermal and weakly compressible** flows for **standard** LBMs, while here the recursive formula is extended to the **thermal and fully compressible** case (see App. F for its derivation) and applied to **high-order** LBMs. The latter reads $\forall n \geq 4$,

$$a_{1,\alpha_1..\alpha_n}^{(n)} = u_{\alpha_n} a_{1,\alpha_1..\alpha_{n-1}}^{(n-1)} + r T_0(\theta - 1) \sum_{l=1}^{n-1} \delta_{\alpha_l \alpha_n} a_{1,\beta_l}^{(n-2)} + \frac{1}{\rho} \sum_{l=1}^{n-1} a_{0,\beta_l}^{(n-2)} a_{1,\alpha_l \alpha_n}^{(2)}$$

$$+ \frac{1}{\rho} \sum_{l=1}^{n-1} \sum_{m>l}^{n-1} a_{0,\beta_{lm}}^{(n-3)} \left(a_{1,\alpha_l \alpha_m \alpha_n}^{(3)} - u_{\alpha_l} a_{1,\alpha_m \alpha_n}^{(2)} - u_{\alpha_m} a_{1,\alpha_l \alpha_n}^{(2)} - u_{\alpha_n} a_{1,\alpha_l \alpha_m}^{(2)} \right), \quad (4.3.5)$$

where $\boldsymbol{a}_1^{(2)}$ and $\boldsymbol{a}_1^{(3)}$ can either be computed thanks to the projection of $f^{(1)}$ onto the Hermite polynomial basis or using finite differences. In the isothermal case ($\theta = 1$), Malaspinas' recursive relation [134] is recovered for $n \geq 3$:

$$a_{1,\alpha_1..\alpha_n}^{(n)} = u_{\alpha_n} a_{1,\alpha_1..\alpha_{n-1}}^{(n-1)} + \frac{1}{\rho} \sum_{l=1}^{n-1} a_{0,\beta_l}^{(n-2)} a_{1,\alpha_l \alpha_n}^{(2)}. \quad (4.3.6)$$

Again, $\boldsymbol{a}_1^{(2)}$ coefficients can be computed by projection or using finite differences. Furthermore, a correct evaluation of $\boldsymbol{a}_1^{(2)}$ requires a proper evaluation of $\boldsymbol{a}_0^{(3)}$ since

$$\boldsymbol{a}_1^{(2)} = -\tau \left[\partial_t \boldsymbol{a}_0^{(2)} + \boldsymbol{\nabla} \cdot \boldsymbol{a}_0^{(3)} \right]. \quad (4.3.7)$$

Thus, in the isothermal case, the equilibrium VDF should theoretically be developed up to the third order. Similarly, in the thermal case, correct calculations of $\boldsymbol{a}_1^{(2)}$ and $\boldsymbol{a}_1^{(3)}$ require a development of $f^{(0)}$ up to the fourth order, which is no more binding than the condition to recover the compressible NSF equations.

4.3.1   Regularization step: Projection vs Recursivity

In the general case of a lattice including V discrete velocities, the dimension of the associated Hilbert space is also V. Assuming the quadrature order of this lattice structure is Q, then Hermite polynomials up to the order $N = (Q-1)/2$ will be orthogonal to each other [106] and may form part of a basis $\mathcal{B} = \mathcal{B}^{\mathcal{H}} \cup \mathcal{B}^{\overline{\mathcal{H}}}$, where

$$\mathcal{B}^{\mathcal{H}} = \left(\boldsymbol{\mathcal{H}}_i^{(0)}, \ldots, \boldsymbol{\mathcal{H}}_i^{(N)} \right) \quad (4.3.8)$$

is a subset of $\mathcal{B}$ entirely composed of Hermite polynomials, while elements of $\mathcal{B}^{\overline{\mathcal{H}}}$ are linearly independent of each others and may not be Hermite polynomials. Using this decomposition, the polynomial coefficients of $f^{(1)}$ can also be recast into two subsets:

$$\left\{\boldsymbol{a}_1^{(0)}, \ldots, \boldsymbol{a}_1^{(N)}\right\}^{\mathcal{B}^{\mathcal{H}}} \quad \& \quad \left\{\boldsymbol{b}_1^{(n)}\right\}_{n>N}^{\mathcal{B}^{\overline{\mathcal{H}}}}, \tag{4.3.9}$$

where coefficients $\boldsymbol{b}_1^{(n)}$ ($n > N$) are supposedly related to nonhydrodynamic behaviors.

The purpose of the PR approach is to keep only Hermite polynomial coefficients, since the mathematical expression of $\boldsymbol{b}_1^{(n)}$ ($n > N$) is usually unknown. After the PR procedure, remaining polynomial coefficients of $f_{i,PR}^{(1),N}$ are

$$\left\{\boldsymbol{a}_{1,\mathrm{PR}}^{(0)}, \ldots, \boldsymbol{a}_{1,\mathrm{PR}}^{(N)}\right\}^{\mathcal{B}^{\mathcal{H}}}, \tag{4.3.10}$$

where contributions from $\mathcal{B}^{\overline{\mathcal{H}}}$ have been completely filtered out. Nevertheless, spurious sources coming from the approximation $f_i^{(1)} \approx (f_i - f_i^{(0)})$ may still be hidden in $\boldsymbol{a}_{1,\mathrm{PR}}^{(n)}$. Hence, this approach reduces the order of the polynomial development, and filters out spurious contributions originating from presumably non-Hermite polynomials. In the particular case of $\mathcal{B}^{\overline{\mathcal{H}}}$ being empty, this regularization step reduces to the standard BGK collision model if $f_i^{(1)}$ is projected onto the *complete* basis $\mathcal{B}$.

Regarding now the RR approach, it further filters out high-order contributions, left by the PR approach, recomputing most coefficients $\boldsymbol{a}_1^{(n)}$ ($n \leq N$) by a CE expansion, and without assuming $f_i^{(1)} \approx (f_i - f_i^{(0)})$. For $f_{i,RR}^{(1),N}$ the remaining coefficients are then

$$\left\{\boldsymbol{a}_{1,\mathrm{RR}}^{(0)}, \ldots, \boldsymbol{a}_{1,\mathrm{RR}}^{(N)}\right\}^{\mathcal{B}^{\mathcal{H}}}, \tag{4.3.11}$$

where $\boldsymbol{a}_{1,\mathrm{RR}}^{(n)} = \boldsymbol{a}_{1,\mathrm{PR}}^{(n)}$ for $n \leq 2$ ($n \leq 3$) in the isothermal (thermal) case, whereas high-order coefficients are recomputed using Eqs. (4.3.6) and (4.3.5). Eventually, while working on a *complete* basis, this approach is the only one leading to the expected filtering behavior.

For velocity sets of interest, the following observations can be made. The D2V37a (D2V17a) is built ensuring that Hermite polynomials orthogonality properties are preserved, up to $N = 4$ ($N = 3$), during the velocity space discretization [119]. Thus it is known for sure that

$$\mathcal{B}_{\mathrm{D2V37a}}^{\mathcal{H}} = \Big(\mathcal{H}_i^{(0)}, \mathcal{H}_{i,x}^{(1)}, \mathcal{H}_{i,y}^{(1)}, \mathcal{H}_{i,xx}^{(2)}, \mathcal{H}_{i,yy}^{(2)}, \mathcal{H}_{i,xy}^{(2)}, \mathcal{H}_{i,xxx}^{(3)}, \mathcal{H}_{i,yyy}^{(3)}, \mathcal{H}_{i,xxy}^{(3)}, \mathcal{H}_{i,xyy}^{(3)}, \tag{4.3.12}$$

$$\mathcal{H}_{i,xxxx}^{(4)}, \mathcal{H}_{i,yyyy}^{(4)}, \mathcal{H}_{i,xxxy}^{(4)}, \mathcal{H}_{i,xyyy}^{(4)}, \mathcal{H}_{i,xxyy}^{(4)}\Big),$$

and

$$\mathcal{B}_{\mathrm{D2V17a}}^{\mathcal{H}} = \Big(\mathcal{H}_i^{(0)}, \mathcal{H}_{i,x}^{(1)}, \mathcal{H}_{i,y}^{(1)}, \mathcal{H}_{i,xx}^{(2)}, \mathcal{H}_{i,yy}^{(2)}, \mathcal{H}_{i,xy}^{(2)}, \mathcal{H}_{i,xxx}^{(3)}, \mathcal{H}_{i,yyy}^{(3)}, \mathcal{H}_{i,xxy}^{(3)}, \mathcal{H}_{i,xyy}^{(3)}\Big), \tag{4.3.13}$$

whereas the true form of $\mathcal{B}_{\mathrm{D2V37a}}^{\overline{\mathcal{H}}}$ and $\mathcal{B}_{\mathrm{D2V17a}}^{\overline{\mathcal{H}}}$ are unknown. Hence, both PR and RR approaches first discard coefficients related to $\mathcal{B}_{\mathrm{D2V37a}}^{\overline{\mathcal{H}}}$ and $\mathcal{B}_{\mathrm{D2V17a}}^{\overline{\mathcal{H}}}$. Then, $\boldsymbol{a}_1^{(n)}$ ($n \leq N$)

are computed either by the PR or by the RR approach. In the particular case of the D2Q9 lattice, Hermite polynomials up to $N = 2$ were first considered for the polynomial expansion [50], leading to

$$\mathcal{B}_{\mathrm{D2Q9}}^{\mathcal{H}} = \left(\mathcal{H}_i^{(0)}, \mathcal{H}_{i,x}^{(1)}, \mathcal{H}_{i,y}^{(1)}, \mathcal{H}_{i,xx}^{(2)}, \mathcal{H}_{i,xy}^{(2)}, \mathcal{H}_{i,yy}^{(2)} \right). \tag{4.3.14}$$

Nevertheless, the development of the VDF can be extended including some third- and fourth-order terms, which also satisfy the orthogonality property conservation (3.1.35):

$$\mathcal{B}_{\mathrm{D2Q9}}^{\mathcal{H},Complete} = \mathcal{B}_{\mathrm{D2Q9}}^{\mathcal{H}} \cup \left(\mathcal{H}_{i,xxy}^{(3)}, \mathcal{H}_{i,xyy}^{(3)}, \mathcal{H}_{i,xxyy}^{(4)} \right) \tag{4.3.15}$$

and $\mathcal{B}_{\mathrm{D2Q9}}^{\overline{\mathcal{H},Complete}} = \varnothing$. In other words, the *complete* basis $\mathcal{B}_{\mathrm{D2Q9}}$ can be derived thanks to the tensor properties of the D2Q9 lattice, which allows the conservation of orthogonality properties for every second-order Hermite polynomial *per direction*. The same applies to the D3Q27 lattice as already demonstrated in Sec. 3.3.3.

Malaspinas has recently shown that developing $f_i^{(0),N}$ onto these *complete* basis helps reducing the $\mathcal{O}(\mathrm{Ma}^3)$ error term in the momentum equation by removing all non-diagonal terms [134]. The *same* development was also done for $f_i^{(1),N}$ during the regularization process. And even if it was not explicitly specified in [134], one should notice that doing a full projection of the nonequilibrium VDF onto $\mathcal{B}_{\mathrm{D2Q9}}$, in order to compute the 9 nonequilibrium coefficients, has no impact at all on the nonequilibrium VDF. As an analogy, it would be pointless to project a 2D vector onto the orthonormal basis of the 2D physical space using the Euclidean scalar product. Hence a *complete* PR approach would be absolutely useless, since it would not filter out any physical information.

4.3.2 Numerical validation

This section will aim at showing some interesting properties of the RR procedure:

1. It enhances numerical stability compared to the PR procedure for both standard and high-order LBMs,

2. It is the only way to filter out nonhydrodynamic spurious sources without discarding any Hermite coefficients,

3. The extension of the RR collision model (4.3.5) helps improving numerical stability for the simulation of thermal and fully compressible flows.

4.3.2.a   Isothermal LBM ($\theta = 1$)

In a first time, the case of isothermal flows is considered. Lattice structures with increasing complexity (D2Q9, D2V17a and D2V37a) are successively used to point out the capability of the RR procedure to deal with both standard and high-order LBMs in a straightforward way. As a reminder, all velocity set definitions are recalled in Tabs. D.1 and D.2.

The case of a thin double shear layer ($k^* = 80$ and $\delta^* = 0.05$) is considered for the reasons discussed in Sec. 4.1.1. The Reynolds number is first fixed to a moderate value of $\text{Re} = u_0 L/\nu = 3 \times 10^4$. This is sufficient to reach the stability limit of the BGK collision model for standard LBMs when an underresolved mesh ($L = 128$) is considered [90]. The stability range of the proposed model is then evaluated varying the Reynolds number from 10^4 to 10^6. Simulations using the D2Q9, the D2V17a and the D2V37a lattices are performed with a freestream Mach number $M_0 = u_0/c_s = 0.2$, 0.35 and 0.57 respectively. These values are chosen in order to: (i) properly distinguish the impact of each collision operator on the numerical stability of each LBM, and (ii) reduce the impact of the $\mathcal{O}(\text{Ma}^3)$ error terms encountered when the D2Q9 lattice is employed. The initialization step is achieved using the approximation $f_i \approx f_i^{(0)} + f_i^{(1)}$, with $f_i^{(1)}$ computed using analytic formulas for the velocity gradients. This allows to reduce spurious oscillations at the beginning of the simulation as demonstrated in [135]. Finally, it should be noted that for all simulations below, $f_i^{(0)}$ is expanded to the maximal authorized order, i.e, $N = 3$ for the D2V17a, and $N = 4$ for both the D2Q9 and the D2V37a, using their associated Hermite tensor basis (see App. D & App. G for more details on this last point).

Extensive results concerning the case at $\text{Re} = 3 \times 10^4$ are compiled in Figs. 4.4, 4.5 and 4.6 for the D2Q9, the D2V17a and the D2V37a lattices respectively. All models are compared to a reference solution obtained using the BGK collision model with $L = 2048$. Several partial conclusions can be drawn from these results.

Firstly, correct kinetic-energy-related evolutions are recovered for all computations, even using a relatively coarse mesh ($L = 128$). Regarding mean and standard deviation of the enstrophy, a convergence study has been conducted, leading to the choice of a centered and fourth-order-accurate finite-difference scheme for the gradient evaluation. Nevertheless small errors are still observed, when the Mach number is increased, even for $L = 256$. Thus recovering the proper evolution of the mean and the standard deviation of the enstrophy is more difficult than obtaining the correct evolution of the same quantities in the case of the kinetic energy. The study of the enstrophy evolution should then be preferred for the accuracy evaluation of LBMs.

Secondly, the new RR approach is more stable than the PR one, at least for the present lattices. As explained in Sec. 4.3.1, this originates from a better computation of nonequilibrium Hermite coefficients $\boldsymbol{a}_1^{(n)}$ from the kinetic theory point of view. This point is further highlighted in Fig. 4.7, where the maximal achievable Mach number M_0^{Max} allowing a stable simulation, up to $t/t_c = 2$, is plotted for Reynolds numbers ranging from 10^4 to 10^6, in the underresolved configuration $L = 128$ and 256. The stability criterion that has been chosen is based on the mean kinetic energy $\langle u^2 \rangle$: a computation is considered to remain stable if $\langle u^2(t \leq 2t_c) \rangle < \langle u^2(t = 0) \rangle$. For a proper comparison, the standard PR and the most stable RR versions associated to each lattice structure are compared. Results obtained in the particular case of $\text{Re} = 3 \times 10^4$ seem to be extendable to a wide range of Reynolds number.

Thirdly, the PR 4 and the BGK collision models give exactly the same results in the particular case of the D2Q9 lattice. This confirms what was anticipated in Sec. 4.3.1, i.e, when the VDF is expanded over the *complete* Hermite basis then the PR 4 and the BGK reduce to the same collision operator. Therefore the only way to reach the full potential

Figure 4.4 − Double shear layer at $M_0 = 0.2$ and Re $= 3 \times 10^4$ for the D2Q9 lattice. From top to bottom: dimensionless mean kinetic energy, standard deviation of the kinetic energy, mean enstrophy and standard deviation of the enstrophy. All quantities are spatially averaged over all the simulation domain. The projection based (PR) and the recursive (RR) regularization, at order $N = 2$, 3 and 4, are compared against the standard collision model (BGK). The first two columns are the results obtained using a $L \times L$ mesh with $L = 128$ and $L = 256$ respectively. The last column illustrates the mesh convergence of the fourth-order recursive regularization (RR 4), where the reference solution was obtained using the BGK collision operator with $L = 2048$. The characteristic time t_c is defined as $t_c = L/u_0$, while the characteristic speed is $u_0 = M_0 c_s$.

Figure 4.5 – Double shear layer at $M_0 = 0.35$ and $Re = 3 \times 10^4$ for the D2V17a lattice. From top to bottom: dimensionless mean kinetic energy, standard deviation of the kinetic energy, mean enstrophy and standard deviation of the enstrophy. All quantities are spatially averaged over all the simulation domain. The projection based (PR) and the recursive (RR) regularization, at order $N = 2$ and 3, are compared against the standard collision model (BGK). The first two columns are the results obtained using a $L \times L$ mesh with $L = 128$ and $L = 256$ respectively. The last column illustrates the mesh convergence of the third-order recursive regularization (RR 3), where the reference solution was obtained using the BGK collision operator with $L = 2048$. The characteristic time t_c is defined as $t_c = L/u_0$, while the characteristic speed is $u_0 = M_0 c_s$.
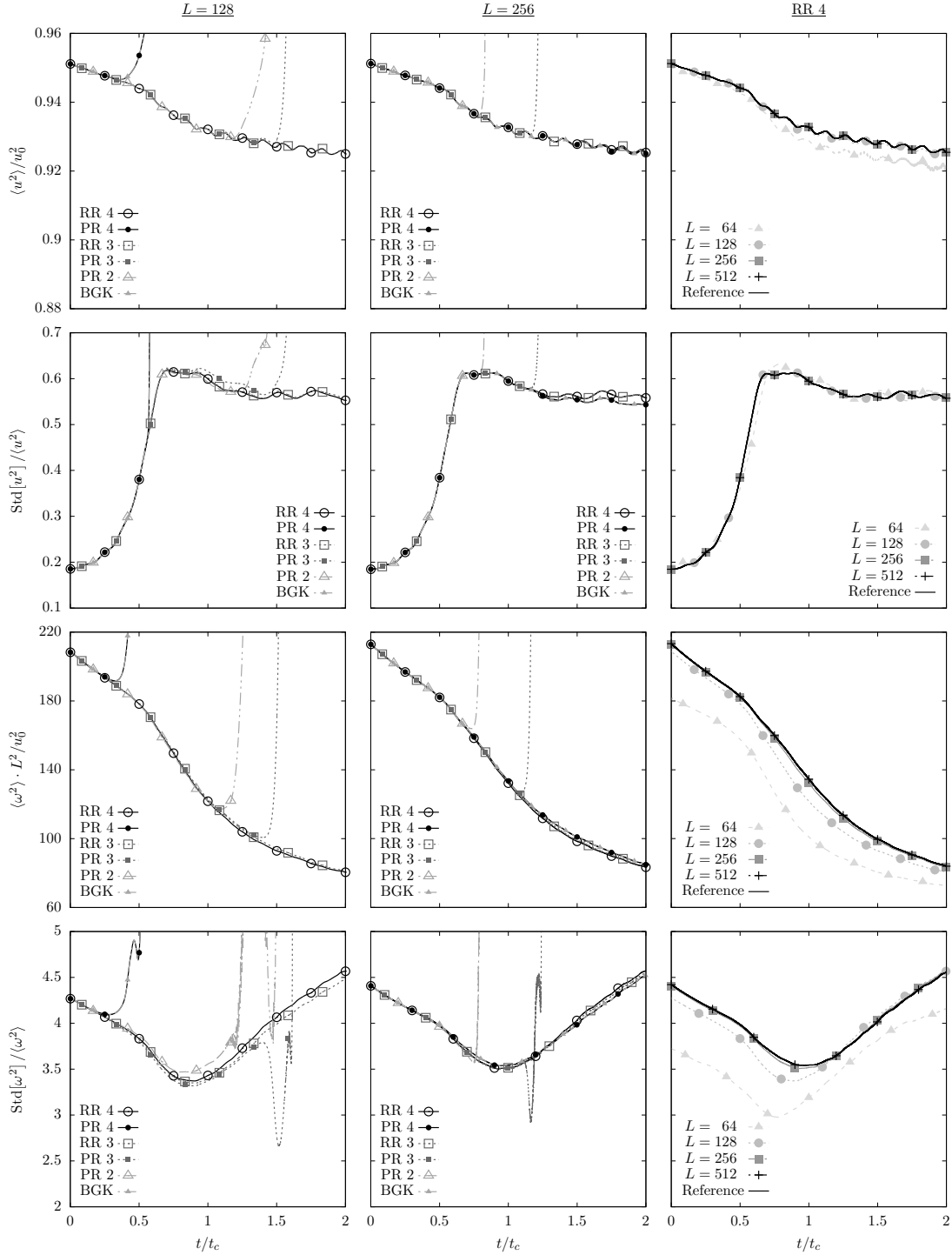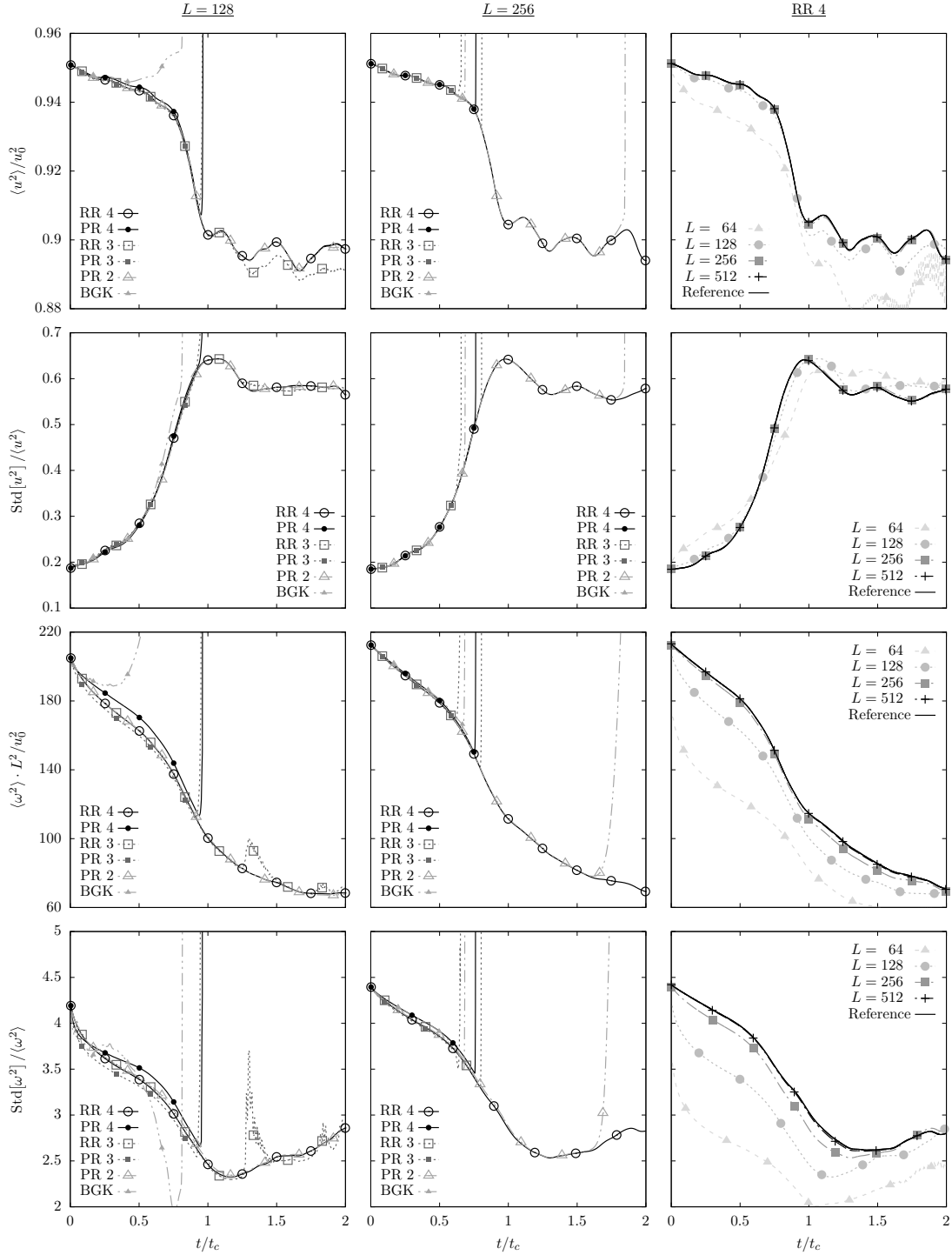
Figure 4.6 – Double shear layer at $M_0 = 0.57$ and $\mathrm{Re} = 3 \times 10^4$ for the D2V37a lattice. From top to bottom: dimensionless mean kinetic energy, standard deviation of the kinetic energy, mean enstrophy and standard deviation of the enstrophy. All quantities are spatially averaged over all the simulation domain. The projection based (PR) and the recursive (RR) regularization, at order $N = 2$, 3 and 4, are compared against the standard collision model (BGK). The first two columns are the results obtained using a $L \times L$ mesh with $L = 128$ and $L = 256$ respectively. The last column illustrates the mesh convergence of the fourth-order recursive regularization (RR 4), where the reference solution was obtained using the BGK collision operator with $L = 2048$. The characteristic time t_c is defined as $t_c = L/u_0$, while the characteristic speed is $u_0 = M_0 c_s$.
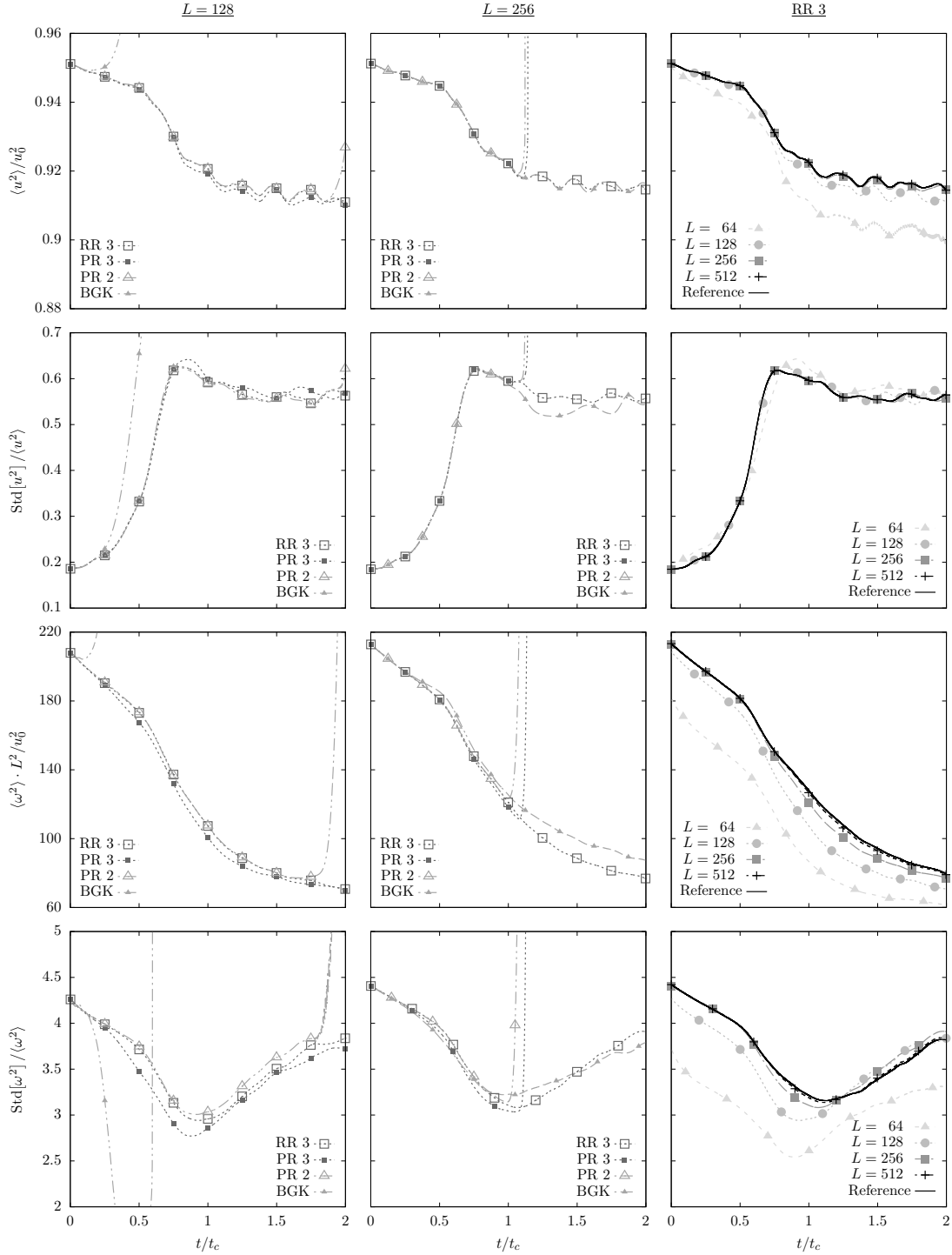
of the D2Q9 lattice is to use the RR procedure.

Lastly, the computational overhead for our *nonoptimized* implementation is $1.5 \leq t_{RR}/t_{BGK} \leq 2$, the lower limit is for the D2Q9 lattice and the upper for the D2V37a one. This is far from being excessive considering the tremendous improvements obtained in terms of numerical stability. Regarding the regularization step itself, the RR approach is always faster (about 20%) than the standard PR one.
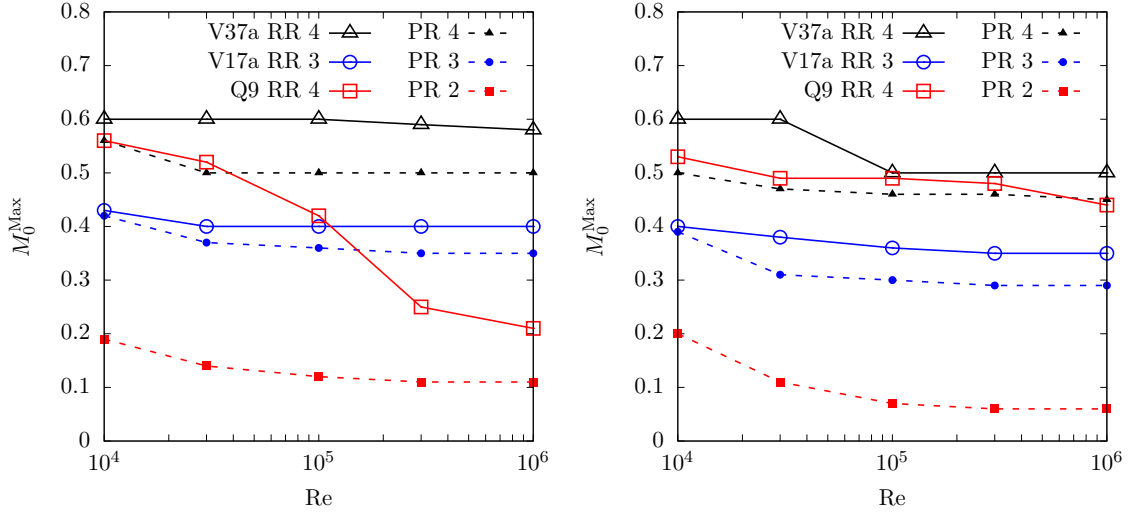
Figure 4.7 – Stability range of the double shear layer simulation using $L = 128$ (left) and 256 (right), for $t \leq 2t_c$, and with the characteristic time $t_c = L/M_0 c_s$. The standard PR (filled symbols) and the most stable RR (open symbols) procedures are compared for every LBMs. The RR approach always shows a higher stability range regarding M_0^{Max}, where the level of accuracy of M_0^{Max} is $\Delta M_0 = 0.01$.

4.3.2.b Fully compressible LBM

To further validate the general RR process, the simulation of thermal and fully compressible flows is now considered. This is done through the numerical computation of the famous Sod shock tube [136], using the most compact lattice structure allowing to ensure the preservation of the orthogonality of all fourth-order Hermite tensors: the D2V37a velocity set [119, 120]. For this purpose, Hermite coefficients $\boldsymbol{a}_0^{(n)}$ and $\boldsymbol{a}_1^{(n)}$ are computed thanks to our proposed extensions (F.2.1) and (4.3.5). Here, two different configurations are studied. They share the same pressure ratio but differ when it comes to their temperature or density ones:

$$(P_L, \rho_L, u_L) = (10, 8, 0), \quad (P_R, \rho_R, u_R) = (1, 1, 0), \tag{4.3.16}$$

$$(P_L, \rho_L, u_L) = (10, 2, 0), \quad (P_R, \rho_R, u_R) = (1, 1, 0), \tag{4.3.17}$$

where subscripts L and R stand for the left and the right states respectively. As already described in Sec. 4.1.2, the computation takes place in a periodic domain of length $2L_x$ centered around the location $x = L_x/2$ where the discontinuity between the two states belongs. The simulation domain is then spatially discretized using $L_x = 400$ grid
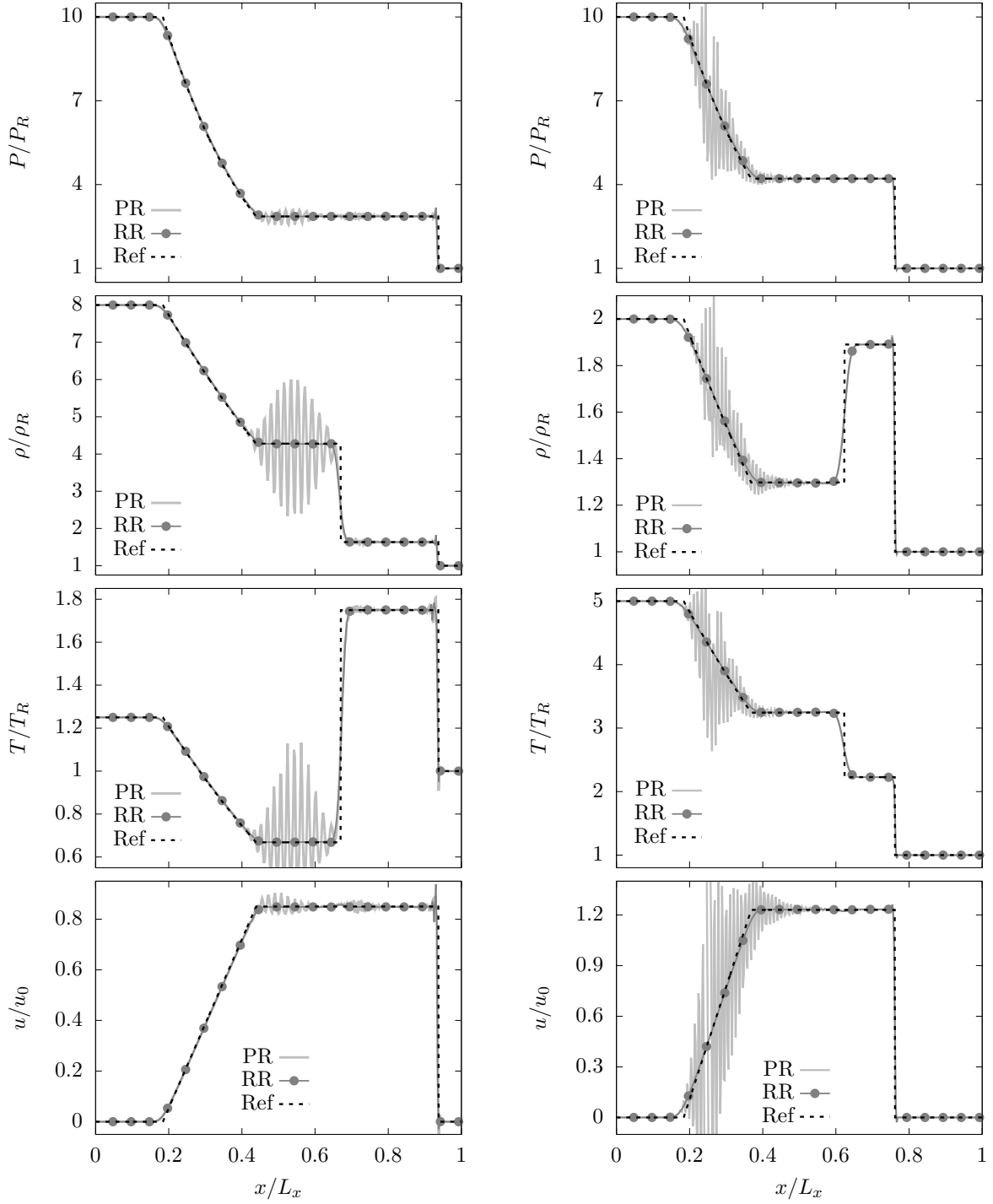
Figure 4.8 – 1D Riemann problem using the D2V37a lattice: $[P_L/P_R, \rho_L/\rho_R] = [10, 8]$ (left) and $[10, 2]$ (right) with $L_x = 400$ grid points, and a relaxation time of $\tau = 0.595$ and $\tau = 0.760$ respectively. From top to bottom: dimensionless pressure, density, temperature and velocity profiles. Results obtained using the fourth-order PR and RR steps are compared to the reference solution (dashed line) for a specific heat ratio $\gamma = 2$. They are plotted at time $t/t_c = 0.2$ (left) and $t/t_c = 0.1$ (right), with the characteristic time $t_c = L_x/\sqrt{\gamma T_R}$.

points. Such a coarse mesh will allow to further highlight the numerical stability issues encountered computing discontinuities.

Results obtained using the PR and the RR processes, at order $N = 4$, are plotted along $[0, L_x]$ in Fig. 4.8. Even though both models are able to properly reproduce the generation and the propagation of all the characteristic waves of this 1D Riemann problem, the PR procedure introduces a coupling between high-order and NSF physics in the form of standing waves, whereas the RR procedure completely filters them out even if small over/undershoots still remain. The latter can be attenuated using either a finer grid or a shock-capturing technique, such as local injections of artificial viscosity using a shock-capturing technique [127].

It must be noted that without regularization steps, the standard LBM encountered severe numerical stability issues for the present configurations, and could not be stabilized even using extremely fine meshes (more than 10000 points in the longitudinal direction). This further points out that the RR collision operator allows to get more stable solutions without degrading the accuracy of the numerical scheme.

4.4 Shock-capturing technique

In the previous section, high-order LBMs based on the RR collision operator were shown to be able to simulate fully compressible flows including shock waves. Here, we intend to further evaluate these high-order LBMs in *realistic conditions*, i.e, with very low kinematic viscosity. In this context, the use of a shock-capturing technique is mandatory to inhibit the onset of spurious (Gibbs) oscillations arising near discontinuities [127]. The goal of the present study is to examine the coupling between regularization steps and a shock-capturing technique. A simple approach is then retained as a first step while the coupling with more complex shock-capturing techniques is deferred to future work.

4.4.1 Principle

Due to its simplicity regarding both physical interpretation and coding, a Jameson-like sensor [137] will be tested hereafter to locally add artificial viscosity. This shock sensor was designed to be active near regions where abrupt fluctuations of pressure are encountered[3]. It is based on the evaluation of a normalized pressure laplacian:

$$s_{\mathrm{J}}(x) \overset{\mathrm{1D}}{=} \frac{|p(x+1) - 2p(x) + p(x-1)|}{|p(x+1)| + 2|p(x)| + |p(x-1)|} \tag{4.4.1}$$

with $0 \leq s_{\mathrm{J}}(x) \leq 1$, and where $x-1$, x and $x+1$ correspond to the left, current and right abscissa respectively.

---

[3]It must be noted that this sensor is not well suited for the simulation of compressible homogeneous and isotropic turbulence, since it cannot properly separate pressure fluctuations induced by turbulence from those induced by the shock wave itself. Nevertheless, it is sufficient to serve its purpose, i.e, study the coupling between the RR procedure and a shock-capturing technique.

Originally, this sensor was designed to detect regions where second- (standard) and fourth-order (hyperviscosity) artificial viscosity[4] needed to be added. This was done through forcing terms that were injected into the momentum and energy equations. Here, it was preferred to include a second-order artificial viscosity component through the redefinition of the discrete relaxation time:

$$\overline{\tau_{\mathrm{J}}}(x) = \tau_{\mathrm{J}}(x) + \frac{1}{2} = \frac{\nu + \nu_{\mathrm{J}}(x)}{c_s^2 \theta} + \frac{1}{2} \qquad (4.4.2)$$

where $\nu_{\mathrm{J}}(x) = A_{\mathrm{J}} s_{\mathrm{J}}(x)$, and $A_{\mathrm{J}} = 0.05\, L_x$ is a constant that has been defined through a series of several shock tube simulations varying mesh sizes. This way of redefining the discrete relaxation time is directly inspired from the large eddy simulation framework, for which an eddy viscosity might be used to take into account the contribution of underresolved turbulent scales through an additional relaxation time [2, 20].

The following configuration is used for the validation of the shock-capturing technique:

$$(P_L, \rho_L, u_L) = (4, 4, 0), \quad (P_R, \rho_R, u_R) = (1, 1, 0), \qquad (4.4.3)$$

hence an uniform temperature profile at the initialization step. Besides, the reference temperature T_0, used for both the nondimensionalization of physical quantities and the computation of the time step (acoustic scaling), will have the value $T_0 = 300\,[K]$ and will be chosen as the initial temperature value. This eventually leads to an uniform temperature profile of $\theta = 1$ in lattice units. It will be shown in Sec. 4.4.4 that this choice does have an impact on the numerical stability of LBMs.

4.4.2   Collision model comparison

Comparisons regarding the coupling between several collision models (BGK, PR and RR) and the above shock-capturing technique are plotted in Fig. 4.9 for $L_x = 10\,000$, 400 and 100. Despite its simplicity, the shock-capturing technique allows to properly stabilize simulations even for $\nu = 0$. For the finest mesh grid ($L_x = 10\,000$), the sensor adds artificial viscosity where it is required, i.e, near discontinuities and especially near the shock wave. Regarding the collision model comparison, the recursive regularized LBM is the best approach to filter out spurious oscillations, upstream of the contact discontinuity, for underresolved grid meshes. On the contrary, the BGK collision model leads to the worst results. This proves that: (1) the present shock-capturing technique alone is not sufficient to obtain satisfactory results, and (2) the proposed stabilization technique (RR) can be coupled to a shock-capturing technique to further filter out spurious oscillations encountered with the simulation of compressible flows including discontinuities. Nevertheless, small oscillations remain between the contact discontinuity and the shock wave for all mesh grids. Two possible explanations would be that they are either due to the definition of the shock-sensor, or to the stability threshold of the LBM itself.

---

[4]By definition, a $2N$th-order artificial viscosity term directly depends on the $2N$th-order derivative of the velocity.
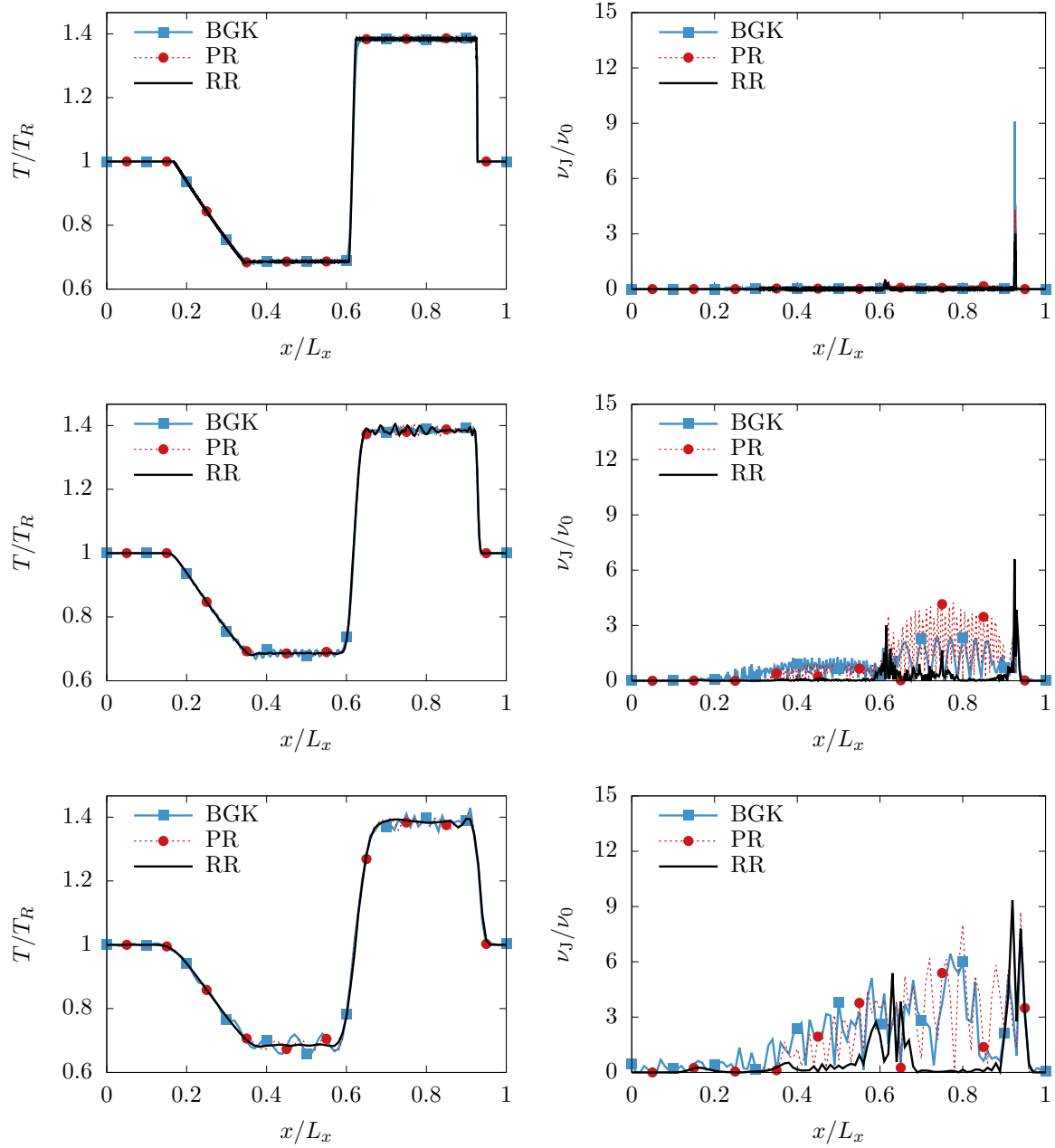
Figure 4.9 – 1D Riemann problem using the D2V37a lattice: $[P_L/P_R, \rho_L/\rho_R] = [4, 4]$ with $\nu = 0$. Jameson-like shock sensor evaluated at the current node. Dimensionless temperature (left) and artificial viscosity (right) profiles are plotted for $L_x = 10\,000$, 400 and 100 grid points (from top to bottom). Both regularized and BGK models are compared. Only the RR approach allows to properly filters out spurious oscillations.

4.4.3   Impact of the sensor evaluation

To further understand the origin of these remaining oscillations, more complex shock sensors are employed. They are still based on Eq. (4.4.1) but its evaluation is now done using either three (3p) or five points (5p). Furthermore, three ways of taking into account the contribution of each point of the stencil are studied:

1. <u>Mean</u>

$$s_{\text{J}}^{3p} = \frac{s_{x-1} + s_x + s_{x+1}}{3}, s_{\text{J}}^{5p} = \frac{s_{x-2} + s_{x-1} + s_x + s_{x+1} + s_{x+2}}{5} \qquad (4.4.4)$$

2. <u>Weighted</u> (D1Q3 & D1Q5)

$$s_{\text{J}}^{3p} = \frac{s_{x-1} + 4s_x + s_{x+1}}{6}, s_{\text{J}}^{5p} = \frac{s_{x-2} + 2s_{x-1} + 6s_x + 2s_{x+1} + s_{x+2}}{12} \qquad (4.4.5)$$

3. <u>Max</u>

$$s_{\text{J}}^{3p} = \max(s_{x-1}, s_x, s_{x+1}), s_{\text{J}}^{5p} = \max(s_{x-2}, s_{x-1}, s_x, s_{x+1}, s_{x+2}) \qquad (4.4.6)$$

Hereafter, only results obtained with the RR approach are shown. Nevertheless, conclusions remain similar for both PR and BGK collision models.

For reasons not fully understood, the finest and the coarsest mesh grids are quasi-insensitive to either the stencil or the evaluation technique of s_{J}. However, it was noticed that increasing the number of evaluation points does allow to reduce the amount of artificial viscosity added locally. Albeit small, discrepancies are observed for the case $L_x = 400$ as shown in Fig. 4.10. The configuration using a 5-point stencil for the evaluation of the maximal value of s_{J} gives the more stable results. Still, some oscillations remain between the contact discontinuity and the shock wave. And even if they are not presented here, similar results are observed with the BGK and the PR collision models.

4.4.4   Initial temperature

The last study, regarding the origin of the remaining spurious oscillations, is based on the influence of the initial temperature field. It is motivated by the fact that oscillations are restricted to the region where temperature values are the higher. The impact of θ is conducted keeping $T_0 = 300 \, [K]$ but varying the value of the uniform temperature profile T_{init}.

θ_{init} is varied from 1.2 to 0.54631, and results obtained with the D2V37a lattice using the RR approach are summarized in Fig. 4.11. Interestingly, oscillations appear to the left/right of the contact discontinuity for low/high values of θ_{init}. This confirms that these oscillations are induced by θ-related stability thresholds of the LBM itself.

Eventually, choosing $\theta = 0.8$ allows to reduce the stencil allocated for the sensor evaluation. Final results obtained with the D2V37a lattice, for the RR approach and with the Max evaluation of s_{J}^{3p} (3pMax), are compared to theoretical results in Fig. 4.12. The above setup definitely allows to simulate compressible flows including discontinuities even with coarse mesh grids ($L_x = 100$).

Figure 4.10 − 1D Riemann problem using the D2V37a lattice (RR approach): $[P_L/P_R, \rho_L/\rho_R] = [4, 4]$ with $\nu = 0$. Impact of the evaluation of the Jameson-like sensor with a 5-point stencil (top), and influence of the stencil for the evaluation using the max function. Dimensionless temperature (left) and artificial viscosity (right) profiles are plotted for $L_x = 400$. The configuration 5pMax gives the best results

Figure 4.11 − 1D Riemann problem using the D2V37a lattice (RR approach): $[P_L/P_R, \rho_L/\rho_R] = [4, 4]$ with $\nu = 0$. Impact of $\theta_{\mathrm{init}} = T_{\mathrm{init}}/T_0$ for the configuration 5pMax, with $\theta_{\mathrm{init}}^{\mathrm{crit}} = 0.54631$ the lower stability threshold. Dimensionless temperature (left) and artificial viscosity (right) profiles are plotted for $L_x = 400$. A proper choice of θ allows to increase the numerical stability of the simulation.
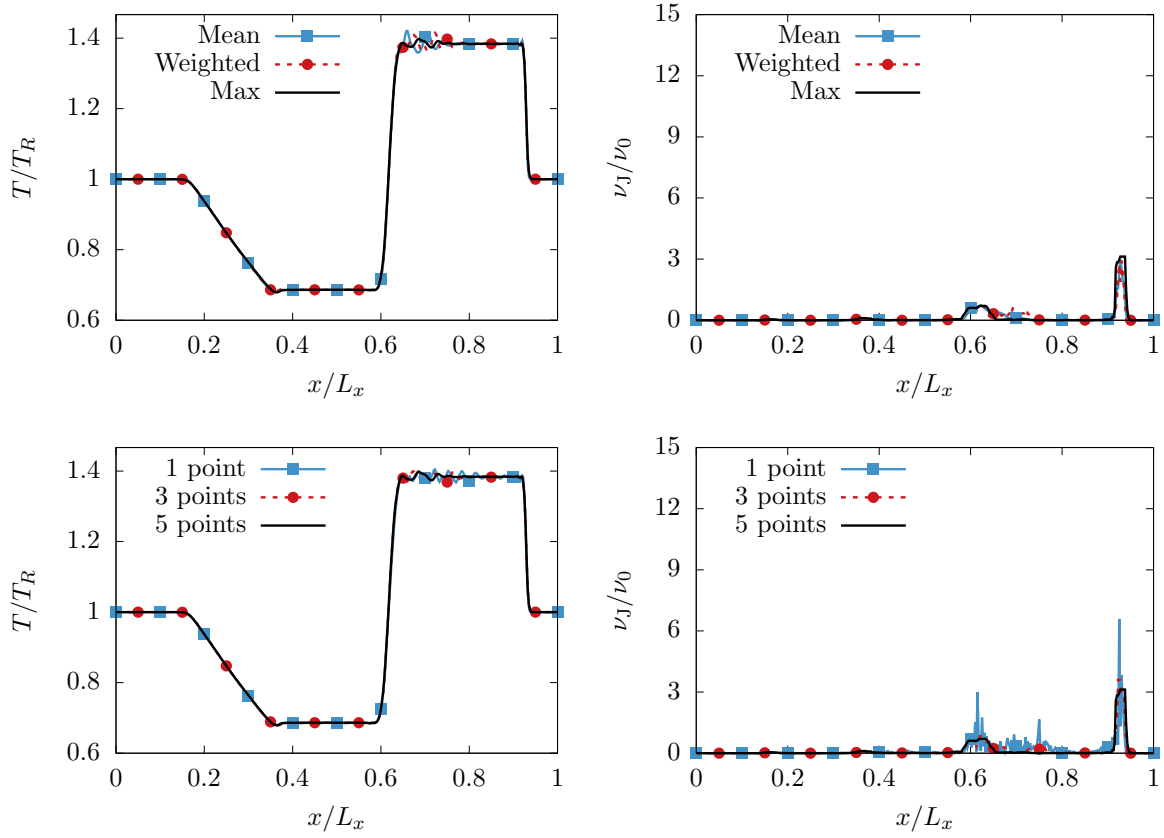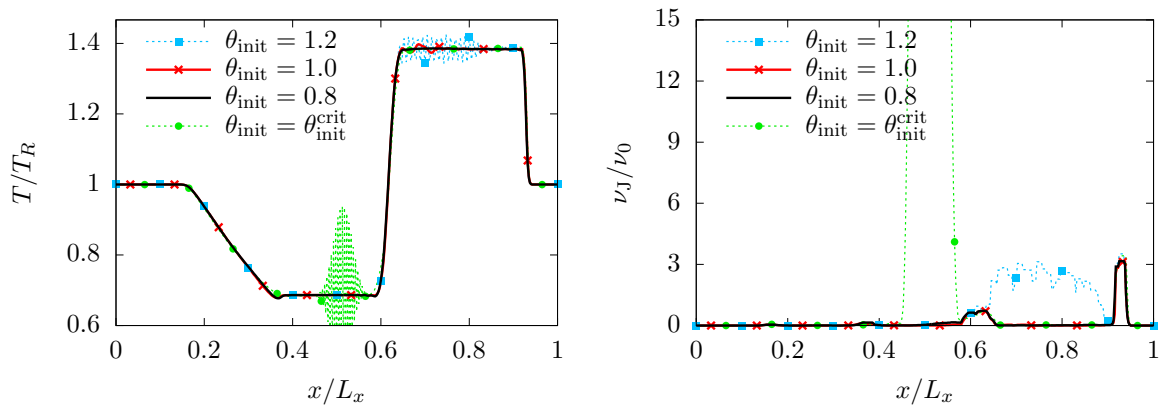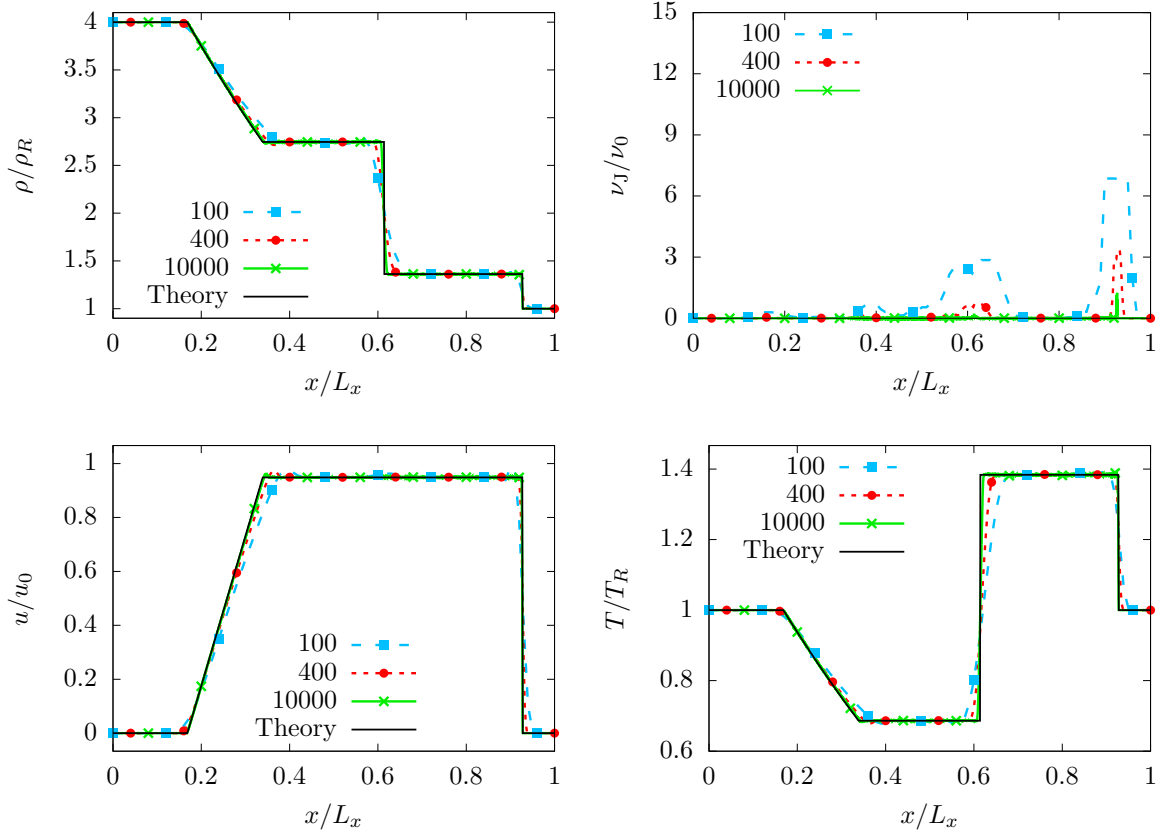
Figure 4.12 – 1D Riemann problem using the D2V37a lattice (RR and 3pMax): $[P_L/P_R, \rho_L/\rho_R] = [4, 4]$ with $\nu = 0$, and $\theta = 0.8$. Dimensionless density, artificial viscosity, velocity and temperature profiles are plotted for $L_x = 10\,000$, 400 and 100 grid points (from top left to bottom right). Results are in excellent agreement with theoretical curves.

4.5 Conclusions

As it was recalled in this chapter, despite a wide range of validity of the standard lattice Boltzmann method (LBM), the simulation of certain flows remains a tedious task: (1) weakly compressible flows at high Reynolds numbers, and (2) fully compressible flows including discontinuities such as shock waves.

In this context, an extension of the recursive regularization (RR) step to high-order LBMs was first proposed. New LBMs, with increased stability range, were then obtained filtering out the nonhydrodynamic contributions to the lattice Boltzmann dynamics. This filtering technique relies on two points: (a) the computation of nonequilibrium coefficients $\boldsymbol{a}_1$ through the CE expansion, eased thanks to (b) the recursive properties of Hermite polynomial basis. This procedure was originally derived in the particular case of isothermal and weakly compressible flow simulations, with standard lattices such as the D2Q9 and the D3Q27. Here, it was further validated using high-order LBMs (the D2V17a and the D2V37a) for the simulation of both isothermal flows and thermal fully compressible flows. The latter was possible thanks to our derivation of general recursive formulas for

the computation of Hermite coefficients $\boldsymbol{a}_0$ and $\boldsymbol{a}_1$. Strong improvements in terms of numerical stability are confirmed for both kinds of simulations, and at a relatively low computational overhead.

To further increase the numerical stability of high-order LBMs, for the simulation of flows including discontinuities in realistic conditions (very small kinematic viscosity), the coupling between the RR approach and a shock-capturing technique was investigated. The latter is commonly used in the CFD community to increase the robustness of numerical schemes near discontinuities while keeping their accuracy in smooth regions. Due to its simplicity, a Jameson-like shock sensor was employed to detect regions where additional (second-order artificial) kinematic viscosity was needed to stabilize simulations. This artificial viscosity was taken into account during the collision step by modifying the definition of the relaxation time, in the same way as for large eddy simulations. All the above procedure eventually led to excellent results with respect to theoretical curves, even in the zero-viscosity limit. It was also pointed out that the initial temperature field must be chosen carefully in order to completely filter out spurious oscillations for coarse mesh grids. It is likely to be linked to the positivity domain of VDFs. The validity of this last hypothesis is deferred to future work.

Now that the RR procedure was shown to increase the numerical stability of both standard and high-order LBMs using numerical test cases, let us take a step back and look at the big picture by studying their linear stability domain in the isothermal context.

Chapter 5

Linear Stability Analysis of the Continuous LBE

Contents

This chapter is dedicated to the linear stability analysis (LSA) of the continuous LBE. It aims at investigating possible differences arising from the velocity discretization, even for several velocity discretizations which were originally built to recover the very same macroscopic behavior. After a brief review of previous LSA conducted in the context of LBMs, the basic features of the LSA are recalled. Hydrodynamic modes, classically encountered with the linearized Navier-Stokes-Fourier equations, are then presented to give the reader the main material to properly understand results. The impact of the velocity discretization is first quantified in the case of the D2Q9 lattice before moving to high-order velocity sets.

5.1   Introduction and brief review

The linear stability analysis (LSA) consists in evaluating the response of a system, described by a given set of either partial or ordinary differential equations (PDEs or ODEs), to a local perturbation. This response is quantified through the computation of the perturbation growth rate and propagation speed. If the former remains negative over time, then the system is able to absorb the perturbation leading to a linearly stable set of equations for the given input parameters. On the contrary, a positive growth rate translates into perturbations of increasing amplitude, eventually leading to a linearly unstable system for the given input parameters.

It is interesting to note that the LSA can be applied to very different research fields leading to very different kinds of results. As an example, the LSA is the cornerstone of hydrodynamic stability studies [138, 139] where it is used to study the growth of excitations/perturbations superimposed to either inviscid or viscous base flows [140–142]. Both space and time evolutions can be investigated in order to understand, prevent or even promote the growth of hydrodynamic instabilities. Concerning numerical schemes, the LSA allows to determine their linear stability range for uniform base flows and assuming a periodic simulation domain, i.e, no boundary conditions.[1] In this particular context, the LSA is most commonly called a von Neumann (or Fourier) analysis owing to the fact that von Neumann was the first to study the linear stability of numerical schemes used to solve discretized PDEs[2].

While a very large number of articles introduce and numerically validate stabilization techniques of LBM in the context of high-Reynolds number flow simulations, only few authors used the LSA to study the stability of LBMs in the lattice-Boltzmann community. One of the first investigation based on the application of the LSA to the discrete set of LBEs, i.e, LBM, was proposed by Sterling *et al.* [147]. In their paper, they studied the impact of constants, belonging to their truncated equilibrium function, on the linear

---

[1]Other methods exist and allow to include the impact of boundary conditions into the LSA [143, 144].

[2]It is interesting to note that this kind of LSA was first developed by John von Neumann in Los Alamos during Wolrd War II. Shortly afterwards, this method was classified until its brief description by Crank and Nicolson [145] in 1947. Eventually, von Neumann coauthored an article [146] in 1950, in which the method was more rigorously presented.

stability of several lattices (hexagonal, square and cubic) assuming an uniform base flow, whereas no proper explanation regarding the origin of instabilities was given. Modifying the input base flow, the influence of shear was further studied by Worthing *et al.* [148], but no more information were provided regarding causes of, or remedies to, linear instabilities. It is only with the work of Lallemand & Luo [128] that mode coupling was identified as one of the possible sources of stability issues. They proposed to use a multi-relaxation-time (MRT) collision model to increase the stability range of LBM. The relaxation parameters of this MRT model were then optimized using the LSA. Their investigation was further pursued with thermal LBM [149] leading to one other remedy to the mode coupling, i.e, the use of hybrid LBM.

More recent evidences suggest the way of building LBMs is directly linked to their linear stability range. Indeed, Siebert and his coworkers [59] showed that a better design of LBM from both the mesoscopic and the macroscopic points of view, i.e, preservation of Hermite polynomial properties during the velocity space discretization, ensures at the same time a good behavior of the related LBE, and the recovery of Navier-Stokes-Fourier (NSF) equations. One of their most striking result comes from their comparison between a previously developed thermal LBM [57] and a fourth-order Hermite-based LBM (D2V37), where the latter completely outperforms the former from the point of view of LSA.

Last papers dealing with the LSA of LBMs, can be divided into two groups. The former aims at improving the stability range of LBMs through the study of more complex collision models, and follows the work of Lallemand & Luo [128, 149]. While Ginzburg and her coworkers [150] focused on a two-relaxation-time (TRT) collision model[3], Dubois *et al.* [152] showed the impact of the moment basis in which the evolution of velocity distribution functions (VDFs) is described. The latter further pointed out the stability increase induced by relaxing moments in a comoving reference frame instead of the standard frame at rest. This led to a first explanation regarding the stabilization property of such a change of reference frame for the collision step, while this process was originally designed using geometrical considerations based on the Galilean invariance principle [95][4]. Regarding the second group of studies, they concentrated on more standard applications of the LSA to numerical schemes. Marié *et al.* [153] compared the spectral properties of the D3Q19-BGK with the ones of optimized numerical schemes dedicated to computational aeroacoustics (CAA). They showed that even if dispersion properties are similar to second- and third-order schemes, the numerical dissipation induced by the 'Collide & Stream' algorithm is similar to a six-order optimized scheme belonging to the state of the art of CAA numerical schemes (Bogey & Bailly scheme [154]). Hence standard LBMs

---

[3]This collision model is a particular case of the more general MRT model, in which relaxation processes associated to odd and even moments are decoupled allocating them their own relaxation time. Another TRT-like model was also proposed by Adhikari & Succi [151], but this time the second relaxation parameter was used to control the behavior of ghost modes, while the first one was related to the control of hydrodynamic modes.

[4]As a reminder, Galilean invariance states that laws of motions should be the same whatever inertial reference frame is considered. It is then interesting to note that standard LBMs, which do not ensure the conservation of high-order ($N \geq 3$) equilibrium moments during the velocity space discretization, lead to a velocity-dependent kinematic viscosity ($\mathcal{O}(\text{Ma}^3)$ error terms in the resulting momentum equation). This is why these LBMs are considered not to be Galilean invariant.

are able to convect information over very long distances with very little loss[5]. It should also be noted that, to the best of the author's knowledge, this is the only work dealing with the LSA of the continuous LBE. When it comes to the work of Ricot *et al.* [126], the LSA was used in order to study the spectral properties of the coupling between a spatial filtering and LBM, in the context of CAA and high-Reynolds number flows simulation. This filtering strategy was proposed as an alternative to the use of MRT collision models which increase stability through the overdamping of acoustic waves[6].

In the present work, we shall further highlight the fact that several LBMs, which were originally designed to recover the very same macroscopic behavior, do have different behaviors regarding both their continuous and discrete sets of equations. One of the main objective is also to quantify the impact both BGK and regularized collision models have on the linear stability range of LBMs. To do so, basic features of LSA are first recalled in Sec. 5.2. This is followed, in Sec. 5.3, by standard results concerning hydrodynamic modes. Then the LSA of the LBE, which is a continuous set of PDEs where continuous stands for continuous space and time derivatives, is conducted in Sec. 5.4. The impact of the space/time discretization, and of regularized collision models, is deferred to Chap. 6. If not otherwise stated, **all quantities considered hereafter will be dimensionless**.

5.2   Principle

The current work only focuses on the time evolution of perturbations superimposed to a mean base flow. To check whether these perturbations will grow in time or not, we need to compute their growth rate. This is done following two successive steps. They are summarized below, while further details are also provided in App. H for the interested reader.

1) **Derivation of linear perturbed equations**
   With this aim in mind, a Taylor expansion of the VDFs and the corresponding collision operator is performed about a mean flow, neglecting second- and high-order terms:

$$f_i \approx \overline{f_i} + f_i', \tag{5.2.1}$$

   with $\overline{f}_i = f_i^{(0)}|_{\overline{\rho},\overline{u},\overline{\theta}}$ (uniform flow), and $(\overline{\rho}, \overline{u}, \overline{\theta})$ the associated mean macroscopic quantities. Applying the same expansion to the general form of the collision term

---

[5]CAA is dedicated to the numerical simulation of aeroacoustics phenomena occuring in turbulent flows. If we consider that purely hydrodynamic pressure fluctuations are of the order of 1000 to 10 000 Pa, then purely acoustic phenomena will generate pressure fluctuations of about 1 to 100 Pa. Hence the numerical accuracy required to capture the generation of acoustic phenomena is about two orders of magnitude higher than for aerodynamic phenomena. This is why the LBM is of particular interest in the context of CAA due to the very low level of numerical dissipation it introduces in simulations.

[6]In general, it is quite difficult to find a way to stabilize LBM in this particular context, since only very few authors derived stabilization techniques which does not deteriorate propagation of sound waves. The work of Xu *et al.* seems to be one of the few trying to use the LSA to optimize MRT collision models for CAA [155,156].

Ω_i, and noticing that it is linked to f_j through the macroscopic quantities used in the definition of the equilibrium state $f_i^{(0)}$, we end up with

$$\Omega_i(f_i) \approx \Omega_i|_{\overline{f_i}} + \sum_{j=0}^{V-1} J_{ij} f_j', \qquad (5.2.2)$$

where $J_{ij} = \left. \frac{\partial \Omega_i}{\partial f_j} \right|_{\overline{f_j}}$ is the Jacobian matrix of the collision operator evaluated at $f_j = \overline{f_j}$, and V the number of discrete velocities. In what follows, the summation over j is dropped. Instead, Einstein's summation rule is considered for the sake of clarity.

By injecting Eqs. (5.2.1) and (5.2.2) in both the force-free LBE (3.2.1) and its space/time discretization ('Collide & Stream' algorithm (3.2.6)), and noticing that mean VDFs $\overline{f_i}$ are particular solutions of the resulting equations, two perturbed equations are obtained:

- Perturbed continuous LBE

$$\partial_t f_i' + \boldsymbol{\xi}_i \cdot \boldsymbol{\nabla} f_i' = J_{ij} f_j'. \qquad (5.2.3)$$

- Perturbed space/time discrete LBE

$$f_i'(\boldsymbol{x} + \xi_i, t + 1) = [\delta_{ij} + J_{ij}] \, f_j'(\boldsymbol{x}, t). \qquad (5.2.4)$$

where lattice Boltzmann units are assumed ($\Delta t = 1$) in the discrete case. These two equations are of particular interest. While Eq. (5.2.3) allows to evaluate the impact of the velocity discretization, Eq. (5.2.4) further highlights the influence of the space/time discretization on the numerical stability of the related LBM.

2) **Solve perturbed equations in the Fourier space**
Solutions of both set of perturbed equations ((5.2.3) & (5.2.4)) are obtained using a Fourier transform. This is equivalent to seeking solutions in the form of monochromatic plane waves evolving in a periodic domain[7]

$$\begin{aligned} f_i' &= A_i \exp[\mathrm{i}(\boldsymbol{k} \cdot \boldsymbol{x} - \omega t)], \quad (\boldsymbol{k}, \omega) \in \mathbb{R}^D \times \mathbb{C} \\ &= A_i \underbrace{\exp[\mathrm{Im}(\omega)t]}_{(a)} \underbrace{\exp[\mathrm{i}(\boldsymbol{k} \cdot \boldsymbol{x} - \mathrm{Re}(\omega)t)]}_{(b)} \end{aligned} \qquad (5.2.5)$$

where (a) is linked to the growth rate (or dissipation) of waves, while (b) gives information about the propagation speed (or dispersion) of numerical waves. Injecting Eq. (5.2.5) into perturbed equations (5.2.3) & (5.2.4) leads to two eigenvalue problems of size V:

---

[7]By definition, a plane wave is a wave composed of an infinite number of parallel wave fronts. Furthermore, the monochromatic property of a wave implies that its amplitude is controlled by a single frequency, hence the sinusoidal evolution of its amplitude. In our case, perturbations of VDFs propagate in the direction of $\boldsymbol{k}$, with an amplitude controlled by $k = ||\boldsymbol{k}||$, and at a velocity $\mathrm{d}\omega_r/\mathrm{d}k$, with $\omega_r = \mathrm{Re}(\omega)$. Here, the definition of the velocity group was considered for the propagation of disturbances, instead of the phase speed ω_r/k, since their velocity is k-dependent (dispersive medium).

- Continuous LBE

$$\boldsymbol{M}_{\boldsymbol{\Omega}}^{\mathbf{C}} \boldsymbol{A} = \omega \boldsymbol{A}, \tag{5.2.6}$$

- Collide & Stream

$$\boldsymbol{M}_{\boldsymbol{\Omega}}^{\mathbf{D}} \boldsymbol{A} = \exp\left(-\mathrm{i}\omega\right) \boldsymbol{A}, \tag{5.2.7}$$

with ω ($\exp\left(-\mathrm{i}\omega\right)$) the eigenvalue, $\boldsymbol{M}_{\boldsymbol{\Omega}}^{\mathbf{C}}$ ($\boldsymbol{M}_{\boldsymbol{\Omega}}^{\mathbf{D}}$) the matrix associated to the continuous (discrete) perturbed equation, and $\boldsymbol{A}$ the eigenvector composed of the perturbations' amplitude.

The growth rate of perturbations ($\mathrm{Im}(\omega)$) is then obtained solving either Eq. (5.2.6) or Eq. (5.2.7). In the general case, this cannot be done analytically. Thus, a numerical library is usually used to compute their solutions. In the present work, a prototype has been developed to study the linear stability properties of LBMs with different types of collision models.

Once ω's are available, plotting their imaginary and real parts will eventually allow to: (i) understand how numerical waves behave in the simulation domain, (ii) confirm if they follow analytic formulas derived from the linearized NSF equations, (iii) distinguish the impact of velocity and space/time discretizations of the BE.

Let us continue with the definition of perturbed equation matrices $\boldsymbol{M}_{\boldsymbol{\Omega}}^{\mathbf{C}}$ and $\boldsymbol{M}_{\boldsymbol{\Omega}}^{\mathbf{D}}$. They directly depend on the chosen perturbed equation, the lattice, the collision model Ω, the wavenumber $\boldsymbol{k}$ and the mean flow $\left(\bar{\rho}, \overline{\boldsymbol{u}}, \bar{\theta}\right)$. If we consider the general collision model Ω, their mathematical expressions are

$$\boldsymbol{M}_{\boldsymbol{\Omega}}^{\mathbf{C}} = \boldsymbol{E}^{\mathbf{C}} + \mathrm{i}\boldsymbol{J}_{\boldsymbol{\Omega}}^{\mathbf{C}} \quad \text{with} \quad E_{ij}^{\mathbf{C}} = (\boldsymbol{k} \cdot \boldsymbol{\xi}_i)\delta_{ij},$$
$$\boldsymbol{M}_{\boldsymbol{\Omega}}^{\mathbf{D}} = \boldsymbol{E}^{\mathbf{D}} \left[\boldsymbol{\delta} + \boldsymbol{J}_{\boldsymbol{\Omega}}^{\mathbf{D}}\right] \quad \text{with} \quad E_{ij}^{\mathbf{D}} = \exp[-\mathrm{i}(\boldsymbol{\xi}_i \cdot \boldsymbol{k})]\delta_{ij},$$

where " i " the imaginary part unit which **must not be confused with** i (the discrete velocity index). $\boldsymbol{J}_{\boldsymbol{\Omega}}^{\mathbf{C}}$ is the Jacobian matrix associated to the collision model Ω in the continuous case, while $\boldsymbol{J}_{\boldsymbol{\Omega}}^{\mathbf{D}}$ is its discrete counterpart. In the particular case of the BGK collision model, we end up with

$$\boldsymbol{J}_{\mathbf{BGK}}^{\mathbf{C}} = -\frac{1}{\tau}\left(\boldsymbol{\delta} - \boldsymbol{J}^{(\mathbf{0})}\right) \quad \& \quad \boldsymbol{J}_{\mathbf{BGK}}^{\mathbf{D}} = -\frac{1}{\tau + 1/2}\left(\boldsymbol{\delta} - \boldsymbol{J}^{(\mathbf{0})}\right), \tag{5.2.8}$$

with $J_{ij}^{(0)} = \left.\frac{\partial f_i^{(0)}}{\partial f_j}\right|_{\overline{f_j}}$ is the Jacobian matrix of the equilibrium state. Regarding regularized collision models, the present work will only focus on their discrete LBE. Corresponding jacobian matrices are

$$\boldsymbol{J}_{\mathbf{PR}}^{\mathbf{D}} = -\frac{1}{\tau + 1/2}\sum_{n=0}^{N} \boldsymbol{A}_{\mathbf{1,PR}}^{(n)} \quad \& \quad \boldsymbol{J}_{\mathbf{RR}}^{\mathbf{D}} = -\frac{1}{\tau + 1/2}\sum_{n=0}^{N} \boldsymbol{A}_{\mathbf{1,RR}}^{(n)}, \tag{5.2.9}$$

with $\boldsymbol{A}_{\mathbf{1,PR}}^{(n)}$ and $\boldsymbol{A}_{\mathbf{1,RR}}^{(n)}$ being related to nonequilibrium coefficients $a_{1,\mathrm{PR}}^{(n)}$ and $a_{1,\mathrm{RR}}^{(n)}$ in the Fourier space. Their derivation is detailed in App. H.

Before moving to the results obtained through the LSA of both the continuous and the discrete LBE, let us recall some basic features about the linearized NSF equations. Furthermore, the overline notation (for mean quantities) will be dropped for the sake of clarity.

5.3 Hydrodynamic modes

In the linear context, where perturbations have small amplitudes with respect to mean flow quantities, the macroscopic behavior of NSF equations can be fully described through three types of characteristic waves [157]. These waves are obtained through the resolution of the eigenvalue problem associated to the linearization of the NSF equations, where no external acceleration is considered in the latter. The three types of characteristic waves are related to the propagation ($\mathrm{Re}(\omega)$) and the dissipation ($\mathrm{Im}(\omega)$) of: (1) shear (ω_S), (2) acoustic ($\omega_\pm$), and (3) entropy/temperature ω_T perturbations. Their analytical formulas read as [157]

$$
\begin{cases}
\mathrm{Re}(\omega_S) = uk \\
\mathrm{Re}(\omega_\pm) = (u \pm c)k \\
\mathrm{Re}(\omega_T) = uk
\end{cases}
\quad \text{and} \quad
\begin{cases}
\mathrm{Im}(\omega_S) = -\nu k^2 \\
\mathrm{Im}(\omega_\pm) = -\frac{1}{2}\left[\left(\frac{2(D-1)}{D}\nu + \nu_b\right) + (\gamma-1)\alpha\right]k^2 \\
\mathrm{Im}(\omega_T) = -\alpha k^2
\end{cases}
\quad (5.3.1)
$$

where ν is the kinematic viscosity, ν_b the bulk viscosity, α the heat diffusivity, γ the heat capacity ratio, $c = \sqrt{\gamma r T}$ the mean speed of sound, r the gas constant, and D the number of dimensions of the geometrical space. Besides, it is assumed here that perturbations propagate in the direction of the mean flow, i.e, $\boldsymbol{u} \cdot \boldsymbol{k} = uk$. If not otherwise stated, we will always consider in the rest of the chapter that $\boldsymbol{u}$ and $\boldsymbol{k}$ are aligned.

The NSF equations is a set of $(D+2)$ conservation equations. Hence $(D+2)$ characteristic waves fully describe the linear behavior of this set of equations. In the one-dimensional case, these hydrodynamic modes are divided into two acoustic waves and one entropy wave. The shear wave, which is linked to transverse velocity perturbations, has no physical meaning in this particular case. For bidimensional flows, one shear wave can further be identified as a solution of the eigenvalue problem. Eventually, three-dimensional flows governed by the NSF equations have their linear behavior fully described by five characteristic waves: two shear waves, two acoustic waves, and one entropy wave. Regarding now the properties of these waves, both shear and entropy waves propagate at the mean flow speed u, whereas forward $(+)$ and backward $(-)$ acoustic waves propagate at $u \pm c$. Furthermore, the attenuation of both shear and entropy waves is directly controlled by their related diffusivity coefficient, i.e, ν and α respectively. Regarding acoustic waves, the attenuation process is divided into three parts: dissipation induced by (i) shear (ν), (ii) compression/dilation (ν_b) and, (iii) thermal agitation (γ and α).

In what follows, we will be interested in 2D isothermal LBM-BGK. In this particular case, only three characteristic waves (one shear wave, and two acoustic waves) compose hydrodynamic modes. Furthermore, the bulk viscosity is linked to its kinematic counterpart through $\nu_b = (2/D)\nu = \nu$. Thus, shear and acoustic waves will have the very same attenuation rate $\mathrm{Im}(\omega_\pm) = \mathrm{Im}(\omega_S) = -\nu k^2$, since the thermal part of the acoustic wave attenuation is null for isothermal LBM-BGK[8].

To help the reader understand the behavior of shear, acoustic and entropy waves in the Fourier space, their dispersion and dissipation properties will be plotted. The case

---

[8]It is interesting to note that in the particular case of 2D thermal LBM-BGK, we now have $(\nu_b, \gamma, \mathrm{Pr}) = (0, 2, 1)$. Hence, all waves follow the very same attenuation process $\mathrm{Im}(\omega_\pm) = \mathrm{Im}(\omega_S) = \mathrm{Im}(\omega_T) = -\nu k^2$.
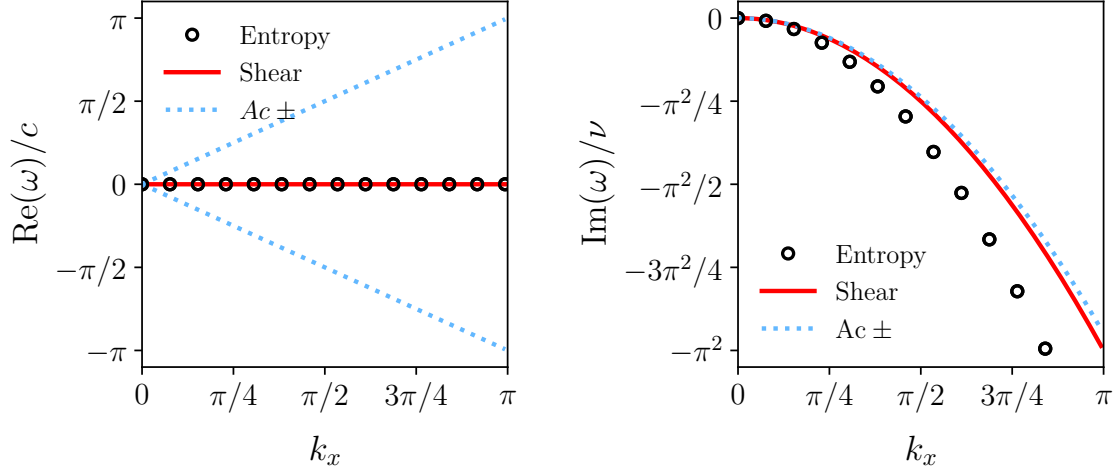
Figure 5.1 – LSA of the NSF equations ($k_y = k_z = 0$): dispersion (left) and dissipation (right) properties of a 3D air flow (Pr = 0.71, $\gamma = 1.4$, $\nu_b = 0$) at rest ($M_0 = 0$). Expressions of theoretical curves are [157]: $\text{Im}(\omega_S)/\nu = -k^2$, $\text{Im}(\omega_\pm)/\nu = -\frac{1}{2}\left[4/3 + (\gamma - 1)/\text{Pr}\right]k^2$, $\text{Im}(\omega_T)/\nu = -k^2/\text{Pr}$, $\text{Re}(\omega_S)/c = \text{Re}(\omega_T)/c = M_0 k$, and $\text{Re}(\omega_\pm)/c = (M_0 \pm 1)k$.
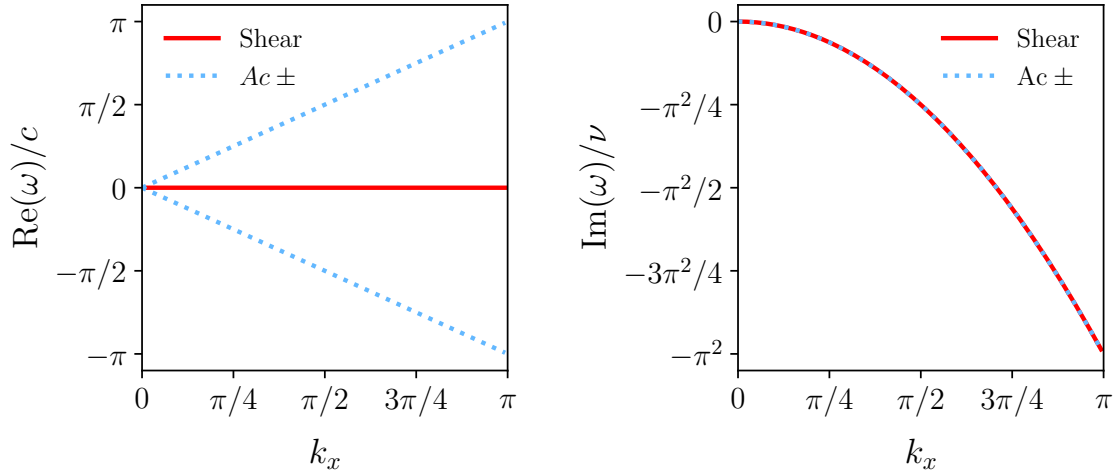
Figure 5.2 – LSA of the Navier-Stokes equations ($k_y = 0$): dispersion (left) and dissipation (right) properties of a 2D gas flow, at rest ($M_0 = 0$), with the same characteristics as for isothermal LBMs ($\nu_b = \nu$). Expressions of theoretical curves are [157]: $\text{Im}(\omega_S)/\nu = \text{Im}(\omega_\pm)/\nu = -k^2$, $\text{Re}(\omega_S)/c = M_0 k$, and $\text{Re}(\omega_\pm)/c = (M_0 \pm 1)k$.

of a 3D air flow (Pr = 0.71, $\gamma = 1.4$, $\nu_b = 0$) is considered in Fig. 5.1, whereas the spectral properties of a 2D isothermal gas flow typical of LBMs of interest ($\nu_b = 0$ and no thermal contributions) are plotted in Fig. 5.2. For both cases, dispersion curves ($\text{Re}(\omega)$) are linear with respect to the wave number $\boldsymbol{k}$, while dissipation rates fit a quadratic trend ($\text{Im}(\omega) \propto k^2$). Furthermore, the propagation speed, or group velocity, of a characteristic wave can be obtained quite easily computing the slope of $\text{Re}(\omega)$.

Hereafter, we will start focusing on results flowing from the LSA applied to the BGK

collision model (Eq. (5.2.8)). If not otherwise stated, the Fourier space will be uniformly spanned using a step of $\Delta k = 0.02$, since it was found to be sufficiently small for a correct convergence of stability curves presented in Sec. 6.1.1.c. Furthermore, only one point over eight will be plotted for the sake of clarity of 1D dispersion and dissipation results.

5.4   LSA of the continuous LBE

This section aims to show that the LSA is a powerful tool allowing to recover general results flowing from the Chapman-Enskog (CE) expansion itself:

- Validity of the asymptotic (macroscopic) behavior of the LBE in the continuum limit $\epsilon \ll 1$ ($\tau \ll 1$) only [39].

- Weakly compressible limit of a second-order accurate LBM (D2Q9), i.e,

$$
\begin{aligned}
\partial_t(\rho) + \partial_\beta \left(\rho u_\beta \right) &= 0, \\
\partial_t(\rho u_\alpha) + \partial_\beta \left(\rho u_\alpha u_\beta + p\delta_{\alpha\beta} \right) &= \partial_\beta(\sigma'_{\alpha\beta}),
\end{aligned}
\tag{5.4.1}
$$

with $\mu = \tau p$, $\sigma'_{\alpha\beta} = \mu \Pi'^{(1)}_{\alpha\beta} - p\delta_{\alpha\beta} = \mu S_{\alpha\beta} - p\delta_{\alpha\beta} + \mathcal{O}\left(\mathrm{Ma}^3\right)$ being the dynamic viscosity and the stress tensor.

Hereafter, deviations from the linear Navier-Stokes-Fourier behavior will then be studied. Furthermore, we will restrict ourselves to the isothermal case.

Regarding the *modus operandi*, we will study in more depth: (a) 2D maps of maximal growth rate to *qualitatively* describe isotropic properties of the perturbations in the Fourier space, (b) 1D dispersion and dissipation curves to *quantitatively* examine the propagation and the attenuation of waves ($k_y = 0$). The focus will be put on results concerning the BGK collision model, while complementary studies regarding regularized collision operators are restricted to the discrete case and presented in Sec. 6.2.

5.4.1   Standard velocity set

To highlight deviations from the macroscopic behavior of interest (linearized Navier-Stokes) that may arise from the velocity space discretization, the LSA of the continuous LBE associated to the D2Q9 velocity set is performed for:

- a mean flow at rest ($M_0 = 0$) and for increasing values of τ,

- a Mach number ranging from 0.0 to 1.0, and for a very small value of τ.

For all configurations, the mean flow is considered to be aligned with the longitudinal axis, i.e, $\phi = \widehat{(\boldsymbol{u}, \boldsymbol{x})} = 0°$, even though all presented conclusions remain valid for any value of ϕ. This study will start with the second-order equilibrium state ($N = 2$) before quantifying the impact of such a choice.
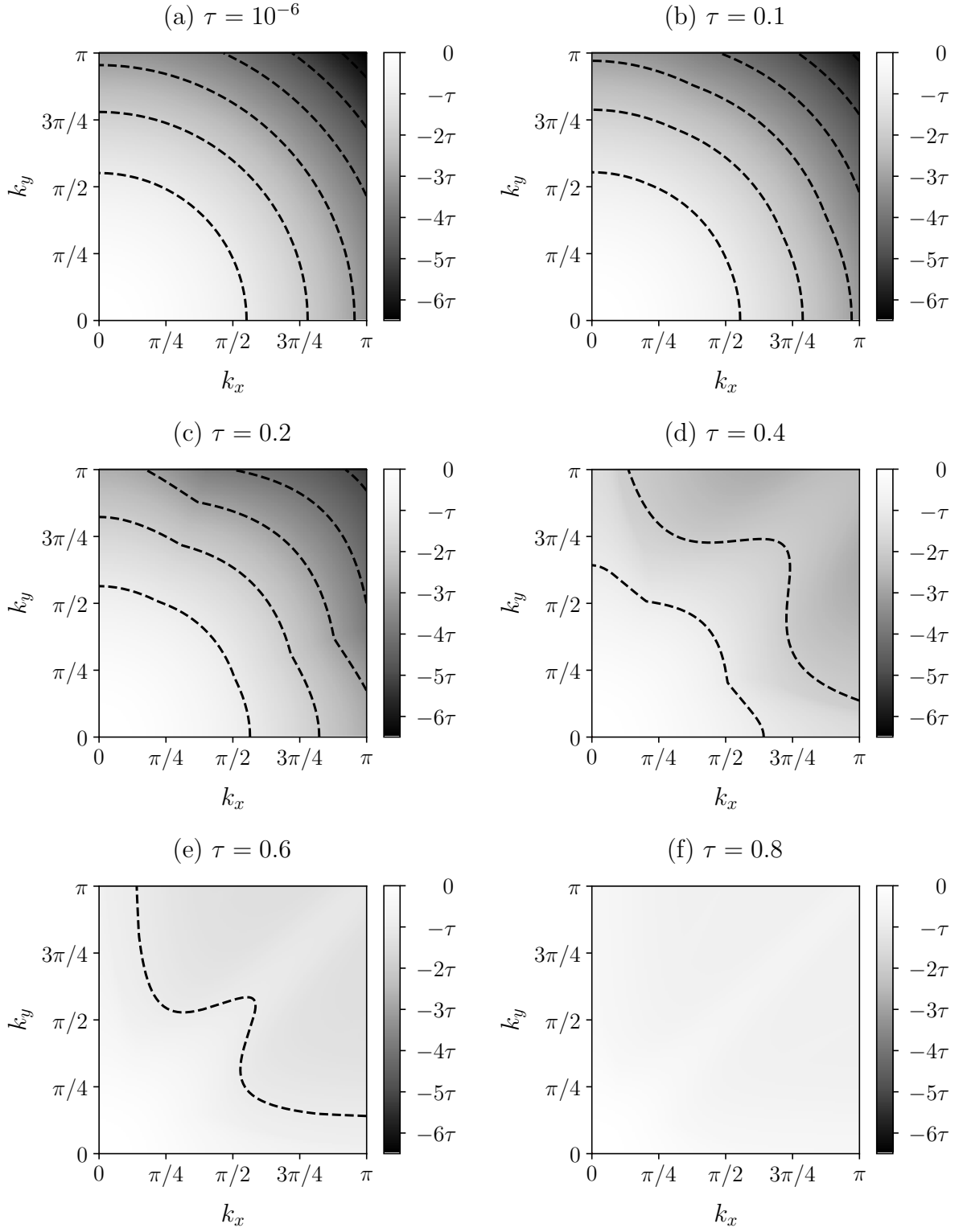
Figure 5.3 – LSA of the continuous D2Q9 BGK ($N = 2$). Maps of maximal growth rate for $M_0 = 0$ and various relaxation times. Dashed isolines correspond to $-\tau$, -2τ, -3τ, -4τ, -5τ and -6τ.
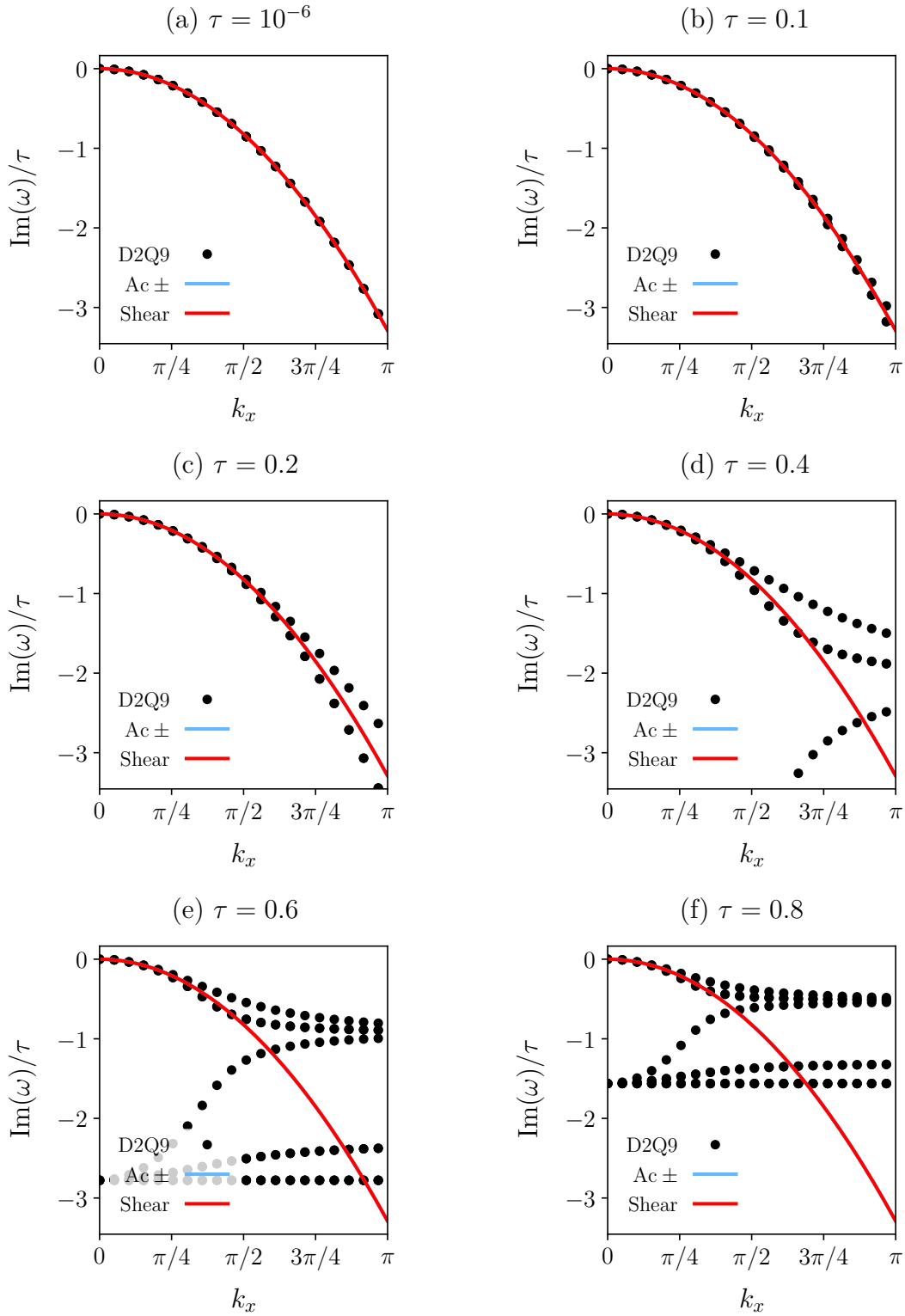
Figure 5.4 − LSA of the continuous D2Q9 BGK ($N = 2$). Impact of the relaxation time on dissipation rates for $M_0 = 0$ and $k_y = 0$. Solid lines correspond to the theoretical dissipation rate of shear and acoustic waves: $\mathrm{Im}(\omega_S) = \mathrm{Im}(\omega_\pm) = -\tau c_s^2 k_x^2$ in lattice units.
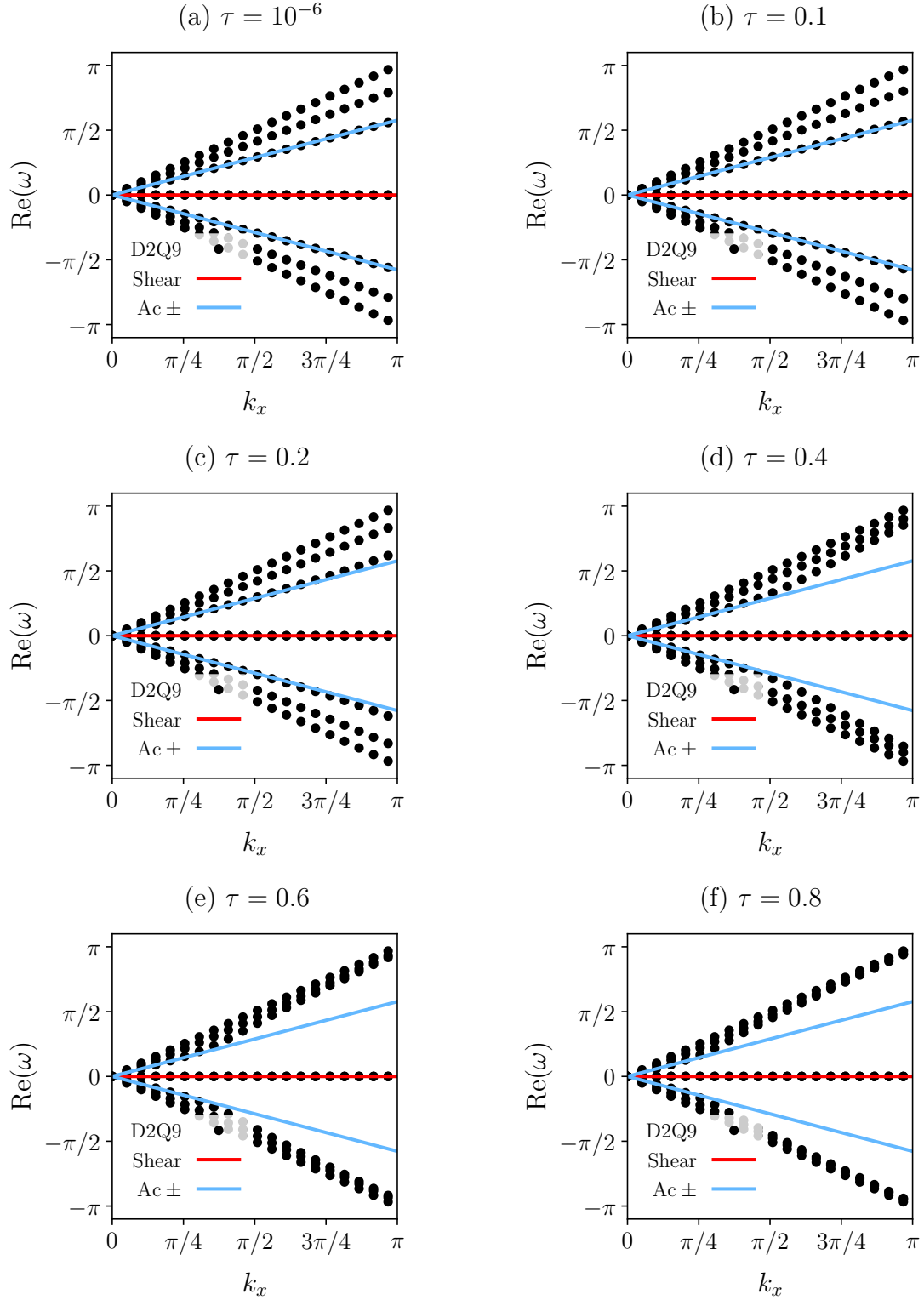
Figure 5.5 − LSA of the continuous D2Q9 BGK ($N = 2$). Impact of the relaxation time on dispersion properties for $M_0 = 0$ and $k_y = 0$. Solid lines correspond to theoretical propagation speeds of shear and acoustic waves: $\mathrm{Re}(\omega_S) = k_x c_s M_0$ and $\mathrm{Re}(\omega_{\pm}) = k_x c_s (M_0 \pm 1)$.

5.4.1.a   Continuum limit violation

Let us first study the impact of using high values of τ on the spectral properties of the D2Q9 lattice. All corresponding maps of maximal growth rate $(\max[\text{Im}(\omega)])$ are compiled in Fig. 5.3. An isotropic behavior, illustrated by the circular shape of the maximal growth rate isocontours, is recovered meaning that the velocity space discretization does not introduce any anisotropy of the maximal growth rate in the (k_x, k_y) plane for a flow at rest, at least in the continuum limit $(\epsilon \ll 1)$. Nevertheless, small deviations appear for $\tau = 0.1$ and become nonnegligible for higher values of the relaxation time. Further explanations regarding this last point are obtained plotting all eigenvalues along the slice $k_y = 0$ (cf Fig. 5.4). From them, it can be concluded that all waves match their theoretical behavior in the continuum limit. Nevertheless, three characteristic tendencies arise when the relaxation time increases and becomes higher than $\tau = 0.1$:

1. Even though $\nu_b = \nu$, the dissipation rates of the shear and acoustic waves start to decouple, leading to severe deviations from the macroscopic behavior of interest.

2. Some nonhydrodynamic waves are independent of k_x, while others start to interact with hydrodynamic waves for $k_x \sim \pi$.

3. Nonhydrodynamic waves are less and less dissipated and this seems to implicitly impact the growth rate linked to hydrodynamic (shear and acoustic) waves.

For the sake of completeness, dispersion properties along $k_y = 0$ are also summarized in Fig. 5.5. As for the dissipation rates, hydrodynamic behaviors are well recovered for $\tau < 0.1$, but discrepancies arise when $\tau \geq 0.1$. These properties remain symmetric with respect to the axis $\text{Re}(\omega) = 0$, at least for $M_0 = 0$, but acoustic waves propagation speeds increase and seem to tend towards $\pm k_x$.

Finally, one should note that even if it was not shown here, nonhydrodynamic waves are present for $\tau = 10^{-6}$, the only reason explaining why they are not visible in Fig. 5.4 is because they have an extremely high dissipation rate $(|\text{Im}(\omega)| \sim 3 \cdot 10^9$, independent of the wave number k). Hence these waves are instantaneously damped as compared to hydrodynamic ones, confirming the continuum limit hypothesis for small values of the relaxation time.

5.4.1.b   Impact of the mean flow

It was previously shown that for low values of τ (continuum limit) the velocity space discretization does not introduce any anisotropy of the maximal growth rate for a flow at rest $(M_0 = 0)$. Nevertheless when the Mach number is increased, anisotropic behaviors start appearing even for a very low value of $\tau = 10^{-6}$, as illustrated in Fig. 5.6. Interestingly, the Mach number only introduce errors in dissipation rates of acoustic and shear waves, but not in their propagation speeds (see Figs. 5.7 and 5.8), as already pointed out in Ref. [153]. The reason behind this phenomenon lies in $\mathcal{O}(\text{Ma}^3)$ error terms of the momentum equation Eq. (3.1.33). This is confirmed when third-order Hermite coefficients are taken into account in the definition of the equilibrium state $f^{(0)}$, as shown in Figs. 5.9

and 5.10. Indeed, adding third-order Hermite coefficients leads to the correct dissipation rate of shear waves while some error still remains for both acoustic waves [134]. Surprisingly, the fourth-order term does not seem to have any impact on the linear stability of the D2Q9 lattice. Knowing this term scales as $\mathcal{O}(\mathrm{Ma}^4)$, it may not be possible to identify its role for small values of M_0. Further investigations will be conducted in Sec. 6.1.1.c regarding this last point.

Now that the basic features about the LSA of a standard velocity discretization have been examined, let us now move to the study of high-order lattices

5.4.2   High-order LBMs

In order to further understand the numerical behavior of LBE, the linear stability analysis is applied to several high-order velocity sets,

- Third-order accurate lattices: D2V17a/b/c/d [120] and D2Q21 [109],

- Fourth-order accurate lattices: D2V37a/b/c/d [120].

All these velocity sets can be built according to the orthogonality preservation of all third- and fourth-order Hermite polynomials [119, 120] allowing VDFs to evolve in the polynomial basis of interest. As a reminder, such lattice structures allow to respectively recover: (a) the isothermal Navier-Stokes equations, i.e, without any $\mathcal{O}(\mathrm{Ma}^3)$ error terms in the momentum equation, and (b) the fully compressible NSF equations. As a reminder, only the isothermal case will be considered in the present work.

The impact of the kinematic viscosity ν on spectral properties of these models are first examined for third-order accurate velocity sets before moving to fourth-order accurate ones. Special attention is paid to the numerical discrepancies arising from the velocity discretization. Here, the intended purpose is to demonstrate that even if several velocity sets lead to the very same macroscopic equations, they will not behave the same way in the Fourier space.

Before looking at results, let us introduce a few recommendations about how to properly compare different velocity sets from the LSA point of view.

5.4.2.a   Best practices for the comparison of velocity sets

One must be careful when comparing velocity discretizations with different lattice constant c_s. Indeed, their spectral properties directly depend on c_s. This point is illustrated in Fig. 5.11 where maps of maximal growth rate are plotted for each third-order accurate model, and with a fixed relaxation time value of $\tau = 10^{-6}$. At first sight, they all seem to have their own behavior. After second thoughts, they all do recover the proper dissipation rate of acoustic and shear waves. The misconception is led by the fact that $\mathrm{Im}(\omega_S) = \mathrm{Im}(\omega_\pm) = -\tau c_s^2 k_x^2$, and $\nu = \tau c_s^2$ in lattice units. Thus, a higher lattice constant induces a higher kinematic viscosity for a given relaxation time.

Reciprocally, running a simulation with a given kinematic viscosity leads to a lower relaxation time when the value of c_s is increased. This should be kept in mind when the
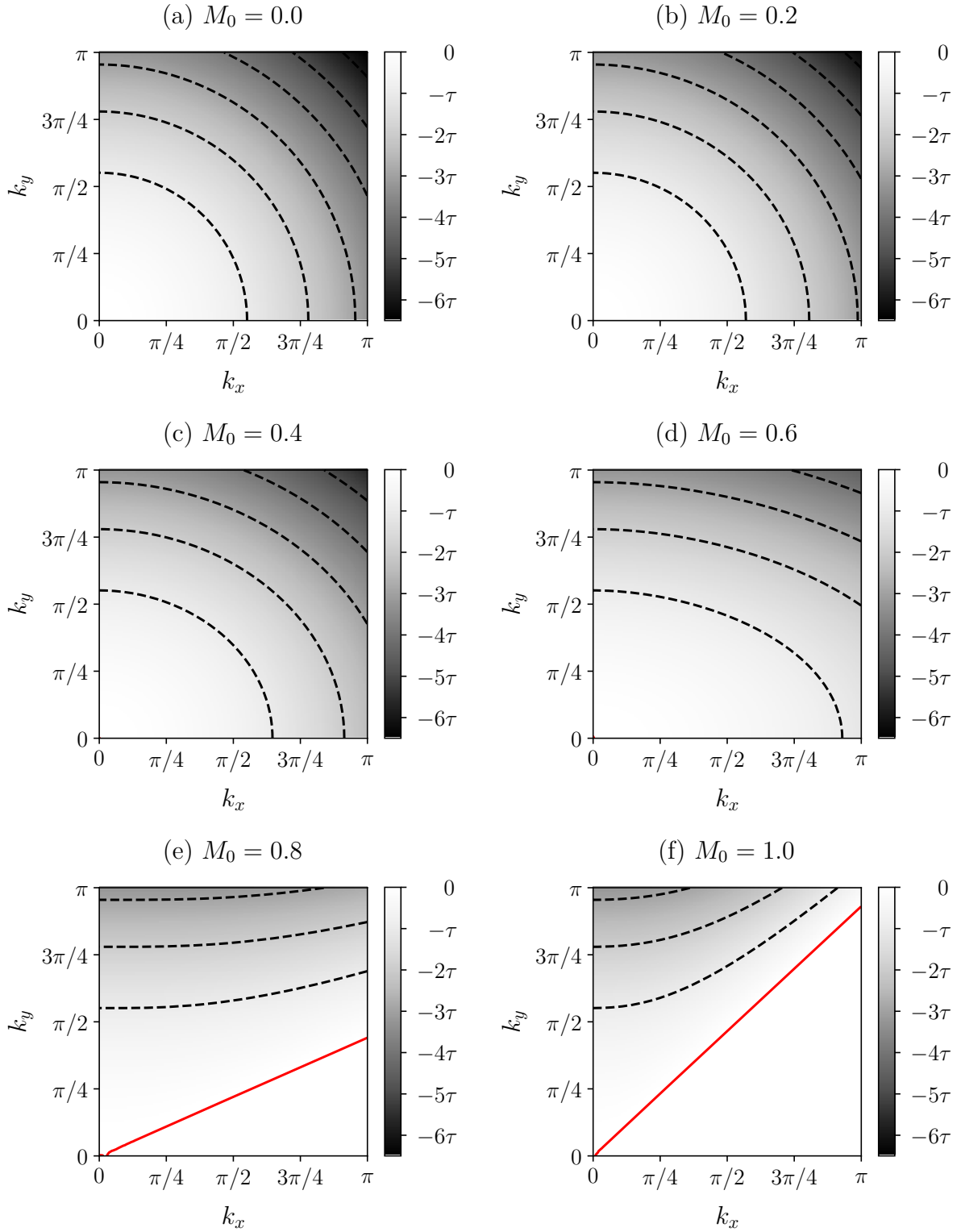
Figure 5.6 − LSA of the continuous D2Q9 BGK ($N = 2$). Impact of the Mach number on maps of maximal growth rate for $\tau = 10^{-6}$. Dashed isolines correspond to $-\tau$, -2τ, -3τ, -4τ, -5τ and -6τ, while the solid line indicates the stability threshold $\max[\mathrm{Im}(\omega)] = 0$.
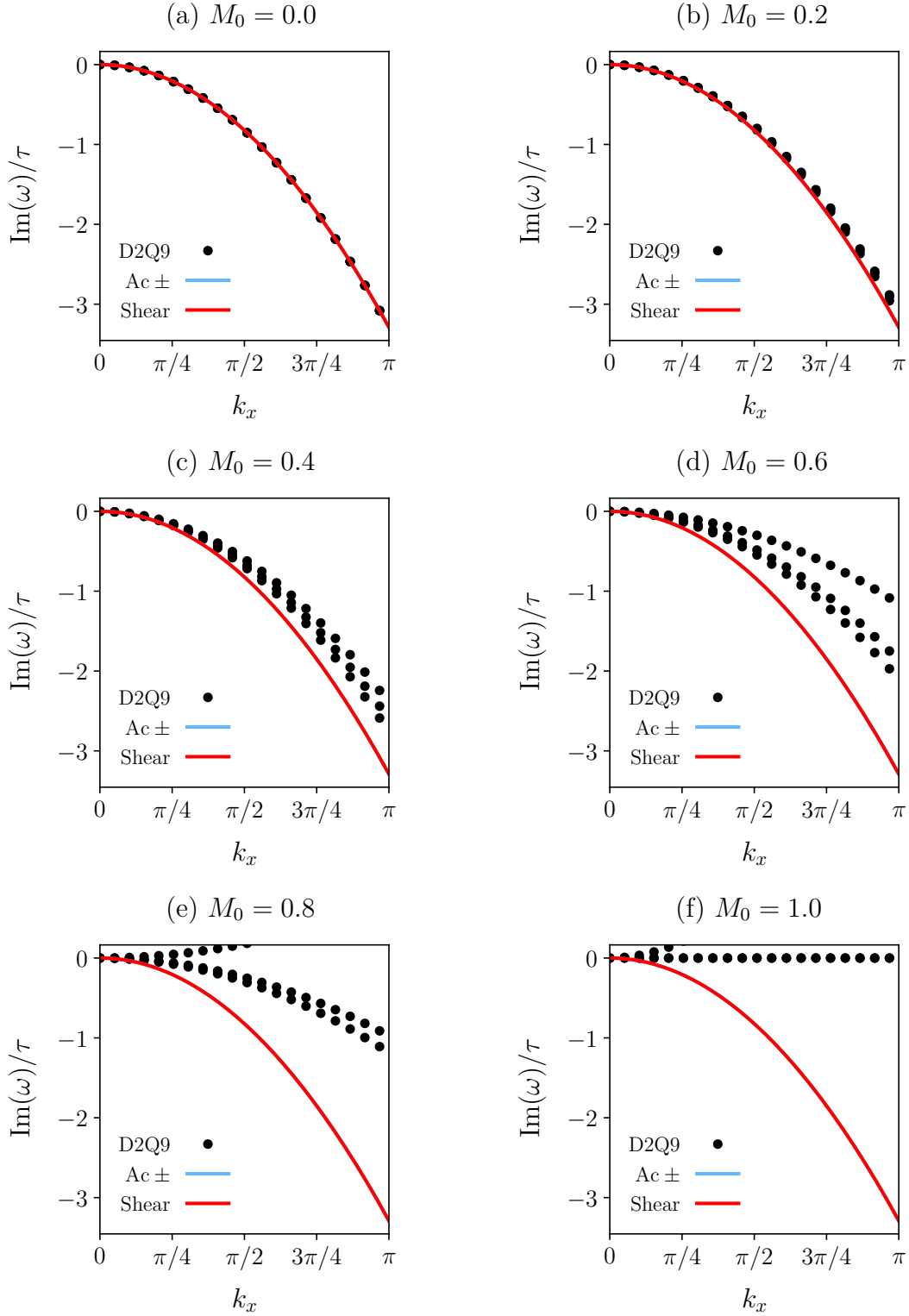
Figure 5.7 – LSA of the continuous D2Q9 BGK ($N = 2$). Impact of the Mach number on dissipation rates for $\tau = 10^{-6}$ and $k_y = 0$. Solid lines correspond to the theoretical dissipation rate of shear and acoustic waves: $\mathrm{Im}(\omega_S) = \mathrm{Im}(\omega_\pm) = -\tau c_s^2 k_x^2$.
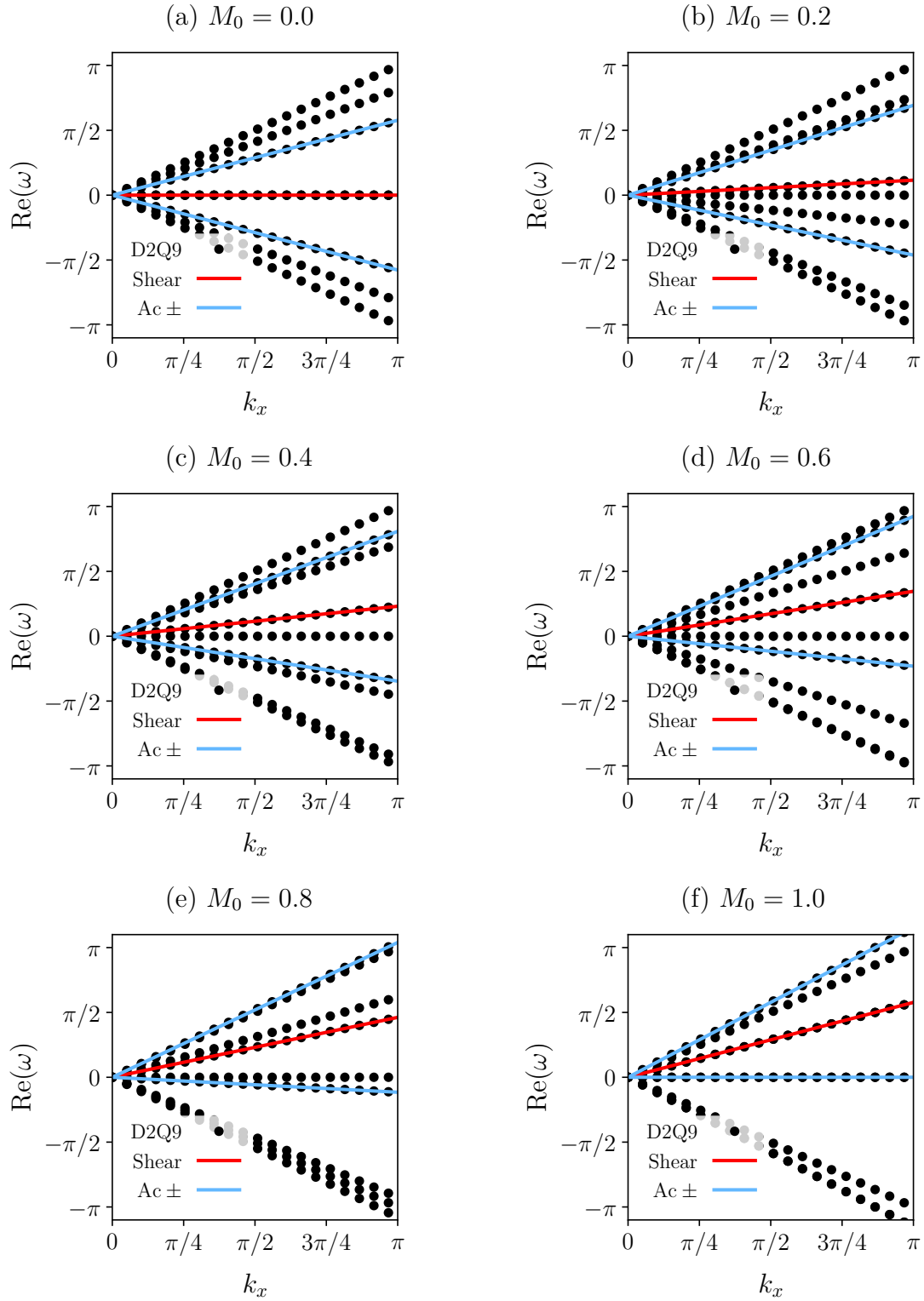
Figure 5.8 − LSA of the continuous D2Q9 BGK. Impact of the Mach number on dispersion properties for $\tau = 10^{-6}$ and $k_y = 0$. Solid lines correspond to theoretical propagation speeds of shear and acoustic waves: $\text{Re}(\omega_S) = k_x c_s M_0$ and $\text{Re}(\omega_\pm) = k_x c_s (M_0 \pm 1)$ in lattice units.
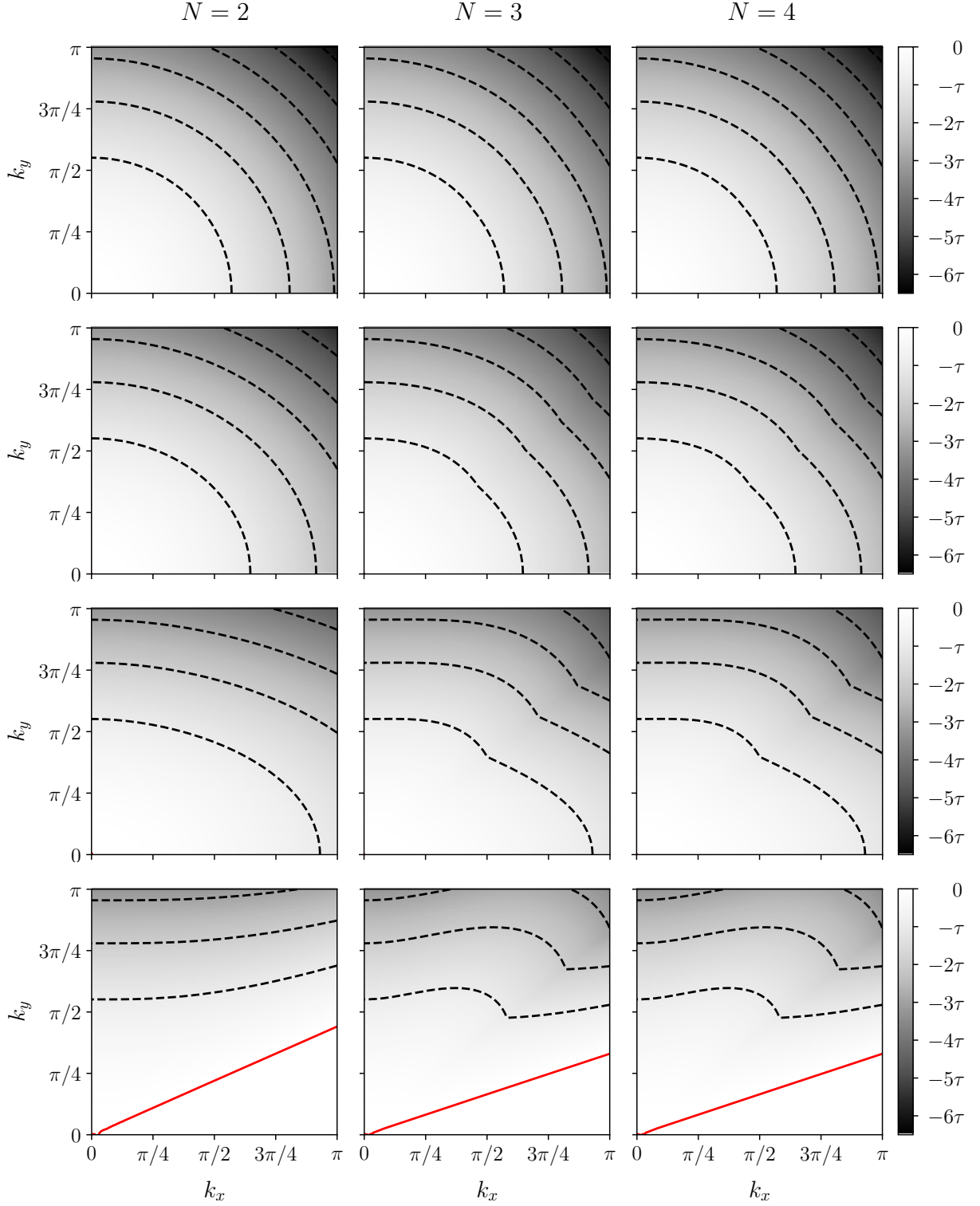
Figure 5.9 – LSA of the continuous D2Q9 BGK. Impact of the equilibrium order on maps of maximal growth rate for $\tau = 10^{-6}$. Rows correspond to $M_0 = 0.2, 0.4, 0.6, 0.8$ (from top to bottom), while columns summarize results for $f_i^{(0)}$ at order $N = 2, 3, 4$ (from left to right). Dashed isolines correspond to $-\tau$, -2τ, -3τ, -4τ, -5τ and -6τ, while the solid line indicates the stability threshold $\max[\text{Im}(\omega)] = 0$.
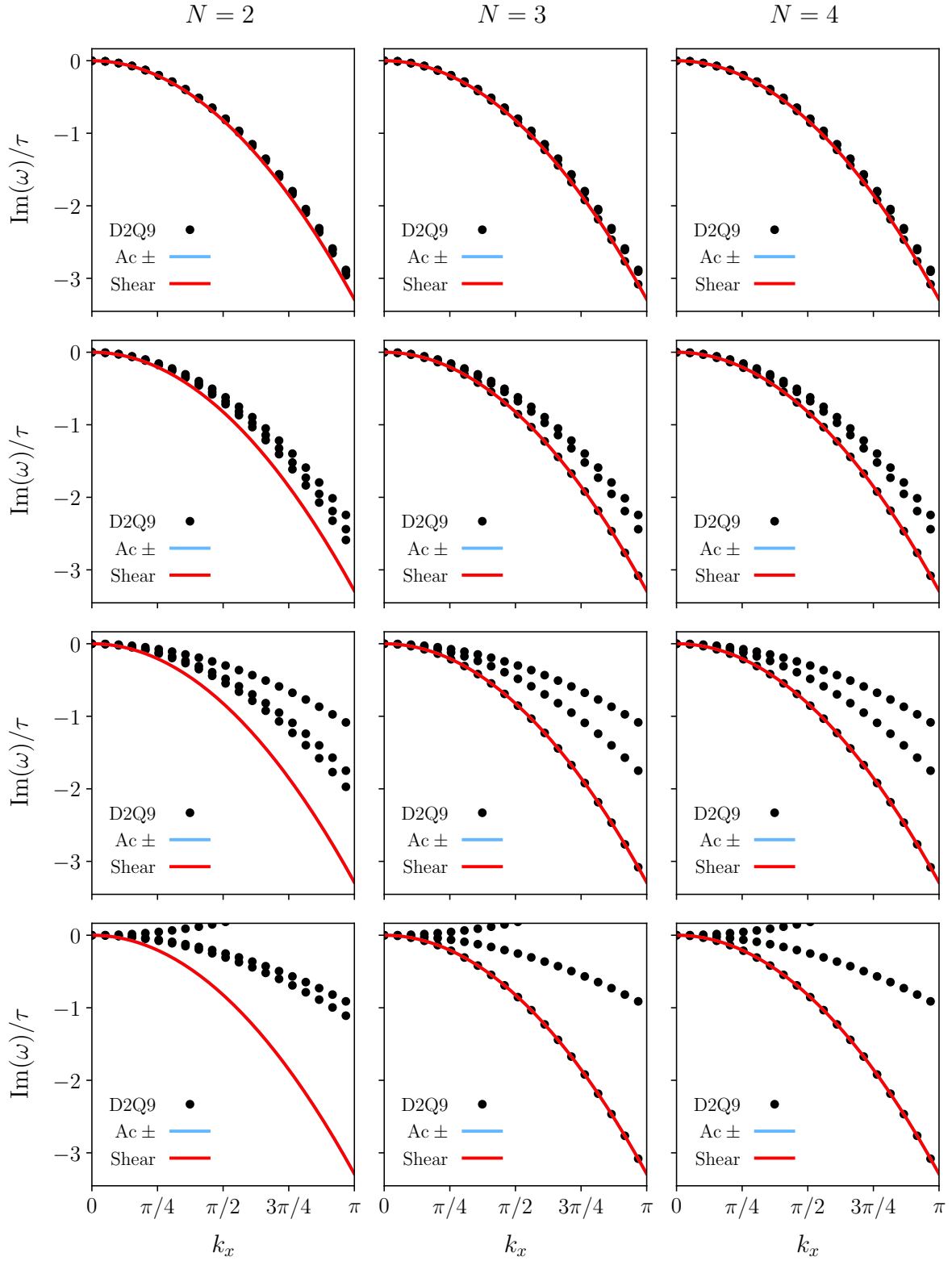
Figure 5.10 – LSA of the continuous D2Q9 BGK. Impact of the equilibrium order on dissipation rates for $\tau = 10^{-6}$ and $k_y = 0$. Rows correspond to $M_0 = 0.2, 0.4, 0.6, 0.8$ (from top to bottom), while columns summarize results for $f_i^{(0)}$ at order $N = 2, 3, 4$ (from left to right). Solid lines correspond to the theoretical dissipation rate of shear and acoustic waves: $\text{Im}(\omega_S) = \text{Im}(\omega_\pm) = -\tau c_s^2 k_x^2$ in lattice units.

acoustic scaling is adopted ($\Delta t \propto \Delta x$). The main reason behind this choice of time step is either to impose the correct speed of sound or to boost the CPU efficiency. Hence using a velocity set with a higher value of c_s is *a priori* a good choice regarding the wallclock time of simulations, but it may eventually lead to a narrower stability range due to the lower value of the relaxation time.

In what follows, the evaluation of numerical properties will then be conducted for a given kinematic viscosity ν instead of a given relaxation time τ. Thus, all maps are now normalized according to the kinematic viscosity ν.

5.4.2.b   LSA of high-order lattices

The impact of high values of the kinematic viscosity is first investigated for third-order accurate velocity sets: D2V17a/b/c/d and D2Q21. In the case of the D2V17a velocity set, LSA results regarding the maximal growth rate maps are reported in Fig. 5.12. As for the D2Q9 lattice, high values of the kinematic viscosity ($\nu \geq 0.01$) also induce nonnegligible deviations from theoretical growth rates. This is confirmed when other third-order LBMs are considered (see Fig. 5.13), even if some models seem to be able to handle high values of ν better than others. This may be linked to the value of the lattice constant c_s. As a matter of fact, the higher the value of c_s the better the dissipation properties seem to be. Nevertheless, this last result should be restricted to velocity sets of the same kind, i.e, D2V17a/b/c/d lattices. Indeed, the D2Q21 lattice constant is such that $c_s^{D2Q21} < c_s^{D2V17c}$, but it clearly shows better spectral properties than the D2V17c velocity discretization.

This last example perfectly highlights the fact that using different velocity discretizations, which were designed to recover the very same macroscopic behavior (isothermal Navier-Stokes), does not ensure that they will share the very same spectral properties. This was predictable for lattice structures with different numbers of discrete speeds, but results concerning D2V17a/b/c/d are particularly interesting for the LBM community.

Regarding the LSA of fourth-order accurate velocity sets (D2V37a/b/c/dà, small deviations to the Navier-Stokes behavior for also observed for $\nu \geq 0.01$. Nevertheless the overall behavior of waves remained isotropic for ν up to $\sim 0.1 - 0.15$, meaning that these velocity sets are more suitable to recover the behavior of high-viscosity flows than D2V17a/b/c/d and D2Q21 lattices. For higher values of ν, discrepancies arose between the four D2V37a/b/c/d lattices, and here the lattice constant c_s could not be at the origin of this phenomenon since it has the same value for all of them.

This concludes the study on deviations induced by the violation of the continuum limit, in the case of high-order velocity discretizations. The focus will now be put on the mean flow impact on the spectral properties of high-order velocity sets.

5.4.2.c   Avoid Mach number restriction using high-order accurate lattices

In Sec. 5.4.1.b the famous $\mathcal{O}(\mathrm{Ma}^3)$ deviation, regarding dissipation rates of both shear and acoustic waves, has been observed applying the LSA to the D2Q9 lattice. To bypass this weakly compressible limitation, high-order velocity discretizations are needed, at least this is the requirement flowing from the CE expansion. Let us see if the LSA is able to reach the same conclusion. To that end, the mean Mach number is increased to
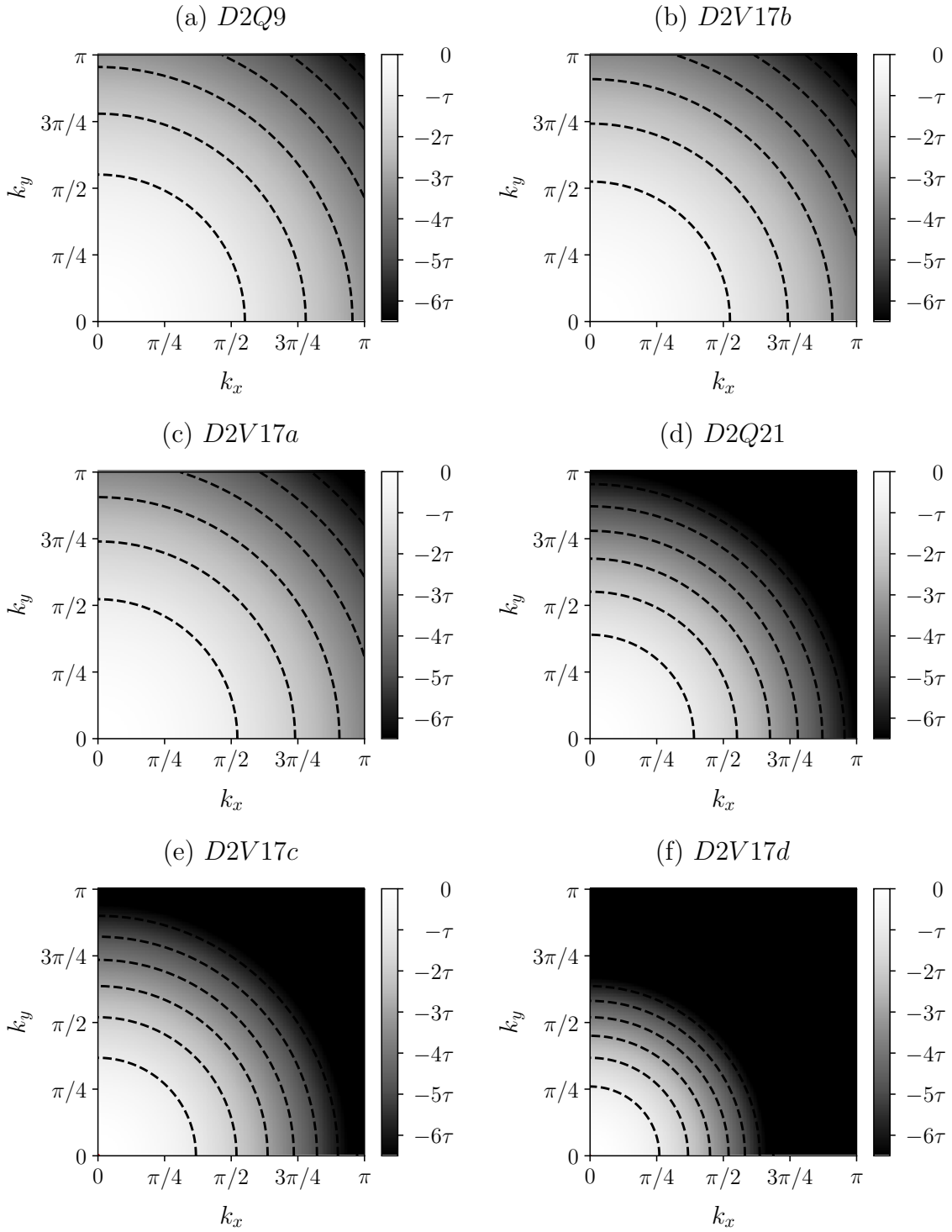
Figure 5.11 – Naive comparison of several LSA of continuous LBE (BGK approximation) for a fixed relaxation time τ. Maps of maximal growth rate for $M_0 = 0$ and $\tau = 10^{-6}$. Dashed isolines correspond to $-\tau$, -2τ, -3τ, -4τ, -5τ and -6τ. As a reminder, $c_s^{D2Q9} < c_s^{D2V17b} < c_s^{D2V17a} < c_s^{D2Q21} < c_s^{D2V17c} < c_s^{D2V17d}$ (their value are summarized in Tab. D.1).
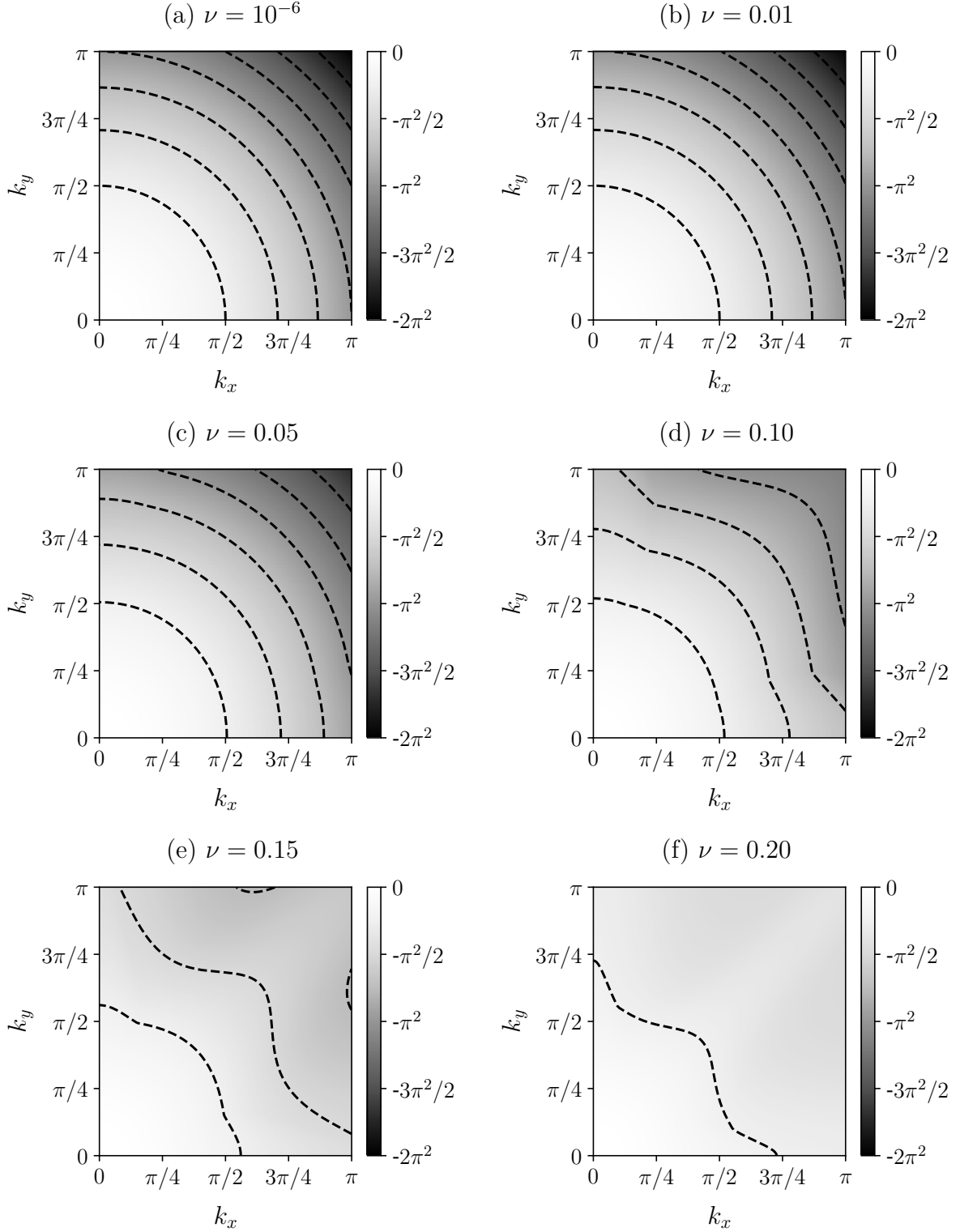
Figure 5.12 − LSA of the continuous D2V17a BGK. Maps of maximal growth rate for $M_0 = 0$ and increasing values of kinematic viscosity ν. Dashed isolines range from $-\pi^2/4$ and $-7\pi^2/4$ with a step of $\pi^2/4$.
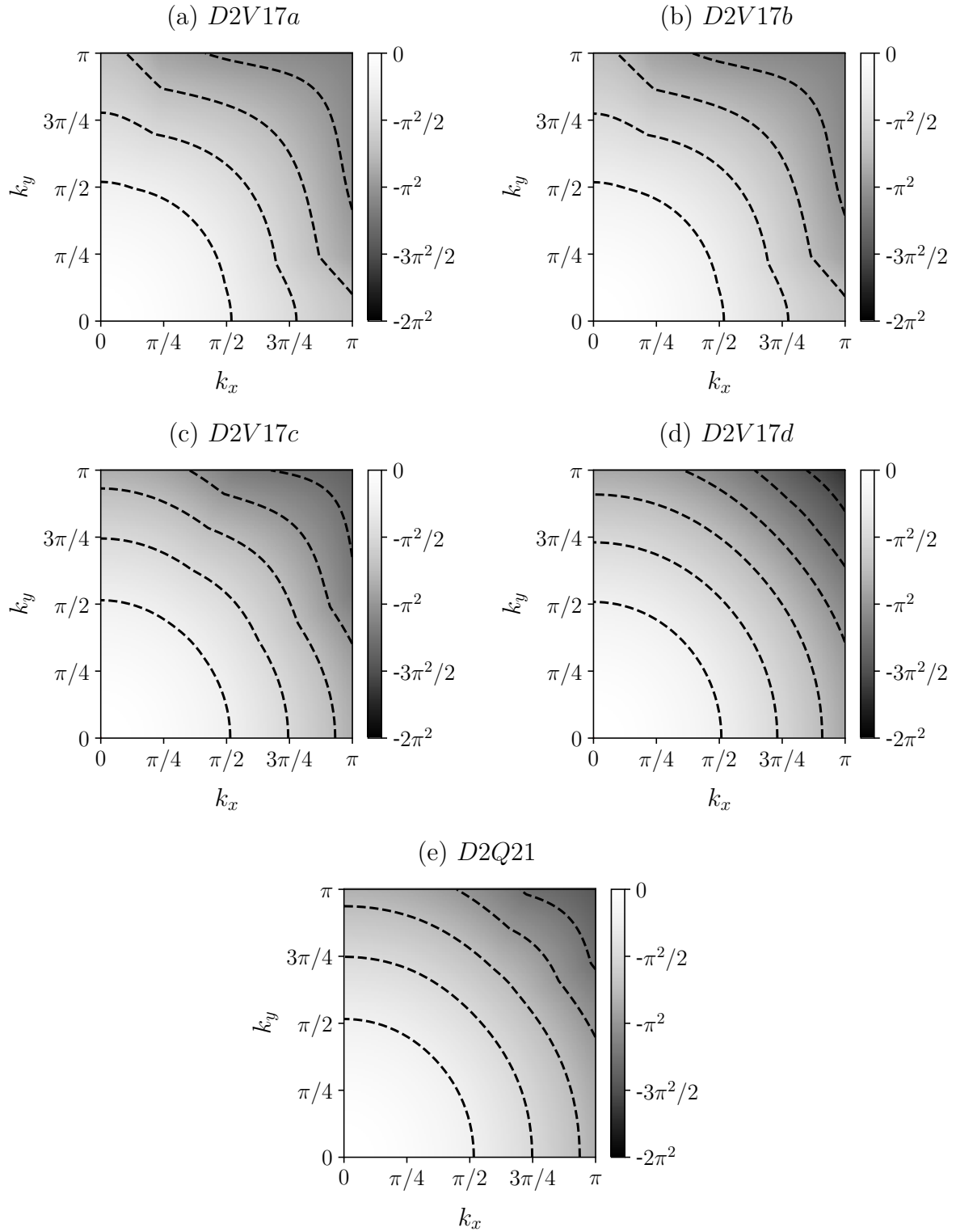
Figure 5.13 – LSA of several third-order continuous LBE (BGK approximation). Maps of maximal growth rate for $M_0 = 0$ and $\nu = 0.1$. Dashed isolines range from $-\pi^2/4$ and $-7\pi^2/4$ with a step of $\pi^2/4$. As a reminder, $c_s^{D2V17b} < c_s^{D2V17a} < c_s^{D2Q21} < c_s^{D2V17c} < c_s^{D2V17d}$ (their value are summarized in Tab. D.1).

$M_0 = 1$, and the kinematic viscosity is kept low ($\nu = 10^{-5}$) for the continuum limit to remain valid. A comparison between the D2Q9, D2V17a and D2V37a lattices is shown in Fig. 5.14. It confirms that using third- or higher-order quadratures allows to recover the proper macroscopic behavior with respect to the Navier-Stokes equations.
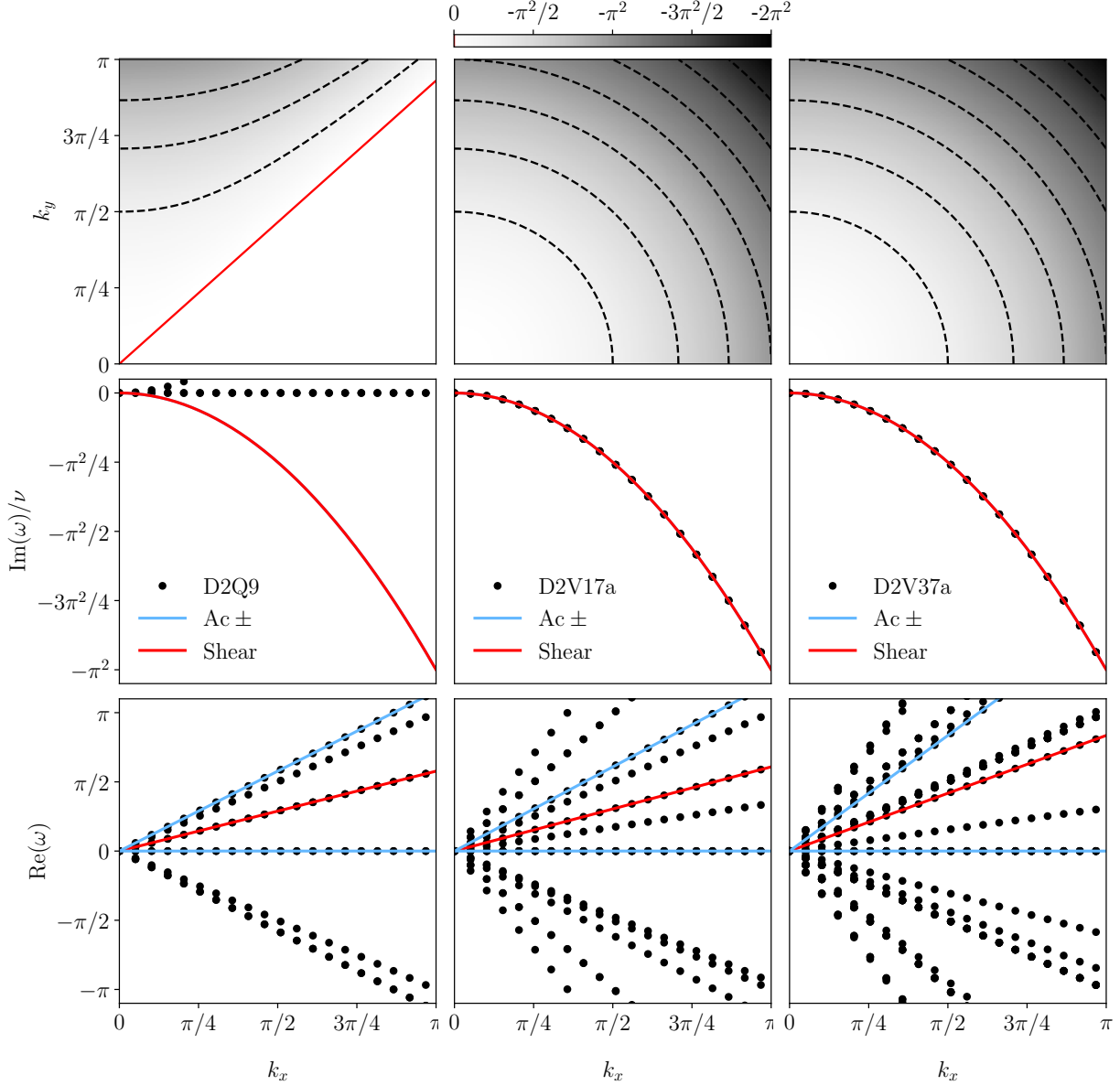
Figure 5.14 – Comparison of LSA results for the continuous D2Q9, D2V17a and D2V37a (BGK collision model). Impact of the Mach number on (first column) maps of maximal growth rate $\max[\mathrm{Im}(\omega)]/\nu$, (second row) dissipation rates and (third row) dispersion properties, for $\nu = 10^{-5}$ and $M_0 = 1$. Rows summarize results for the D2Q9, D2V17a and D2V37a lattices (from left to right). Regarding 2D maps, the solid isoline corresponds to the stability threshold $\max[\mathrm{Im}(\omega)] = 0$, whereas dashed isolines range from $-\pi^2/4$ and $-7\pi^2/4$ with a step of $\pi^2/4$. For 1D plots, symbols and solid lines correspond to LSA results and theoretical curves, where the latter read as: $\mathrm{Im}(\omega_S) = \mathrm{Im}(\omega_\pm) = -\nu k_x^2$, $\mathrm{Re}(\omega_S) = k_x c_s M_0$ and $\mathrm{Re}(\omega_\pm) = k_x c_s (M_0 \pm 1)$ in lattice units.

5.5   Conclusions

In this chapter, the basic features about the linear stability analysis (LSA) of both continuous and discrete partial differential equations (PDEs) were briefly recalled. This was followed by the presentation of the three types of characteristic waves (shear, acoustic and entropy) generally encountered with the linearized Navier-Stokes-Fourier set of equations. This aimed at giving the reader all the necessary material to properly understand the LSA of the (continuous) lattice Boltzmann equation (LBE). One simplification was considered in this chapter: only isothermal versions of standard and high-order velocity sets were studied.

The LSA of the continuous LBE allowed to quantify the impact of the velocity discretization on the macroscopic behavior recovered by this set of PDEs. It confirmed the ability of such an approach to be considered as an alternative to the CE expansion. More specifically, the LSA led to the recovery of proper propagation speeds and attenuation rates of characteristic waves belonging to the linearized Navier-Stokes set of equations, but only to the extend that: (1) the continuum limit was achieved ($\tau \ll 1$), and (2) the correct velocity discretization was employed. As an example, the famous Mach-dependent deviation of attenuation rates was observed with the D2Q9 lattice, whereas the expected behavior was obtained using higher order lattices. In addition, this LSA allowed to demonstrate that even if several velocity sets lead to the very same macroscopic equations, they do not behave the same way in the Fourier space. This last point suggests that velocity sets sharing the same quadrature order may also exhibit different stability domains after the space/time discretization of the LBE. The validity of this hypothesis will be studied in the next chapter.

Chapter 6

Linear Stability Analysis of the Discrete LBE

Contents

This chapter is dedicated to the linear stability analysis (LSA) of the discrete LBE obtained through the space/time discretization of the continuous LBE. It is chosen to study the impact of the numerical discretization in the context of LBM, i.e, 'Collide & Stream' algorithm. Starting with LBMs-BGK, the spectral properties of regularized LBMs are then analysed for a large number of velocity sets. This approach eventually allows to properly compare the stability ranges of BGK and regularized collision models for both standard and high-order LBMs.

6.1   Discrete VS Continuous LSA

To further understand the numerical behavior of LBMs, the LSA of the 'Collide & Stream' algorithm (called hereafter 'discrete LBE') is now considered and compared to the LSA of the continuous LBE.

6.1.1   D2Q9 BGK

This study is first restricted to the D2Q9 lattice coupled with the BGK collision model. If not otherwise stated, the equilibrium VDF is evaluated including Hermite polynomials up to second order ($N = 2$). Without loss of generality, the configuration of a flow at rest ($M_0 = 0$), with a viscosity of $\nu = 10^{-5}$, is first considered for this investigation.

6.1.1.a   Flow at rest

To properly quantify the influence of the numerical discretization, results obtained for both the continuous and discrete LBE (D2Q9 BGK) are compiled in Fig. 6.1. The first impact of the numerical discretization that should be pointed out is the strong anisotropic behavior of the maximal growth rate it induces. More precisely, the numerical discretization introduces both dissipation and dispersion errors. In other words, when hydrodynamic waves are not sufficiently discretized they will neither propagate at the correct speed nor be dissipated correctly.

Another key thing to notice is that nonhydrodynamic modes start to interact with hydrodynamic ones even if the kinematic viscosity is very small. It was previously reported (Sec. 5.4.1.a) that their impact becomes significant for $\nu \geq 0.1$ in the continuous case. Thus, nonhydrodynamic behaviors might override hydrodynamic ones, due to their very low dissipation rate, for very high wave numbers ($k \sim \pi$). One of these nonhydrodynamic waves is characterized by a phase which switches between $+\pi$ and $-\pi$, meaning its amplitude changes sign at each time step.

Finally, it should be noted that for a mean flow at rest no positive growth rates were found, meaning that this LBM is linearly stable for $M_0 = 0$ no matter the value of ν.
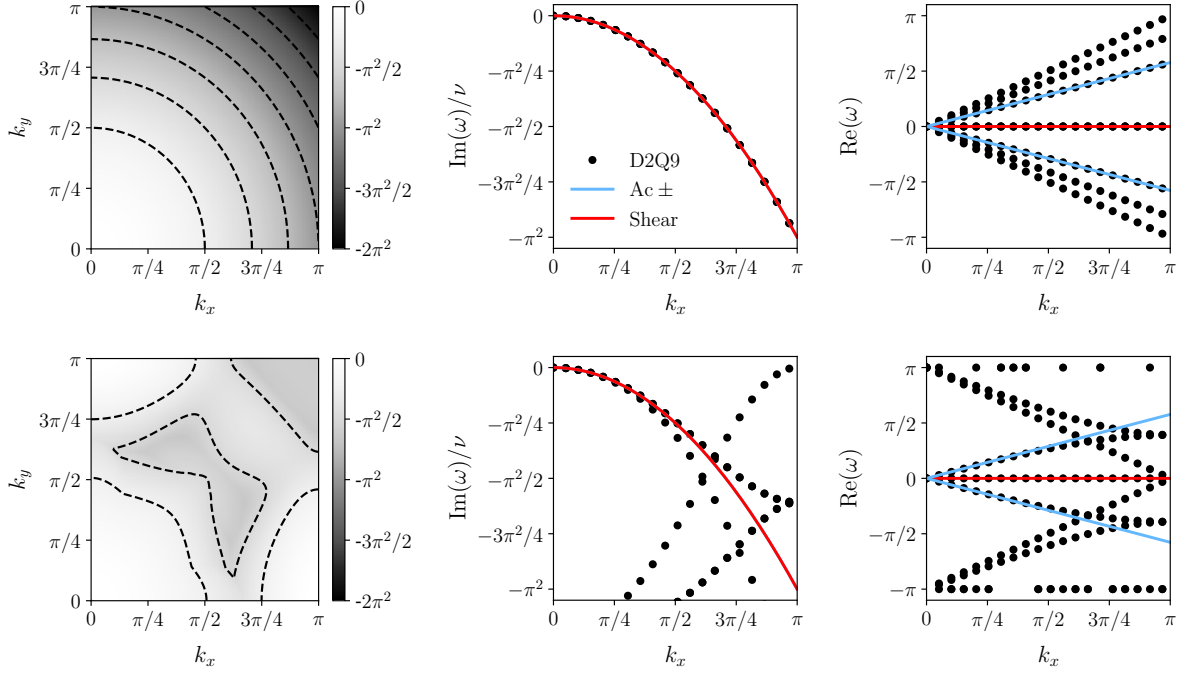
Figure 6.1 – Comparison of LSA results for the D2Q9 BGK. Impact of the numerical discretization for $M_0 = 0$ and $\nu = 10^{-5}$: (top) continuous and (bottom) discrete LBE. Maps of dimensionless maximal growth rate, dissipation rates and dispersion properties (from left to right). Regarding 2D maps, dashed isolines range from $-\pi^2/4$ to $-7\pi^2/4$ with a step of $\pi^2/4$. For 1D plots, symbols and solid lines correspond to LSA results and theoretical curves, where the latter read as: $\text{Im}(\omega_S) = \text{Im}(\omega_\pm) = -\nu k_x^2$, $\text{Re}(\omega_S) = k_x c_s M_0$ and $\text{Re}(\omega_\pm) = k_x c_s (M_0 \pm 1)$ in lattice units.

6.1.1.b Impact of the mean flow

The flow orientation with respect to the mesh grid will be characterized using the angle $\phi = \widehat{(\boldsymbol{u}, \boldsymbol{x})}$. Due to symmetry properties, it will be restricted to $[0, \pi/4]$ as originally proposed in [59, 128]. In what follows, even if the value of ϕ has an impact on the spectral properties, the particular case of $\phi = 0$ is sufficient to highlight the main differences between the LSA of both perturbed equations. If not otherwise stated, $\phi = 0$ in the following and in Chap. 6.

The impact of the mean flow is considered by successively increasing the value of the Mach number, using two different equilibrium states ($N = 2$ and 3). Results for $M_0 = 0.1$, 0.2 and 0.4 are shown in Fig. 6.2. From them several remarks can be made:

- The discrete LBE is no more unconditionally stable for small values of ν. As an example, the lower stability limit for $N = 2$ and $M_0 = 0.1$ is $\nu^{\min} \sim 0.001$.

- Increasing the mean Mach number further widens unstable areas in the Fourier space. In the previous example, increasing the mean Mach number from $M_0 = 0.1$ to $M_0 = 0.2$ further reduces the stability range ($\nu^{\min} \sim 0.01$).

- A third-order equilibrium state improves the linear stability of the present LBM. For
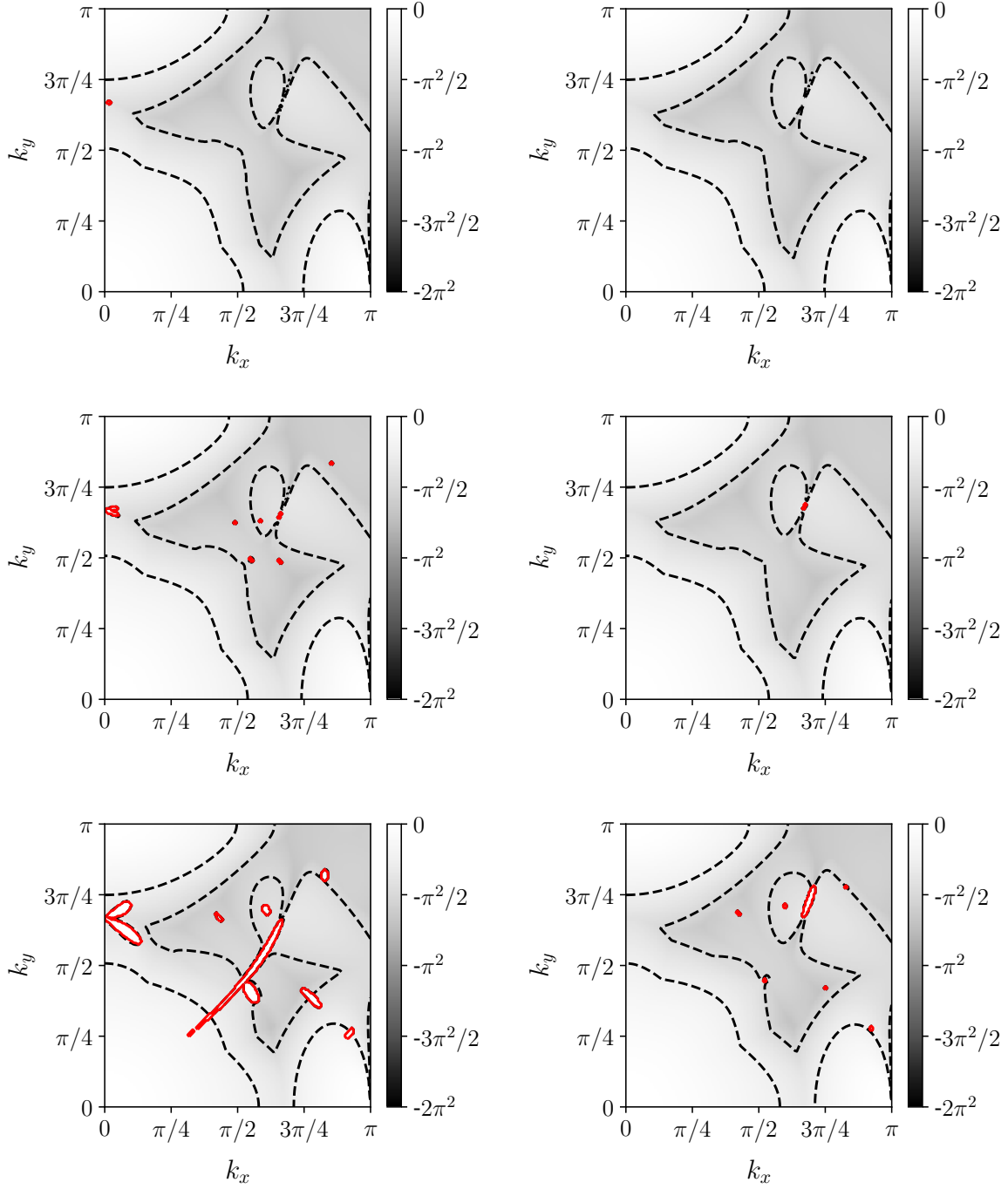
Figure 6.2 – LSA of the discrete LBE - D2Q9 BGK case. Impact of the Mach number on maps of dimensionless maximal growth rate, for $N = 2$ (first column) and $N = 3$ (second column), with $\nu = 10^{-5}$. From top to bottom, rows summarize results for $\phi = 0$ & $M_0 = 0.1$, 0.2 and 0.4 respectively. The solid isoline corresponds to the stability threshold $\max[\mathrm{Im}(\omega)] = 0$. Dashed isolines range from $-\pi^2/4$ to $-7\pi^2/4$ with a step of $\pi^2/4$. For present configurations, results corresponding to $N = 4$ are indistinguishable from those obtained with $N = 3$, and thus are not shown here.

$M_0 = 0.1$, there are no more unstable areas whatever the value of ν. Nevertheless, they start appearing for higher values of M_0.

- An equilibrium state defined on the complete basis ($N = 4$) was also tested but it led to the very same results as those from the $N = 3$ case. This conclusion was also reached for the LSA of the continuous LBE as reported in Sec. 5.4.1.b.

It should be noted that the stability increase induced by either the third- or the fourth-order equilibrium state strongly depends on the flow orientation ϕ. Their impact on the linear stability of the D2Q9 lattice is further studied below.

6.1.1.c   Stability domain

To properly quantify the stability range of the D2Q9 BGK for different equilibrium states, a parametric study based on the LSA has been conducted. Originally, the very same *modus operandi* as depicted in [59, 128] was followed:

- for $1/(\tau + 1/2) \in [1.90, 1.99] \cup \{1.995, 1.999, 1.9995\}$ the maximal mean Mach number M_0^{Max} is obtained by checking that no values of the maximal growth rate are positive,

- the most unstable case is considered to be when the wavevector $\boldsymbol{k}$ is aligned with the mean flow, i.e, $\widehat{(\boldsymbol{k}, \boldsymbol{u})} = 0$,

- the wave number and the mean flow orientation are restricted to the following values $k = ||\boldsymbol{k}|| \in [0, \pi]$ and $\phi \in [0, \pi/4]$ spaced by intervals of $\Delta k = 0.005$ and $\Delta \phi = \pi/100$.

Before comparing results obtained for $N = 2$, 3 and 4, the above protocol has been challenged through a convergence study using the $N = 2$ case. It aimed at (a) evaluating the validity of the alignment hypothesis for the most unstable case, and (b) optimizing the number of eigenvalue problems needed to be solved for a proper evaluation of the stability range of a given LBM (cf Fig. 6.3). This study shows the alignment hypothesis overestimates the stability range of the D2Q9 BGK with $N = 2$. Furthermore, both the wave number and angle intervals can be increased from $(\Delta k, \Delta \phi) = (0.005, \pi/180)$ to $(0.020, 5\pi/180)$ since all curves almost coincide for the case with no alignment hypothesis. This will allow to drastically reduce the number of eigenvalue problems that need to be solved to obtain stability ranges of interest.

To conclude, the impact of the equilibrium state truncation is investigated. Stability curves obtained for $N = 2$, 3 and 4 are shown in Fig. 6.4. For all configurations, the well known stability limit of LBM for high-Reynolds flows, corresponding to a narrower stability domain in the zero-viscosity limit, is recovered. Furthermore, the hypothesis of alignment between $\boldsymbol{k}$ and $\boldsymbol{u}$ leads to overestimations of stability ranges. This confirms previous conclusions regarding the proper way to evaluate linear stability ranges of LBM. Regarding the impact of the truncation order N, the case $N = 4$ is always more stable than for $N = 2$, while $N = 3$ leads to the worst results. This is quite astonishing since taking into account third-order Hermite tensors in the polynomial expansion allows to

discard all non-diagonal error terms in the definition of the viscous stress tensor [134]. It was then expected that including these terms would help improving the linear stability of the D2Q9 BGK. On the contrary, fourth-order Hermite tensors do not have any impact on the macroscopic behavior of the D2Q9 lattice (at the Navier-Stokes level), but they do increase the linear stability range of the present LBM. The above results clearly illustrate
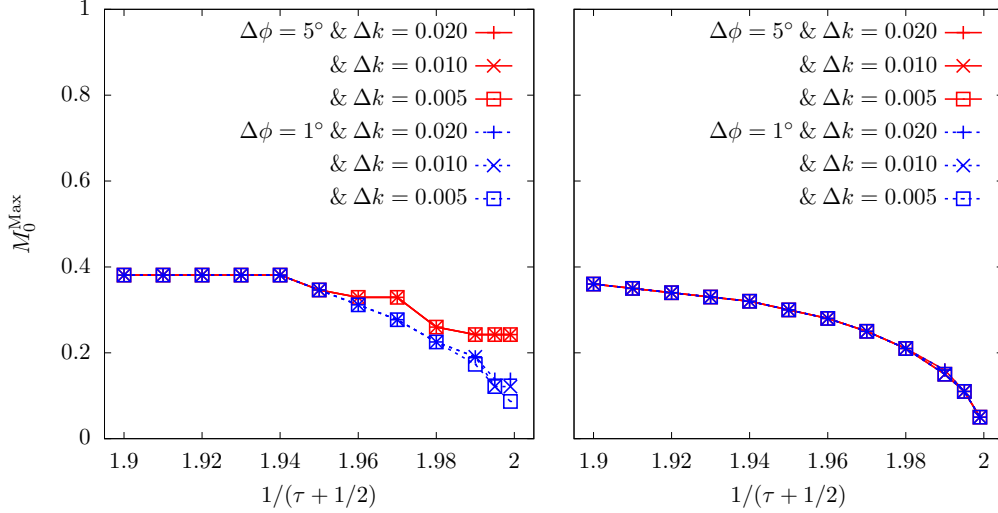
Figure 6.3 − Stability range of the D2Q9 BGK ($N = 2$): M_0^{Max} vs $1/(\tau + 1/2)$. Convergence study on wave number and angular steps $(\Delta k, \Delta \phi)$: (left) $\widehat{(\boldsymbol{k}, \boldsymbol{u})} = 0$ and (right) no hypothesis regarding $\widehat{(\boldsymbol{k}, \boldsymbol{u})}$. The alignment hypothesis always lead to an overestimation of the stability range. The optimal choice to properly evaluate stability ranges is $(\Delta k, \Delta \phi) = (0.020, 5\pi/180)$. The accuracy level of stability curves is $\Delta M_0 = 0.01$.
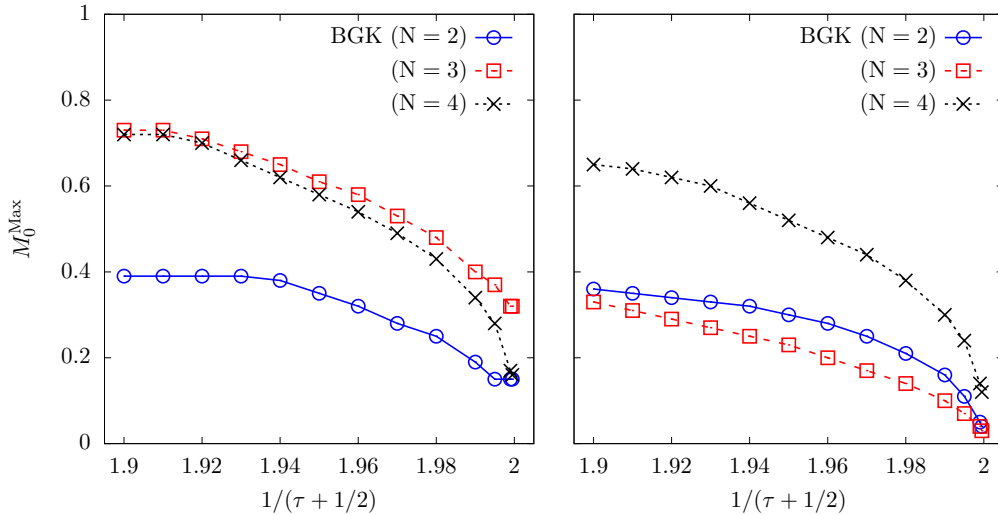
Figure 6.4 − Stability range of the D2Q9 BGK: M_0^{Max} vs $1/(\tau + 1/2)$. Impact of the equilibrium state truncation for: (left) $\widehat{(\boldsymbol{k}, \boldsymbol{u})} = 0$ and (right) no hypothesis regarding $\widehat{(\boldsymbol{k}, \boldsymbol{u})}$. The alignment hypothesis always lead to an overestimation of the stability range. Parameters used for the evaluation of stability curves are $(\Delta k, \Delta \phi) = (0.02, 5\pi/180)$, with an accuracy level of $\Delta M_0 = 0.01$.

the fact that the flow orientation ϕ must be taken into account in order to properly understand and evaluate the linear behavior of LBMs.

These analysis allowed to understand the impact of the space/time discretization of the LBE on the numerical stability of the resulting D2Q9 LBM. They will now be extended to the case of high-order LBMs.

6.1.2   High-order LBMs-BGK

As for the D2Q9 lattice, the impact of the space/time discretization on the spectral properties of high-order LBMs-BGK is studied by comparing results obtained by both the continuous and the discrete perturbed equations (Eq. (5.2.8)). Here, the question remains the same as in Sec. 5.4.2: assuming several LBMs recover the very same macroscopic behavior, do they share similar spectral properties? Small discrepancies were found in the continuous case, but will they disappear or further increase after the space/time discretization?

The comparison is first restricted to a mean flow at rest ($M_0 = 0$) with a dimensionless viscosity of $\nu = 10^{-5}$. Results for third-order LBMs-BGK are compiled in Fig. 6.5, whereas those of fourth-order ones are summarized in 6.6. Furthermore, the number of points used to plot present results has been raised from one point over eight to one point over four. This aims to ease the reading of dispersion and dissipation curves. The most striking observation to emerge from the data comparison is the impact of the numerical discretization, on the spectral properties of high-order LBMs, which is definitely higher than in the particular case of the D2Q9 BGK. While propagation speeds and dissipation rates of hydrodynamic modes remained close to analytic solutions for a large range of wave numbers for the D2Q9-BGK, discrepancies between LSA and analytic results appear for small values of k_x for all high-order models. Furthermore, present error levels are far higher than in the case of the D2Q9 lattice when the longitudinal wave number becomes higher than $\pi/4$. More precisely, dissipation rates fastly increase before reaching the limit imposed by nonhydrodynamic waves. Regarding the dispersion behavior, all of high-order models do not seem to be able to recover the proper propagation speed of both shear and acoustic waves. Even more surprising are abrupt changes of slopes encountered with acoustic waves occurring several times for the whole range of k_x. Ghost and hydrodynamic waves seem to switch behaviors when they get closer to each other. Assuming this hypothesis is valid, huge parts of the theoretical dispersion curves still remain not recovered. This kind of behavior is highly undesirable since it may lead to mode coupling and to numerical instabilities [149]. With the aim of avoiding mode coupling, and thus increasing the linear stability of LBM, several approaches have been proposed other the past few years: spatial filtering [126], two-equation based LBM (DDF [116] or hybrid [149]) or more sophisticated collision models [128]. The ability of regularization steps to prevent such phenomena from occurring will be investigated, in Sec. 6.2, for both standard and high-order velocity sets.

Regarding the linear stability of these high-order LBMs-BGK, as previously seen for the D2Q9-BGK, they are unconditionally stable for a flow at rest ($M_0 = 0$). Nevertheless, increasing the mean Mach number leads to the appearance of unstable areas on 2D maps
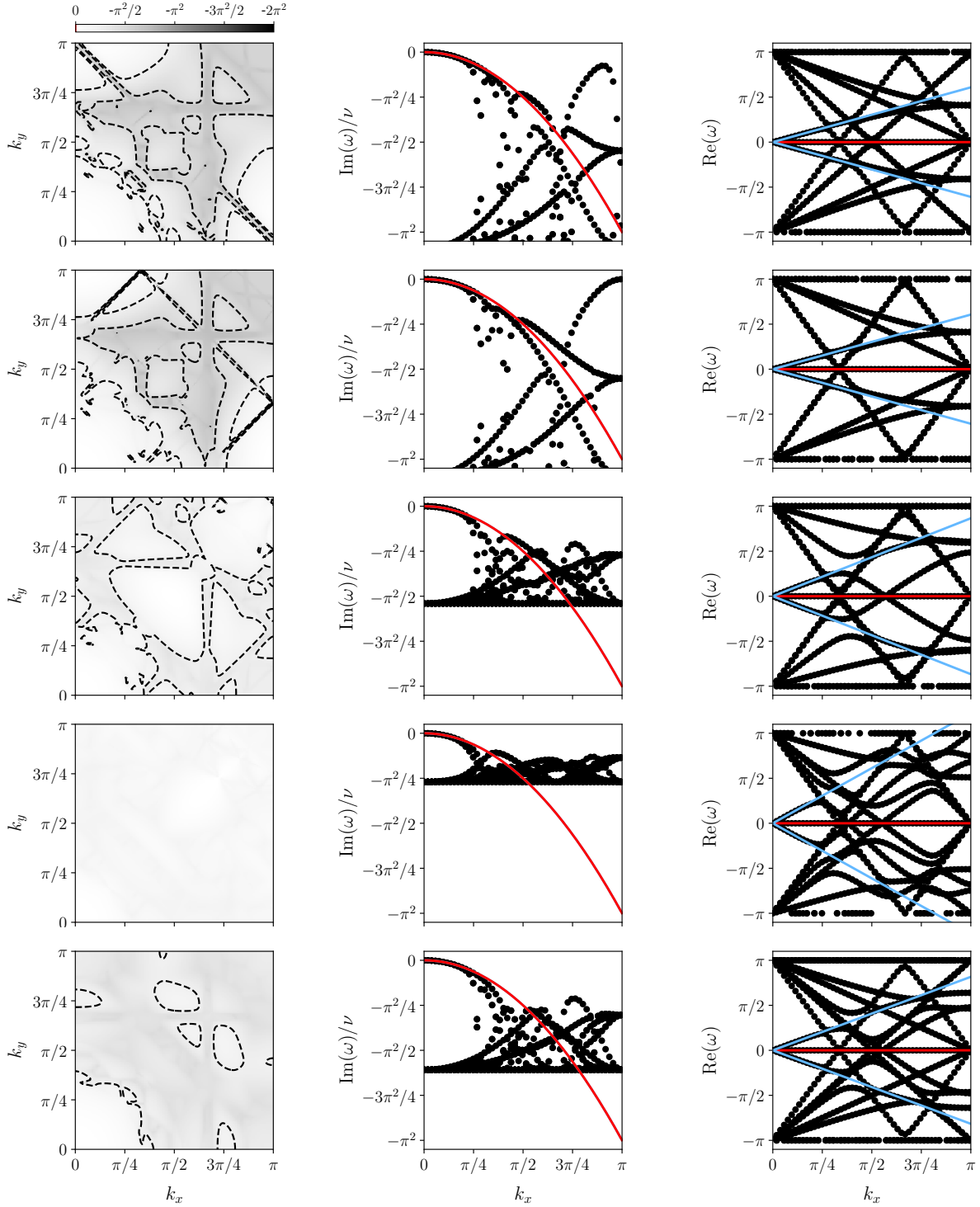
Figure 6.5 – Comparison of LSA results for third-order LBM-BGK: D2V17a, V17b, V17c, V17d, and Q21 (from top to bottom). Impact of the numerical discretization for $M_0 = 0$ and $\nu = 10^{-5}$. Maps of dimensionless maximal growth rate, dissipation rates and dispersion properties (from left to right). Regarding 2D maps, dashed isolines range from $-\pi^2/4$ to $-7\pi^2/4$ with a step of $\pi^2/4$. For 1D plots, symbols and solid lines correspond to LSA results and theoretical curves, where the latter read as: $\text{Im}(\omega_S) = \text{Im}(\omega_\pm) = -\nu k_x^2$, $\text{Re}(\omega_S) = k_x c_s M_0$ and $\text{Re}(\omega_\pm) = k_x c_s (M_0 \pm 1)$ in lattice units.

of maximal growth rate. To properly quantify the impact of the numerical discretization on the linear stability of these LBMs, the maximal achievable mean Mach number (M_0^{Max}) is searched for several values of $1/(\tau + 1/2)$. The evaluation protocol remains the same as in Sec. 6.1.1.c. Data resulting from these comparisons are plotted in Fig. 6.7 and confirm that different LBMs, which were originally designed to recover the same macroscopic behavior, do have very different linear stability ranges. More specifically, the variability
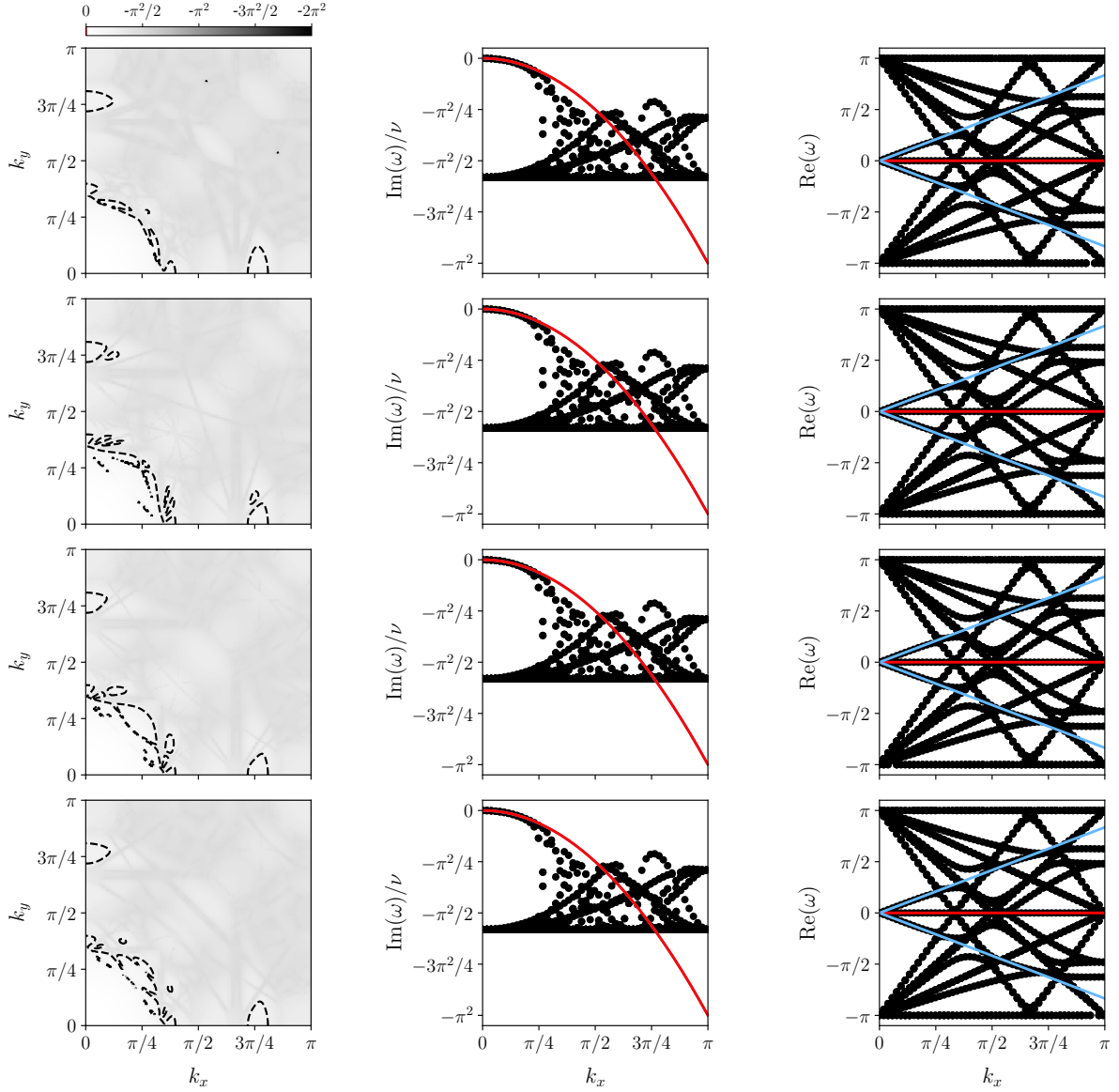
Figure 6.6 – Comparison of LSA results for fourth-order LBM-BGK: D2V37a, V37b, V37c, and V37d (from top to bottom). Impact of the numerical discretization for $M_0 = 0$ and $\nu = 10^{-5}$. Maps of dimensionless maximal growth rate, dissipation rates and dispersion properties (from left to right). Regarding 2D maps, dashed isolines range from $-\pi^2/4$ to $-7\pi^2/4$ with a step of $\pi^2/4$. For 1D plots, symbols and solid lines correspond to LSA results and theoretical curves, where the latter read as: $\mathrm{Im}(\omega_S) = \mathrm{Im}(\omega_\pm) = -\nu k_x^2$, $\mathrm{Re}(\omega_S) = k_x c_s M_0$ and $\mathrm{Re}(\omega_\pm) = k_x c_s (M_0 \pm 1)$ in lattice units.
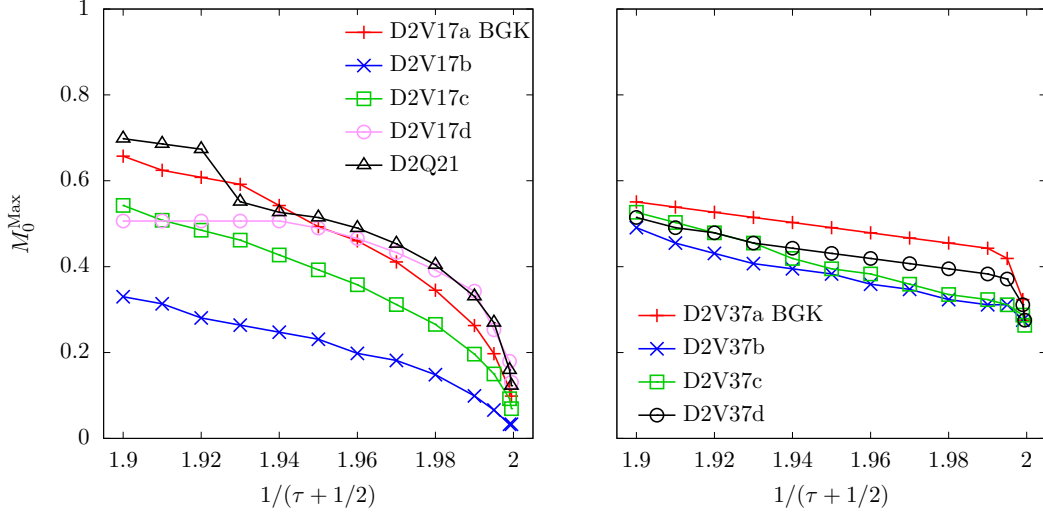
Figure 6.7 – Stability range of high-order LBM: M_0^{Max} vs $1/(\tau + 1/2)$. Impact of the collision model on third-order (left) and fourth-order (right) LBM-BGK. Parameters used for the evaluation of stability curves are $(\Delta k, \Delta \phi) = (0.02, 5\pi/180)$, with an accuracy level of $\Delta M_0 = 0.01$.

of M_0^{Max} is extremely high for third-order LBMs, and nonnegligible for fourth-order ones when τ is far from the zero-viscosity limit. Once again, a convergence trend is observed for $\tau \sim 0$. Surprisingly, some third-order LBMs remain competitive with respect to fourth-order ones, at least for $1/(\tau + 1/2) \in [1.90, 1.98]$. Nevertheless, all $V37$ velocity sets show the best stability properties in the zero-viscosity limit.

6.2 Regularized collision models

To properly understand the spectral behavior of regularization steps, the following study is divided into two parts. First, their impact is investigated in the particular case of the D2Q9 velocity set, with an equilibrium state expanded over the *complete* Hermite polynomial basis ($N = 4$). Second, the filtering abilities of both PR and RR procedures are analysed in the Fourier space for both third- and fourth-order LBMs.

6.2.1 D2Q9 using the complete basis

Starting with the D2Q9 lattice, the BGK collision model is compared to all versions of the PR and RR steps using $N = 4$. Nevertheless, it has also been checked that general trends presented below remain the same for $N = 2$ and 3. Without loss of generality, the present study is first restricted to a mean base flow at rest ($M_0 = 0$), and the kinematic viscosity is kept very low ($\nu = 10^{-5}$). Resulting LSA data are summarized in Fig. 6.8. From them, several remarks can be pointed out.

As expected, when the number of nonequilibrium coefficients taken into account in the PR approach is increased, the spectral behavior of the BGK collision operator is progressively recovered. As already explained in Sec. 4.3.1, this is induced by the fact that
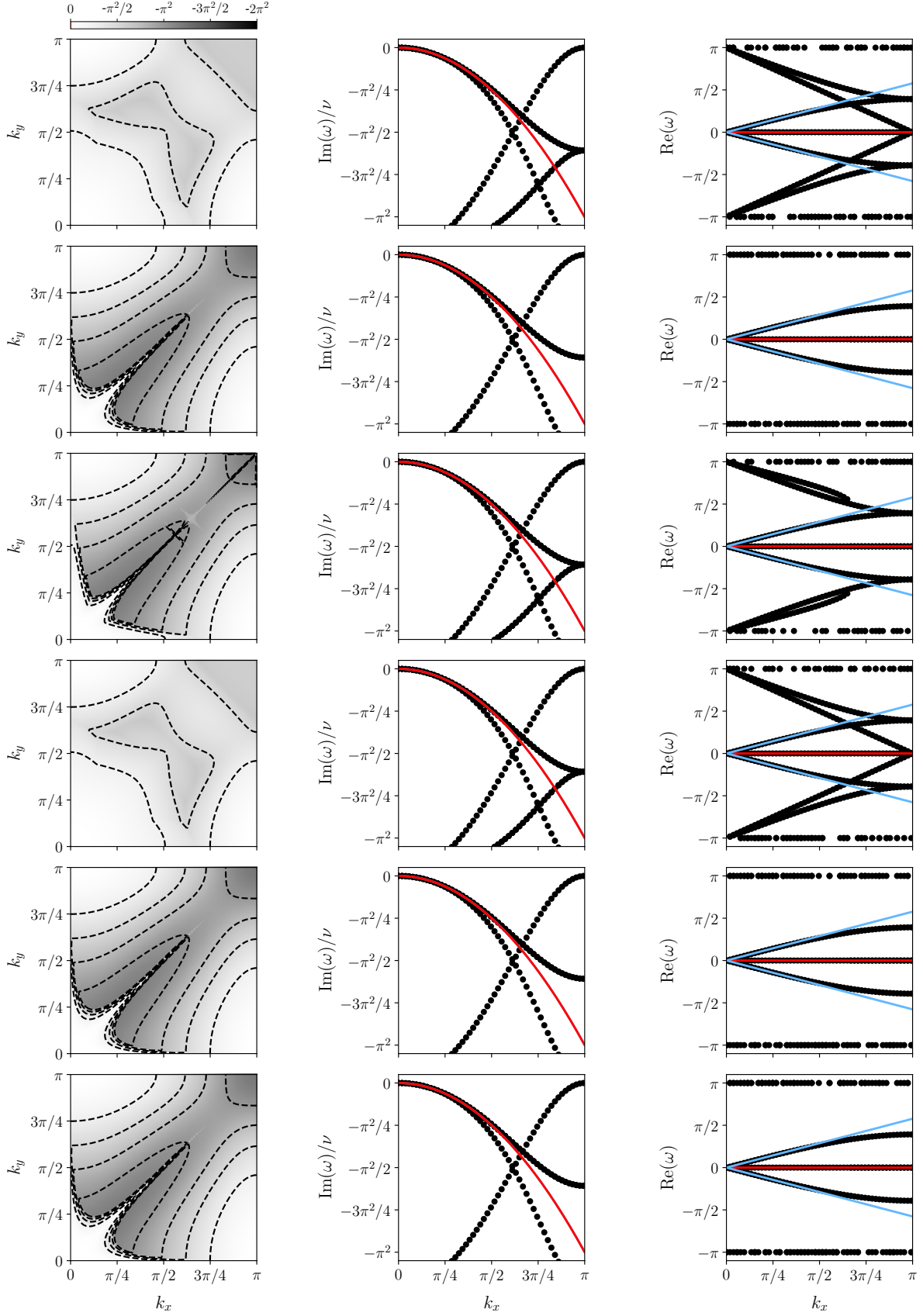
Figure 6.8 – Comparison of collision models for the D2Q9 lattice ($N = 4$): BGK, PR2, PR3, PR4, RR3 and RR4 (from top to bottom). Impact of the numerical discretization for $M_0 = 0$ and $\nu = 10^{-5}$. Maps of dimensionless maximal growth rate, dissipation rates and dispersion properties (from left to right). Regarding 2D maps, dashed isolines range from $-\pi^2/4$ to $-7\pi^2/4$ with a step of $\pi^2/4$. For 1D plots, symbols and solid lines correspond to LSA results and theoretical curves, where the latter read as: $\mathrm{Im}(\omega_S) = \mathrm{Im}(\omega_\pm) = -\nu k_x^2$, $\mathrm{Re}(\omega_S) = k_x c_s M_0$ and $\mathrm{Re}(\omega_\pm) = k_x c_s (M_0 \pm 1)$ in lattice units.

projecting the nonequilibrium part of the VDF onto the *complete* Hermite polynomial basis does not filter any information. Keeping the PR approach, it is also confirmed that the more information is filtered (PR2) the less nonhydrodynamic waves remain intact in the Fourier space. Indeed, discrete relaxation parameters $(\tau + 1/2)$ associated to $\mathcal{H}_{xxy}^{(3)}$, $\mathcal{H}_{xyy}^{(3)}$ and $\mathcal{H}_{xxyy}^{(4)}$ are fixed to a very high value ($\tau = 1/2$ in lattice units). This overdamping of nonequilibrium components allows to force the proper macroscopic behavior that should be recovered if the continuum limit hypothesis was preserved during the numerical discretization, at least for nonhydrodynamic modes. Regarding recursive regularized collision models, similar behaviors as for the PR2 approach are recovered. However, all polynomials coefficients are kept in the case of the RR4 model. This confirms the latter is able to properly filter out nonhydrodynamic spurious behaviors without decreasing the accuracy, i.e, order, of the polynomial expansion. Still, one nonhydrodynamic mode remains even using this RR collision model, and its impact on spectral properties is non-negligible for $k \sim \pi$. Its origin might be linked to $\boldsymbol{a}_1^{(2)}$ coefficients which are the only ones that are not properly recomputed during the regularization step. Using the finite-difference discretization to compute velocity gradients of $\boldsymbol{a}_1^{(2)}$ coefficients might help with this last point. The latter idea has not been tested yet, and it is deferred to future studies.

To properly differentiate the impact of PR2, RR3 or RR4 collision models on the spectral properties of the D2Q9, stability ranges are now investigated. Data corresponding to all collision operators are plotted in Fig. 6.9, and all truncation orders of $f^{(0)}$ are considered for the sake of completeness. Despite very similar spectral properties of PR2, RR3 and RR4 collision models for a mean base flow at rest, it is clear that all collision models do have very different linear stability ranges. Surprisingly, the PR2 collision model can be less stable than standard BGK collision models. At first sight, it might be in contradiction with previously reported results [107, 108], as for example the double shear layer test case used in Sec. 4.3.2.a. After second thought, it is necessary to take into account the area where growth rates become positive in the Fourier space. Indeed, considering a

Figure 6.9 – Impact of the collision model on the stability range of the D2Q9 LBM for several truncation order N of the equilibrium VDF: M_0^{Max} vs $1/(\tau + 1/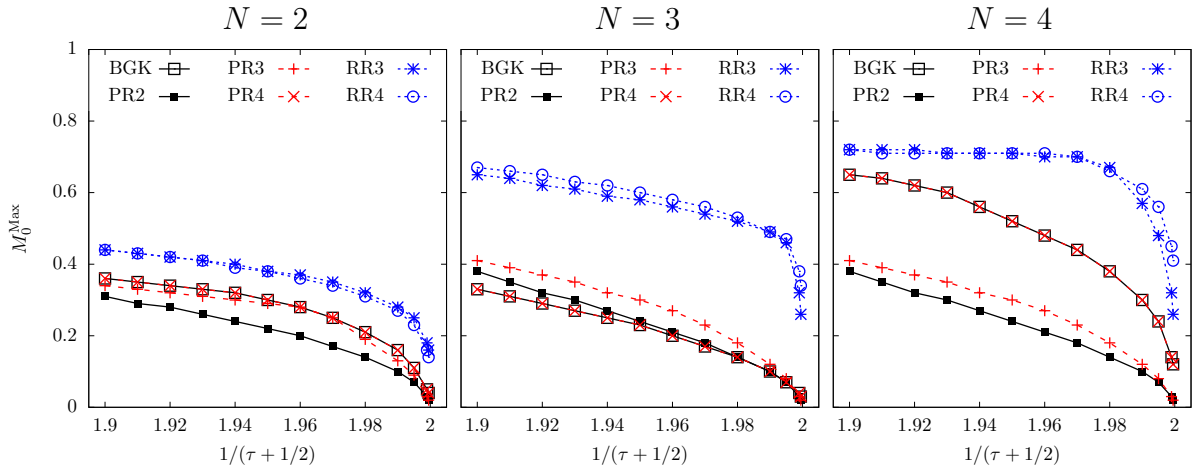2)$. Parameters used for the evaluation of stability curves are $(\Delta k, \Delta \phi) = (0.02, 5\pi/180)$, with an accuracy level of $\Delta M_0 = 0.01$.

periodic numerical simulation discretized using a given mesh, there will be a cutoff wave number k_c for which growth rate associated to lower wave numbers will not have any impact of the linear stability of the related simulation. Hence, underresolved mesh grids might naturally filter out linear instabilities. This is why the PR2 collision model led to more stable results, than those with the BGK collision model, when a 128×128 mesh grid was used in Fig. 4.4. The last remark concerns RR collision models. As expected from both the Chapman-Enskog expansion and previously presented numerical results (Chap. 4), the recursive computation of nonequilibrium coefficients of the polynomial expansion does allow to drastically increase the linear stability range of single-relaxation-time-like collision models. This remains true for all truncation orders of $f^{(0)}$, confirming the general stabilization property of the recursive approach for the D2Q9 LBM.

Let us now consider the impact of both regularization steps on the spectral properties of high-order LBMs.

6.2.2 High-order LBMs

Previous studies are now conducted in the case of third- and fourth-order LBMs. The impact of the PR and the RR collision models will successively be analysed starting with the D2V17a/b/c/d and the D2Q21 lattices, and then followed with the D2V37a/b/c/d lattices.

6.2.2.a Third-order LBMs

Let us start with data obtained using the PR3 collision model with third-order LBMs (Fig. 6.10). Contrary to the D2Q9 velocity set, this collision model only allows to partially filter out nonhydrodynamic behaviors. Regarding 1D dispersion curves, this leads to severe interactions between non-filtered ghost modes and hydrodynamics waves for all third-order models. It is clear that nonhydrodynamic modes interact with shear and acoustic waves. Nevertheless, the V17a and V17b lattices emerge as the best candidates, closely followed by the V17c and the Q21. The V17d definitely shows a very poor behavior regarding the propagation of shear and acoustic waves. Concerning dissipation properties of these numerical schemes, there is no doubt about the fact that the regularization step eliminated the dissipation threshold, that was previously imposed by nonhydrodynamic modes in the particular case of the BGK collision model (see Fig. 6.5 for a reminder). Consequently, a large overdamping of shear and acoustic waves is observed for all models. If we now move to the results obtained with the RR3 collision model, Fig. 6.11 confirms filtering properties of this approach. Indeed, almost all nonhydrodynamic waves are filtered out as seen on dispersion curves. Besides, excellent agreement with theoretical curves are recovered even for large values of the wavenumber. As previously suggested, the V17d shows the worst results of all third-order LBMs. For all numerical schemes, only little impact is observed on their dissipation properties compared to results obtained with the PR3 collision model.

To conclude this study, the impact of both regularization steps on the linear stability range of third-order LBMs is now analysed. Resulting data are compiled in Fig. 6.12

Figure 6.10 − Comparison of LSA results for third-order LBM-PR3: D2V17a, V17b, V17c, V17d, and Q21 (from top to bottom). Impact of the numerical discretization for $M_0 = 0$ and $\nu = 10^{-5}$. Maps of dimensionless maximal growth rate, dissipation rates and dispersion properties (from left to right). Regarding 2D maps, dashed isolines range from $-\pi^2/4$ to $-7\pi^2/4$ with a step of $\pi^2/4$. For 1D plots, symbols and solid lines correspond to LSA results and theoretical curves, where the latter read as: $\mathrm{Im}(\omega_S) = \mathrm{Im}(\omega_\pm) = -\nu k_x^2$, $\mathrm{Re}(\omega_S) = k_x c_s M_0$ and $\mathrm{Re}(\omega_\pm) = k_x c_s(M_0 \pm 1)$ in lattice units.

Figure 6.11 − Comparison of LSA results for third-order LBM-RR3: D2V17a, V17b, V17c, V17d, and Q21 (from top to bottom). Impact of the numerical discretization for $M_0 = 0$ and $\nu = 10^{-5}$. Maps of dimensionless maximal growth rate, dissipation rates and dispersion properties (from left to right). Regarding 2D maps, dashed isolines range from $-\pi^2/4$ to $-7\pi^2/4$ with a step of $\pi^2/4$. For 1D plots, symbols and solid lines correspond to LSA results and theoretical curves, where the latter read as: $\mathrm{Im}(\omega_S) = \mathrm{Im}(\omega_\pm) = -\nu k_x^2$, $\mathrm{Re}(\omega_S) = k_x c_s M_0$ and $\mathrm{Re}(\omega_\pm) = k_x c_s (M_0 \pm 1)$ in lattice units.

with those obtained with the BGK collision model. The PR3 approach tends to slightly reduce the discrepancies between all V17 models as compared to results obtained with the BGK collision model. Furthermore, only performances of the Q21 are enhanced in the zero-viscosity limit, whereas the stability range of all models is reduced for higher values of the relaxation time, with the exception of the V17b lattice. Regarding the RR3 collision model, it also allows to homogenize results obtained with all V17 models. Besides, it increases all maximal mean Mach numbers in the zero-viscosity limit.

Figure 6.12 – Impact of the collision model on the stability range of third-order LBMs: M_0^{Max} vs $1/(\tau + 1/2)$. From left to right, BGK, PR3 and RR3 collision models. Parameters used for the evaluation of stability curves are $(\Delta k, \Delta \phi) = (0.02, 5\pi/180)$, with an accuracy level of $\Delta M_0 = 0.01$.

6.2.2.b Fourth-order LBMs

The impact of regularized collision models on the spectral properties of all V37 lattices is now considered. Starting with results obtained with the PR4 collision model (see Fig. 6.13), similar conclusion as for third-order LBMs can be drawn from them. Indeed, nonhydrodynamic modes are partially filtered out as it can be seen on dispersion curves. Moreover, the dissipation limit that was imposed by nonhydrodynamic waves is also no longer present. This eventually leads to an overdissipation of shear and acoustic waves. When it comes to the recursive approach (Fig. 6.14), the proper filtering behavior that was observed with both second- and third-order LBMs is well recovered here. Besides, all models share very similar spectral properties. Of course, shear and acoustic waves are still overdamped, but they now propagate at the correct speed even for very large values of the wavenumber.

To conclude this analysis, let us have a look at linear stability ranges of all V37 velocity sets when they are coupled with regularization steps. Results are plotted in Fig. 6.15 with those obtained with the BGK collision model. They confirm the PR4 collision model tends to attenuate discrepancies between all V37 lattices, and leads to an almost perfect match of all stability ranges. Unfortunately, this collision operator induces a very poor stability behavior of fourth-order LBMs in the zero-viscosity limit. On the contrary, the recursive approach drastically improves their linear behavior for the whole range of relaxation time
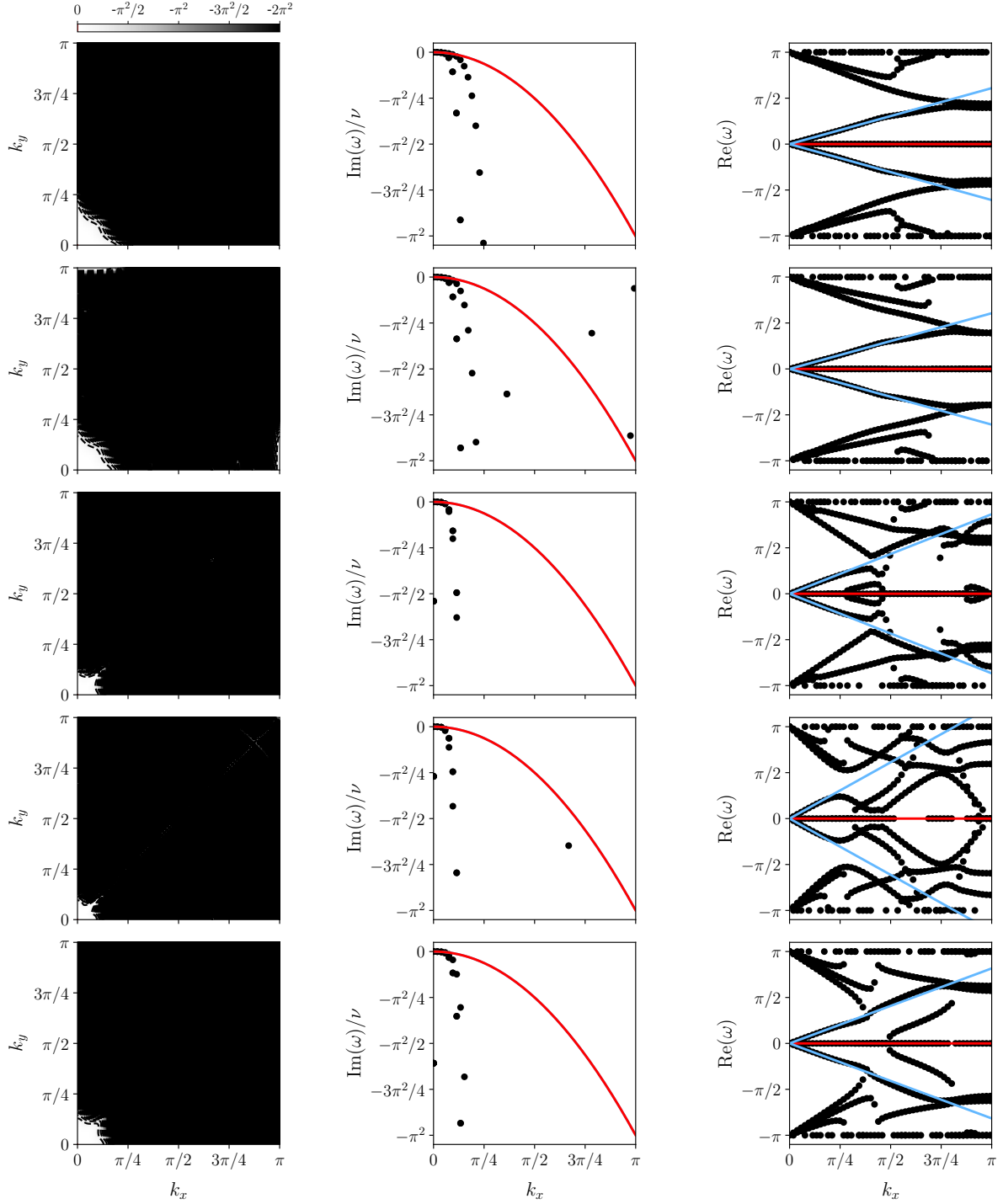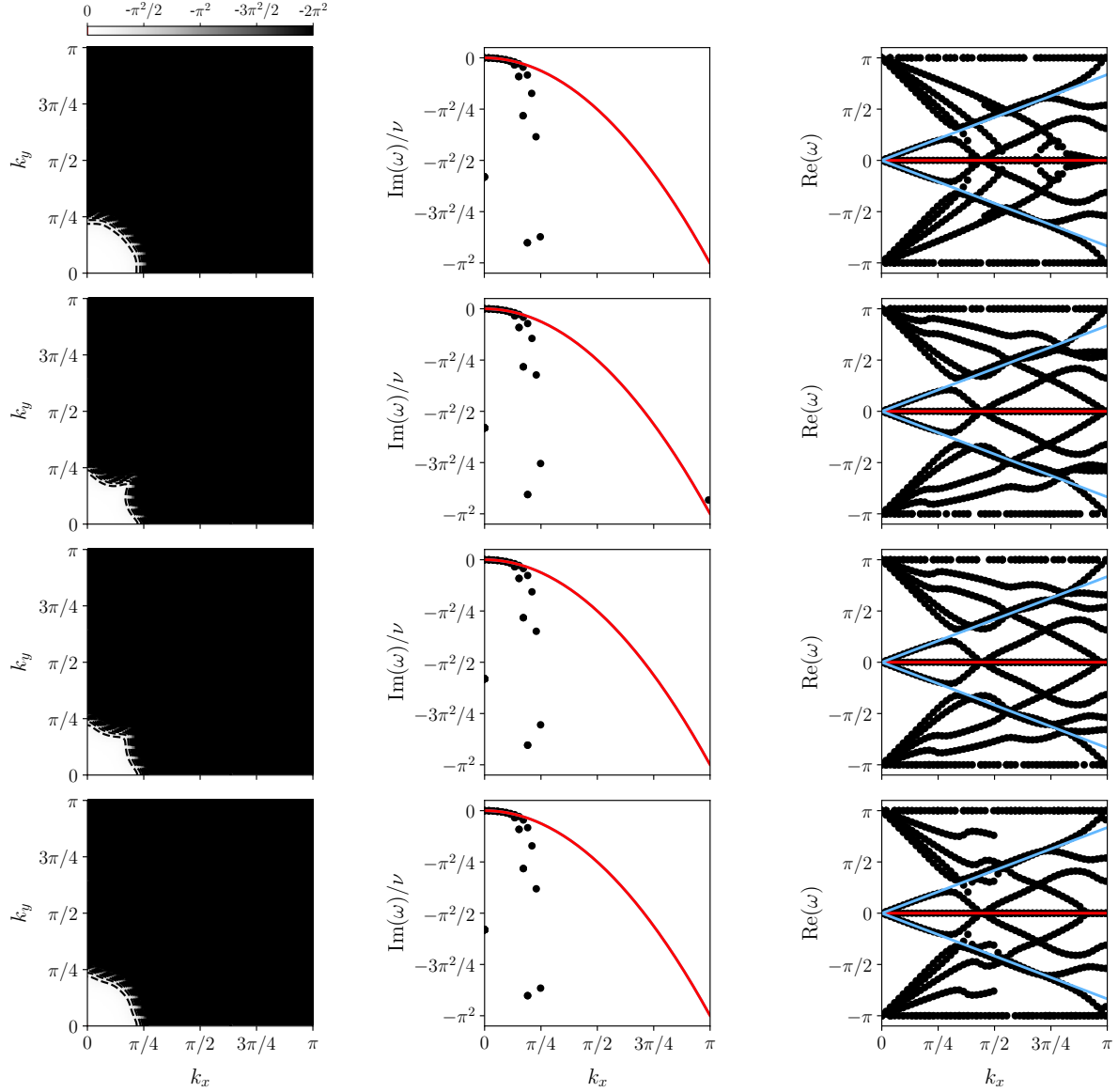
Figure 6.13 – Comparison of LSA results for fourth-order LBM-PR4: D2V37a, V37b, V37c, and V37d (from top to bottom). Impact of the numerical discretization for $M_0 = 0$ and $\nu = 10^{-5}$. Maps of dimensionless maximal growth rate, dissipation rates and dispersion properties (from left to right). Regarding 2D maps, dashed isolines range from $-\pi^2/4$ to $-7\pi^2/4$ with a step of $\pi^2/4$. For 1D plots, symbols and solid lines correspond to LSA results and theoretical curves, where the latter read as: $\mathrm{Im}(\omega_S) = \mathrm{Im}(\omega_\pm) = -\nu k_x^2$, $\mathrm{Re}(\omega_S) = k_x c_s M_0$ and $\mathrm{Re}(\omega_\pm) = k_x c_s (M_0 \pm 1)$ in lattice units.
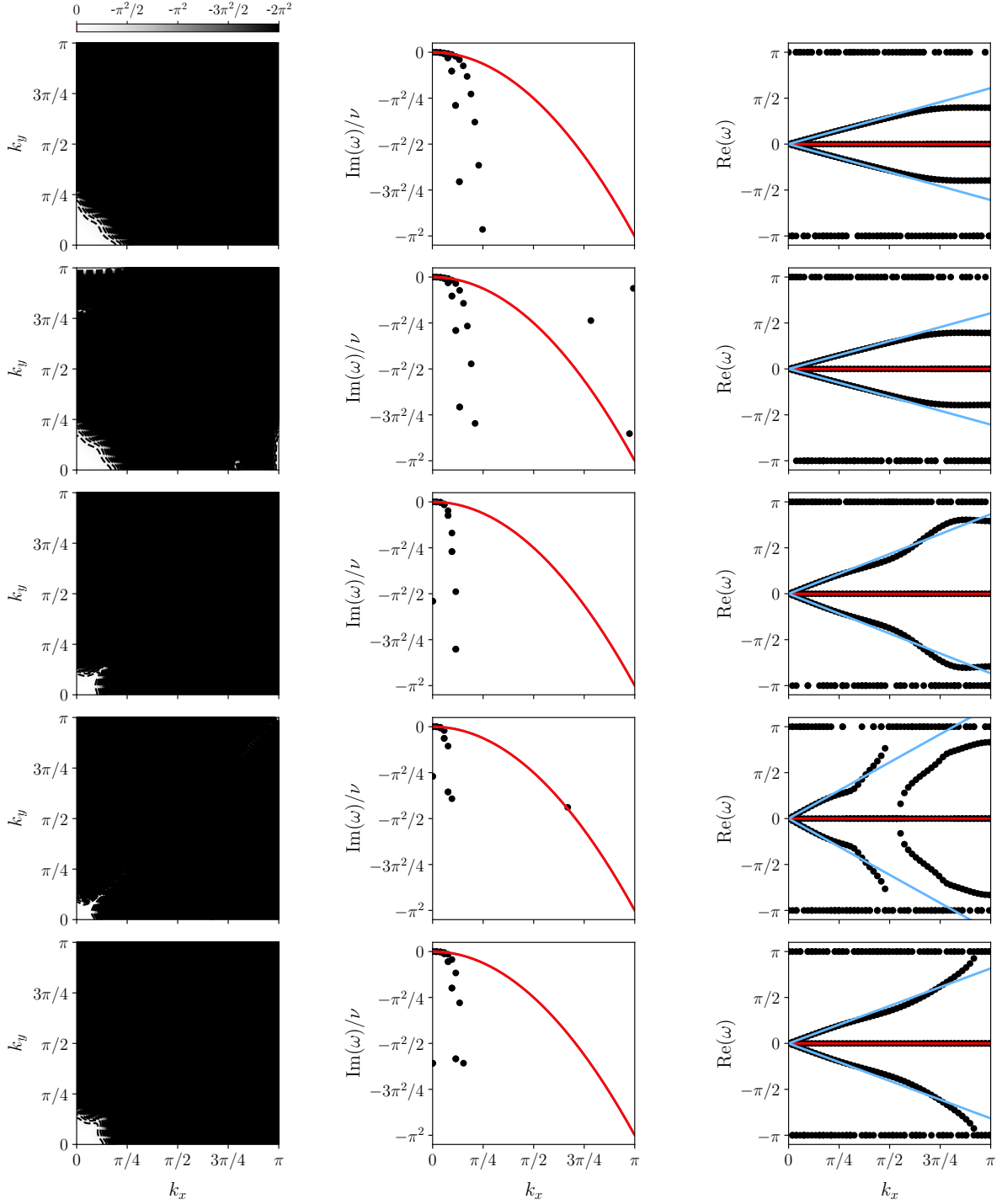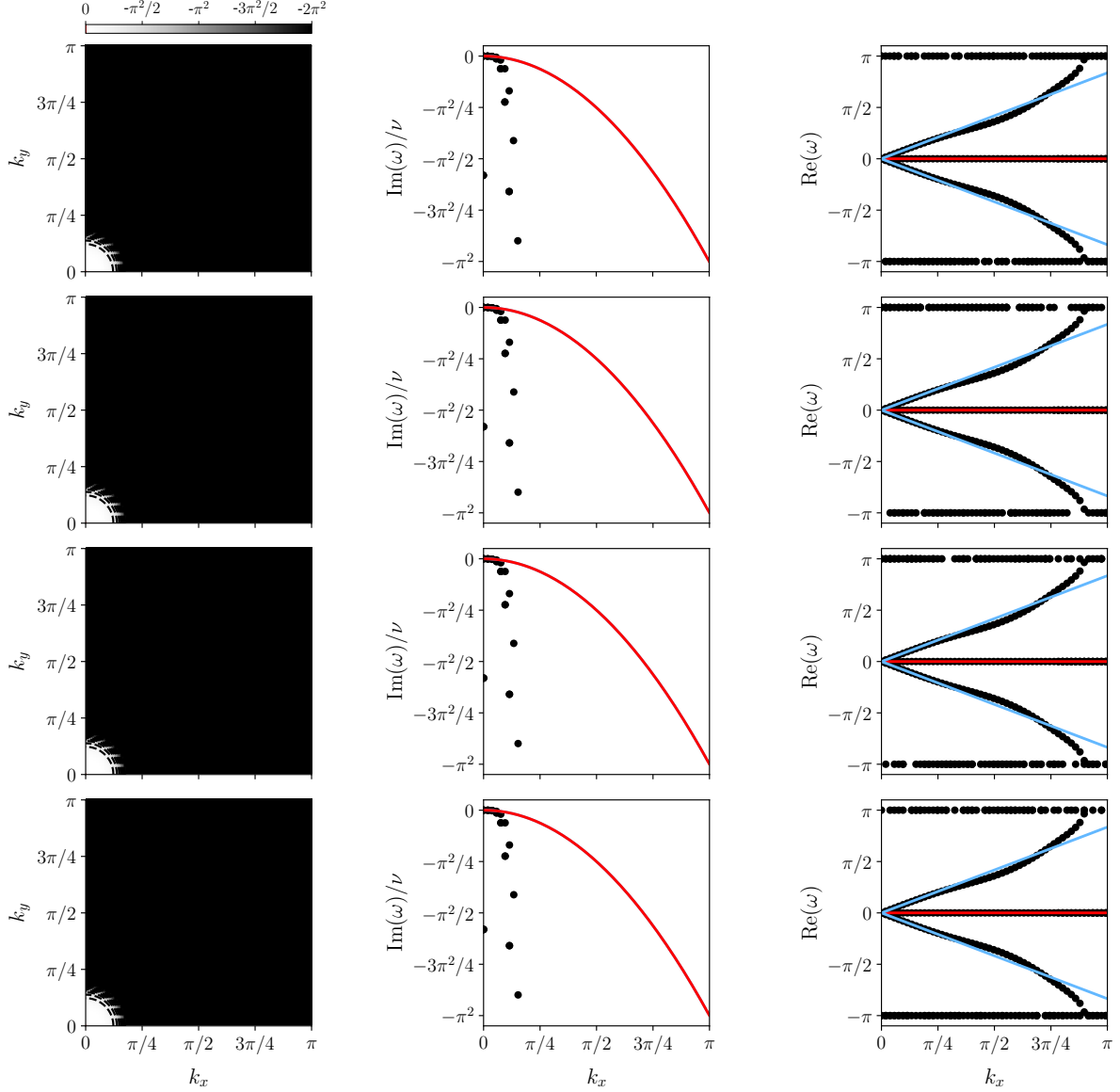
Figure 6.14 − Comparison of LSA results for fourth-order LBM-RR4: D2V37a, V37b, V37c, and V37d (from top to bottom). Impact of the numerical discretization for $M_0 = 0$ and $\nu = 10^{-5}$. Maps of dimensionless maximal growth rate, dissipation rates and dispersion properties (from left to right). Regarding 2D maps, dashed isolines range from $-\pi^2/4$ to $-7\pi^2/4$ with a step of $\pi^2/4$. For 1D plots, symbols and solid lines correspond to LSA results and theoretical curves, where the latter read as: $\mathrm{Im}(\omega_S) = \mathrm{Im}(\omega_\pm) = -\nu k_x^2$, $\mathrm{Re}(\omega_S) = k_x c_s M_0$ and $\mathrm{Re}(\omega_\pm) = k_x c_s (M_0 \pm 1)$ in lattice units.

values considered. This confirms, once again, the superiority of the recursive approach over the projection-based regularization step, at least in the context of the present study (isothermal LBMs).
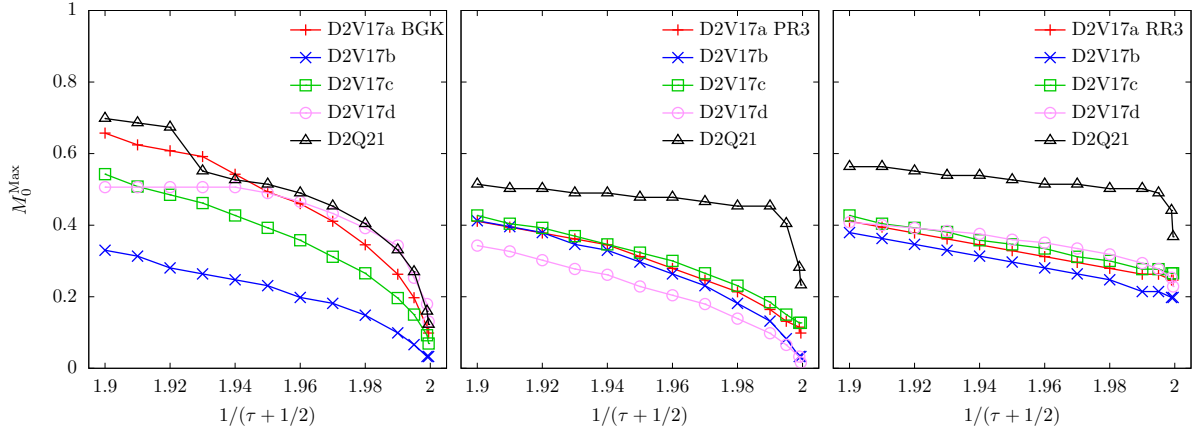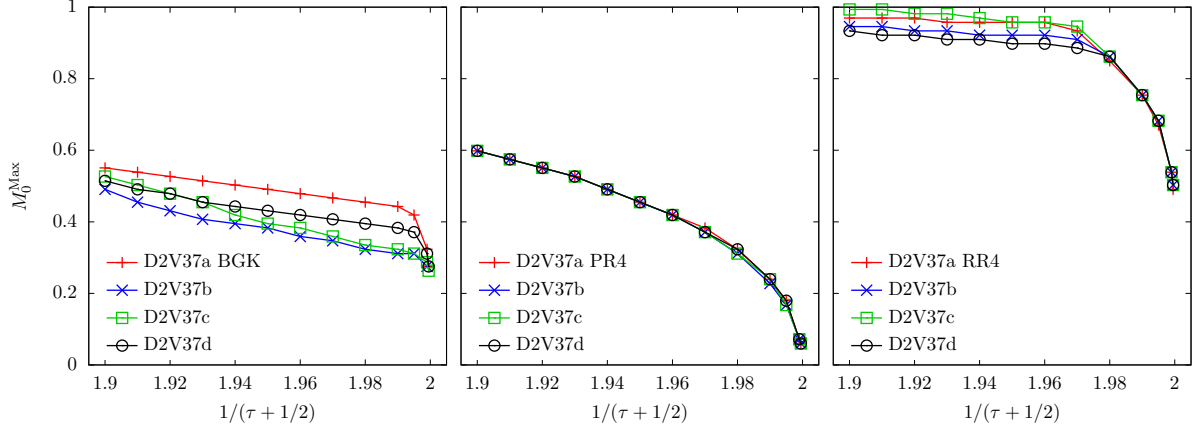

Figure 6.15 – Impact of the collision model on the stability range of fourth-order LBMs: M_0^{Max} vs $1/(\tau + 1/2)$. From left to right, BGK, PR4 and RR4 collision models. Parameters used for the evaluation of stability curves are $(\Delta k, \Delta \phi) = (0.02, 5\pi/180)$, with an accuracy level of $\Delta M_0 = 0.01$.

6.3 Conclusions

In this chapter, the LSA of the discrete LBE was conducted considering the most commonly used space/time discretization, namely, the 'Collide & Stream' algorithm. General trends were obtained by comparing present results with theoretical dispersion and dissipation curves. The numerical discretization was shown to introduce both dispersion and dissipation errors with respect to the spatial wavenumber k. In other words, the attenuation and the propagation of characteristic waves, such as shear and acoustic waves, directly depends on the grid mesh, and more specifically on the number of points used to discretize these waves. Of course, the expected behavior was always recovered in the $k \to 0$ limit, i.e, for a quasi-infinite number of points per wavelength.

In addition, it was confirmed that all high-order LBMs do not share the same numerical behavior. This was further highlighted computing linear stability ranges of each LBM, and quantifying the impact of collision models. Starting with the D2Q9 lattice, changing the truncation order of both $f_i^{(0)}$ and $f_i^{(1)}$ led to very different results. Both third- and fourth-order recursive regularization steps (RR3 and RR4) outperformed the BGK and the projection-based regularized (PR) collision models regarding linear stability ranges. Their stabilization properties were even better when the complete Hermite polynomial basis ($N = 4$) is used. The recursive approach was also shown to properly filter out nonhydrodynamic waves, hence preventing possible mode couplings that are known to lead to stability issues. These conclusions were further confirmed using third- and fourth-order collision models. A linear stability enhancement was obtained in the zero-viscosity limit for all four versions of the D2V17 lattice and the D2Q21 lattice, with

the latter showing the best results. Regarding the four D2V37 velocity sets, outstanding improvements were observed for the whole range of relaxation time values when the RR4 collision model was used. Furthermore, the D2V37c lattice led to the wider stability range.

All in all, the superiority of the RR approach, over both the PR and the BGK collision models, was proven for a very large number of lattices in the isothermal context.

Chapter 7

Conclusions & Perspectives

The lattice Boltzmann method (LBM) is a very specific numerical discretization of the Boltzmann equation – the milestone of the kinetic theory of gases. For the last thirty years, it has been shown to be of particular interest in various fields of research including computational fluid mechanics (CFD). Despite a wide range of validity of standard LBMs, the simulation of certain flows remains a tedious task: (1) weakly compressible flows at high Reynolds numbers, and (2) fully compressible flows including discontinuities such as shock waves. While several solutions have been proposed to tackle the simulation of isothermal flows in the zero-viscosity limit, numerical schemes that were developed for the simulation of fully compressible flows are not affordable in the industrial context.

In the present PhD work, it was then proposed to identify the origin of stability issues as a starting point, and then to propose solutions of interest for both academic and industry groups. For the simulation of low viscosity, thermal, and compressible flows including discontinuities, such as shockwaves, two types of instabilities were found. The first one is linked to low values of the kinematic viscosity, whereas the second instability source directly comes from the behavior of the lattice Boltzmann numerical scheme ('Collide & Stream') in the presence of discontinuities. Hence, a coupling between a shock-capturing technique, commonly used in the CFD community, and the high-order extension of the recursive regularized LBM (RR-LBM) was presented as a way to tackle both issues at the same time. This choice was mainly motivated by the fact the RR collision model is compatible with a very large number of velocity sets, and thus can cover a large panel of different physics in a systematic way (subsonic, transonic and supersonic regimes). Furthermore, this new LBM is still based on the 'Collide & Stream' algorithm, and allows to keep a similar CPU efficiency as for the standard BGK-LBM. Eventually, it is consistent with the requirements of industrial simulations, such as octree based refinement techniques and curved boundary conditions.

More precisely, the recursive regularized (RR) approach was first shown to drastically improve the numerical stability of the D2Q9, D2V17a and the D2V37a lattices in the isothermal context, with respect to the BGK and the standard projection-based regularized (PR) collision models. The famous double shear layer test case was used for this purpose. The extension to thermal and fully compressible flows, of the RR approach, was thoroughly derived and validated before being coupled with a shock-capturing technique.

The latter was validated using the D2V37a velocity set and 1D Riemann problems (Sod shocktube) in the zero-viscosity limit. Resulting data compared very well with theoretical curves even in underresolved conditions.

Despite stability gains reported above, two questions remained at that time: (1) Is it possible to quantify the numerical stability of lattice Boltzmann numerical schemes in a general way?, and (2) Do velocity sets, which were designed to recover the very same macroscopic behavior, share similar numerical stability ranges? The first question is related to the fact that it is generally difficult to compare stabilization techniques without undergoing a great number of numerical test cases. Hence, a general way to compare the stability domain of several collision models is, as an example, deeply needed. The second question concerns choices that have to be made when high-order LBMs are required. Indeed, several velocity sets have been proposed over the past two decades in order to tackle the simulation of moderate to high-Mach number flows. The question of how to choose the best lattice, i.e, that shows the best tradeoff between robustness and accuracy, is then of uttermost importance. These two questions have been tackled through the use of linear stability analysis (LSA) in the isothermal context.

Both continuous and discrete lattice Boltzmann equations (LBE), in the sense of partial derivatives, were successively studied for a very large number of velocity sets (D2Q9, D2V17a/b/c/d, D2Q21 and D2V37a/b/c/d). The LSA of the continuous LBE was shown to be an alternative to the Chapman-Enskog expansion to determine its macroscopic behaviors[1], at least in the linear regime where the amplitude of perturbations are assumed to be small as compared to mean flow quantities. In other words, this kind of LSA confirmed the proper macroscopic behavior that was recovered if and only if (1) the continuum limit was verified ($\tau \ll 1$), and (2) the proper velocity discretization was employed. Using the 'Collide & Stream' algorithm, the LSA of the discrete LBE was then conducted to further understand the impact of this very specific space/time discretization on the stability domain of the overall numerical scheme. Two general trends emerged from this study. First, it was shown that all lattices led to different numerical behaviors, whatever the number of discrete velocities or the value of their lattice constant. Second, the filtering behavior of the RR approach led to larger stability domains with respect to both the BGK and the PR approaches. This last result is rather general since it was observed for all velocity sets of interest.

All in all, this PhD work was dedicated to (a) the derivation of new stabilization techniques for high-order LBMs, and (b) the understanding of numerical instabilities through the LSA of both continuous and discrete LBEs. This was done to avoid the standard and iterative *trial and error* way to derive more robust numerical schemes.

The proposed high-order extension of the RR collision model was proven to be of particular interest for the simulation of low viscosity, thermal and compressible flows, due to its enhanced stability and accuracy properties. Flowing from the Hermite polynomial expansion framework, this collision model was straightforwardly extended to a very large number of velocity sets. This is definitely one of the main strength of this stabilization

---

[1]As originally proposed by Lallemand & Luo [128].

technique as compared to, for instance, standard MRT [128] and cascaded [95,96] collision models. Nevertheless further investigations are still required to properly quantify the full potential, and the limitations of such an approach, especially in the industrial context. As an example, flows including external accelerations, boundary conditions, octree based mesh refinement technique, and LBMs with two sets of populations (DDF) need to be taken into account in the RR framework. These studies are mandatory to make the RR-LBM affordable for industry groups.

As this manuscript is being written, the extension of the LSA to both thermal high-order LBMs and DDF-LBMs has started. It will allow to further enrich available data, and to better understand triggering mechanisms of instabilities. Regarding other collision models, it is scheduled to study the linear stability properties of MRT, entropic, cascaded and cumulant collision models in the context of the D2Q9 lattice. It should allow to rigorously compare stability properties of each collision model. Eventually, while results concerning eigenvalues were studied in the present work, the study of eigenvectors is also considered. It will allow to better understand causes of mode couplings, and thus origins of numerical instabilities. This should lead to a further extension of the high-order RR collision model.

Note finally that the current PhD work, and parallel activities, are related to the following publications, conference papers and training/teaching sessions.

Ranked *A* papers

- **C. Coreixas**, G. Wissocq, G. Puigt, J.-F. Boussuge & P. Sagaut, Recursive regularization step for high-order lattice Boltzmann methods, *Phys. Rev. E*, 2017, 96.

- **C. Coreixas** *et al.*, Linear stability analysis of recursive regularized lattice Boltzmann methods, under preparation for submission to *Phys. Rev. E*.

- **C. Coreixas** *et al.*, Impact of the collision model on the linear stability analysis of lattice Boltzmann methods, under preparation for submission to *Phys. Rev. E*.

Conference papers

- **C. Coreixas**, Round Cavity Noise Simulations using Lattice-Boltzmann Solver, *11th PEGASUS-AIAA Student Conference*, 2015.

- A. Sengissen, J.-C. Giret, **C. Coreixas** & J.-F. Boussuge, Simulations of LAGOON landing-gear noise using Lattice Boltzmann Solver, *21st AIAA/CEAS Aeroacoustics Conference*, 2015, 2993.

- **C. Coreixas**, G. Wissocq, G. Puigt, J.-F. Boussuge & P. Sagaut, General regularization step for standard and high-order lattice Boltzmann methods, *14th ICMMES*, 2017.

Online course - Trainings

- Small private online course (SPOC): Fundamentals of lattice Boltzmann method

- Instructor-led training session at CERFACS: Implementation and use of the lattice Boltzmann method

- Practicals about the lattice Boltzmann method, at ISAE-Supaéro (graduate school of aeronautical engineering)

More details about these training/teaching experiences are available in App. I.

Appendix A

Industrial Solver - LaBS

A.1   Presentation of the solver

LaBS (**La**ttice **B**oltzmann **S**olver) software has been developed within a consortium of industrial companies (Renault, Airbus, CS), academic laboratories (Aix-Marseille University, École Centrale de Lyon, Laboratoire de Mathématiques d'Orsay) and strong partnerships with others entities (CERFACS, ONERA, Alstom, GANTHA, Matelys, Kalray) through two successive projects, namely, 'LaBS' (2011-2014) and 'CLIMB' (2015-2018) projects.

This code relies on a D3Q19 formulation, with a particular regularized collision model for a better robustness / accuracy tradeoff. Turbulence is handled according to the large-eddy simulation (LES [87, 158]) approach, using either high-order explicit spatial filtering techniques [126], or a dedicated subgrid scale model (the **S**hear **I**mproved **S**magorinsky **M**odel, SISM [159]). Near wall turbulence is modeled using wall laws accounting for adverse pressure gradient [160] and curvature effects. Among all available boundary conditions, non-reflective boundary conditions can be enforced to avoid spurious reflections [161]. Furthermore, boundary conditions are coupled with an inverse distance weighting method [162] to handle curved geometries. Finally, all the above characteristics, supplemented with an octree based grid refinement technique [20], allow LaBS software to simulate realistic configurations. Some of the aforementioned functionalities are explained in more details below.

A.2   Functionalities

The subgrid scale model: allows to take into account small-scale physical processes (energy transfer from large scales to small ones through dissipation) that occur at length-scales that cannot possibly be resolved by the grid cell size. The SISM, presented hereafter, is a modified version of the Smagorinsky subgrid scale model which belongs to the family of eddy viscosity models [159]. For the latters, underresolved turbulence is taken into account through the eddy viscosity ν_t (Boussinesq hypothesis) which is simply added to the kinematic one $\nu_{tot} = \nu + \nu_t$. Furthermore, the turbulent viscosity is computed in

such a way that it tends to zero at walls:

$$\nu_t^{SISM} = (C_s\Delta)^2|S - \overline{S}| \quad \xrightarrow[\text{wall}]{S=\overline{S}} \quad 0, \tag{A.2.1}$$

where $S_{\alpha\beta} = (\partial_\alpha u_\beta + \partial_\beta u_\alpha)/2$ and $\overline{S}$ is computed here through a temporal moving average of S *i.e* $\overline{S} = \frac{1}{N}\sum_{n=0}^{N-1} S(t - n\Delta t)$.

The selective spatial filtering: consists in a spatial average of quantities of interest, and leads to a modified kinematic viscosity. The latter is then wavelength-dependent which allows to dissipate spurious small spatial scales (high wave numbers) keeping the largest ones (small wave numbers) unaffected. As an example, the more robust (and less costly) approach is based on the spatial filtering of macroscopic quantities [126]:

$$\begin{cases} \langle\rho\rangle = \rho(\mathbf{x}) - \sigma\sum_{\alpha=1}^{D}\sum_{n=-N}^{N} d_n\rho(\mathbf{x}_\alpha - n\mathbf{x}_\alpha) \\[2em] \langle\mathbf{u}\rangle = \mathbf{u}(\mathbf{x}) - \sigma\sum_{\alpha=1}^{D}\sum_{n=-N}^{N} d_n\mathbf{u}(\mathbf{x}_\alpha - n\mathbf{x}_\alpha) \end{cases}, \tag{A.2.2}$$

where N is the number of points of the damping stencil (here $N = 3$ which leads to a 7-point stencil in each spatial direction), $0 \le \sigma \le 1$ is the strength of the filter and $d_n = d_{-n}$ are the damping coefficients ($d_0 = 5/16$, $d_1 = -15/64$, $d_2 = 3/32$ and $d_3 = -1/64$ [126]).

The finite-difference boundary conditions: allows to reconstruct missing populations using information from the macroscopic quantities [99]. Indeed, at the Navier-Stokes level of physics

$$f = f^{eq} + f^{neq} \approx f^{(0)}(\rho, \mathbf{u}, T) + f^{(1)}(\rho, \mathbf{u}, T, \boldsymbol{\nabla}(\mathbf{u}), \boldsymbol{\nabla}(T)). \tag{A.2.3}$$

Thus, macroscopic quantities (and their gradients) can be used to build distribution functions compliant (in the continuum limit $\epsilon \ll 1$) with the Navier-Stokes set of equations.

The inverse distance weighting method: is a spatial interpolation that estimates the unknown quantities of interest with a weighted average of the values available at neighbor points:

$$A(\mathbf{x}) = \sum_k \gamma_k(\mathbf{x})A(\mathbf{x}_k) \qquad \text{with} \qquad A = \rho, \mathbf{u}, \text{ or } T \tag{A.2.4}$$

and

$$\gamma_k(\mathbf{x}) = \frac{d(\mathbf{x}, \mathbf{x}_k)^{-p}}{\sum_k d(\mathbf{x}, \mathbf{x}_k)^{-p}} \tag{A.2.5}$$

where $d(\mathbf{x}, \mathbf{x}_k) = \sqrt{(x - x_k)^2 + (y - y_k)^2 + (z - z_k)^2}$ is the euclidean distance between the two points $\mathbf{x}$ and $\mathbf{x}_k$, and p is an integer such as $p \ge 2$. This spatial interpolation

allows to extend the above boundary conditions to curved ones.

Let us now continue with recursive regularized (RR) LBMs that have been studied as possible candidates for the simulation of fully compressible flows.

A.3   3D extension of high-order RR-LBMs

Thanks to the Hermite polynomial expansion framework, the 3D extension of the new recursive regularized (RR) LBM is straightforward. Hence the focus was put on the investigation of 3D third- and fourth-order LBMs, which were constructed following the preservation of the orthogonality properties of Hermite polynomials. Furthermore, it was chosen to only consider lattices with a minimal number of velocities, and as compact as possible, to not deteriorate too much HPC efficiency of the 'Collide & Stream' algorithm.

Flowing from the work of Shan [120], two possible candidates were found for the simulation of isothermal flows without Mach number restrictions (third-order LBMs). They are both based on a 39-velocity discretization of the Boltzmann equation. Regarding the simulation of fully compressible flows, Shan also proposed to use the D3Q103 [120]. They are illustrated in Fig. A.1, and their characteristics are summarized in Tab. D.3.

In addition, the use of DDF models was adopted to further reduce the number of equations that need to be solved at each time step and for each grid point (see App. C for theoretical details about DDF approaches). The coupling between the two high-order LBMs was also investigated. The Boussinesq coupling was successfully implemented and validated. Nevertheless, the choice regarding the ideal gas coupling remains an open question. Indeed, it can either be done implicitly through the equilibrium VDF [64], or explicitly changing the definition of the equation of state using a forcing term [8, 163]. The last approach is the most stable one, but it introduces error terms that need to be corrected. This is even worse when second-order LBMs (D3Q19 or D3Q27 lattices) are considered for the DDF model.

The last step to further improve the efficiency of compressible LBMs is to replace the second (thermal) LBM by an energy equation discretized using standard numerical schemes. This is differed to future investigations.

Regarding boundary conditions, several layers of boundary conditions are required to properly reconstruct missing populations. Current models are based on regularized boundary conditions coupled with the inverse distance weighted interpolation.
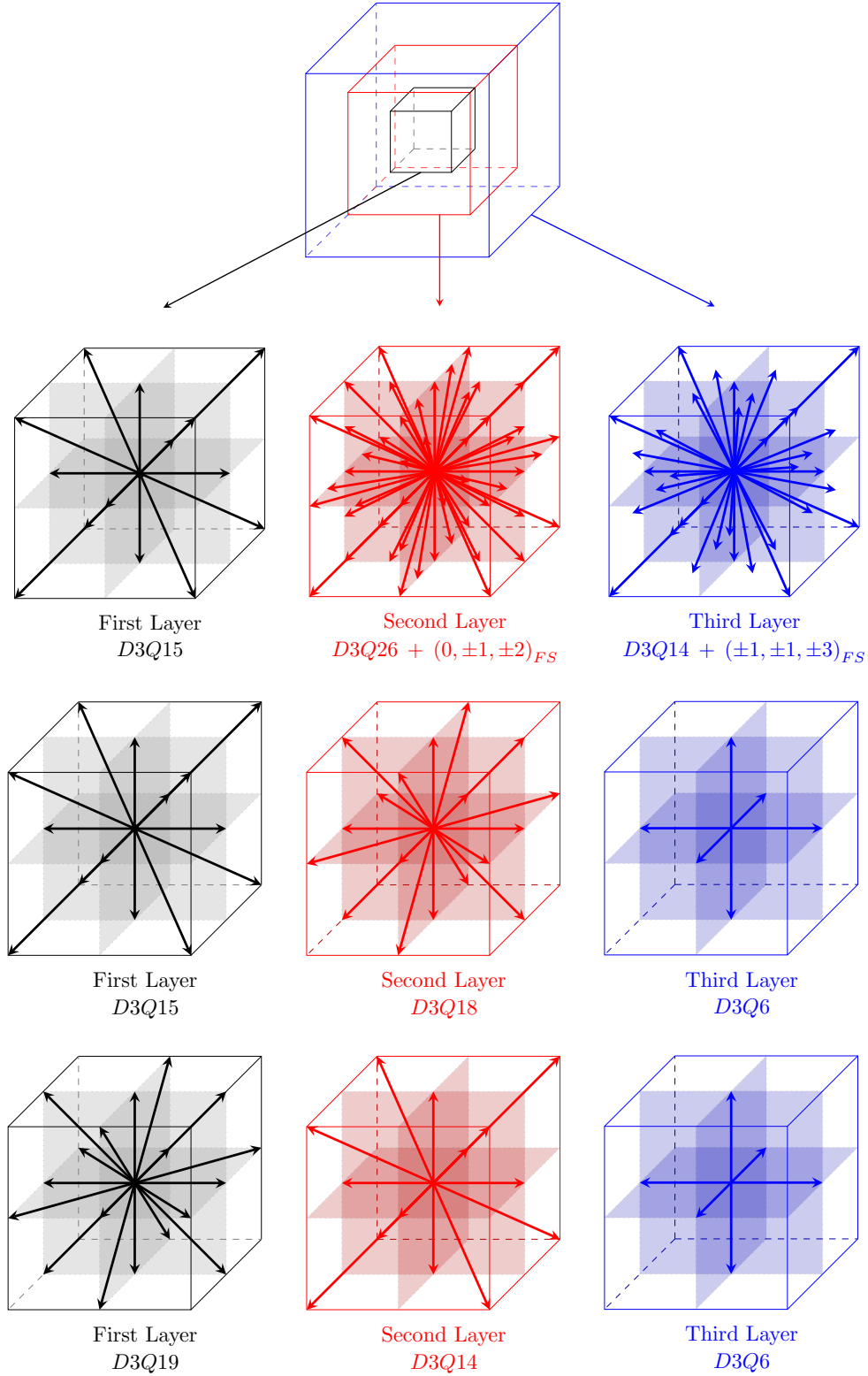
Figure A.1 − Illustration of 3D high-order LBMs of interest: D3Q103, D3Q39a/b lattices (from top to bottom). They are all composed of three layers of velocities. If not otherwise stated, each component of the velocities belongs to ±1, ±2 and ±3 for the first, second and third layer respectively. D3Q6, D3Q14 and D3Q18 lattices correspond to D3Q7, D3Q15 and D3Q19 lattices where the velocity $(0, 0, 0)$ has been discarded. Data are compiled from [120].

Appendix B

Background on multivariate Hermite tensors

This appendix aims at providing the main definitions and properties of multivariate Hermite tensors (or polynomials), and their coefficients. They are first given in the continuous case related to the continuous velocity space, whereas the last part of this appendix highlights the main differences with the discrete case used after both the velocity space and the numerical discretizations. If not otherwise specified, all properties below are given for any vector in $\mathbb{R}^D$.

B.1 Definition

In the multivariate case, Hermite polynomials are commonly defined by

$$\boldsymbol{\mathcal{H}}^{(n)}(\boldsymbol{\xi}^*) = \frac{(-1)^n}{\omega(\boldsymbol{\xi}^*)} \boldsymbol{\nabla}^n_{\boldsymbol{\xi}^*} \omega(\boldsymbol{\xi}^*), \tag{B.1.1}$$

with

$$\omega(\boldsymbol{\xi}^*) = \frac{1}{(2\pi)^{D/2}} \exp\left(-\frac{(\xi^*)^2}{2}\right), \tag{B.1.2}$$

$\boldsymbol{\nabla}^n_{\boldsymbol{\xi}^*}$ being the n-th derivative with respect to the peculiar velocity $\boldsymbol{\xi}^*$. They are of uttermost importance in the LBM framework, since they can be used to ensure the preservation of the equilibrium VDF moments, during the velocity discretization, through the Gauss-Hermite quadrature [104–106,119]. To do so, it is recommended to change the definition of both Hermite polynomials (B.1.1) and their associated weight (B.1.2).

B.2 Normalization

In the most general case, three different types of peculiar velocity can be chosen [119]:

1. Temperature- and flow-dependent velocities

$$\boldsymbol{\xi}^* = (\boldsymbol{\xi} - \boldsymbol{u})/\sqrt{rT}, \tag{B.2.1}$$

2. Temperature–dependent velocities

$$\boldsymbol{\xi}^* = \boldsymbol{\xi}/\sqrt{rT}, \tag{B.2.2}$$

3. Constant velocities

$$\boldsymbol{\xi}^* = \boldsymbol{\xi}/\sqrt{rT_0}, \tag{B.2.3}$$

where T_0 is a reference temperature, and can be linked to the velocity discretization.

This leads to three different types of weights and Hermite polynomials. Nevertheless, the normalization (B.2.1) would imply that the position of particles changes at each time step as in the model of Sun [71], which is known to require complicated reconstruction techniques to get the VDFs values at each grid node. In the second case, particles will be located between two aligned grid nodes at each time step, hence requiring an interpolation technique in the same spirit as the one used for off-lattice LBMs [60]. Furthermore, in both previous cases, the independence of $\boldsymbol{\xi}$ with respect to $(\boldsymbol{x},t)$ is lost. This introduces a number of difficulties in the Chapman-Enskog expansion, where now $\partial_t(\boldsymbol{\xi}f) \neq \boldsymbol{\xi}\partial_t f$ and $\nabla(\boldsymbol{\xi}f) \neq \boldsymbol{\xi}\nabla f$. The last normalization allows to have a consistent definition of Hermite polynomials and their weight, i.e, that remains valid for both isothermal and thermal LBMs in both the continuous and discrete cases. Using Eq. (B.2.3), we finally end up with the following definitions:

$$\boldsymbol{\mathcal{H}}^{(n)}(\boldsymbol{\xi}) = \frac{(-rT_0)^n}{\omega(\boldsymbol{\xi})} \boldsymbol{\nabla}_{\boldsymbol{\xi}}^n \omega(\boldsymbol{\xi}), \tag{B.2.4}$$

with

$$\omega(\boldsymbol{\xi}) = \frac{1}{(2\pi rT_0)^{D/2}} \exp\left(-\frac{\xi^2}{2rT_0}\right), \tag{B.2.5}$$

and where $1/(rT_0)^{D/2}$ has been added to $\omega(\boldsymbol{\xi})$ to ensure that $\int \omega(\boldsymbol{\xi})\mathrm{d}\boldsymbol{\xi} = 1$. Hence the equilibrium VDF becomes

$$f^{(0)} = \frac{\rho}{\theta^{D/2}} \, \omega\left(\frac{\boldsymbol{\xi} - \boldsymbol{u}}{\sqrt{\theta}}\right), \tag{B.2.6}$$

with $\theta = T/T_0$ the normalized temperature.

B.3   Hermite tensors and coefficients

In this work, Hermite polynomials up to the fourth order are sufficient to recover the physics of interest. Using Eqs. (B.2.4) and (B.2.5), they read as

$$\mathcal{H}^{(0)} = 1,$$

$$\mathcal{H}_{\alpha}^{(1)} = \xi_\alpha,$$

$$\mathcal{H}_{\alpha\beta}^{(2)} = \xi_{\alpha\beta} - rT_0\delta_{\alpha\beta},$$

$$\mathcal{H}_{\alpha\beta\gamma}^{(3)} = \xi_{\alpha\beta\gamma} - rT_0\left(\xi_\alpha\delta_{\beta\gamma} + \xi_\beta\delta_{\alpha\gamma} + \xi_\gamma\delta_{\alpha\beta}\right),$$

$$\mathcal{H}_{\alpha\beta\gamma\delta}^{(4)} = \xi_{\alpha\beta\gamma\delta} - rT_0\left(\xi_{\alpha\beta}\delta_{\gamma\delta} + \xi_{\alpha\gamma}\delta_{\beta\delta} + \xi_{\alpha\delta}\delta_{\beta\gamma} + \xi_{\beta\gamma}\delta_{\alpha\delta} + \xi_{\beta\delta}\delta_{\alpha\gamma} + \xi_{\gamma\delta}\delta_{\alpha\beta}\right)$$
$$+ (rT_0)^2\left(\delta_{\alpha\beta}\delta_{\gamma\delta} + \delta_{\alpha\gamma}\delta_{\beta\delta} + \delta_{\alpha\delta}\delta_{\beta\gamma}\right),$$

where $(\alpha, \beta, \gamma, \delta) \in \{x, y\}^4$ in 2D, and $\{x, y, z\}^4$ in 3D. Furthermore, Hermite polynomial coefficients $\boldsymbol{a}^{(n)}$ are defined by

$$\boldsymbol{a}^{(n)}(\boldsymbol{x}, t) = \int f(\boldsymbol{x}, \boldsymbol{\xi}, t) \boldsymbol{\mathcal{H}}^{(n)}(\boldsymbol{\xi}) \, \mathrm{d}\boldsymbol{\xi} \tag{B.3.1}$$

Considering the equilibrium VDF (B.2.6), Hermite polynomials coefficients are computed as follows

$$\begin{aligned}
\boldsymbol{a}_0^{(n)}(\boldsymbol{x}, t) &= \int f^{(0)}(\boldsymbol{x}, \boldsymbol{\xi}, t) \boldsymbol{\mathcal{H}}^{(n)}(\boldsymbol{\xi}) \, \mathrm{d}\boldsymbol{\xi}, \\
&= \int \frac{\rho}{\theta^{D/2}} \, \omega\left(\frac{\boldsymbol{\xi} - \boldsymbol{u}}{\sqrt{\theta}}\right) \boldsymbol{\mathcal{H}}^{(n)}(\boldsymbol{\xi}) \, \mathrm{d}\boldsymbol{\xi}, \\
&= \int \frac{\rho}{\theta^{D/2}} \, \omega(\boldsymbol{X}) \boldsymbol{\mathcal{H}}^{(n)}(\sqrt{\theta}\boldsymbol{X} + \boldsymbol{u}) \theta^{D/2} \, \mathrm{d}\boldsymbol{X}, \\
&= \rho \int \omega(\boldsymbol{X}) \boldsymbol{\mathcal{H}}^{(n)}(\sqrt{\theta}\boldsymbol{X} + \boldsymbol{u}) \, \mathrm{d}\boldsymbol{X}.
\end{aligned}$$

where the change of variable $\boldsymbol{X} = (\boldsymbol{\xi} - \boldsymbol{u})/\sqrt{\theta}$ has been used. Up to $n = 4$, equilibrium Hermite coefficients then read as

$$\begin{aligned}
a_0^{(0)} &= \rho, \\
a_{0,\alpha}^{(1)} &= \rho u_\alpha, \\
a_{0,\alpha\beta}^{(2)} &= \rho u_\alpha u_\beta + \rho r T_0 (\theta - 1) \delta_{\alpha\beta}, \\
a_{0,\alpha\beta\gamma}^{(3)} &= \rho u_\alpha u_\beta u_\gamma + \rho r T_0 (\theta - 1) \left(u_\alpha \delta_{\beta\gamma} + u_\beta \delta_{\alpha\gamma} + u_\gamma \delta_{\alpha\beta}\right), \\
a_{0,\alpha\beta\gamma\delta}^{(4)} &= \rho u_\alpha u_\beta u_\gamma u_\delta + \rho (r T_0)^2 (\theta - 1)^2 \left(\delta_{\alpha\beta}\delta_{\gamma\delta} + \delta_{\alpha\gamma}\delta_{\beta\delta} + \delta_{\alpha\delta}\delta_{\beta\gamma}\right) \\
&\quad + \rho r T_0 (\theta - 1) \left(u_\alpha u_\beta \delta_{\gamma\delta} + u_\alpha u_\gamma \delta_{\beta\delta} + u_\alpha u_\delta \delta_{\beta\gamma} + u_\beta u_\gamma \delta_{\alpha\delta} + u_\beta u_\delta \delta_{\alpha\gamma} + u_\gamma u_\delta \delta_{\alpha\beta}\right).
\end{aligned}$$

where Eq. (E.2.2) has been used to compute general Gaussian integrals. Eventually, the Hermite polynomial expansion of the equilibrium VDF is

$$f^{(0)}(\boldsymbol{x}, \boldsymbol{\xi}, t) = \omega(\boldsymbol{\xi}) \sum_{n=0}^{\infty} \frac{1}{n!(r T_0)^n} \boldsymbol{a}_0^{(n)}(\boldsymbol{x}, t) : \boldsymbol{\mathcal{H}}^{(n)}(\boldsymbol{\xi}). \tag{B.3.2}$$

All above formulas can readily be restricted to the isothermal case taking $\theta = 1$.

For readers who are accustomed to the Taylor expansion of the equilibrium VDF, more details regarding its link to the generative function of Hermite polynomials, and the reason why the Hermite polynomial expansion is preferred here, are given in Sec. B.5.

B.4   Taylor series expansion

Before moving to the presentation of the relationship between Taylor and Hermite polynomial expansion of the equilibrium VDF, let us recall some basic features about the Taylor expansion. Without loss of generality, the following mathematical derivation is restricted to $\mathbb{R}$.

The purpose of the Taylor series expansion is to approximate a given function $g \colon u \mapsto g(u)$ about a given point $u = u_0$ using polynomials. The way this series expansion is built flows from the following principle. If we need to approximate g at $u_0 = 0$ by another function $y \colon u \mapsto y(u)$, the most straightforward approximation would be the constant function $y \colon u \mapsto y(u) = g(0)$. But this approximation is quite far from accurately representing the expected behavior of g about $u = 0$. Hence, we can also impose that y and g share the same slope at $u = 0$. This leads to

$$y^{(1)}(0) = g^{(1)}(0),$$

so that after integrating $y^{(1)}$ we obtain

$$y(u) = g^{(1)}(0)u + A,$$

with A the integration constant whose values is obtained for $u = 0$, i.e, $A = y(0) = g(0)$. A further improvement would require the equality of the second derivatives:

$$y^{(2)}(0) = g^{(2)}(0).$$

By integrating two times, the new approximation of g about $u = 0$ is

$$y \colon u \mapsto y(u) = g(0) + g^{(1)}(0)u + g^{(1)}(0)\frac{u}{2}.$$

Continuing the previous protocol, we can require that

$$\forall l \le m, \ y^{(l)}(0) = g^{(l)}(0),$$

so that

$$y(u) = \sum_{l=0}^{m} g^{(l)}(0)\frac{u^l}{l!}.$$

Taking $n \to \infty$, we end up with the Taylor series expansion about 0 (or MacLaurin series) of g:

$$y(u) = \sum_{l=0}^{\infty} g^{(l)}(0)\frac{u^l}{l!}. \tag{B.4.1}$$

B.5   Link to the Hermite polynomial expansion

Let us start with the following function

$$f_H(\boldsymbol{\xi}, \boldsymbol{u}) = \exp\left(\frac{2\boldsymbol{u} \cdot \boldsymbol{\xi} - u^2}{2rT_0}\right). \tag{B.5.1}$$

To avoid any cumbersome algebra, the present derivation is restricted to the 1D case. The function $f_H(\xi, u)$ is 'sufficiently smooth' (has continuous derivatives of all orders for

both ξ and u) to be expanded in power series. The MacLaurin series in u of Eq. (B.5.1) reads as,

$$f_H(\xi, u) = \sum_{n=0}^{\infty} \frac{f_H^{(n)}(\xi, 0)}{n!} \frac{u^n}{(2rT_0)^n}, \qquad (B.5.2)$$

with $f_H^{(n)}(\xi, u)$ the nth partial derivative of f_H with respect to u. Starting from

$$f_H^{(n)}(\xi, 0) = \frac{\partial^{(n)}}{\partial u} \left[\exp\left(\frac{2\boldsymbol{u} \cdot \boldsymbol{\xi} - u^2}{2rT_0} \right) \right]\Bigg|_{u=0},$$

$$= \exp\left(\frac{\xi^2}{2rT_0} \right) \frac{\partial^{(n)}}{\partial u} \left[\exp\left(-\frac{(\xi - u)^2}{2rT_0} \right) \right]\Bigg|_{u=0},$$

the change of variable $X = (\xi - u)/\sqrt{2rT_0}$ leads to

$$f_H^{(n)}(\xi, 0) = \exp\left(\frac{\xi^2}{2rT_0} \right) (-2rT_0)^{n/2} \frac{\partial^{(n)}}{\partial X} \left[\exp\left(-X^2 \right) \right]\Bigg|_{X=\xi/2rT_0},$$

since $\partial_X = -\sqrt{2rT_0}\partial_u$. This then reads as

$$f_H^{(n)}(\xi, 0) = \exp\left(\frac{\xi^2}{2rT_0} \right) (-2rT_0)^n \frac{\partial^{(n)}}{\partial \xi} \left[\exp\left(-\frac{\xi^2}{2rT_0} \right) \right],$$

$$= 2^n \frac{(-rT_0)^n}{\omega(\xi)} \frac{\partial^{(n)}}{\partial \xi} \omega(\xi),$$

$$= 2^n \mathcal{H}^{(n)}(\xi), \qquad (B.5.3)$$

using the 1D versions of the Gaussian weight ω (B.2.5) and Hermite polynomials (B.2.4). Injecting Eq. (B.5.3) in Eq. (B.5.2) finally leads to

$$f_H(\xi, u) = \sum_{n=0}^{\infty} \frac{1}{n!(rT_0)^n} \mathcal{H}^{(n)}(\xi) u^n. \qquad (B.5.4)$$

Hence f_H is the generative function of Hermite polynomials. Assuming Eq. (B.5.4) is valid for $\mathbb{R}^D$, and considering the *isothermal* equilibrium VDF, we end up with

$$f^{(0)} = \frac{\rho}{(2\pi rT_0)^{D/2}} \exp\left[\frac{(\boldsymbol{\xi} - \boldsymbol{u})^2}{2rT_0} \right],$$

$$= \rho\omega(\boldsymbol{\xi}) f_H(\boldsymbol{\xi}, \boldsymbol{u}),$$

$$= \omega(\boldsymbol{\xi}) \sum_{n=0}^{\infty} \frac{1}{n!(rT_0)^n} \boldsymbol{\mathcal{H}}^{(n)}(\xi) : \boldsymbol{a}_0^{(n)},$$

where the definition of Hermite coefficients at equilibrium $\boldsymbol{a}_0^{(n)} = \rho\boldsymbol{u}^n$ has been used (its derivation is given in Sec. F.2). Thus, both Taylor and Hermite polynomial expansions of the equilibrium VDF are equivalent in the *isothermal* case. Nevertheless, deviations have been noticed for the more general thermal equilibrium VDF [116]. This is one of the reason why the Hermite polynomial expansion is preferred in the present work.

B.6   Rodrigues' formula

This recursive formula is based on the following computation

$$\frac{\partial \mathcal{H}_{\alpha_1 \ldots \alpha_n}^{(n)}}{\partial \xi_{\alpha_{n+1}}} = (rT_0)^n \left[\frac{\xi_{\alpha_{n+1}}}{rT_0} \frac{1}{\omega(\boldsymbol{\xi})} \boldsymbol{\nabla}_{\xi}^n \omega(\boldsymbol{\xi}) + \frac{1}{\omega(\boldsymbol{\xi})} \boldsymbol{\nabla}_{\xi}^{n+1} \omega(\boldsymbol{\xi}) \right],$$

$$= \frac{1}{rT_0} \left(\xi_{\alpha_{n+1}} \mathcal{H}_{\alpha_1 \ldots \alpha_n}^{(n)} - \mathcal{H}_{\alpha_1 \ldots \alpha_n \alpha_{n+1}}^{(n+1)} \right), \tag{B.6.1}$$

and on the expression below [103]

$$\frac{\partial \mathcal{H}_{\alpha_1 \ldots \alpha_n}^{(n)}}{\partial \xi_{\alpha_{n+1}}} = \sum_{j=1}^{n} \delta_{\alpha_i \alpha_{n+1}} \mathcal{H}_{\alpha_1 \ldots \alpha_{i-1} \alpha_{i+1} \ldots \alpha_n}^{(n-1)}. \tag{B.6.2}$$

Hence combining Eqs. (B.6.1) and (B.6.2) leads to the multivariate version of Rodrigues' formula:

$$\xi_{\alpha_{n+1}} \mathcal{H}_{\alpha_1 \ldots \alpha_n}^{(n)} = \mathcal{H}_{\alpha_1 \ldots \alpha_n \alpha_{n+1}}^{(n+1)} + rT_0 \sum_{j=1}^{n} \delta_{\alpha_j \alpha_{n+1}} \mathcal{H}_{\alpha_1 \ldots \alpha_{j-1} \alpha_{j+1} \ldots \alpha_n}^{(n-1)}. \tag{B.6.3}$$

The latter will be used in App. F for the derivation of recursive formulas ($\boldsymbol{a}_0^{(n)}$ and $\boldsymbol{a}_1^{(n)}$).

B.7   Orthogonality properties

Hermite polynomials (B.2.4) form an orthogonal basis with respect to the weighted scalar product (using the Gaussian weight (B.2.5)) [103]

$$\left\langle \mathcal{H}_{\alpha_1 \ldots \alpha_n}^{(n)} | \mathcal{H}_{\beta_1 \ldots \beta_m}^{(m)} \right\rangle \equiv \int \omega \mathcal{H}_{\alpha_1 \ldots \alpha_n}^{(n)} \mathcal{H}_{\beta_1 \ldots \beta_m}^{(m)} \mathrm{d}\boldsymbol{\xi} = (rT_0)^n \delta_{nm} (\delta_{\alpha_1 \beta_1} \ldots \delta_{\alpha_n \beta_m} + \mathrm{perm}). \tag{B.7.1}$$

Here, perm corresponds to cyclic permutation of indexes α_i inside $\boldsymbol{\alpha} = (\alpha_1, \ldots, \alpha_n)$, and β_j inside $\boldsymbol{\beta} = (\beta_1, \ldots, \beta_m)$. As an example, let us take the particular case of $n = m = 3$. The RHS of Eq. (B.7.1) then reduces to

$$(rT_0)^3 (\delta_{\alpha_1 \beta_1} \delta_{\alpha_2 \beta_2} \delta_{\alpha_3 \beta_3} + \delta_{\alpha_1 \beta_1} \delta_{\alpha_2 \beta_3} \delta_{\alpha_3 \beta_2}$$

$$+ \delta_{\alpha_1 \beta_2} \delta_{\alpha_2 \beta_1} \delta_{\alpha_3 \beta_3} + \delta_{\alpha_1 \beta_2} \delta_{\alpha_2 \beta_3} \delta_{\alpha_3 \beta_1}$$

$$+ \delta_{\alpha_1 \beta_3} \delta_{\alpha_2 \beta_2} \delta_{\alpha_3 \beta_1} + \delta_{\alpha_1 \beta_3} \delta_{\alpha_2 \beta_1} \delta_{\alpha_3 \beta_2}),$$

and

$$\mathrm{perm} = \delta_{\alpha_1 \beta_1} \delta_{\alpha_2 \beta_3} \delta_{\alpha_3 \beta_2} + \delta_{\alpha_1 \beta_2} \delta_{\alpha_2 \beta_1} \delta_{\alpha_3 \beta_3} + \delta_{\alpha_1 \beta_2} \delta_{\alpha_2 \beta_3} \delta_{\alpha_3 \beta_1} + \delta_{\alpha_1 \beta_3} \delta_{\alpha_2 \beta_1} \delta_{\alpha_3 \beta_2} + \delta_{\alpha_1 \beta_3} \delta_{\alpha_2 \beta_2} \delta_{\alpha_3 \beta_1}.$$

B.8   Discrete case

The numerical discretization of the LBE is linked to the lattice constant c_s, the latter being used to impose the on-lattice condition during the velocity discretization [119]. This constant can further be related to the isothermal speed of sound

through $\sqrt{rT_0} = c_s \Delta x / \Delta t$ [121]. For the 'Collide & Stream' algorithm, lattice units $(\Delta x = \Delta t = 1)$ are employed, hence previous formulas now become:

Hermite polynomials

$$\boldsymbol{\mathcal{H}}_i^{(n)} = \frac{(-c_s^2)^n}{\omega(\boldsymbol{\xi}_i)} \boldsymbol{\nabla}_{\boldsymbol{\xi}_i}^n \omega(\boldsymbol{\xi}_i), \tag{B.8.1}$$

leading to

$$\mathcal{H}_i^{(0)} = 1,$$
$$\mathcal{H}_{i,\alpha}^{(1)} = \xi_{i,\alpha},$$
$$\mathcal{H}_{i,\alpha\beta}^{(2)} = \xi_{i,\alpha\beta} - c_s^2 \delta_{\alpha\beta},$$
$$\mathcal{H}_{i,\alpha\beta\gamma}^{(3)} = \xi_{i,\alpha\beta\gamma} - c_s^2 \left(\xi_{i,\alpha}\delta_{\beta\gamma} + \xi_{i,\beta}\delta_{\alpha\gamma} + \xi_{i,\gamma}\delta_{\alpha\beta} \right),$$
$$\mathcal{H}_{i,\alpha\beta\gamma\delta}^{(4)} = \xi_{i,\alpha\beta\gamma\delta} - c_s^2 \left(\xi_{i,\alpha\beta}\delta_{\gamma\delta} + \xi_{i,\alpha\gamma}\delta_{\beta\delta} + \xi_{i,\alpha\delta}\delta_{\beta\gamma} + \xi_{i,\beta\gamma}\delta_{\alpha\delta} + \xi_{i,\beta\delta}\delta_{\alpha\gamma} + \xi_{i,\gamma\delta}\delta_{\alpha\beta} \right)$$
$$\qquad + c_s^4 \left(\delta_{\alpha\beta}\delta_{\gamma\delta} + \delta_{\alpha\gamma}\delta_{\beta\delta} + \delta_{\alpha\delta}\delta_{\beta\gamma} \right),$$

Hermite polynomial coefficients

$$\boldsymbol{a}^{(n)}(\boldsymbol{x},t) = \sum_i f_i(\boldsymbol{x},\boldsymbol{\xi}_i,t) \boldsymbol{\mathcal{H}}_i^{(n)}(\boldsymbol{\xi}_i), \tag{B.8.2}$$

which gives for the equilibrium VDF

$$a_0^{(0)} = \rho,$$
$$a_{0,\alpha}^{(1)} = \rho u_\alpha,$$
$$a_{0,\alpha\beta}^{(2)} = \rho u_\alpha u_\beta + \rho c_s^2(\theta - 1)\delta_{\alpha\beta},$$
$$a_{0,\alpha\beta\gamma}^{(3)} = \rho u_\alpha u_\beta u_\gamma + \rho c_s^2(\theta - 1) \left(u_\alpha \delta_{\beta\gamma} + u_\beta \delta_{\alpha\gamma} + u_\gamma \delta_{\alpha\beta} \right),$$
$$a_{0,\alpha\beta\gamma\delta}^{(4)} = \rho u_\alpha u_\beta u_\gamma u_\delta + \rho c_s^4(\theta - 1)^2 \left(\delta_{\alpha\beta}\delta_{\gamma\delta} + \delta_{\alpha\gamma}\delta_{\beta\delta} + \delta_{\alpha\delta}\delta_{\beta\gamma} \right)$$
$$\qquad + \rho c_s^2(\theta - 1) \left(u_\alpha u_\beta \delta_{\gamma\delta} + u_\alpha u_\gamma \delta_{\beta\delta} + u_\alpha u_\delta \delta_{\beta\gamma} + u_\beta u_\gamma \delta_{\alpha\delta} + u_\beta u_\delta \delta_{\alpha\gamma} + u_\gamma u_\delta \delta_{\alpha\beta} \right),$$

Hermite series of the VDF

$$f_i = \omega_i \sum_{n=0}^{\infty} \frac{1}{n!(c_s^2)^n} \boldsymbol{a}^{(n)} : \boldsymbol{\mathcal{H}}_i^{(n)}, \tag{B.8.3}$$

Gaussian weight

$$\omega(\boldsymbol{\xi}_i) = \frac{1}{(2\pi c_s^2)^{D/2}} \exp\left(-\frac{\xi_i^2}{2c_s^2} \right), \tag{B.8.4}$$

Inner product

$$\langle g|h \rangle = \sum_i \omega_i \, g(\boldsymbol{\xi}_i) \, h(\boldsymbol{\xi}_i), \tag{B.8.5}$$

Orthogonality properties

$$\left\langle \mathcal{H}_{i,\alpha_1\ldots\alpha_n}^{(n)} | \mathcal{H}_{i,\beta_1\ldots\beta_m}^{(m)} \right\rangle = \sum_i \omega_i \mathcal{H}_{i,\alpha_1\ldots\alpha_n}^{(n)} \mathcal{H}_{i,\beta_1\ldots\beta_m}^{(m)} = (c_s^2)^n \delta_{nm} (\delta_{\alpha_1\beta_1} \ldots \delta_{\alpha_n\beta_m} + \text{perm}), \tag{B.8.6}$$

Rodrigues' formula

$$\xi_{i,\alpha_{n+1}} \mathcal{H}^{(n)}_{i,\alpha_1\ldots\alpha_n} = \mathcal{H}^{(n+1)}_{i,\alpha_1\ldots\alpha_n\alpha_{n+1}} + c_s^2 \sum_{j=1}^{n} \delta_{\alpha_j\alpha_{n+1}} \mathcal{H}^{(n-1)}_{i,\alpha_1\ldots\alpha_{j-1}\alpha_{j+1}\ldots\alpha_n}. \qquad (B.8.7)$$

Appendix C

Chapman-Enskog

This appendix aims at providing all the details regarding the macroscopic behavior of most common LBMs. With this idea in mind, the Chapman-Enskog (CE) expansion of single distribution function (SDF) and double distribution function (DDF) LBMs is conducted, and the associated macroscopic behaviors are determined. Limitations of each approach are highlighted, and corresponding solutions are proposed to recover the physics of interest.

C.1   Single distribution function approach

In what follows, the case of LBMs based on the evolution of a single velocity distribution function (VDF) is considered, and its macroscopic behavior is first recovered for the particular case of the LBM-BGK.

   The multiscale analysis of the Boltzmann equation is done, at the Navier-Stokes level, assuming that $f = f^{(0)} + f^{(1)} + \mathcal{O}(\epsilon^2)$ with $f^{(0)} \sim \mathcal{O}(1)$, $f^{(1)} \sim \mathcal{O}(\epsilon)$ and $\tau = \mu/p \sim \mathcal{O}(\epsilon)$, with ϵ proportional to the Knudsen number. This means that in the continuum limit $(\epsilon \ll 1)$, $f^{(0)} + f^{(1)} \sim f^{(0)}$. Under this assumption, the BE becomes

$$\partial_t f^{(0)} + \boldsymbol{\xi} \cdot \boldsymbol{\nabla} f^{(0)} = -\frac{1}{\tau}(f^{(1)}). \qquad (C.1.1)$$

To go further, the statistical moments of both $f^{(0)}$ and $f^{(1)}$ are required. Their formula are given as follows

$$\int f^{(0)} \mathrm{d}\boldsymbol{\xi} = \rho, \qquad\qquad \int f^{(1)} \mathrm{d}\boldsymbol{\xi} = 0,$$

$$\int \xi_\alpha f^{(0)} \mathrm{d}\boldsymbol{\xi} = \rho u_\alpha, \qquad\qquad \int \xi_\alpha f^{(1)} \mathrm{d}\boldsymbol{\xi} = 0,$$

$$\int \xi_\alpha \xi_\beta f^{(0)} \mathrm{d}\boldsymbol{\xi} = \Pi^{(0)}_{\alpha\beta}, \qquad\qquad \int \xi_\alpha \xi_\beta f^{(1)} \mathrm{d}\boldsymbol{\xi} = \Pi^{(1)}_{\alpha\beta}, \qquad (C.1.2)$$

$$\int \xi_\alpha \xi_\beta \xi_\gamma f^{(0)} \mathrm{d}\boldsymbol{\xi} = Q^{(0)}_{\alpha\beta\gamma}, \qquad\qquad \int \xi_\alpha \xi_\beta \xi_\gamma f^{(1)} \mathrm{d}\boldsymbol{\xi} = Q^{(1)}_{\alpha\beta\gamma},$$

$$\int \xi_\alpha \xi_\beta \xi_\gamma \xi_\delta f^{(0)} \mathrm{d}\boldsymbol{\xi} = R^{(0)}_{\alpha\beta\gamma\delta}, \qquad\qquad \int \xi_\alpha \xi_\beta \xi_\gamma \xi_\delta f^{(1)} \mathrm{d}\boldsymbol{\xi} = R^{(1)}_{\alpha\beta\gamma\delta},$$

where

$$
\Pi_{\alpha\beta}^{(0)} = \rho u_\alpha u_\beta + p\delta_{\alpha\beta}, \; \Pi_{\alpha\beta}^{(1)} = -\tau \left[\partial_t \Pi_{\alpha\beta}^{(0)} + \partial_\gamma Q_{\alpha\beta\gamma}^{(0)} \right],
$$
$$
Q_{\alpha\beta\gamma}^{(0)} = \rho u_\alpha u_\beta u_\gamma + p \left[u_\alpha \delta_{\beta\gamma} + u_\beta \delta_{\alpha\gamma} + u_\gamma \delta_{\alpha\beta} \right], \; Q_{\alpha\beta\gamma}^{(1)} = -\tau \left[\partial_t Q_{\alpha\beta\gamma}^{(0)} + \partial_\delta R_{\alpha\beta\gamma\delta}^{(0)} \right], \tag{C.1.3}
$$

and

$$
R_{\alpha\beta\gamma\delta}^{(0)} = \rho u_\alpha u_\beta u_\gamma u_\delta + p(u_\alpha u_\beta \delta_{\gamma\delta} + u_\alpha u_\gamma \delta_{\beta\delta} + u_\alpha u_\delta \delta_{\beta\gamma} + u_\beta u_\gamma \delta_{\alpha\delta} + u_\beta u_\delta \delta_{\alpha\gamma} + u_\gamma u_\delta \delta_{\alpha\beta})
$$
$$
+ prT(\delta_{\alpha\beta}\delta_{\gamma\delta} + \delta_{\alpha\gamma}\delta_{\beta\delta} + \delta_{\alpha\delta}\delta_{\beta\gamma}), \tag{C.1.4}
$$

with half of its contracted form, or trace, being

$$
r_{\alpha\beta}^{(0)} = \frac{1}{2} R_{\alpha\beta\gamma\gamma}^{(0)} = [\rho E + 2p]u_\alpha u_\beta + p[rT + E]\delta_{\alpha\beta}. \tag{C.1.5}
$$

Eventually, the zeroth, first and second (half of the trace) moments of Eq. (C.1.1) leads to the following set of macroscopic equations:

$$
\begin{cases}
\partial_t(\rho) + \partial_\beta(\rho u_\beta) = 0, \\[4pt]
\partial_t(\rho u_\alpha) + \partial_\beta(\rho u_\alpha \rho u_\beta + p\delta_{\alpha\beta}) = -\partial_\beta(\Pi_{\alpha\beta}^{(1)}), \\[4pt]
\partial_t(\rho E) + \partial_\beta([\rho E + p]\, u_\beta) = -\partial_\beta(q_\beta^{(1)}),
\end{cases} \tag{C.1.6}
$$

where the RHS terms belong to the Navier-Stokes level (nonequilibrium state $f^{(1)}$), whereas the LHS terms are already encountered at the Euler level (equilibrium state $f^{(0)}$).

This system of equations needs to be closed. To do so, nonequilibrium parts of the momentum flux $\Pi_{\alpha\beta}^{(1)}$ and the energy flux $q_\beta^{(1)}$ remain to be computed. Starting from Eq. (C.1.3) and using Eq. (C.1.2), we obtain

$$
\Pi_{\alpha\beta}^{(1)} = -\tau \left[\partial_t \Pi_{\alpha\beta}^{(0)} + \partial_\gamma Q_{\alpha\beta\gamma}^{(0)} \right]
$$
$$
= -\tau \left[\partial_t(\rho u_\alpha u_\beta + p\delta_{\alpha\beta}) + \partial_\gamma(\rho u_\alpha u_\beta u_\gamma + p\left[u_\alpha \delta_{\beta\gamma} + u_\beta \delta_{\alpha\gamma} + u_\gamma \delta_{\alpha\beta} \right]) \right], \tag{C.1.7}
$$
$$
q_\beta^{(1)} = -\tau \left[\partial_t q_\beta^{(0)} + \partial_\gamma r_{\beta\gamma}^{(0)} \right]
$$
$$
= -\tau \left[\partial_t([\rho E + p]u_\beta) + \partial_\gamma([\rho E + 2p]u_\beta u_\gamma + p[rT + E]\delta_{\beta\gamma}) \right]. \tag{C.1.8}
$$

To properly complete the computation of these nonequilibrium parts, we just need to get ride of all the ∂_t terms. Since the RHS terms of Eqs. (C.1.7) and (C.1.8) are linked to moments of $f^{(0)}$, the following Euler level macroscopic equations can then be used to further complete the computation of $\Pi_{\alpha\beta}^{(1)}$ and $q_\beta^{(1)}$:

$$
\Pi_{\alpha\beta}^{(1)} \quad \Bigg| \quad
\begin{aligned}
\partial_t(\rho u_\alpha u_\beta) + \partial_\gamma(\rho u_\alpha u_\beta u_\gamma) &= -u_\alpha \partial_\beta p - u_\beta \partial_\alpha p, \\[6pt]
\partial_t(p) + \partial_\gamma(p u_\gamma) &= -\frac{2}{D} p \partial_\gamma u_\gamma,
\end{aligned} \tag{C.1.9}
$$

and

$$q_\beta^{(1)} \left| \begin{array}{l} \partial_t(pu_\beta) + \partial_\gamma(pu_\beta u_\gamma) = -\dfrac{2}{D}pu_\beta\partial_\delta u_\delta - rT\partial_\beta p, \\[2mm] \partial_t(\rho E u_\beta) + \partial_\gamma([\rho E + p]\, u_\beta u_\gamma) = -E\partial_\beta p + pu_\gamma\partial_\gamma u_\beta. \end{array} \right. \tag{C.1.10}$$

This leads to

$$\begin{aligned} \Pi_{\alpha\beta}^{(1)} &= -\tau \left[\left[\partial_t(\rho u_\alpha u_\beta) + \partial_\gamma(\rho u_\alpha u_\beta u_\gamma) + \partial_\alpha(pu_\beta) + \partial_\beta(pu_\alpha) \right] + \left[\partial_t p + \partial_\gamma(pu_\gamma) \right] \delta_{\alpha\beta} \right] \\ &= -\tau \left[p\left(\partial_\alpha u_\beta + \partial_\beta u_\alpha\right) - p\left(\frac{2}{D}\partial_\gamma u_\gamma\right)\delta_{\alpha\beta} \right] \\ &= -\tau p \left[S_{\alpha\beta} - \left(\frac{2}{D}\partial_\gamma u_\gamma\right)\delta_{\alpha\beta} \right], \end{aligned} \tag{C.1.11}$$

and

$$\begin{aligned} q_\beta^{(1)} &= -\tau \left[\partial_t([\rho E + p]u_\beta) + \partial_\gamma([\rho E + 2p]u_\beta u_\gamma + p[rT + E]\delta_{\beta\gamma}) \right] \\ &= -\tau \left[\left[\partial_t(\rho E u_\beta) + \partial_\gamma([\rho E + p]u_\beta u_\gamma + pE\delta_{\beta\gamma}) \right] + \left[\partial_t(pu_\beta) + \partial_\gamma(pu_\beta u_\gamma + prT\delta_{\beta\gamma}) \right] \right] \\ &= -\tau \left[p\left[u_\gamma\partial_\gamma u_\beta + \partial_\beta E\right] + p\left[-\frac{2}{D}(u_\gamma\delta_{\beta\gamma})\partial_\delta u_\delta + \partial_\beta(rT) \right] \right] \\ &= -\tau p \left[r(1 + \frac{D}{2})\partial_\beta T + \left[\partial_\beta\left(\frac{u_\gamma^2}{2}\right) - u_\gamma\partial_\beta u_\gamma + u_\gamma\left[\partial_\beta u_\gamma + \partial_\gamma u_\beta\right] - u_\gamma\left(\frac{2}{D}\partial_\delta u_\delta\right)\delta_{\beta\gamma} \right] \right] \\ &= -\tau p \left[c_p\partial_\beta T \right] + u_\gamma\Pi_{\beta\gamma}^{(1)}. \end{aligned} \tag{C.1.12}$$

Finally, the set of macroscopic equations, recovered from the LBE through the CE expansion at the Navier-Stokes level, is:

$$\begin{aligned} &\partial_t(\rho) + \partial_\beta\left(\rho u_\beta\right) = 0, \\ &\partial_t(\rho u_\alpha) + \partial_\beta\left(\rho u_\alpha u_\beta + p\delta_{\alpha\beta}\right) = \partial_\beta(\sigma_{\alpha\beta}), \\ &\partial_t(\rho E) + \partial_\beta\left(\rho E u_\beta\right) = \partial_\beta\left(\lambda'\partial_\beta T\right) + \partial_\beta\left(u_\gamma\sigma_{\beta\gamma}\right), \end{aligned} \tag{C.1.13}$$

with $\mu = \tau p$, $\lambda' = \tau p c_p$ and $\boldsymbol{\sigma} = -\mu\boldsymbol{\Pi}^{(1)} - p\boldsymbol{\delta} = \mu\left(\boldsymbol{S} - (\frac{2}{D}\partial_\gamma u_\gamma)\boldsymbol{\delta}\right) - p\boldsymbol{\delta}$ are respectively the dynamic viscosity, the thermal conductivity and the stress tensor of the SDF model.

Before continuing, some remarks should be taken into account:

- Using only one relaxation time τ to describe both aerodynamic and thermal relaxations towards the thermodynamic equilibrium $f^{(0)}$ is irrelevant, and leads to $\lambda' = \mu c_p$, i.e, $Pr = 1$. The same comment can be made regarding the bulk viscosity μ_b which is null here.

- The Prandtl number restriction can be dealt with using either Shakhov's collision operator [164] or the ellipsoidal statistical BGK (ES-BGK [165, 166]) model, which

are directly linked to the more recent quasi-equilibrium approach [167]. A DDF-LBM could also be used to deal with this limitation [116, 168, 169]. Regarding the bulk viscosity limitation, one can carefully modify the equilibrium state [118, 170]. Finally, MRT-like collision models can be used to tackle both restrictions [30, 115].

- Besides being the number of space dimensions, D is also the number of degrees of freedom (DoFs) of the gas molecules since $2E = 2e + u^2$ with $2e = DrT$. Thus, only translations in the D directions of the physical space are allowed for gas molecules. This means that the recovered set of macroscopic equations is restricted to the description of monatomic gas behavior only. For diatomic gas molecules, rotational DoFs need to be accounted for. One can do this using either a double distribution approach [116], a modified speed of sound [121] or a MRT approach [128].

The above remarks are mainly linked to the use of a SDF with its associated BGK collision operator. A DDF approach will now be considered with the purpose of decoupling aerodynamic and thermal relaxation processes.

C.2 Double distribution function approach

As a first attempt to construct a total energy based LBM using two equations, one can start with the work of He *et al.* [168]. They proposed a set of two Boltzmann equations in order to recover the proper behavior, with respect to both aerodynamic and thermal relaxation processes, using two BGK collision operators:

$$
\begin{aligned}
\partial_t f + \boldsymbol{\xi} \cdot \boldsymbol{\nabla} f &= -\frac{1}{\tau_f}(f - f^{(0)}), \\
\partial_t h + \boldsymbol{\xi} \cdot \boldsymbol{\nabla} h &= -\frac{1}{\tau_h}(h - h^{(0)}),
\end{aligned}
\tag{C.2.1}
$$

with $h = \frac{1}{2}\xi^2 f$. The evolution of the density and the total energy distributions of particles in the velocity space are described by f and h respectively, τ_f and τ_h being their associated relaxation time. Furthermore, their corresponding statistical moments are

$$
\begin{aligned}
\int f^{(0)} \mathrm{d}\boldsymbol{\xi} &= \rho, & \int f^{(1)} \mathrm{d}\boldsymbol{\xi} &= 0, \\
\int \xi_\alpha f^{(0)} \mathrm{d}\boldsymbol{\xi} &= \rho u_\alpha, & \int \xi_\alpha f^{(1)} \mathrm{d}\boldsymbol{\xi} &= 0, \\
\int \xi_\alpha \xi_\beta f^{(0)} \mathrm{d}\boldsymbol{\xi} &= \Pi^{(0)}_{\alpha\beta}, & \int \xi_\alpha \xi_\beta f^{(1)} \mathrm{d}\boldsymbol{\xi} &= \Pi^{(1)}_{\alpha\beta}, \\
\int \xi_\alpha \xi_\beta \xi_\gamma f^{(0)} \mathrm{d}\boldsymbol{\xi} &= Q^{(0)}_{\alpha\beta\gamma}, & \int \xi_\alpha \xi_\beta \xi_\gamma f^{(1)} \mathrm{d}\boldsymbol{\xi} &= Q^{(1)}_{\alpha\beta\gamma},
\end{aligned}
\tag{C.2.2}
$$

and

$$\int h^{(0)}\mathrm{d}\boldsymbol{\xi} = \rho E, \qquad\qquad \int h^{(1)}\mathrm{d}\boldsymbol{\xi} = 0,$$

$$\int \xi_\alpha h^{(0)}\mathrm{d}\boldsymbol{\xi} = \Psi_\alpha^{(0)}, \qquad\qquad \int \xi_\alpha h^{(1)}\mathrm{d}\boldsymbol{\xi} = \Psi_\alpha^{(1)}, \qquad (C.2.3)$$

$$\int \xi_\alpha \xi_\beta h^{(0)}\mathrm{d}\boldsymbol{\xi} = \Gamma_{\alpha\beta}^{(0)},$$

with $\Pi_{\alpha\beta}^{(0)}$, $\Pi_{\alpha\beta}^{(1)}$, $Q_{\alpha\beta\gamma}^{(0)}$ and $Q_{\alpha\beta\gamma}^{(1)}$ defined in Eq. (C.1.3) and

$$\Psi_\alpha^{(0)} = (\rho E + p)u_\alpha, \quad \Psi_\alpha^{(1)} = -\tau_h \left[\partial_t \Psi_\alpha^{(0)} + \partial_\gamma \Gamma_{\alpha\gamma}^{(0)} \right],$$

$$\Gamma_{\alpha\beta}^{(0)} = [\rho E + 2p]u_\alpha u_\beta + p[rT + E]\delta_{\alpha\beta}. \qquad (C.2.4)$$

More specifically, the proper recovery of macroscopic equations, up to the Navier-Stokes momentum equation, requires the computation of the statistical moments of f up to $Q_{\alpha\beta\gamma}^{(0)}$ (calculation of $\Pi_{\alpha\beta}^{(1)}$). Moreover, the analogy between f and h allows to predict that the calculation of the statistical moments of h up to $\Gamma_{\alpha\beta}^{(0)}$ is sufficient to derive the proper energy equation at the Navier-Stokes level, since the latter is linked to the contracted-fourth-order statistical moment of $f^{(0)}$ as follows:

$$\Gamma_{\alpha\beta}^{(0)} = r_{\alpha\beta}^{(0)} = \frac{1}{2}R_{\alpha\beta\gamma\gamma}^{(0)} = \int \xi_\alpha \xi_\beta \frac{\xi_\gamma^2}{2} f^{(0)}\mathrm{d}\boldsymbol{\xi}. \qquad (C.2.5)$$

Hence, the macroscopic equations, recovered by Eq. (C.2.1) in the continuum limit ($\epsilon \ll 1$) and with the Navier-Stokes level of the CE expansion, are

$$\partial_t(\rho) + \partial_\beta (\rho u_\beta) = 0,$$

$$\partial_t(\rho u_\alpha) + \partial_\beta (\rho u_\alpha u_\beta + p\delta_{\alpha\beta}) = \partial_\beta(\sigma_{\alpha\beta}), \qquad (C.2.6)$$

$$\partial_t(\rho E) + \partial_\beta (\rho E u_\beta) = \partial_\beta (\lambda \partial_\beta T) + \partial_\beta \left(u_\gamma \sigma'_{\beta\gamma} \right),$$

with $\mu = \tau_f p$, $\lambda = \tau_h p c_p$ and $\boldsymbol{\sigma}' = -\frac{\lambda}{c_p}\boldsymbol{\Pi}^{(1)} - p\boldsymbol{\delta} = \frac{\lambda}{c_p}\left(\boldsymbol{S} - (\frac{2}{D}\partial_\gamma u_\gamma)\boldsymbol{\delta} \right) - p\boldsymbol{\delta}$ being respectively the dynamic viscosity, the thermal conductivity and the stress tensor of the DDF model.

In contrast to the SDF model, the double relaxation process allows to properly model the heat diffusion in the total energy equation. Nevertheless, $\Psi_\alpha^{(1)}$ is computed through the thermal relaxation process (τ_h) instead of the isothermal one (τ_f). This introduces a new error in the viscous heat dissipation term:

$$\boldsymbol{\sigma}' - p\boldsymbol{\delta} = \frac{\tau_h}{\tau_f}(\boldsymbol{\sigma}' - p\boldsymbol{\delta}) \qquad \text{with} \qquad \frac{\tau_h}{\tau_f} = \frac{1}{Pr}. \qquad (C.2.7)$$

C.3 Correct viscous heat diffusion: Guo's model

The total energy based DDF model introduced previously encounters a limitation regarding the viscous heat dissipation. This is due to an ill-posed collision term Ω_h. Indeed,

Ω_h is linked to the rate of change, induced by collisions, of the total energy distribution function h. Thus, this collision term should include two contributions:

$$\Omega_h = \Omega_i + \Omega_m \qquad \text{with} \qquad \begin{cases} \Omega_i & : \text{internal energy part} \\ \Omega_m & : \text{mechanical energy part} \end{cases} \tag{C.3.1}$$

The mechanical energy collision operator can be evaluated as follows:

$$\Omega_m = \left(\frac{\xi^2}{2} - \frac{(\boldsymbol{\xi} - \boldsymbol{u})^2}{2} \right) \Omega' \equiv Z\Omega'. \tag{C.3.2}$$

From Woods' theory [171], one may infer that Ω' and Ω_f have the same time scale. Hence, the following BGK approximation can be used

$$\Omega_m = -\frac{Z}{\tau_f}(f - f^{(0)}). \tag{C.3.3}$$

Regarding now Ω_i, the HCD (He-Chen-Doolen) model [168] could be used. But, this would introduce a new variable in the process (the internal energy distribution function). To avoid this difficulty, the substitution "$h - Zf$" was proposed by Guo *et al.* [116], which leads to:

$$\Omega_i = -\frac{1}{\tau_h} \left[\left(h - h^{(0)} \right) - Z \left(f - f^{(0)} \right) \right], \tag{C.3.4}$$

where now τ_h is the timescale related to the internal energy relaxation process.

Finally, Guo's model reads the following expression for the Boltzmann equation related to the total energy distribution function h:

$$\partial_t h + \boldsymbol{\xi} \cdot \boldsymbol{\nabla} h = -\frac{1}{\tau_h}(h - h^{(0)}) + \frac{Z}{\tau_{hf}}(f - f^{(0)}) \quad \text{with} \quad \begin{cases} \dfrac{1}{\tau_{hf}} = \dfrac{1}{\tau_h} - \dfrac{1}{\tau_f} \\ Z = \boldsymbol{\xi} \cdot \boldsymbol{u} - u^2/2 \end{cases} \tag{C.3.5}$$

The calculation of the statistical moments of the RHS of Eq. (C.3.5) results now in

$$\int \Omega_h \mathrm{d}\boldsymbol{\xi} = \int -\frac{1}{\tau_h} h^{(1)} + \frac{\xi_\gamma u_\gamma - u^2/2}{\tau_{hf}} f^{(1)} \mathrm{d}\boldsymbol{\xi} = -\frac{1}{\tau_h} \times 0 + \frac{1}{\tau_{hf}}(0 \times u_\gamma - 0 \times u^2/2) = 0,$$

$$\int \xi_\alpha \Omega_h \mathrm{d}\boldsymbol{\xi} = -\frac{1}{\tau_h} \Psi_\alpha^{(1)} + \frac{1}{\tau_{hf}}(\Pi_{\alpha\gamma}^{(1)} u_\gamma - 0 \times u^2/2) = p\left[c_p \partial_\alpha T \right] + p\frac{\tau_f}{\tau_h}(S_{\alpha\gamma} - (\tfrac{2}{D}\partial_\delta u_\beta)\delta_{\alpha\gamma})u_\gamma,$$

$$\tag{C.3.6}$$

with the corresponding total energy equation

$$\partial_t(\rho E) + \partial_\beta \left(\rho E u_\beta \right) = \partial_\beta \left(\lambda \partial_\beta T \right) + \partial_\beta \left(u_\gamma \sigma_{\beta\gamma} \right), \tag{C.3.7}$$

where the correct viscous heat diffusion term is recovered, i.e, $\boldsymbol{\sigma} - p\boldsymbol{\delta} = \mu \left(\boldsymbol{S} - (\tfrac{2}{D}\partial_\gamma u_\gamma)\boldsymbol{\delta} \right)$.

Several points are worth noting:

- When the total energy based DDF LBM is considered, Guo's collision term must be employed if phenomena induced by viscous heat diffusion are not negligible (as with thermal Couette flows), otherwise using a simple BGK collision operator is sufficient.

- The second part of Z is not relevant at the Navier-Stokes level (only $\mathbf{\Gamma}^{(1)}$ and higher-order moments computations are affected by it), thus assuming $Z = \boldsymbol{\xi} \cdot \boldsymbol{u}$ is a "free" optimization (CPU time gain without accuracy loss).

C.4 Extension to polyatomic gases

Using the previous definition of the thermal equilibrium VDF ($h^{(0)} = \frac{1}{2}\xi^2 f^{(0)}$), we have

$$\frac{1}{\rho} \int h^{(0)} \mathrm{d}\boldsymbol{\xi} = E = e + \frac{u^2}{2} \tag{C.4.1}$$

where $e = \frac{DrT}{2} = \frac{D}{2}rT_0\theta$, D being the number of physical dimensions, $\theta = T/T_0$, and T_0 is the reference temperature. Thus, the internal energy of gas molecules is only linked to the translational (internal) DoFs through D. In order to properly recover the behavior of polyatomic gases, rotational and vibrational DoFs should also be included in the definition of the internal energy of the system. Several approaches have been proposed [64, 116, 169] to circumvent this issue. They consist in taking into account the physics linked to these DoFs through the evolution of a new VDF. In the context of DDF LBM, this can simply be done redefining the equilibrium state of the thermal VDF as follows:

$$h^{(0),b} = \frac{1}{2}\left[\xi^2 + (b-D)rT_0\theta\right]f^{(0)} = h^{(0)} + \frac{(b-D)rT_0\theta}{2}f^{(0)} \quad \text{with} \quad b = D + K \tag{C.4.2}$$

where K is the number of DoFs linked to rotation and vibration motions, while b takes into account all internal DoFs. Indeed, if we recompute the statistical moments of h with respect to $\boldsymbol{\xi}$, we recover the following formula:

$$\int h^{(0),b}\mathrm{d}\boldsymbol{\xi} = \rho E + \int \frac{(b-D)rT_0\theta}{2}f^{(0)}\mathrm{d}\boldsymbol{\xi} = \rho\left(brT_0\theta + u^2\right)/2 \equiv \rho E_b$$

$$\int h^{(0),b}\xi_\alpha \mathrm{d}\boldsymbol{\xi} = (\rho E_b + p)u_\alpha \tag{C.4.3}$$

$$\int h^{(0),b}\xi_\alpha\xi_\beta \mathrm{d}\boldsymbol{\xi} = (\rho E_b + p)u_\alpha u_\beta + p(E_b + rT_0\theta)\delta_{\alpha\beta}$$

Assuming now that $h^b = h^{(0),b} + h^{(1),b}$ at the Navier-Stokes level, the preservation of energy through collision implies that

$$\int h^{(1),b}\mathrm{d}\boldsymbol{\xi} = \int \left(h^{(1)} + \frac{(b-D)rT_0\theta}{2}f^{(1)}\right)\mathrm{d}\boldsymbol{\xi} = 0, \tag{C.4.4}$$

so that

$$\int h \mathrm{d}\boldsymbol{\xi} = \int h^{(0),b} \mathrm{d}\boldsymbol{\xi} = \rho E. \tag{C.4.5}$$

Hence the redefinition of the thermal equilibrium state (C.4.2) allows to take into account rotational and vibrational DoFs of molecules, without introducing error terms (at the Navier-Stokes) in the macroscopic behavior of the DDF-LBM.

Appendix D

Lattices

Here the link between velocity sets and Hermite tensors is emphasized. To properly choose which Hermite polynomials should be taken into account in the expansion of f_i, the preservation of the orthogonality property of these polynomials, with respect to the weighted scalar product, is considered [119]. As a reminder, this condition is as follows

$$\frac{1}{(2\pi r T_0)^{D/2}} \int_{\mathbb{R}^D} \mathcal{H}_{\boldsymbol{\alpha}}^{(n)} \mathcal{H}_{\boldsymbol{\beta}}^{(m)} e^{-\left(\boldsymbol{\xi}^2/2r T_0\right)} \, \mathrm{d}\boldsymbol{\xi} = \sum_i \omega_i \mathcal{H}_{i,\boldsymbol{\alpha}}^{(n)} \mathcal{H}_{i,\boldsymbol{\beta}}^{(m)} \qquad (D.0.1)$$

with $c_s^2 = r T_0$ in lattice units. All 2D third- and fourth-order LBMs used in the present PhD work are illustrated in Fig. D.1. Their main characteristics are summarized in Tab. D.1, while their Hermite polynomials basis are compiled in Tab. D.2. Concerning 3D models of interest, both their characteristics and Hermite polynomial basis are recalled in Tab. D.3. The convention from [106] was used to describe the properties of each velocity set: $E_{D,Q}^V$ where D is the number of physical dimensions, Q is the degree of precision of the quadrature, and V is the number of discrete velocities. Furthermore, all velocities obtained by cyclic permutations and/or reflections with respect to each axis are omitted for the sake of clarity. In addition,

To conclude this appendix, expressions of the VDFs for the most complex lattices described herein ($E_{2,9}^{37}$ and $E_{3,9}^{103}$) are given by:

$$
\begin{aligned}
f_i^{(0),2D} = \omega_i \Bigg[&\mathcal{H}_i^{(0)} a_0^{(0)} + \frac{1}{c_s^2} \left(\mathcal{H}_{i,x}^{(1)} a_{0,x}^{(1)} + \mathcal{H}_{i,y}^{(1)} a_{0,y}^{(1)} \right) \\
&+ \frac{1}{2c_s^4} \left(\mathcal{H}_{i,xx}^{(2)} a_{0,xx}^{(2)} + 2\mathcal{H}_{i,xy}^{(2)} a_{0,xy}^{(2)} + \mathcal{H}_{i,yy}^{(2)} a_{0,yy}^{(2)} \right) \\
&+ \frac{1}{6c_s^6} \left(\mathcal{H}_{i,xxx}^{(3)} a_{0,xxx}^{(3)} + 3\mathcal{H}_{i,xxy}^{(3)} a_{0,xxy}^{(3)} + 3\mathcal{H}_{i,yyx}^{(3)} a_{0,yyx}^{(3)} + \mathcal{H}_{i,yyy}^{(3)} a_{0,yyy}^{(3)} \right) \\
&+ \frac{1}{24c_s^8} \Big(\mathcal{H}_{i,xxxx}^{(4)} a_{0,xxxx}^{(4)} + 4\mathcal{H}_{i,xxxy}^{(4)} a_{0,xxxy}^{(4)} + 6\mathcal{H}_{i,xxyy}^{(4)} a_{0,xxyy}^{(4)} \\
&\qquad\qquad + 4\mathcal{H}_{i,yyyx}^{(4)} a_{0,yyyx}^{(4)} + \mathcal{H}_{i,yyyy}^{(4)} a_{0,yyyy}^{(4)} \Big) \Bigg],
\end{aligned}
$$
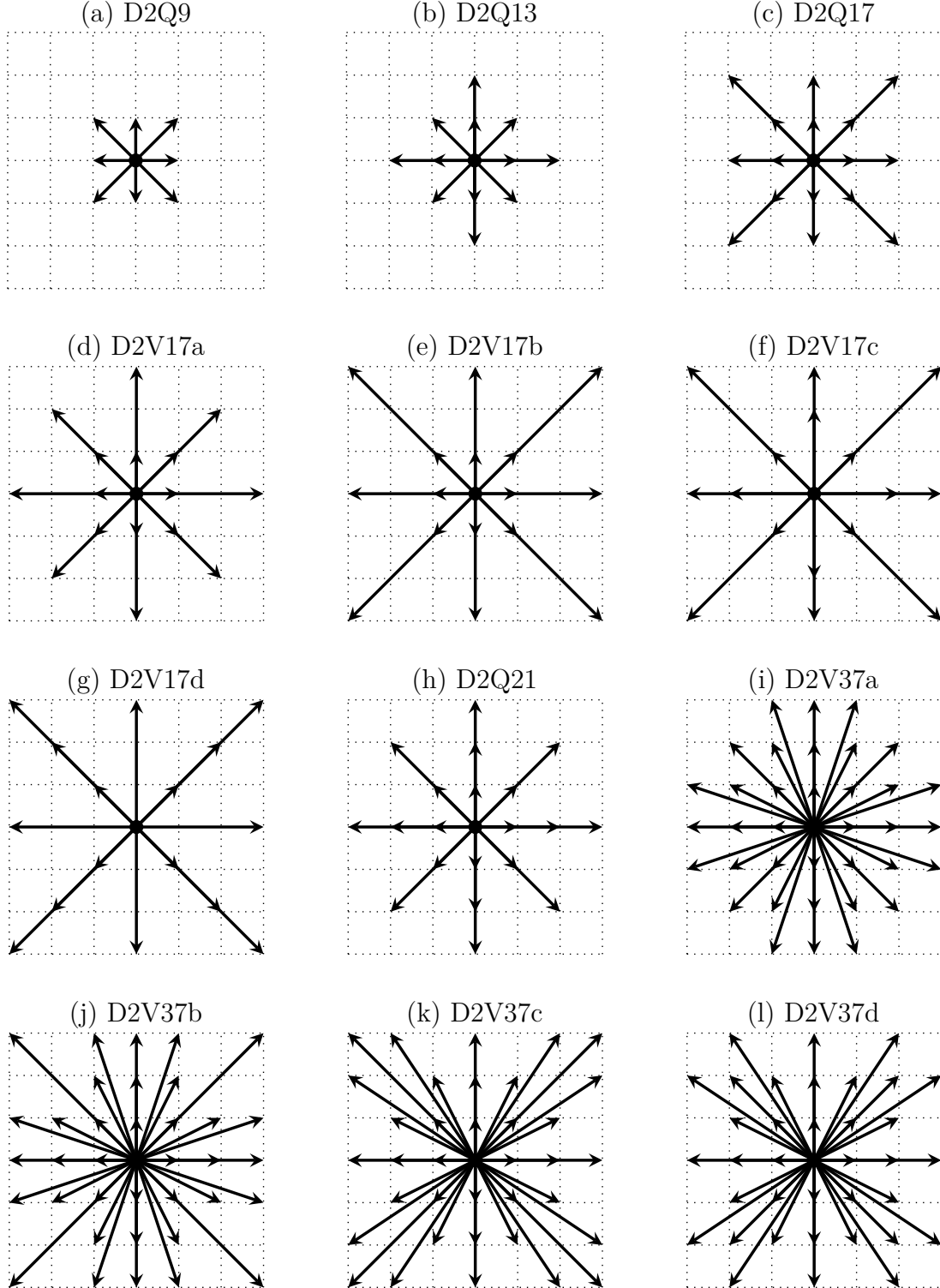
Figure D.1 – Illustration of standard and high-order velocity sets. Second-order lattice structures ((a)-(c)) allow to preserve orthogonality properties of Hermite polynomials up to $N = 2$, and thus are dedicated to the simulation of isothermal and weakly compressible flows. The simulation of isothermal flows without any Mach number limitation are possible with third-order velocity sets ((d)-(h)), assuming a Hermite polynomial expansion up to $N = 3$. Eventually, the physics described by the Navier-Stokes-Fourier equations ($N = 4$) is recovered thanks to fourth-order LBMs ((i)-(l)). The main difference between DnQm and DnVm lattice notations comes from the way these lattice structures are build as explained in Sec. 3.3. Data are compiled from [109, 119, 120, 124, 172] and herein references.

Group	$\boldsymbol{\xi}_i$	p	$E^9_{2,5}$	$E^{17a}_{2,7}$	$E^{17b}_{2,7}$	$E^{17c}_{2,7}$	$E^{17d}_{2,7}$	$E^{21}_{2,7}$
1	$(0,0)$	1	4/9	0.4020514690911259840	0.40667105856457524959	455/1152	35/288	91/324
2	$(1,0)$	4	1/9	0.11615486649778153371	0.11473665961010276470			1/12
3	$(1,1)$	4	1/36	0.03300635362298691422	0.03333896406679150159	243/2048	45/256	2/27
4	$(2,0)$	4				81/2560		7/360
6	$(2,2)$	4		0.00007907860216591786			9/640	1/432
7	$(3,0)$	4			0.00025841454978746788	0.00025126267064870766	1/1440	1/36
10	$(3,3)$	4			0.00000534901131321673	5/18432	23/11520	1/1620
	$1/c_s$		$\sqrt{3}$	1.64343060879795421769	1.64947240657615323833	$2/\sqrt{3}$	$\sqrt{2/3}$	$\sqrt{3/2}$

Group	$\boldsymbol{\xi}_i$	p	$E^{37a}_{2,9}$	$E^{37b}_{2,9}$	$E^{37c}_{2,9}$	$E^{37d}_{2,9}$
1	$(0,0)$	1	0.23315066913235250228	0.20391691645511587744	0.20716276763653500795	0.21614581395270060924
2	$(1,0)$	4	0.10730609154221900241	0.12754484339569051192	0.12541475355788420752	0.11935119729447242665
3	$(1,1)$	4	0.05766785988879488203	0.04375371798953321924	0.04512306145669441492	0.04916543229896893550
4	$(2,0)$	4	0.01420821615845075026	0.00813659060240929741	0.00862346827962216698	0.01024041661653197522
5	$(2,1)$	8	0.00535304900051377523	0.00940079937120807713	0.00912693067777583799	0.00811633796720720785
6	$(2,2)$	4	0.00101193759267357547			0.00016169483369098082
7	$(3,0)$	4	0.00024530102775771734	0.00069505106894597311	0.00071533763882984267	0.00067042240724901467
8	$(3,1)$	8	0.00028341425299419821	0.00003042985482580434		
9	$(3,2)$	8			0.00003042985482580434	0.00007085356324854955
10	$(3,3)$	4		0.00002810937757426598	0.00001796609263233120	
	$1/c_s$		1.19697977039307435897	1.19697977039307435897	1.19697977039307435897	1.19697977039307435897

Table D.1 – Summary of 2D (top) third-, and (bottom) fourth-order LBMs. For each lattice structure, the convention $E^V_{D,Q}$ is adopted to summarize all the characteristics of interest, namely, the number of discrete velocities V, the quadrature order Q, and the number of dimensions D [120]. Furthermore, p stands for the number of discrete speeds of each velocity group, while their associated weights ω_i compose the right part of the table. The last row consists of the value of the normalization constant (the inverse of the lattice constant c_s) needed for the on-grid property of the lattice structure $((\xi_{i,x}, \xi_{i,y}) \in \mathbb{Z}^2)$. Lattice structures data are compiled from [109, 120].

and for the 3D extension,

$$
\begin{aligned}
f_i^{(0),3D} = f_i^{(0),2D} + \omega_i \Bigg[&\frac{1}{c_s^2} \mathcal{H}_{i,z}^{(1)} a_{0,z}^{(1)} + \frac{1}{2c_s^4} \left(\mathcal{H}_{i,zz}^{(2)} a_{0,zz}^{(2)} + 2\mathcal{H}_{i,xz}^{(2)} a_{0,xz}^{(2)} + 2\mathcal{H}_{i,yz}^{(2)} a_{0,yz}^{(2)} \right) \\
&+ \frac{1}{6c_s^6} \Big(\mathcal{H}_{i,zzz}^{(3)} a_{0,zzz}^{(3)} + 3\mathcal{H}_{i,zzx}^{(3)} a_{0,zzx}^{(3)} + 3\mathcal{H}_{i,zzy}^{(3)} a_{0,zzy}^{(3)} \\
&\quad + 3\mathcal{H}_{i,xxz}^{(3)} a_{0,xxz}^{(3)} + 3\mathcal{H}_{i,yyz}^{(3)} a_{0,yyz}^{(3)} + 6\mathcal{H}_{i,xyz}^{(3)} a_{0,xyz}^{(3)} \Big) \\
&+ \frac{1}{24c_s^8} \Big(\mathcal{H}_{i,zzzz}^{(4)} a_{0,zzzz}^{(4)} + 4\mathcal{H}_{i,zzzx}^{(4)} a_{0,zzzx}^{(4)} + 4\mathcal{H}_{i,zzzy}^{(4)} a_{0,zzzy}^{(4)} + 6\mathcal{H}_{i,xxzz}^{(4)} a_{0,xxzz}^{(4)} \\
&\quad + 6\mathcal{H}_{i,yyzz}^{(4)} a_{0,yyzz}^{(4)} + 12\mathcal{H}_{i,xxyz}^{(4)} a_{0,xxyz}^{(4)} + 12\mathcal{H}_{i,yyxz}^{(4)} a_{0,yyxz}^{(4)} + 12\mathcal{H}_{i,zzxy}^{(4)} a_{0,zzxy}^{(4)} \Big) \Bigg].
\end{aligned}
$$

In the case of $f_i^{(1)}$ the very same terms, as for the equilibrium part $f_i^{(0)}$, have to be taken into account [134]. Furthermore, corresponding third-order counterparts of $f_i^{(0)}$ and $f_i^{(1)}$ are simply obtained discarding $\boldsymbol{a}_0^{(4)}$ and $\boldsymbol{a}_1^{(4)}$.

Lattice	$\mathcal{H}^{(0)}$	$\mathcal{H}_x^{(1)}$	$\mathcal{H}_{xx}^{(2)}$	$\mathcal{H}_{xy}^{(2)}$	$\mathcal{H}_{xxx}^{(3)}$	$\mathcal{H}_{xxy}^{(3)}$	$\mathcal{H}_{xxxx}^{(4)}$	$\mathcal{H}_{xxxy}^{(4)}$	$\mathcal{H}_{xxyy}^{(4)}$
$E_{2,5}^{9}$	⭕	⭕	⭕	⭕	✗	⭕	✗	✗	⭕
$E_{2,5}^{13}$	⭕	⭕	⭕	⭕	✗	✗	✗	✗	✗
$E_{2,5}^{17}$	⭕	⭕	⭕	⭕	✗	✗	✗	✗	✗
$E_{2,7}^{17a}$	⭕	⭕	⭕	⭕	⭕	⭕	✗	✗	✗
$E_{2,7}^{17b}$	⭕	⭕	⭕	⭕	⭕	⭕	✗	✗	✗
$E_{2,7}^{17c}$	⭕	⭕	⭕	⭕	⭕	⭕	✗	✗	✗
$E_{2,7}^{17d}$	⭕	⭕	⭕	⭕	⭕	⭕	✗	✗	✗
$E_{2,7}^{21}$	⭕	⭕	⭕	⭕	⭕	⭕	✗	✗	✗
$E_{2,9}^{37a}$	⭕	⭕	⭕	⭕	⭕	⭕	⭕	⭕	⭕
$E_{2,9}^{37b}$	⭕	⭕	⭕	⭕	⭕	⭕	⭕	⭕	⭕
$E_{2,9}^{37c}$	⭕	⭕	⭕	⭕	⭕	⭕	⭕	⭕	⭕
$E_{2,9}^{37d}$	⭕	⭕	⭕	⭕	⭕	⭕	⭕	⭕	⭕

Table D.2 – Hermite tensor basis of some common standard and high-order two-dimensional lattice structures. For each lattice structure, the convention $E_{D,Q}^{V}$ is adopted to summarize all the characteristics of interest, namely, the number of discrete velocities V, the quadrature order Q, and the number of dimensions D [120]. Regarding Hermite tensors, they are classified into two categories: those belonging to the basis (⭕) and those which do not (✗). Data are compiled from [120, 124]. It is interesting to note that both $E_{2,5}^{13}$ (D2Q13) and $E_{2,5}^{17}$ (D2Q17) are only second-order LBMs when non-customized equilibrium states are considered.

Group	$\boldsymbol{\xi}_i$	p	$E_{3,5}^{19}$	$E_{3,5}^{27}$	$E_{3,7}^{39a}$	$E_{3,7}^{39b}$	$E_{3,9}^{103}$
1	$(0,0,0)$	1	1/3	8/27	1/12	8/27	0.03263335176447115946
2	$(1,0,0)$	6	1/18	2/27	1/12	2/81	0.09765683359033457422
3	$(1,1,0)$	12	1/36	1/54		32/729	
4	$(1,1,1)$	8		1/216	1/27		0.02809775029025733562
5	$(2,0,0)$	6			2/135	16/3645	0.00104525956043006146
6	$(2,1,0)$	24					0.00570532901689481599
7	$(2,2,0)$	12			1/432		0.00061193926982974783
8	$(2,2,2)$	8				1/5832	0.00015596415937428372
9	$(3,0,0)$	6			1/1620	2/10935	0.00028444325180005520
10	$(3,1,1)$	24					0.00013069837598519158
11	$(3,3,3)$	8					0.00000122319450132305
	$1/c_s$		$\sqrt{3}$	$\sqrt{3}$	$\sqrt{3/2}$	$3/2$	1.19697977039307435897

Lattice	$\mathcal{H}^{(0)}$	$\mathcal{H}_x^{(1)}$	$\mathcal{H}_{xx}^{(2)}$	$\mathcal{H}_{xy}^{(2)}$	$\mathcal{H}_{xxx}^{(3)}$	$\mathcal{H}_{xxy}^{(3)}$	$\mathcal{H}_{xyz}^{(3)}$	$\mathcal{H}_{xxxx}^{(4)}$	$\mathcal{H}_{xxxy}^{(4)}$	$\mathcal{H}_{xxyy}^{(4)}$	$\mathcal{H}_{xxyz}^{(4)}$	$\mathcal{H}_{xxyyz}^{(5)}$	$\mathcal{H}_{xxyyzz}^{(6)}$
$E_{3,5}^{19}$	◯	◯	◯	◯	✗	◯	✗	✗	✗	✗	✗	✗	✗
$E_{3,5}^{27}$	◯	◯	◯	◯	✗	◯	◯	✗	✗	◯	✗	◯	◯
$E_{3,7}^{39a}$	◯	◯	◯	◯	◯	◯	◯	✗	✗	✗	✗	✗	✗
$E_{3,7}^{39b}$	◯	◯	◯	◯	◯	◯	◯	✗	✗	✗	✗	✗	✗
$E_{3,9}^{103}$	◯	◯	◯	◯	◯	◯	◯	◯	◯	◯	◯	✗	✗

Table D.3 – Description of some common standard and high-order three-dimensional lattice structures (top), and their associated Hermite tensor basis (bottom). For each lattice structure, the convention $E_{D,Q}^V$ is adopted to summarize all the characteristics of interest, namely, the number of discrete velocities V, the quadrature order Q, and the number of dimensions D [120]. Furthermore, p stands for the number of discrete speeds of each velocity group, while their associated weights ω_i compose the right part of the table. The last row consists of the value of the normalization constant (the inverse of the lattice constant c_s) needed for the on-grid property of the lattice structure ($(\xi_{i,x}, \xi_{i,y}, \xi_{i,z}) \in \mathbb{Z}^3$). Regarding Hermite tensors, they are classified into two categories: those belonging to the basis (◯) and those which do not (✗). Lattice structures data are compiled from [120, 124].

Appendix E

Formulas linked to Gaussian integrals

Some useful formulas regarding Gaussian integrals in the multivariate case are derived hereafter. They allow to ease the construction of lattices based on the conservation of Hermite polynomials orthogonality properties.

E.1   Multivariate Gaussian integral

Let us start by showing that

$$I = \int_{\mathbb{R}} e^{-x^2/2\beta} \, \mathrm{d}x = \sqrt{2\pi\beta}. \tag{E.1.1}$$

The most widely known proof of Eq. (E.1.1) is based on the use of polar coordinates. Taking only positive values,

$$J_x = \int_0^{+\infty} e^{-x^2/2\beta} \, \mathrm{d}x = I/2$$

since $x \mapsto \exp[-x^2]$ is an even function. We then have

$$J_x J_y = \int_0^{+\infty} e^{-x^2/2\beta} \, \mathrm{d}x \int_0^{+\infty} e^{-y^2/2\beta} \, \mathrm{d}y = \int_0^{+\infty} \int_0^{+\infty} e^{-(x^2+y^2)/2\beta} \, \mathrm{d}x\mathrm{d}y,$$

where $J_x J_y$ corresponds to an integral over one quadrant of $\mathbb{R}^2$, which can be computed quite easily using polar coordinates. Indeed, the change of variables $r^2 = x^2 + y^2$ leads to $r\mathrm{d}r\mathrm{d}\phi = \mathrm{d}x\mathrm{d}y$ with the new integral bounds $[0, +\infty[\times[0, \pi/2[$. Thus $J_x J_y$ leads to

$$J_x J_y = J_r = \int_{r=0}^{+\infty} \int_{\phi=0}^{\pi/2} e^{-r^2/2\beta} \, r\mathrm{d}r\mathrm{d}\phi,$$

$$= \int_{\phi=0}^{\pi/2} \mathrm{d}\phi \int_{r=0}^{+\infty} re^{-r^2/2\beta} \, \mathrm{d}r,$$

$$= \frac{\pi}{2}\beta.$$

Hence

$$I = 2\sqrt{J_r} = \sqrt{2\pi\beta}$$

∎

If we now assume that $\boldsymbol{x}$ is a vector belonging to $\mathbb{R}^D$, D being a non-zero positive integer, Eq. (E.1.1) becomes

$$I_n = \int_{\mathbb{R}^D} e^{-x^2/2\beta} \,\mathrm{d}\boldsymbol{x} = \prod_{i=1}^{D}\left(\int_{\mathbb{R}} e^{-x^2/2\beta} \,\mathrm{d}x\right) = (2\pi\beta)^{D/2}. \qquad (E.1.2)$$

E.2 Extended formula

To build lattices based on the preservation of orthogonality properties of Hermite polynomials, the following general expression is required

$$\mathbb{I}(n) = \int_{\mathbb{R}} x^n e^{-x^2/2\beta} \,\mathrm{d}x = \left(\frac{\beta}{2}\right)^p \frac{(2p)!}{p!}\sqrt{2\pi\beta} \qquad \text{if } n = 2p, \qquad (E.2.1)$$

$$= 0 \qquad\qquad \text{otherwise.}$$

Let us prove Eq. (E.2.1) using mathematical induction. Starting with $n = 0$,

$$\mathbb{I}(0) = \int_{\mathbb{R}} e^{-x^2/2\beta} \,\mathrm{d}x \overset{(E.1.1)}{=} \sqrt{2\pi\beta} = \left(\frac{\beta}{2}\right)^0 \frac{0!}{0!}\sqrt{2\pi\beta}$$

since by definition $0! = 1$. Furthermore,

$$\mathbb{I}(1) = \int_{\mathbb{R}} x e^{-x^2/2\beta} \,\mathrm{d}x = 0$$

because $x \mapsto x\exp[-x^2]$ is an odd function. Assuming now that Eq. (E.2.1) is true for $n \leq 2k$, let us consider the case $n = 2k + 1$. Using the integration by part,

$$\mathbb{I}(2k+1) = \int_{\mathbb{R}} x^{2k+1} e^{-x^2/2\beta} \,\mathrm{d}x$$

$$= \int_{\mathbb{R}} x^{2k}(x e^{-x^2/2\beta}) \,\mathrm{d}x$$

$$= 0 - (-2k\beta)\mathbb{I}(2k-1)$$

$$= 0$$

since $\mathbb{I}(2k-1) = 0$. The final integral to compute is $\mathbb{I}(2k+2)$. Once again the integration by parts is used, and leads to

$$\mathbb{I}(2k+2) = \int_{\mathbb{R}} x^{2k+2} e^{-x^2/2\beta} \,\mathrm{d}x$$

$$= 0 - [-(2k+1)\beta]\mathbb{I}(2k)$$

$$= \frac{(2k+2)(2k+1)\beta}{2(k+1)} \left(\frac{\beta}{2}\right)^k \frac{(2k)!}{k!} \sqrt{2\pi\beta}$$

$$= \left(\frac{\beta}{2}\right)^{k+1} \frac{(2k+2)!}{(k+1)!} \sqrt{2\pi\beta}$$

∎

The multivariate version of Eq. (E.2.1) is also obtained thanks to the separation of variables resulting in the product of D integrals of type (E.2.1), where $D \in \mathbb{N}^*$. The corresponding expression reads as

$$\mathbb{I}(n) = \int_{\mathbb{R}^D} \boldsymbol{x}^n e^{-x^2/2\beta} \, \mathrm{d}\boldsymbol{x} = \left(\frac{\beta}{2}\right)^p \frac{(2p)!}{p!} (2\pi\beta)^{D/2} \qquad \text{if } n = 2p, \qquad (\text{E.2.2})$$

$$= 0 \qquad \text{otherwise.}$$

Appendix F

Recursive formulas

F.1   Non-equilibrium coefficients

The aim of this section is to prove the following recursive relation,$\forall n \geq 4$,

$$
a_{1,\alpha_1..\alpha_n}^{(n)} = u_{\alpha_n} a_{1,\alpha_1..\alpha_{n-1}}^{(n-1)} + c_s^2(\theta - 1) \sum_{i=1}^{n-1} \delta_{\alpha_i \alpha_n} a_{1,\beta_i}^{(n-2)} + \frac{1}{\rho} \sum_{i=1}^{n-1} a_{0,\beta_i}^{(n-2)} a_{1,\alpha_i \alpha_n}^{(2)}
$$

$$
+ \frac{1}{\rho} \sum_{i=1}^{n-1} \sum_{j>i}^{n-1} a_{0,\beta_{ij}}^{(n-3)} \left(a_{1,\alpha_i \alpha_j \alpha_n}^{(3)} - u_{\alpha_i} a_{1,\alpha_j \alpha_n}^{(2)} - u_{\alpha_j} a_{1,\alpha_i \alpha_n}^{(2)} - u_{\alpha_n} a_{1,\alpha_i \alpha_j}^{(2)} \right). \quad \text{(F.1.1)}
$$

where some mathematical notations are used for the sake of clarity: (1) β_i is used when the index α_i is omitted, e.g., $a_{0,\beta_i}^{(n)} \equiv a_{0,\alpha_1..\alpha_{i-1}\alpha_{i+1}..\alpha_n}^{(n)}$, and (2) if α_i and α_j are omitted then β_{ij} is used.

The following relations are needed to prove (4.3.5):

- *The Hermite coefficient based LBE* [106]

$$
\forall n \geq 1, \quad a_{1,\alpha_1..\alpha_n}^{(n)} = -\tau \left[\partial_t a_{0,\alpha_1..\alpha_n}^{(n)} + \partial_\gamma a_{0,\alpha_1..\alpha_n \gamma}^{(n+1)} + c_s^2 \sum_{i=1}^{n} \partial_{\alpha_i} a_{0,\beta_i}^{(n-1)} \right], \quad \text{(F.1.2)}
$$

  where Einstein summation notation is used on subscript γ,

- *The recursive formula for Hermite coefficients at equilibrium* (App. F.2)

$$
\forall n \geq 2, \quad a_{0,\alpha_1..\alpha_n}^{(n)} = u_{\alpha_n} a_{0,\alpha_1..\alpha_{n-1}}^{(n-1)} + (\theta - 1) c_s^2 \sum_{i=1}^{n-1} \delta_{\alpha_i \alpha_n} a_{0,\beta_i}^{(n-2)}, \quad \text{(F.1.3)}
$$

- *Euler's equations*

$$
\partial_t \rho + \partial_\gamma (\rho u_\gamma) = 0, \quad \text{(F.1.4)}
$$

$$
\rho \partial_t (u_\alpha) + \rho u_\gamma \partial_\gamma (u_\alpha) + \partial_\alpha p = 0, \quad \text{(F.1.5)}
$$

$$
\partial_t \theta + u_\gamma \partial_\gamma \theta + \frac{2}{D} \theta \partial_\gamma u_\gamma = 0, \quad \text{(F.1.6)}
$$

Let us now move on to the proof itself.

STEP 1: Boltzmann equation associated to Hermite coefficients (F.1.2) at order $(n-1)$.

$$\forall n \geq 2, \quad u_{\alpha_n} a^{(n-1)}_{1,\alpha_1..\alpha_{n-1}} = -\tau \left[u_{\alpha_n} \partial_t a^{(n-1)}_{0,\alpha_1..\alpha_{n-1}} + u_{\alpha_n} \partial_\gamma a^{(n)}_{0,\alpha_1..\alpha_{n-1}\gamma} + c_s^2 \sum_{i=1}^{n-1} u_{\alpha_n} \partial_{\alpha_i} a^{(n-2)}_{0,\beta_i} \right]$$

$$= -\tau \left[\partial_t \left(u_{\alpha_n} a^{(n-1)}_{0,\alpha_1..\alpha_{n-1}} \right) - a^{(n-1)}_{0,\alpha_1..\alpha_{n-1}} \partial_t u_{\alpha_n} + \partial_\gamma \left(u_{\alpha_n} a^{(n)}_{0,\alpha_1..\alpha_{n-1}\gamma} \right) \right.$$

$$\left. - a^{(n)}_{0,\alpha_1..\alpha_{n-1}\gamma} \partial_\gamma u_{\alpha_n} + c_s^2 \sum_{i=1}^{n-1} \partial_{\alpha_i} \left(u_{\alpha_n} a^{(n-2)}_{0,\beta_i} \right) - c_s^2 \sum_{i=1}^{n-1} a^{(n-2)}_{0,\beta_i} \partial_{\alpha_i} u_{\alpha_n} \right].$$

where the derivation by parts rule is used.

STEP 2: Remove all time derivatives ∂_t.

First, we use Eq. (F.1.3),

$$u_{\alpha_n} a^{(n-1)}_{1,\alpha_1..\alpha_{n-1}} = -\tau \left[\underbrace{\partial_t a^{(n)}_{0,\alpha_1..\alpha_n} + \partial_\gamma a^{(n+1)}_{0,\alpha_1..\alpha_n\gamma} + c_s^2 \sum_{i=1}^{n} \partial_{\alpha_i} a^{(n-1)}_{0,\beta_i}}_{(i)} \right.$$

$$\underbrace{- a^{(n-1)}_{0,\alpha_1..\alpha_{n-1}} \partial_t u_{\alpha_n} - a^{(n)}_{0,\alpha_1..\alpha_{n-1}\gamma} \partial_\gamma u_{\alpha_n}}_{(ii)}$$

$$\underbrace{- c_s^2 \partial_{\alpha_n} a^{(n-1)}_{0,\alpha_1..\alpha_{n-1}} - c_s^2 \sum_{i=1}^{n-1} a^{(n-2)}_{0,\beta_i} \partial_{\alpha_i} u_{\alpha_n}}_{(iii)}$$

$$\underbrace{- c_s^2 \sum_{i=1}^{n-1} \delta_{\alpha_i \alpha_n} \partial_t \left((\theta-1) a^{(n-2)}_{0,\beta_i} \right) - c_s^2 \sum_{i=1,i\neq n}^{n+1} \delta_{\alpha_i \alpha_n} \partial_\gamma \left((\theta-1) a^{(n-1)}_{0,\beta_i\gamma} \right)}_{(iv)}$$

$$\left. \underbrace{- c_s^4 \sum_{i=1}^{n-1} \sum_{j=1,j\neq i}^{n-1} \delta_{\alpha_j \alpha_n} \partial_{\alpha_i} \left((\theta-1) a^{(n-3)}_{0,\beta_{ij}} \right)}_{(v)} \right].$$

for $n \geq 3$. Then, thanks to Eq. (F.1.2) one can replace $\partial_t a^{(n)}_{0,\alpha_1..\alpha_n}$ by

$$(i) = -\frac{1}{\tau} a^{(n)}_{1,\alpha_1..\alpha_n}$$

and

$$(ii) = -a^{(n-1)}_{0,\alpha_1..\alpha_{n-1}} (\partial_t u_{\alpha_n} + u_\gamma \partial_\gamma u_{\alpha_n}) - c_s^2 (\theta-1) \partial_\gamma u_{\alpha_n} \sum_{i=1}^{n-1} \delta_{\alpha_i \gamma} a^{(n-2)}_{0,\beta_i}.$$

In the same spirit as for Chapman-Enskog expansion, Euler's equation of momentum (Eq. (F.1.5)) is used to replace the time derivative $\partial_t u_{\alpha_n}$. In addition to that, removing the implicit summation on γ leads to

$$(ii) = a^{(n-1)}_{0,\alpha_1..\alpha_{n-1}} \frac{1}{\rho}\partial_{\alpha_n} p - c_s^2(\theta - 1)\sum_{i=1}^{n-1} a^{(n-2)}_{0,\beta_i}\partial_{\alpha_i} u_{\alpha_n},$$

so that

$$(ii) + (iii) = a^{(n-1)}_{0,\alpha_1..\alpha_{n-1}} \frac{1}{\rho}\partial_{\alpha_n} p - c_s^2\theta\sum_{i=1}^{n-1} a^{(n-2)}_{0,\beta_i}\partial_{\alpha_i} u_{\alpha_n} - c_s^2\partial_{\alpha_n} a^{(n-1)}_{0,\alpha_1..\alpha_{n-1}}.$$

Let us now focus on (iv) and (v):

$$(iv) = \underbrace{-c_s^2\sum_{i=1}^{n-1}\delta_{\alpha_i\alpha_n}\left[a^{(n-2)}_{0,\beta_i}\partial_t\theta + a^{(n-1)}_{0,\beta_i\gamma}\partial_\gamma\theta\right]}_{(iv.i)} \underbrace{-c_s^2(\theta-1)\sum_{i=1}^{n-1}\delta_{\alpha_i\alpha_n}\left[\partial_t a^{(n-2)}_{0,\beta_i} + \partial_\gamma a^{(n-1)}_{0,\beta_i\gamma}\right]}_{(iv.ii)}$$

$$\underbrace{-c_s^2(\theta-1)\partial_{\alpha_n} a^{(n-1)}_{0,\alpha_1..\alpha_{n-1}} - c_s^2 a^{(n-1)}_{0,\alpha_1..\alpha_{n-1}}\partial_{\alpha_n}\theta}_{(iv.iii)},$$

$$(v) = \underbrace{-c_s^4(\theta-1)\sum_{i=1}^{n-1}\sum_{j=1,j\neq i}^{n-1}\delta_{\alpha_j\alpha_n}\partial_{\alpha_i} a^{(n-3)}_{0,\beta_{ij}}}_{(v.i)} \underbrace{-c_s^4\sum_{i=1}^{n-1}\sum_{j=1,j\neq i}^{n-1}\delta_{\alpha_j\alpha_n} a^{(n-3)}_{0,\beta_{ij}}\partial_{\alpha_i}\theta}_{(v.ii)}.$$

Once again, one can replace $\partial_t a^{(n-2)}_{0,\beta_i}$ using (F.1.2),

$$(iv.ii) + (v.i) = \frac{1}{\tau}c_s^2(\theta-1)\sum_{i=1}^{n-1}\delta_{\alpha_i\alpha_n} a^{(n-2)}_{1,\beta_i}.$$

Moreover, since $\partial_{\alpha_n} p = \rho c_s^2\partial_{\alpha_n}\theta + c_s^2\theta\partial_{\alpha_n}\rho$ we can rearrange several terms as follows,

$$(ii) + (iii) + (iv.iii) = a^{(n-1)}_{0,\alpha_1..\alpha_{n-1}}\frac{c_s^2\theta}{\rho}\partial_{\alpha_n}\rho - c_s^2\theta\sum_{i=1}^{n-1} a^{(n-2)}_{0,\beta_i}\partial_{\alpha_i} u_{\alpha_n} - c_s^2\theta\partial_{\alpha_n} a^{(n-1)}_{0,\alpha_1..\alpha_{n-1}}.$$

By using (F.1.3), one gets

$$(iv.i) = -c_s^2\sum_{i=1}^{n-1}\delta_{\alpha_i\alpha_n}\left[a^{(n-2)}_{0,\beta_i}\partial_t\theta + \left(u_\gamma a^{(n-2)}_{0,\beta_i} + c_s^2(\theta-1)\sum_{j=1,j\neq i}^{n-1}\delta_{\alpha_j\gamma} a^{(n-3)}_{0,\beta_{ij}}\right)\partial_\gamma\theta\right]$$

$$= -c_s^2\sum_{i=1}^{n-1}\delta_{\alpha_i\alpha_n} a^{(n-2)}_{0,\beta_i}(\partial_t\theta + u_\gamma\partial_\gamma\theta) - c_s^4(\theta-1)\partial_\gamma\theta\sum_{i=1}^{n-1}\sum_{j=1,j\neq i}^{n-1}\delta_{\alpha_i\alpha_n}\delta_{\alpha_j\gamma} a^{(n-3)}_{0,\beta_{ij}}.$$

The last time derivative $\partial_t\theta$ is removed thanks to (F.1.6). Further simplifications, using the implicit summation on γ in the second term, lead to

$$(iv.i) + (v.ii) = \frac{2c_s^2\theta}{D}\partial_\gamma u_\gamma\sum_{i=1}^{n-1}\delta_{\alpha_i\alpha_n} a^{(n-2)}_{0,\beta_i} - c_s^4\theta\sum_{i=1}^{n-1}\sum_{j=1,j\neq i}^{n-1}\delta_{\alpha_i\alpha_n} a^{(n-3)}_{0,\beta_{ij}}\partial_{\alpha_j}\theta.$$

Eventually, regrouping all terms leads to, $\forall n \geq 3$,

$$u_{\alpha_n} a_{1,\alpha_1..\alpha_{n-1}}^{(n-1)} = a_{1,\alpha_1..\alpha_n}^{(n)} - c_s^2(\theta-1)\sum_{i=1}^{n-1}\delta_{\alpha_i\alpha_n}a_{1,\beta_i}^{(n-2)} + \tau c_s^2\theta\sum_{i=1}^{n-1}a_{0,\beta_i}^{(n-2)}\left(\partial_{\alpha_i}u_{\alpha_n} - \frac{2}{D}\delta_{\alpha_i\alpha_n}\partial_\gamma u_\gamma\right)$$

$$+ \tau c_s^4\theta\sum_{i=1}^{n-1}\sum_{j=1,j\neq i}^{n-1}\delta_{\alpha_i\alpha_n}a_{0,\beta_{ij}}^{(n-3)}\partial_{\alpha_j}\theta - \tau c_s^2\frac{\theta}{\rho}a_{0,\alpha_1..\alpha_{n-1}}^{(n-1)}\partial_{\alpha_n}\rho + \tau c_s^2\theta\partial_{\alpha_n}a_{0,\alpha_1..\alpha_{n-1}}^{(n-1)}.$$

$$(\text{F}.1.7)$$

STEP 3: Dispose of $\partial_{\alpha_n}a_{0,\alpha_1..\alpha_{n-1}}^{(n-1)}$ *via* the Maxwell-Boltzmann equilibrium state $f^{(0)}$.

By the chain rule,

$$\forall n \geq 3, \quad \partial_{\alpha_n}a_{0,\alpha_1..\alpha_{n-1}}^{(n-1)} = \int \partial_{\alpha_n}f^{(0)}(\boldsymbol{\xi})\mathcal{H}_{\alpha_1..\alpha_{n-1}}^{(n-1)}\mathrm{d}\boldsymbol{\xi}$$

$$= \int \left(\partial_\rho f^{(0)}\partial_{\alpha_n}\rho + \partial_{u_\gamma}f^{(0)}\partial_{\alpha_n}u_\gamma + \partial_\theta f^{(0)}\partial_{\alpha_n}\theta\right)\mathcal{H}_{\alpha_1..\alpha_{n-1}}^{(n-1)}\mathrm{d}\boldsymbol{\xi},$$

and since $f^{(0)} = \frac{\rho}{(2\pi c_s^2\theta)^{D/2}}\exp\left[-\frac{(\boldsymbol{\xi}-\boldsymbol{u})^2}{2c_s^2\theta}\right]$, the following derivatives can be obtained:

$$\begin{cases} \partial_\rho f^{(0)} = \dfrac{1}{\rho}f^{(0)}, \\[2mm] \partial_{u_\gamma}f^{(0)} = \dfrac{\xi_\gamma - u_\gamma}{c_s^2\theta}f^{(0)}, \\[2mm] \partial_\theta f^{(0)} = \left[-\dfrac{D}{2\theta} + \dfrac{1}{2c_s^2\theta^2}(\xi_\gamma - u_\gamma)^2\right]f^{(0)}. \end{cases} \qquad (\text{F}.1.8)$$

Hence

$$\partial_{\alpha_n}a_{0,\alpha_1..\alpha_{n-1}}^{(n-1)} = \frac{1}{\rho}a_{0,\alpha_1..\alpha_{n-1}}^{(n-1)}\partial_{\alpha_n}\rho + \frac{1}{c_s^2\theta}\partial_{\alpha_n}u_\gamma\int(\xi_\gamma - u_\gamma)\mathcal{H}_{\alpha_1..\alpha_{n-1}}^{(n-1)}f^{(0)}(\boldsymbol{\xi})\mathrm{d}\boldsymbol{\xi}$$

$$- \frac{D}{2\theta}a_{0,\alpha_1..\alpha_{n-1}}^{(n-1)}\partial_{\alpha_n}\theta + \frac{1}{2c_s^2\theta^2}\partial_{\alpha_n}\theta\int(\xi_\gamma - u_\gamma)^2\mathcal{H}_{\alpha_1..\alpha_{n-1}}^{(n-1)}f^{(0)}(\boldsymbol{\xi})\mathrm{d}\boldsymbol{\xi},$$

and by integration by parts, one can show that

$$\int(\xi_\gamma - u_\gamma)\mathcal{H}_{\alpha_1..\alpha_{n-1}}^{(n-1)}f^{(0)}(\boldsymbol{\xi})\mathrm{d}\boldsymbol{\xi} = \theta c_s^2\sum_{i=1}^{n-1}\delta_{\alpha_i\gamma}a_{0,\beta_i}^{(n-2)},$$

$$\int(\xi_\gamma - u_\gamma)^2\mathcal{H}_{\alpha_1..\alpha_{n-1}}^{(n-1)}f^{(0)}(\boldsymbol{\xi})\mathrm{d}\boldsymbol{\xi} = Dc_s^2\theta a_{0,\alpha_1..\alpha_{n-1}}^{(n-1)} + \theta^2 c_s^4\sum_{i=1}^{n-1}\sum_{j=1,j\neq i}^{n-1}\delta_{\alpha_i\alpha_j}a_{0,\beta_{ij}}^{(n-3)}.$$

$$(\text{F}.1.9)$$

Then, removing the implicit summation on γ leads to

$$\forall n \geq 3, \quad \partial_{\alpha_n}a_{0,\alpha_1..\alpha_{n-1}}^{(n-1)} = \frac{1}{\rho}a_{0,\alpha_1..\alpha_{n-1}}^{(n-1)}\partial_{\alpha_n}\rho + \sum_{i=1}^{n-1}a_{0,\beta_i}^{(n-2)}\partial_{\alpha_n}u_{\alpha_i} + \frac{c_s^2}{2}\sum_{i=1}^{n-1}\sum_{j=1}^{n-1}\delta_{\alpha_i\alpha_j}a_{0,\beta_{ij}}^{(n-3)}\partial_{\alpha_n}\theta.$$

Injecting this expression in (F.1.7) gives, $\forall n \geq 3$,

$$a_{1,\alpha_1..\alpha_n}^{(n)} = u_{\alpha_n} a_{1,\alpha_1..\alpha_{n-1}}^{(n-1)} + c_s^2(\theta - 1) \sum_{i=1}^{n-1} \delta_{\alpha_i \alpha_n} a_{1,\beta_i}^{(n-2)}$$

$$- \tau c_s^2 \theta \sum_{i=1}^{n-1} a_{0,\beta_i}^{(n-2)} \left(\partial_{\alpha_i} u_{\alpha_n} + \partial_{\alpha_n} u_{\alpha_i} - \frac{2}{D} \delta_{\alpha_i \alpha_n} \partial_\gamma u_\gamma \right)$$

$$- \tau c_s^4 \theta \sum_{i=1}^{n-1} \sum_{j>i}^{n-1} \left(\delta_{\alpha_i \alpha_n} \partial_{\alpha_j} \theta + \delta_{\alpha_j \alpha_n} \partial_{\alpha_i} \theta + \delta_{\alpha_i \alpha_j} \partial_{\alpha_n} \theta \right) a_{0,\beta_{ij}}^{(n-3)}. \qquad \text{(F.1.10)}$$

Finally, knowing that

$$a_{1,\alpha\beta}^{(2)} = -\tau \rho c_s^2 \theta \left(\partial_\alpha u_\beta + \partial_\beta u_\alpha - \frac{2}{D} \delta_{\alpha\beta} \partial_\gamma u_\gamma \right) \equiv \Pi_{\alpha\beta}^{(1)} \approx \sum_i \xi_\alpha \xi_\beta \left(f_i - f_i^{(0)} \right),$$

$$a_{1,\alpha\beta\gamma}^{(3)} = u_\alpha a_{1,\beta\gamma}^{(2)} + u_\beta a_{1,\alpha\gamma}^{(2)} + u_\gamma a_{1,\alpha\beta}^{(2)} - \tau \rho \theta c_s^4 \left(\delta_{\alpha\beta} \partial_\gamma \theta + \delta_{\alpha\gamma} \partial_\beta \theta + \delta_{\beta\gamma} \partial_\alpha \theta \right)$$

$$\equiv Q_{\alpha\beta\gamma}^{(1)} \approx \sum_i \xi_\alpha \xi_\beta \xi_\gamma \left(f_i - f_i^{(0)} \right),$$

leads to (F.1.1), which is valid for $n \geq 4$.

∎

Particularity of the isothermal case

The same kind of recursive relation can be obtained in the isothermal case, after noticing that this assumption has two important consequences in the previous derivation:

- the temperature is constant ($\theta = 1$),

- the term $-\dfrac{2}{D} \delta_{\alpha_i \alpha_n} \partial_\gamma u_\gamma$ disappears in (F.1.10), leading to a non-zero bulk viscosity $\mu_b = \dfrac{2}{D} \mu$ [118].

Thus equation (F.1.10) becomes

$$\forall n \geq 3, \ a_{1,\alpha_1..\alpha_n}^{(n)} = u_{\alpha_n} a_{1,\alpha_1..\alpha_{n-1}}^{(n-1)} - \tau c_s^2 \sum_{i=1}^{n-1} a_{0,\beta_i}^{(n-2)} \left(\partial_{\alpha_i} u_{\alpha_n} + \partial_{\alpha_n} u_{\alpha_i} \right), \qquad \text{(F.1.11)}$$

and knowing that

$$a_{1,\alpha\beta}^{(2)} = -\tau \rho c_s^2 (\partial_\alpha u_\beta + \partial_\beta u_\alpha),$$

Malaspinas' recursive formula [134] can be recovered:

$$a_{1,\alpha_1..\alpha_n}^{(n)} = u_{\alpha_n} a_{1,\alpha_1..\alpha_{n-1}}^{(n-1)} + \frac{1}{\rho} \sum_{i=1}^{n-1} a_{0,\beta_i}^{(n-2)} a_{1,\alpha_i \alpha_n}^{(2)} \qquad \text{(F.1.12)}$$

F.2   Equilibrium coefficients

The aim of this section is to prove the following relation

$$\forall n \geq 2, \quad a^{(n)}_{0,\alpha_1..\alpha_n} = u_{\alpha_n} a^{(n-1)}_{0,\alpha_1..\alpha_{n-1}} + (\theta - 1)c_s^2 \sum_{i=1}^{n-1} \delta_{\alpha_i \alpha_n} a^{(n-2)}_{0,\beta_i}, \qquad \text{(F.2.1)}$$

which simplifies in

$$\forall n \geq 2, \quad a^{(n)}_{0,\alpha_1..\alpha_n} = u_{\alpha_n} a^{(n-1)}_{0,\alpha_1..\alpha_{n-1}}$$

for the isothermal case ($\theta = 1$). To this end, the Rodrigues relation over Hermite polynomials will be used:

$$\forall n \geq 2, \quad \xi_{\alpha_n} \mathcal{H}^{(n-1)}_{\alpha_1..\alpha_{n-1}} = \mathcal{H}^{(n)}_{\alpha_1..\alpha_n} + c_s^2 \sum_{i=1}^{n-1} \delta_{\alpha_i \alpha_n} \mathcal{H}^{(n-2)}_{\beta_i}. \qquad \text{(F.2.2)}$$

Using this relation, one gets, for $n \geq 2$:

$$a^{(n)}_{0,\alpha_1..\alpha_n} = \int \mathcal{H}^{(n)}_{\alpha_1..\alpha_n}(\boldsymbol{\xi}) f^{(eq)}(\boldsymbol{\xi}) \mathrm{d}\boldsymbol{\xi} = \int \xi_{\alpha_n} \mathcal{H}^{(n-1)}_{\alpha_1..\alpha_{n-1}} f^{(eq)}(\boldsymbol{\xi}) \mathrm{d}\boldsymbol{\xi} - c_s^2 \sum_{i=1}^{n-1} \delta_{\alpha_i \alpha_n} \int \mathcal{H}^{(n-2)}_{\beta_i} f^{(eq)}(\boldsymbol{\xi}) \mathrm{d}\boldsymbol{\xi}$$

$$= \underbrace{\int c_{\alpha_n} \mathcal{H}^{(n-1)}_{\alpha_1..\alpha_{n-1}} f^{(eq)}(\boldsymbol{\xi}) \mathrm{d}\boldsymbol{\xi}}_{I} + u_{\alpha_n} a^{(n-1)}_{0,\alpha_1..\alpha_{n-1}} - c_s^2 \sum_{i=1}^{n-1} \delta_{\alpha_i \alpha_n} a^{(n-2)}_{0,\beta_i},$$

where $\boldsymbol{c} = \boldsymbol{\xi} - \boldsymbol{u}$. By integration by parts, the first term gives

$$I = \theta c_s^2 \int \partial_{\xi_{\alpha_n}} \mathcal{H}^{(n-1)}_{\alpha_1..\alpha_{n-1}} f^{(eq)}(\boldsymbol{\xi}) \mathrm{d}\boldsymbol{\xi}.$$

Finally, using the fact that

$$\partial_{\xi_{\alpha_n}} \mathcal{H}^{(n-1)}_{\alpha_1..\alpha_{n-1}} = \sum_{i=1}^{n-1} \delta_{\alpha_i \alpha_n} \mathcal{H}^{(n-2)}_{\beta_i},$$

one gets

$$I = \theta c_s^2 \sum_{i=1}^{n-1} \delta_{\alpha_i \alpha_n} a^{(n-2)}_{0,\beta_i},$$

so that

$$\forall n \geq 2, \quad a^{(n)}_{0,\alpha_1..\alpha_n} = u_{\alpha_n} a^{(n-1)}_{0,\alpha_1..\alpha_{n-1}} + (\theta - 1)c_s^2 \sum_{i=1}^{n-1} \delta_{\alpha_i \alpha_n} a^{(n-2)}_{0,\beta_i}.$$

■

Appendix G

Implementation Details

This appendix summarizes all the necessary material to properly implement the recursive regularization procedure, in both 2D and 3D, for some common and high-order lattice structures. As a reminder, the purpose of this step is to rebuilt the discrete VDF f_i knowing the macroscopic properties of the flow (density ρ, velocity $\boldsymbol{u}$ and temperature θ) and their gradients:

$$f_i^{reg} = f_i^{(0),reg} + f_i^{(1),reg} = \sum_n \frac{1}{n! c_s^{2n}} \mathcal{H}_{i,\alpha}^{(n)} \left(a_{0,\alpha}^{(n)} + a_{1,\alpha}^{(n)} \right).$$

G.1 Hermite tensors

The definition of Hermite tensors up to the fourth order (sufficient for the recovery of Navier-Stokes' equations) is

$$
\begin{aligned}
\mathcal{H}_i^{(0)} &= 1, \\
\mathcal{H}_{i,\alpha}^{(1)} &= \xi_{i,\alpha}, \\
\mathcal{H}_{i,\alpha\beta}^{(2)} &= \xi_{i,\alpha\beta} - c_s^2 \delta_{\alpha\beta}, \\
\mathcal{H}_{i,\alpha\beta\gamma}^{(3)} &= \xi_{i,\alpha\beta\gamma} - c_s^2 \left(\xi_{i,\alpha}\delta_{\beta\gamma} + \xi_{i,\beta}\delta_{\alpha\gamma} + \xi_{i,\gamma}\delta_{\alpha\beta} \right), \\
\mathcal{H}_{i,\alpha\beta\gamma\delta}^{(4)} &= \xi_{i,\alpha\beta\gamma\delta} - c_s^2 \left(\xi_{i,\alpha\beta}\delta_{\gamma\delta} + \xi_{i,\alpha\gamma}\delta_{\beta\delta} + \xi_{i,\alpha\delta}\delta_{\beta\gamma} + \xi_{i,\beta\gamma}\delta_{\alpha\delta} + \xi_{i,\beta\delta}\delta_{\alpha\gamma} + \xi_{i,\gamma\delta}\delta_{\alpha\beta} \right) \\
&\quad + c_s^4 \left(\delta_{\alpha\beta}\delta_{\gamma\delta} + \delta_{\alpha\gamma}\delta_{\beta\delta} + \delta_{\alpha\delta}\delta_{\beta\gamma} \right),
\end{aligned}
$$

where the following mathematical notations $\xi_{i,\alpha\beta} \equiv \xi_{i,\alpha}\xi_{i,\beta}$, $\xi_{i,\alpha\beta\gamma} \equiv \xi_{i,\alpha}\xi_{i,\beta}\xi_{i,\gamma}$, $\xi_{i,\alpha\beta\gamma\delta} \equiv \xi_{i,\alpha}\xi_{i,\beta}\xi_{i,\gamma}\xi_{i,\delta}$ is used for the sake of compacity.
In 2D, $(\alpha, \beta, \gamma, \delta) \in \{x, y\}^4$ and thus only two different values can be chosen for each index. This simplifies the definition of Hermite polynomials into:

$$
\begin{aligned}
\mathcal{H}_i^{(0)} &= 1, \\
\mathcal{H}_{i,x}^{(1)} &= \xi_{i,x}, \\
\mathcal{H}_{i,xx}^{(2)} &= \xi_{i,x}^2 - c_s^2, \quad \mathcal{H}_{i,xy}^{(2)} = \xi_{i,x}\xi_{i,y},
\end{aligned}
$$

$$\mathcal{H}_{i,xxx}^{(3)} = \left(\xi_{i,x}^2 - 3c_s^2\right)\xi_{i,x}, \ \mathcal{H}_{i,xxy}^{(3)} = \left(\xi_{i,x}^2 - c_s^2\right)\xi_{i,y},$$
$$\mathcal{H}_{i,xxxx}^{(4)} = \xi_{i,x}^4 - 6c_s^2\xi_{i,x}^2 + 3c_s^4, \ \mathcal{H}_{i,xxxy}^{(4)} = \left(\xi_{i,x}^2 - 3c_s^2\right)\xi_{i,x}\xi_{i,y}, \ \mathcal{H}_{i,xxyy}^{(4)} = (\xi_{i,x}^2 - c_s^2)(\xi_{i,y}^2 - c_s^2).$$

In 3D, $(\alpha, \beta, \gamma, \delta) \in \{x, y, z\}^4$ and therefore one more value can be chosen for each index. This adds the following Hermite polynomials:

$$\mathcal{H}_{i,xyz}^{(3)} = \xi_{i,x}\xi_{i,y}\xi_{i,z},$$
$$\mathcal{H}_{i,xxyz}^{(4)} = \xi_{i,x}^2\xi_{i,y}\xi_{i,z} - c_s^2\xi_{i,y}\xi_{i,z} + c_s^4.$$

Due to symmetry properties of Hermite tensors $(\mathcal{H}_{i,y}^{(1)}, \mathcal{H}_{i,z}^{(1)}, \mathcal{H}_{i,yy}^{(2)}, \mathcal{H}_{i,zz}^{(2)}, \mathcal{H}_{i,xz}^{(2)}, \mathcal{H}_{i,yz}^{(2)}, \mathcal{H}_{i,yyy}^{(3)},$ $\mathcal{H}_{i,zzz}^{(3)}, \ \mathcal{H}_{i,xxz}^{(3)}, \ \mathcal{H}_{i,yyx}^{(3)}, \ \mathcal{H}_{i,yyz}^{(3)}, \ \mathcal{H}_{i,yyyy}^{(4)}, \ \mathcal{H}_{i,zzzz}^{(4)}, \ \mathcal{H}_{i,xxxz}^{(4)}, \ \mathcal{H}_{i,yyyx}^{(4)}, \ \mathcal{H}_{i,yyyz}^{(4)}, \ \mathcal{H}_{i,xxzz}^{(4)}, \ \mathcal{H}_{i,yyzz}^{(4)},$ $\mathcal{H}_{i,yyxz}^{(4)}, \ \mathcal{H}_{i,zzxy}^{(4)})$ can be obtained changing x by y or z in the above formulas. By definition, the very same property is also available for $a_{0,\boldsymbol{\alpha}}^{(n)}$ and $a_{1,\boldsymbol{\alpha}}^{(n)}$.

G.2   Hermite coefficients at equilibrium

The recursive definition of Hermite coefficients at equilibrium is first recalled (F.2.1). Up to the fourth order, they read

$$a_0^{(0)} = \rho,$$
$$a_{0,\alpha}^{(1)} = u_\alpha a_0^{(0)},$$
$$a_{0,\alpha\beta}^{(2)} = u_\beta a_{0,\alpha}^{(1)} + (\theta - 1)c_s^2\delta_{\alpha\beta}a_0^{(0)},$$
$$a_{0,\alpha\beta\gamma}^{(3)} = u_\gamma a_{0,\alpha\beta}^{(2)} + (\theta - 1)c_s^2\left(\delta_{\alpha\gamma}a_{0,\beta}^{(1)} + \delta_{\beta\gamma}a_{0,\alpha}^{(1)}\right),$$
$$a_{0,\alpha\beta\gamma\delta}^{(4)} = u_\delta a_{0,\alpha\beta\gamma}^{(3)} + (\theta - 1)c_s^2\left(\delta_{\alpha\delta}a_{0,\beta\gamma}^{(2)} + \delta_{\beta\delta}a_{0,\alpha\gamma}^{(2)} + \delta_{\gamma\delta}a_{0,\alpha\beta}^{(2)}\right).$$

This becomes in 2D,

$$a_0^{(0)} = \rho,$$
$$a_{0,x}^{(1)} = u_x a_0^{(0)},$$
$$a_{0,xx}^{(2)} = u_x a_{0,x}^{(1)} + (\theta - 1)c_s^2 a_0^{(0)}, \ a_{0,xy}^{(2)} = u_y a_{0,x}^{(1)},$$
$$a_{0,xxx}^{(3)} = u_x a_{0,xx}^{(2)} + 2(\theta - 1)c_s^2 a_{0,x}^{(1)}, \ a_{0,xxy}^{(3)} = u_y a_{0,xx}^{(2)},$$
$$a_{0,xxxx}^{(4)} = u_x a_{0,xxx}^{(3)} + 3(\theta - 1)c_s^2 a_{0,xx}^{(2)}, \ a_{0,xxxy}^{(4)} = u_y a_{0,xxx}^{(3)}, \ a_{0,xxyy}^{(4)} = u_y a_{0,xxy}^{(3)} + (\theta - 1)c_s^2 a_{0,xx}^{(2)}.$$

And the 3D extension adds the following coefficients,

$$a_{0,xyz}^{(3)} = u_z a_{0,xy}^{(2)},$$
$$a_{0,xxyz}^{(4)} = u_z a_{0,xxy}^{(3)}.$$

G.3 First-order off-equilbrium Hermite coefficients

The recursive definition of first-order (with respect to the Knudsen number) off-equilibrium Hermite coefficients Eq. (4.3.5), up to the fourth order (with respect to the VDF moments), reads

$$
\begin{aligned}
a_1^{(0)} &= 0, \\
a_{1,\alpha}^{(1)} &= 0, \\
a_{1,\alpha\beta}^{(2)} &= \Pi_{\alpha\beta}^{(1)} = -\mu c_s^2 \theta \Big[S_{\alpha\beta} - \left(\tfrac{2}{D} \partial_\gamma u_\gamma \right) \delta_{\alpha\beta} \Big], \\
a_{1,\alpha\beta\gamma}^{(3)} &= Q_{\alpha\beta\gamma}^{(1)} = \left(u_\alpha a_{1,\beta\gamma}^{(2)} + u_\beta a_{1,\alpha\gamma}^{(2)} + u_\gamma a_{1,\alpha\beta}^{(2)} \right) - \mu c_s^2 (\delta_{\alpha\beta}\partial_\gamma\theta + \delta_{\alpha\gamma}\partial_\beta\theta + \delta_{\beta\gamma}\partial_\alpha\theta), \\
a_{1,\alpha\beta\gamma\delta}^{(4)} &= \left(u_\alpha a_{1,\beta\gamma\delta}^{(3)} + u_\beta a_{1,\alpha\gamma\delta}^{(3)} + u_\gamma a_{1,\alpha\beta\delta}^{(3)} + u_\delta a_{1,\alpha\beta\gamma}^{(3)} \right) \hspace{2cm} \text{(G.3.1)} \\
&\quad + \Big[c_s^2(\theta-1)\delta_{\alpha\beta} - u_\alpha u_\beta \Big] a_{1,\gamma\delta}^{(2)} + \Big[c_s^2(\theta-1)\delta_{\alpha\gamma} - u_\alpha u_\gamma \Big] a_{1,\beta\delta}^{(2)} \\
&\quad + \Big[c_s^2(\theta-1)\delta_{\alpha\delta} - u_\alpha u_\delta \Big] a_{1,\beta\gamma}^{(2)} + \Big[c_s^2(\theta-1)\delta_{\beta\gamma} - u_\beta u_\gamma \Big] a_{1,\alpha\delta}^{(2)} \\
&\quad + \Big[c_s^2(\theta-1)\delta_{\beta\delta} - u_\beta u_\delta \Big] a_{1,\alpha\gamma}^{(2)} + \Big[c_s^2(\theta-1)\delta_{\gamma\delta} - u_\gamma u_\delta \Big] a_{1,\alpha\beta}^{(2)},
\end{aligned}
$$

with $S_{\alpha\beta} = \partial_\alpha u_\beta + \partial_\beta u_\alpha$, and $\mu = \rho c_s^2 \theta \tau$ is the dynamic viscosity.

For the 2D case, this simplifies into,

$$
\begin{aligned}
a_1^{(0)} &= 0, \\
a_{1,x}^{(1)} &= 0, \\
a_{1,xx}^{(2)} &= \Pi_{xx}^{(1)} = -\mu c_s^2 \theta \Big[S_{xx} - \tfrac{2}{D} \partial_\gamma u_\gamma \Big], \quad a_{1,xy}^{(2)} = \Pi_{xy}^{(1)} = -\tau \rho c_s^2 \theta S_{xy} \\
a_{1,xxx}^{(3)} &= Q_{xxx}^{(1)} = 3 \left(u_x a_{1,xx}^{(2)} - \mu c_s^2 \partial_x \theta \right), \quad a_{1,xxy}^{(3)} = Q_{xxy}^{(1)} = \left(2u_x a_{1,xy}^{(2)} + u_y a_{1,xx}^{(2)} \right) - \mu c_s^2 \partial_y \theta, \\
a_{1,xxxx}^{(4)} &= 4u_x a_{1,xxx}^{(3)} + 6 \Big[c_s^2(\theta-1) - u_x^2 \Big] a_{1,xx}^{(2)}, \hspace{2cm} \text{(G.3.2)} \\
a_{1,xxxy}^{(4)} &= \left(3u_x a_{1,xxy}^{(3)} + u_y a_{1,xxx}^{(3)} \right) + 3 \Big[c_s^2(\theta-1) - u_x^2 \Big] a_{1,xy}^{(2)} - 3u_x u_y a_{1,xx}^{(2)}, \\
a_{1,xxyy}^{(4)} &= 2 \left(u_x a_{1,yyx}^{(3)} + u_y a_{1,xxy}^{(3)} \right) + \Big[c_s^2(\theta-1) - u_x^2 \Big] a_{1,yy}^{(2)} + \Big[c_s^2(\theta-1) - u_y^2 \Big] a_{1,xx}^{(2)} \\
&\quad - 4u_x u_y a_{1,xy}^{(2)}.
\end{aligned}
$$

And for the 3D extension, more coefficients need to be taken into account,

$$
\begin{aligned}
a_{1,xyz}^{(3)} &= Q_{xyz}^{(1)} = u_x a_{1,yz}^{(2)} + u_y a_{1,xz}^{(2)} + u_z a_{1,xy}^{(2)}, \\
a_{1,xxyz}^{(4)} &= \left(2u_x a_{1,xyz}^{(3)} + u_y a_{1,xxz}^{(3)} + u_z a_{1,xxy}^{(3)} \right) + \Big[c_s^2(\theta-1) - u_x^2 \Big] a_{1,yz}^{(2)} \\
&\quad - 2u_x \left(u_y a_{1,xz}^{(2)} + u_z a_{1,xy}^{(2)} \right) - u_y u_z a_{1,xx}^{(2)}.
\end{aligned}
$$

Here attention must be paid to the way $a^{(2)}_{1,\alpha\beta}$ and $a^{(3)}_{1,\alpha\beta\gamma}$ are computed. One can use finite differences to evaluate the velocity and temperature gradients, but it will degrade the accuracy of the algorithm. Instead, we propose the following idea for LBM allowing the preservation of moments of the VDF up to the fourth order (*D2V37* and *D3Q103*):

1. Compute $a^{(2)}_{1,\alpha\beta}$ using the definition of the second-order moment of the VDF,

$$a^{(2)}_{1,\alpha\beta} \approx \sum_i \mathcal{H}^{(2)}_{\alpha\beta}\Big(f_i - f_i^{(0)}\Big). \tag{G.3.3}$$

   This is justified by the fact that the error introduced by the approximation $f_i = \sum_n f_i^{(n)} \approx f_i^{(0)} + f_i^{(1)}$, with $f_i^{(n)} \sim \mathcal{O}(\epsilon^n)$, should be small enough when the LBM allows to conserve moments of the VDF up to the fourth order.

2. Compute $a^{(3)}_{1,\alpha\beta\gamma}$ using the definition of the third-order moment of the VDF,

$$a^{(3)}_{1,\alpha\beta\gamma} \approx \sum_i \mathcal{H}^{(3)}_{\alpha\beta\gamma}\Big(f_i - f_i^{(0)}\Big).$$

3. Average the contributions of all $a^{(3)}_{1,\alpha\beta\gamma}$ to the temperature gradients,

$$\mu c_s^2 \partial_x \theta \stackrel{2D}{=} \frac{1}{2}\Big[\Big(u_x a^{(2)}_{1,xx} - a^{(3)}_{1,xxx}/3\Big) + \Big(2u_y a^{(2)}_{1,xy} + u_x a^{(2)}_{1,yy} - a^{(3)}_{1,yyx}\Big)\Big] \tag{G.3.4}$$

$$\stackrel{3D}{=} \frac{1}{3}\Big[\Big(u_x a^{(2)}_{1,xx} - a^{(3)}_{1,xxx}/3\Big) + \Big(2u_y a^{(2)}_{1,xy} + u_x a^{(2)}_{1,yy} - a^{(3)}_{1,yyx}\Big)$$

$$+ \Big(2u_z a^{(2)}_{1,xz} + u_x a^{(2)}_{1,zz} - a^{(3)}_{1,zzx}\Big)\Big] \tag{G.3.5}$$

4. Reconstruct $a^{(3)}_{1,\alpha\beta\gamma}$ using Eq. (G.3.2) thanks to Eqs. (G.3.3) & (G.3.5).

G.4   Regularized collision operator

The regularization procedure of pre-collision VDFs can be interpreted as a particular collision step where

$$f_i^{coll} = f_i^{(0),reg} + \Big(1 - \frac{1}{\tau}\Big)f_i^{(1),reg} = \omega_i \sum_n \frac{A_{\boldsymbol{\alpha}}^{(n)}}{n!c_s^{2n}}\mathcal{H}^{(n)}_{i,\boldsymbol{\alpha}}\Big(a^{(n)}_{0,\boldsymbol{\alpha}} + \Big(1 - \frac{1}{\tau_{n,\boldsymbol{\alpha}}}\Big)a^{(n)}_{1,\boldsymbol{\alpha}}\Big),$$

with $A_{\boldsymbol{\alpha}}^{(n)}$ being the number of times each Hermite tensors appears in the expansion. As an example, $\mathcal{H}^{(3)}_{i,xxy}$ appears three times in the above development since $\mathcal{H}^{(3)}_{i,xxy} = \mathcal{H}^{(3)}_{i,xyx} = \mathcal{H}^{(3)}_{i,yxx}$. This property is taken into account imposing $A^{(3)}_{xxy} = 3$. And more generally,

$$A_{\boldsymbol{\alpha}}^{(n)} \stackrel{2D}{=} \binom{n}{n_x} = \frac{n!}{n_x!(n - n_x)!} = \frac{(n_x + n_y)!}{n_x!n_y!}, \tag{G.4.1}$$

$$\stackrel{3D}{=} \binom{n}{n_x} \binom{(n-n_x)}{n_y} = \frac{(n_x + n_y + n_z)!}{n_x! n_y! n_z!}. \qquad \text{(G.4.2)}$$

It flows from Pascal's triangle and pyramid rules (also called binomial and trinomial expansions) using n_x, n_y and n_z the number of occurrences of x, y and z in $\boldsymbol{\alpha} = (\alpha_1, .., \alpha_n)$ respectively. It should be noted that Eq. (G.4) is the most general form of the regularized collision step, which allows to decouple the relaxation process specific to each Hermite coefficients. A similar formula was previously given by Shan & Chen [115] where all Hermite coefficients belonging to the same expansion order n were related by the same relaxation time, *i.e.*, $\tau_{n,\boldsymbol{\alpha}} \longrightarrow \tau_n$. The latter formulation allows to preserve isotropy properties of the LBM and is thus preferred.

Appendix H

LSA - Eigenvalue problems

This appendix is dedicated to the derivation of eigenvalue problems associated to the BGK and regularized collision models.

H.1 Eigenvalue problem for a general collision term

Let us start from the force-free LBE with a general collision model,

$$\partial_t f_i + \boldsymbol{\xi}_i \cdot \boldsymbol{\nabla} f_i = \Omega_i^{\mathrm{C}}. \tag{H.1.1}$$

A first-order Taylor expansion around a uniform mean flow leads to

$$f_i \approx \overline{f_i} + f_i' \quad \& \quad \Omega_i^*(f_j) \approx \Omega_i^*|_{\overline{f_j}} + J_{ij}^* f_j', \tag{H.1.2}$$

where $J_{ij}^* = \left.\frac{\partial \Omega_i^*}{\partial f_j}\right|_{\overline{f_j}}$ is the Jacobian matrix of either the continuous ($* = C$) or the discrete ($* = D$) collision operator evaluated at $f_j = \overline{f_j}$. The overline superscript indicates uniform mean quantities. Einstein's summation rule is used on index "j".

Injecting Eq. (H.1.2) into Eq. (H.1.1), we obtain

$$\partial_t f_i' + \boldsymbol{\xi}_i \cdot \boldsymbol{\nabla} f_i' = J_{ij}^{\mathrm{C}} f_j' - \underbrace{\left(\partial_t \overline{f_i} + \boldsymbol{\xi}_i \cdot \boldsymbol{\nabla} \overline{f_i} - \Omega_i^{\mathrm{C}}|_{\overline{f_j}} \right)}_{A}.$$

with $A = 0$ since $\overline{f_i}$ is by definition solution of Eq. (H.1.1). Eventually, we end up with the following continuous LBE for perturbations

$$\boxed{\boxed{\partial_t f_i' + \boldsymbol{\xi}_i \cdot \boldsymbol{\nabla} f_i' = J_{ij}^{\mathrm{C}} f_j'}} \tag{H.1.3}$$

If we now apply the very same protocol to the space/time discrete LBE,

$$f_i(\boldsymbol{x} + \xi_i, t + 1) = f_i(\boldsymbol{x}, t) + \Omega_i^{\mathrm{D}}(\boldsymbol{x}, t), \tag{H.1.4}$$

this leads to

$$f_i'(\boldsymbol{x} + \xi_i, t + 1) = f_i'(\boldsymbol{x}, t) + J_{ij}^{\mathrm{D}}(\boldsymbol{x}, t) f_j'(\boldsymbol{x}, t) - \underbrace{\left(\overline{f_i}(\boldsymbol{x} + \xi_i, t + 1) - \overline{f_i}(\boldsymbol{x}, t) + \Omega_i^{\mathrm{D}}|_{\overline{f_i}}(\boldsymbol{x}, t) \right)}_{B},$$

with $B = 0$ since $\overline{f_i}(\boldsymbol{x}, t)$ is by definition solution of Eq. (H.1.4). The associated perturbed equation is then

$$\boxed{f_i'(\boldsymbol{x} + \xi_i, t + 1) = \left[\delta_{ij} + J_{ij}^{\mathrm{D}}\right] f_j'(\boldsymbol{x}, t)} \tag{H.1.5}$$

To derive eigenvalue problems which will lead to the computation of perturbation growth rates, the monochromatic plane wave assumption is adopted for VDFs perturbations:

$$f_i' = A_i \exp[\mathrm{i}(\boldsymbol{k} \cdot \boldsymbol{x} - \omega t)]. \tag{H.1.6}$$

Since we are only interested in the time evolution of perturbations, only the time frequency ω will be complex. This leads to $(\boldsymbol{k}, \omega) \in \mathbb{R}^D \times \mathbb{C}$. With the assumption of monochromatic plane waves (H.1.6), the continuous perturbed LBE (H.1.1) becomes

$$(-\mathrm{i}\omega + \mathrm{i}\boldsymbol{\xi}_i \cdot \boldsymbol{k}) f_i' = J_{ij}^{\mathrm{C}} f_j'$$

or equivalently,

$$\boxed{\omega \boldsymbol{X} = \left[\boldsymbol{E}^{\mathbf{C}} + \mathrm{i}\boldsymbol{J}^{\mathrm{C}}\right] \boldsymbol{X}} \quad \textbf{Eigenvalue problem (continuous)},$$

with ω the eigenvalue, $X_i = f_i'$ the eigenvector, and $E_{ij}^{\mathrm{C}} = (\boldsymbol{\xi}_i \cdot \boldsymbol{k}) \delta_{ij}$. In the discrete case, the monochromatic plane wave assumption leads to

$$\exp[\mathrm{i}(\omega - \boldsymbol{\xi}_i \cdot \boldsymbol{k})] f_i'(\boldsymbol{x}, t) = \left[\delta_{ij} + J_{ij}^{\mathrm{D}}\right] f_j'(\boldsymbol{x}, t),$$

so that

$$\boxed{\exp(-\mathrm{i}\omega) \boldsymbol{X} = \boldsymbol{E}^{\mathbf{D}} \left[\boldsymbol{\delta} + \boldsymbol{J}^{\mathrm{D}}\right] \boldsymbol{X}} \quad \textbf{Eigenvalue problem (discrete)},$$

with $\exp(-\mathrm{i}\omega)$ the eigenvalue, $X_i = f_i'$ the eigenvector, and $E_{ij}^{\mathrm{D}} = \exp[-\mathrm{i}(\boldsymbol{\xi}_i \cdot \boldsymbol{k})] \delta_{ij}$.

H.2 BGK collision model

For the BGK collision model,

$$\Omega_i^{\mathrm{C}} = -\frac{1}{\tau}\left(f_i - f_i^{(0)}\right) \quad \& \quad \Omega_i^{\mathrm{D}} = -\frac{1}{\tau + 1/2}\left(f_i - f_i^{(0)}\right)$$

hence

$$J_{ij}^{\mathrm{C}} = -\frac{1}{\tau}\left(\delta_{ij} - J_{ij}^{(0)}\right) \quad \& \quad J_{ij}^{\mathrm{D}} = -\frac{1}{\tau + 1/2}\left(\delta_{ij} - J_{ij}^{(0)}\right),$$

with $J_{ij}^{(0)} = \left.\dfrac{\partial f_i^{(0)}}{\partial f_j}\right|_{f_j = \overline{f_j}}$. As an example, if we consider an equilibrium function truncated at first order $(N = 1)$

$$f_i^{(0),N=1} = \omega_i \rho \left(1 + \frac{\boldsymbol{\xi}_i \cdot \boldsymbol{u}}{c_s^2}\right), \tag{H.2.1}$$

then

$$J_{ij}^{(0),N=1} = \omega_i \left(1 + \frac{\boldsymbol{\xi}_i \cdot \boldsymbol{\xi}_j}{c_s^2} \right) \tag{H.2.2}$$

since $\rho = \sum_i f_i$ and $\rho \boldsymbol{u} = \sum_i \xi_i f_i$. To linearize high-order truncations of $f_i^{(0)}$, it is necessary to express all macroscopic quantities with respect to moments of $f_i^{(0)}$. Since a large number of velocity sets are considered in the present work, the linearization process is eased using standard numerical libraries.

Eventually, eigenvalue problems related to the BGK collision operator read as

$$\boxed{\omega \boldsymbol{X} = \left[\boldsymbol{E}^{\mathbf{C}} - \frac{\mathrm{i}}{\tau} \left(\boldsymbol{\delta} - \boldsymbol{J}^{(0)} \right) \right] \boldsymbol{X}} \quad \textbf{Eigenvalue problem (continuous)},$$

and

$$\boxed{\exp(-\mathrm{i}\omega)\boldsymbol{X} = \boldsymbol{E}^{\mathbf{D}} \left[\boldsymbol{\delta} - \frac{1}{\tau + 1/2} \left(\boldsymbol{\delta} - \boldsymbol{J}^{(0)} \right) \right] \boldsymbol{X}} \quad \textbf{Eigenvalue problem (discrete)}.$$

H.3   Regularized collision models

Regarding regularized collision models, the present study is restricted to the discrete case (H.1). Before detailing the linearization of this collision model, let us recall the general expression of the single-relaxation-time regularized collision model:

$$\Omega_i^D = -\frac{1}{\tau + 1/2} \sum_n \frac{\omega_i}{n! c_s^2} \boldsymbol{a}_1^{(n)} : \boldsymbol{\mathcal{H}}_i^{(n)}, \tag{H.3.1}$$

where

$$\boldsymbol{a}_{1,\mathrm{PR}}^{(n)} = \sum_i \left(f_i - f_i^{(0)} \right) \boldsymbol{\mathcal{H}}_i^{(n)} \quad \& \quad \boldsymbol{a}_{1,\mathrm{RR}}^{(n)} = \sum_i f_i^{(1)} \boldsymbol{\mathcal{H}}_i^{(n)}. \tag{H.3.2}$$

The subscript PR stands for the projection based regularized collision model, while RR is for the recursive approach. In the case of the PR process, coefficients of its jacobian matrix read as

$$J_{ij,\mathrm{PR}}^{\mathrm{D}} = -\frac{1}{\tau + 1/2} \sum_n \frac{\omega_i}{n! c_s^2} \left[\sum_l \left(\delta_{lj} - J_{lj}^{(0)} \right) \mathcal{H}_l^{(n)} \right] \mathcal{H}_i^{(n)}$$

$$= -\frac{1}{\tau + 1/2} \sum_n A_{ij,\mathrm{PR}}^{(n)}$$

For the RR approach, the recursive formula for the computation of $\boldsymbol{a}_{1,\mathrm{RR}}^{(n)}$ (4.3.6) requires further linearizations. As an example, $a_{1,xxx}^{(3)} = 3u_x a_{1,xx}^{(2)}$ in the isothermal case. Hence

$$\frac{\partial a_{1,xxx}^{(3)}}{\partial f_j} = 3 \left(u_x \frac{\partial a_{1,xx}^{(2)}}{\partial f_j} + a_{1,xx}^{(2)} \frac{\partial u_x}{\partial f_j} \right).$$

Nevertheless, the form of $J^{\mathrm{D}}_{ij,\mathrm{RR}}$ remains similar to $J^{\mathrm{D}}_{ij,\mathrm{PR}}$. Eventually, the eigenvalue problem related to regularized LBMs reads as

$$
\exp(-\mathrm{i}\omega)\boldsymbol{X} = \boldsymbol{E}^{\mathbf{D}}\left[\boldsymbol{\delta} - \frac{1}{\tau + 1/2}\sum_{n}\boldsymbol{A}^{(n)}\right]\boldsymbol{X}
$$

Eigenvalue problem (discrete).

Appendix I

Online Course & Instructor-Led Trainings

Some parallel activities conducted within the framework of the present PhD work are summarized below. They include designing, developing and carrying out an online course and training sessions.

I.1 E-Learning: Small Private Online Course

Starting with the massive open online course (MOOC), it is an online open access course with no restriction on the number of participants. It aims at providing knowledge on a particular topic, and promotes the communication between participants through forums. During this PhD work, a particular version of the MOOC, named SPOC (small private online course), was developed at CERFACS under the supervision of Jean-François Parmentier ('Fundamentals of lattice Boltzmann method'). Typically, SPOCs are fully online training sessions on a particular topic. They are divided into consecutive weeks (typically 3 to 6), and are based on learning activities delivered each week. They focus on a conceptual understanding of the meaning of equations and how they apply in practical cases. These SPOCs are organized around activities especially designed to make participants interact between each other, involving a deep processing of the scientific content previously shown in short videos (about 5-min long).

Here, a SPOC was created to provide engineers, MS and PhD students a basic, but essential, understanding of the LBM. As a starting, three major learning objectives were chosen, and allowed to design four weeks of online courses. In our opinion, it was mandatory that at the end of the SPOC, participants must be able to: (i) evaluate the relevance of using LBM for a given case (benefits and limitations as compared to standard NSF solvers), (ii) choose the appropriate lattice and equilibrium VDF depending on physical phenomena of interest, and (iii) explain the numerical efficiency of LBMs (wall-clock time and accuracy) with respect to standard NSF solvers.

With this idea in mind, a particular topic was assigned to each week. The first week is dedicated to the presentation of general features of the LBM. The second week deals with the origin of the LBM, namely, the kinetic theory of gases and more specifically its

milestone: the Boltzmann equation. The third week aims at explaining how to numerically solve the Boltzmann equation, starting with the velocity space discretization and it coupling with the numerical discretization through the 'Collide & Stream' algorithm. The last week is devoted to recalls on notions introduced in previous weeks, supplemented with a 'live session' during which more practical aspect are tackled. The online course concludes with an examination, in the form of a MCQ (multiple choice quiz), that leads to a certificate.

This collaborative work was done under the supervision of J.-F. Parmentier, and with the help of G. Wissocq, F. Renard, T. Astoul, J.-F. Boussuge. The latter took part to the 'live session'. G. W., F. R., T. A. and the present author contributed to the creation of activities, MCQs, open questions and videos for the first three weeks, and also designed the final examination. J.-F. P. strongly helped every aforementioned people with their work.

I.2   Instructor-Led Trainings

Two additional trainings were designed and conducted within the framework of the present PhD work.

The first one consisted in praticals for MS students at 'ISAE-Supaéro' (graduate school of aeronautical engineering), in Toulouse, France. Since a strong interest in LBMs has rapidly grown in both aerospace industry and research groups, N. Gourdain (Professor at ISAE-Supaéro) proposed the creation of praticals about LBMs, which would be designed for students' best pedagogical/career interests. Under his supervision, J.-F. Boussuge, G. Wissocq and the present author designed a two-hour session to help students understanding the basic features of the LBM, and practicing its coding through fill-in-the-blank like implementation activities.

The second instructor-led training was conducted at CERFACS in the form of a one-day training session, and was supervised by J.-F. Boussuge ('Implementation and use of the lattice Boltzmann method'). It aimed at providing engineers and PhD students with the basic features about the LBM. This instructor-led training session was designed in such a way that theoretical notions could be understood through practical cases including fill-in-the-blank like coding.

Bibliography

[1] H. Yu, S. S. Girimaji, and L.-S. Luo. Lattice Boltzmann simulations of decaying homogeneous isotropic turbulence. *Phys. Rev. E*, 71:016708, 2005. (Cited on page 1.)

[2] P. Sagaut. Toward advanced subgrid models for lattice-Boltzmann-based large-eddy simulation: Theoretical formulations. *Comput. Math. Appl.*, 59(7):2194 – 2199, 2010. (Cited on pages 1, 16, 39, and 54.)

[3] S. Ponce Dawson, S. Chen, and G. D. Doolen. Lattice Boltzmann computations for reaction-diffusion equations. *J. Chem. Phys.*, 98(2):1514–1523, 1993. (Cited on page 1.)

[4] O. Filippova and D. Hänel. A novel lattice BGK approach for low Mach number combustion. *J. Comput. Phys.*, 158(2):139 – 160, 2000. (Cited on page 1.)

[5] C. Lin, A. Xu, G. Zhang, and Y. Li. Double-distribution-function discrete Boltzmann model for combustion. *Combust. Flame*, 164:137 – 151, 2016. (Cited on page 1.)

[6] X. Shan and H. Chen. Lattice Boltzmann model for simulating flows with multiple phases and components. *Phys. Rev. E*, 47:1815–1819, 1993. (Cited on page 1.)

[7] X. Shan and H. Chen. Simulation of nonideal gases and liquid-gas phase transitions by the lattice Boltzmann equation. *Phys. Rev. E*, 49:2941–2948, 1994. (Cited on page 1.)

[8] L. Chen, Q. Kang, Y. Mu, Y.-L. He, and W.-Q. Tao. A critical review of the pseudopotential multiphase lattice Boltzmann model: Methods and applications. *Int. J. Heat Mass Transfer*, 76(0):210 – 236, 2014. (Cited on pages 1 and 113.)

[9] M. A. Mazloomi, S. S. Chikatamarla, and I. V. Karlin. Entropic lattice Boltzmann method for multiphase flows: Fluid-solid interfaces. *Phys. Rev. E*, 92:023308, 2015. (Cited on page 1.)

[10] T. Ye, N. Phan-Thien, and C. T. Lim. Particle-based simulations of red blood cells—a review. *J. Biomech.*, 49(11):2255 – 2266, 2016. (Cited on page 1.)

[11] P. J. Dellar. Lattice kinetic schemes for magnetohydrodynamics. *J. Comput. Phys.*, 179(1):95 – 126, 2002. (Cited on page 1.)

[12] P. J. Dellar. Lattice kinetic formulation for ferrofluids. *J. Stat. Phys.*, 121(1-2):105–118, 2005. (Cited on page 1.)

[13] P. J. Dellar. Moment equations for magnetohydrodynamics. *J. Stat. Mech. Theor. Exp.*, 06:P06003, 2009. (Cited on page 1.)

[14] P. J. Dellar. Electromagnetic waves in lattice Boltzmann magnetohydrodynamics. *Europhys. Lett.*, 90(5):50002, 2010. (Cited on page 1.)

[15] S. Succi, M. Mendoza, F. Mohseni, and I. Karlin. Relativistic lattice kinetic theory: Recent developments and future prospects. *Eur. Phys. J. Spec. Top.*, 223(11):2177–2188, 2014. (Cited on page 1.)

[16] F. Mohseni, M. Mendoza, S. Succi, and H. J. Herrmann. Lattice Boltzmann model for resistive relativistic magnetohydrodynamics. *Phys. Rev. E*, 92:023309, 2015. (Cited on page 1.)

[17] S. Succi. Lattice Boltzmann schemes for quantum applications. *Comput. Phys. Commun.*, 146(3):317 – 323, 2002. (Cited on page 1.)

[18] D. Lapitski and P. J. Dellar. Convergence of a three-dimensional quantum lattice Boltzmann scheme towards solutions of the dirac equation. *Philos. Trans. R . Soc. London, Ser. A*, 369(1944):2155–2163, 2011. (Cited on page 1.)

[19] D. Lagrava. *Revisiting grid refinement algorithms for the lattice Boltzmann method.* PhD thesis, University of Geneva, 2012. (Cited on page 1.)

[20] H. Touil, D. Ricot, and E. Lévêque. Direct and large-eddy simulation of turbulent flows on composite multi-resolution grids by the lattice Boltzmann method. *J. Comput. Phys.*, 256(0):220 – 233, 2014. (Cited on pages 1, 39, 54, and 111.)

[21] F. Gendre, D. Ricot, G. Fritz, and P. Sagaut. Grid refinement for aeroacoustics in the lattice Boltzmann method: A directional splitting approach. *Phys. Rev. E*, 96:023311, 2017. (Cited on page 1.)

[22] R. Kotapati, A. Keating, S. Kandasamy, et al. The lattice-Boltzmann-VLES method for automotive fluid dynamics simulation, a review. Technical report, SAE Technical Paper, 2009. (Cited on page 1.)

[23] A. Sengissen, J.-C. Giret, C. Coreixas, and J.-F. Boussuge. Simulations of LA-GOON landing-gear noise using lattice Boltzmann solver. In *21st AIAA/CEAS Aeroacoustics Conference*, page 2993, 2015. (Cited on page 1.)

[24] D. Casalino, A. F. Ribeiro, E. Fares, et al. Towards lattice-Boltzmann prediction of turbofan engine noise. In *20th AIAA/CEAS Aeroacoustics Conference*, page 3101, 2014. (Cited on page 1.)

[25] A. F. Ribeiro, B. Konig, D. Singh, et al. Buffet simulations with a lattice-Boltzmann based transonic solver. In *55th AIAA Aerospace Sciences Meeting*, page 1438, 2017. (Cited on pages 1 and 19.)

[26] F. Schornbaum and U. Rüde. Massively parallel algorithms for the lattice Boltzmann method on nonuniform grids. *SIAM J. Sci. Comput*, 38(2):C96–C126, 2016. (Cited on page 1.)

[27] M. R. Khorrami, E. Fares, and D. Casalino. Towards full aircraft airframe noise prediction: lattice Boltzmann simulations. *AIAA Paper*, 2481:2014, 2014. (Cited on page 1.)

[28] L. Boltzmann. Weitere studien über das wärmegleichgewicht unter gasmolekülen. *Wien. Ber.*, 66:275–370, 1872. (Cited on pages 1, 8, and 9.)

[29] C. Coreixas, G. Wissocq, G. Puigt, J.-F. Boussuge, and P. Sagaut. Recursive regularization step for high-order lattice Boltzmann methods. *Phys. Rev. E*, 96:033306, 2017. (Cited on pages 2 and 43.)

[30] T. Krüger, H. Kusumaatmaja, A. Kuzmin, et al. *The Lattice Boltzmann Method: Principles and Practice*. Springer International Publishing, 2017. (Cited on pages 3, 27, 32, 40, and 126.)

[31] L. Euler. Principes généraux du mouvement des fluides. *Mem. Acad. Roy. Sci. Berlin*, 1755. (Cited on page 6.)

[32] C. Navier. Mémoire sur les lois du mouvement des fluides. *Mem. Acad. Sci. Inst. Fr*, 6(1823):389–416, 1823. (Cited on page 7.)

[33] A. L. Cauchy. Sur l'équilibre et le mouvement des liquides et des fluides élastiques. *Mem. Acad. Sci. Inst. Fr*, 11:413–418, 1829. (Cited on page 7.)

[34] G. Stokes. On the theories of the internal friction of fluids in motion, and of the equilibrium and moption of elastic fluids. *Trans. Camb. Philos. Soc.*, 8:287, 1845. (Cited on page 7.)

[35] J. Fourier. Mémoire d'analyse sur le mouvement de la chaleur dans les fluides. *Mem. Acad. Sci. Inst. Fr.*, 12:507–530, 1833. (Cited on page 7.)

[36] G. Kirchhoff. Uber den einfluss der warmeleitung in einem gase auf die schallbewegung. *Ann. der. Phys.*, 134:177–193, 1868. (Cited on page 7.)

[37] R. K. Zeytounian. *Navier-Stokes-Fourier equations: a rational asymptotic modelling point of view*. Springer Science & Business Media, 2012. (Cited on page 7.)

[38] J. C. Maxwell. On the dynamical theory of gases. *Philos. Trans. Roy. Soc. London*, 157:49–88, 1867. (Cited on page 8.)

[39] S. Chapman and T. Cowling. *The Mathematical Theory of Non-uniform Gases: An Account of the Kinetic Theory of Viscosity, Thermal Conduction and Diffusion in Gases.* Cambridge University Press, 1970. (Cited on pages 10, 24, and 69.)

[40] P. Bhatnagar, E. Gross, and M. Krook. A model for collision processes in gases. I. Small amplitude processes in charged and neutral one-component systems. *Phys. Rev.*, 94:511–525, 1954. (Cited on pages 10 and 23.)

[41] J. Von Neumann and A. W. Burks. *Theory of self-reproducing automata.* University of Illinois Press Urbana, 1996. (Cited on page 10.)

[42] J. E. Broadwell. Study of rarefied shear flow by the discrete velocity method. *J. Fluid Mech.*, 19(3):401–414, 1964. (Cited on page 10.)

[43] R. Gatignol. *Théorie cinétique des gaz à répartition discrète de vitesses.* Springer verlag, 1975. (Cited on page 10.)

[44] J. Hardy, Y. Pomeau, and O. de Pazzis. Time evolution of a two-dimensional model system. I. Invariant states and time correlation functions. *J. Math. Phys.*, 14(12):1746–1759, 1973. (Cited on page 10.)

[45] U. Frisch, B. Hasslacher, and Y. Pomeau. Lattice-gas automata for the Navier-Stokes equation. *Phys. Rev. Lett.*, 56:1505–1508, 1986. (Cited on page 10.)

[46] D. d'Humieres, P. Lallemand, and U. Frisch. Lattice gas models for 3D hydrodynamics. *Europhys. Lett.*, 2(4):291, 1986. (Cited on page 10.)

[47] G. R. McNamara and G. Zanetti. Use of the Boltzmann equation to simulate lattice-gas automata. *Phys. Rev. Lett.*, 61:2332–2335, 1988. (Cited on page 11.)

[48] F. Higuera and J. Jimenez. Boltzmann approach to lattice gas simulations. *Europhys. Lett.*, 9(7):663, 1989. (Cited on page 11.)

[49] H. Chen, S. Chen, and W. H. Matthaeus. Recovery of the Navier-Stokes equations using a lattice-gas Boltzmann method. *Phys. Rev. A*, 45:R5339–R5342, 1992. (Cited on page 11.)

[50] Y. H. Qian, D. D'Humières, and P. Lallemand. Lattice BGK models for Navier-Stokes equation. *Europhys. Lett.*, 17(6):479, 1992. (Cited on pages 11, 28, and 46.)

[51] X. He and L.-S. Luo. A priori derivation of the lattice Boltzmann equation. *Phys. Rev. E*, 55:R6333–R6336, 1997. (Cited on page 11.)

[52] S. Succi. Lattice Boltzmann 2038. *Europhys. Lett.*, 109(5):50001, 2015. (Cited on page 11.)

[53] F. J. Alexander, S. Chen, and J. D. Sterling. Lattice Boltzmann thermohydrodynamics. *Phys. Rev. E*, 47:R2249–R2252, 1993. (Cited on page 12.)

[54] G. R. McNamara, A. L. Garcia, and B. J. Alder. A hydrodynamically correct thermal lattice Boltzmann model. *J. Stat. Phys.*, 87(5):1111–1121, 1997. (Cited on page 12.)

[55] D. d'Humieres. Generalized lattice-Boltzmann equations. *Prog. Astronaut. Aeronaut.*, 159:450–458, 1992. (Cited on page 12.)

[56] Y. H. Qian and S. A. Orszag. Lattice BGK models for the Navier-Stokes equation: Nonlinear deviation in compressible regimes. *Europhys. Lett.*, 21(3):255, 1993. (Cited on page 12.)

[57] Y. Chen, H. Ohashi, and M. Akiyama. Thermal lattice Bhatnagar-Gross-Krook model without nonlinear deviations in macrodynamic equations. *Phys. Rev. E*, 50:2776–2783, 1994. (Cited on pages 12 and 63.)

[58] Y. Chen, H. Ohashi, and M. Akiyama. Heat transfer in lattice BGK modeled fluid. *J. Stat. Phys.*, 81(1-2):71–85, 1995. (Cited on page 12.)

[59] D. N. Siebert, L. A. Hegele, and P. C. Philippi. Lattice Boltzmann equation linear stability analysis: Thermal and athermal models. *Phys. Rev. E*, 77:026707, 2008. (Cited on pages 13, 63, 89, and 91.)

[60] P. Pavlo, G. Vahala, and L. Vahala. Higher order isotropic velocity grids in lattice methods. *Phys. Rev. Lett.*, 80:3960–3963, 1998. (Cited on pages 13 and 116.)

[61] M. Watari and M. Tsutahara. Two-dimensional thermal model of the finite-difference lattice Boltzmann method with high spatial isotropy. *Phys. Rev. E*, 67:036306, 2003. (Cited on pages 13 and 35.)

[62] M. Watari. Finite difference lattice Boltzmann method with arbitrary specific heat ratio applicable to supersonic flow simulations. *Physica A*, 382(2):502 – 522, 2007. (Cited on page 13.)

[63] T. Kataoka and M. Tsutahara. Lattice Boltzmann model for the compressible Navier-Stokes equations with flexible specific-heat ratio. *Phys. Rev. E*, 69:035701, 2004. (Cited on pages 13 and 35.)

[64] Q. Li, Y. L. He, Y. Wang, and W. Q. Tao. Coupled double-distribution-function lattice Boltzmann method for the compressible Navier-Stokes equations. *Phys. Rev. E*, 76:056705, 2007. (Cited on pages 13, 14, 113, and 129.)

[65] Q. Li, Y. L. He, Y. Wang, and W. Q. Tao. Erratum: Coupled double-distribution-function lattice Boltzmann method for the compressible Navier-Stokes equations [phys. rev. e **76** , 056705 (2007)]. *Phys. Rev. E*, 76:069902, 2007. (Cited on page 13.)

[66] L. Pareschi and G. Russo. Implicit-explicit runge-kutta schemes and applications to hyperbolic systems with relaxation. *J. Sci. Comput.*, 25, 2005. (Cited on page 13.)

[67] Y.-B. Gan, A.-G. Xu, G.-C. Zhang, et al. Finite-difference lattice Boltzmann scheme for high-speed compressible flow: Two-dimensional case. *Commun. Theor. Phys.*, 50(1):201, 2008. (Cited on page 13.)

[68] A.-G. Xu, G.-C. Zhang, Y.-B. Gan, F. Chen, and X.-J. Yu. Lattice Boltzmann modeling and simulation of compressible flows. *Front. Phys.*, 7(5):582–600, 2012. (Cited on page 13.)

[69] A. Nejat and V. Abdollahi. A critical study of the compressible lattice Boltzmann methods for Riemann problem. *J. Sci. Comput.*, 54(1):1–20, 2013. (Cited on page 13.)

[70] F. Chen, A.-G. Xu, G.-C. Zhang, and Y.-L. Wang. Two-dimensional MRT LB model for compressible and incompressible flows. *Front. Phys.*, 9(2):246–254, 2014. (Cited on page 13.)

[71] C. Sun. Lattice-Boltzmann models for high speed flows. *Phys. Rev. E*, 58:7283–7287, 1998. (Cited on pages 14 and 116.)

[72] C. Sun. Adaptive lattice Boltzmann model for compressible flows: Viscous and conductive properties. *Phys. Rev. E*, 61:2645–2653, 2000. (Cited on page 14.)

[73] C. Sun. Simulations of compressible flows with strong shocks by an adaptive lattice Boltzmann model. *J. Comput. Phys.*, 161(1):70 – 84, 2000. (Cited on page 14.)

[74] C. Sun and A. T. Hsu. Three-dimensional lattice Boltzmann model for compressible flows. *Phys. Rev. E*, 68:016303, 2003. (Cited on page 14.)

[75] C. Sun and A. T. Hsu. Multi-level lattice Boltzmann model on square lattice for compressible flows. *Comput. Fluids*, 33(10):1363 – 1385, 2004. (Cited on page 14.)

[76] K. Qu, C. Shu, and Y. T. Chew. Alternative method to construct equilibrium distribution functions in lattice-Boltzmann method simulation of inviscid compressible flows at high Mach number. *Phys. Rev. E*, 75:036706, 2007. (Cited on page 14.)

[77] K. Qu, C. Shu, and Y. T. Chew. Simulation fo shock-wave propagation with finite volume lattice Boltzmann method. *Int. J. Mod. Phys. C*, 18(04):447–454, 2007. (Cited on page 14.)

[78] K. Qu. *Development of Lattice Boltzmann Method for Compressible Flows*. PhD thesis, National University of Singapore, 2009. (Cited on page 14.)

[79] K. Li and C. Zhong. A lattice Boltzmann model for simulation of compressible flows. *Int. J. Numer. Meth. Fluids*, 77(6):334–357, 2014. (Cited on page 14.)

[80] Z. Guo, K. Xu, and R. Wang. Discrete unified gas kinetic scheme for all Knudsen number flows: Low-speed isothermal case. *Phys. Rev. E*, 88:033305, 2013. (Cited on page 15.)

[81] Z. Guo, R. Wang, and K. Xu. Discrete unified gas kinetic scheme for all Knudsen number flows. II. Thermal compressible case. *Phys. Rev. E*, 91:033313, 2015. (Cited on pages 15 and 35.)

[82] P. Wang, L.-P. Wang, and Z. Guo. Comparison of the lattice Boltzmann equation and discrete unified gas-kinetic scheme methods for direct numerical simulation of decaying turbulent flows. *Phys. Rev. E*, 94:043304, 2016. (Cited on page 15.)

[83] N. Frapolli, S. S. Chikatamarla, and I. V. Karlin. Entropic lattice Boltzmann model for compressible flows. *Phys. Rev. E*, 92:061301, 2015. (Cited on pages 16 and 17.)

[84] L.-S. Luo, W. Liao, X. Chen, Y. Peng, and W. Zhang. Numerics of the lattice Boltzmann method: Effects of collision models on the lattice Boltzmann simulations. *Phys. Rev. E*, 83:056710, 2011. (Cited on page 16.)

[85] I. V. Karlin, S. Succi, and S. S. Chikatamarla. Comment on "numerics of the lattice Boltzmann method: Effects of collision models on the lattice Boltzmann simulations". *Phys. Rev. E*, 84:068701, 2011. (Cited on page 16.)

[86] L.-S. Luo. Reply to "comment on 'numerics of the lattice Boltzmann method: Effects of collision models on the lattice Boltzmann simulations'". *Phys. Rev. E*, 86:048701, 2012. (Cited on page 16.)

[87] E. Garnier, N. Adams, and P. Sagaut. *Large eddy simulation for compressible flows.* Springer Science & Business Media, 2009. (Cited on pages 16 and 111.)

[88] O. Malaspinas, M. Deville, and B. Chopard. Towards a physical interpretation of the entropic lattice Boltzmann method. *Phys. Rev. E*, 78:066705, 2008. (Cited on page 16.)

[89] I. V. Karlin, F. Bösch, and S. S. Chikatamarla. Gibbs' principle for the lattice-kinetic theory of fluid dynamics. *Phys. Rev. E*, 90:031302, 2014. (Cited on pages 16 and 42.)

[90] F. Bösch, S. S. Chikatamarla, and I. Karlin. Entropic multi-relaxation models for simulation of fluid turbulence. *ESAIM Proc.*, 52:1–24, 2015. (Cited on pages 16 and 47.)

[91] F. Bösch, S. S. Chikatamarla, and I. V. Karlin. Entropic multirelaxation lattice Boltzmann models for turbulent flows. *Phys. Rev. E*, 92:043309, 2015. (Cited on pages 16 and 39.)

[92] B. Dorschner, F. Bösch, S. S. Chikatamarla, K. Boulouchos, and I. V. Karlin. Entropic multi-relaxation time lattice Boltzmann model for complex flows. *J. Fluid Mech.*, 801:623–651, 2016. (Cited on page 16.)

[93] N. Frapolli. *Entropic lattice Boltzmann models for thermal and compressible flows.* PhD thesis, ETH Zurich, 2017. (Cited on pages 16 and 17.)

[94] S. S. Chikatamarla and I. V. Karlin. Lattices for the lattice Boltzmann method. *Phys. Rev. E*, 79:046701, 2009. (Cited on pages 16 and 32.)

[95] M. Geier, A. Greiner, and J. G. Korvink. Cascaded digital lattice Boltzmann automata for high Reynolds number flow. *Phys. Rev. E*, 73:066705, 2006. (Cited on pages 17, 42, 63, and 109.)

[96] M. Geier, A. Greiner, and J. G. Korvink. A factorized central moment lattice Boltzmann method. *Eur. Phys. J. Spec. Top.*, 171(1):55–61, 2009. (Cited on pages 17 and 109.)

[97] N. Frapolli, S. S. Chikatamarla, and I. V. Karlin. Entropic lattice Boltzmann model for gas dynamics: Theory, boundary conditions, and implementation. *Phys. Rev. E*, 93:063302, 2016. (Cited on pages 17 and 27.)

[98] N. Frapolli, S. S. Chikatamarla, and I. V. Karlin. Multispeed entropic lattice Boltzmann model for thermal flows. *Phys. Rev. E*, 90:043306, 2014. (Cited on page 17.)

[99] J. Latt, B. Chopard, O. Malaspinas, M. Deville, and A. Michler. Straight velocity boundaries in the lattice Boltzmann method. *Phys. Rev. E*, 77:056703, 2008. (Cited on pages 17 and 112.)

[100] V. A. Rykov. A model kinetic equation for a gas with rotational degrees of freedom. *Fluid Dyn.*, 10(6):959–966, 1975. (Cited on pages 17 and 27.)

[101] X. Nie, X. Shan, and H. Chen. Thermal lattice Boltzmann model for gases with internal degrees of freedom. *Phys. Rev. E*, 77:035701, 2008. (Cited on pages 17, 18, and 27.)

[102] B. Dorschner, N. Frapolli, S. S. Chikatamarla, and I. V. Karlin. Grid refinement for entropic lattice Boltzmann models. *Phys. Rev. E*, 94:053311, 2016. (Cited on page 17.)

[103] H. Grad. Note on N-dimensional Hermite polynomials. *Commun. Pure Appl. Math.*, 2(4):325–330, 1949. (Cited on pages 18 and 120.)

[104] H. Grad. On the kinetic theory of rarefied gases. *Commun. Pure Appl. Math.*, 2(4):331–407, 1949. (Cited on pages 18, 22, and 115.)

[105] X. Shan and X. He. Discretization of the velocity space in the solution of the Boltzmann equation. *Phys. Rev. Lett.*, 80:65–68, 1998. (Cited on pages 18, 23, and 115.)

[106] X. Shan, X.-F. Yuan, and H. Chen. Kinetic theory representation of hydrodynamics: a way beyond the Navier–Stokes equation. *J. Fluid Mech.*, 550:413–441, 2006. (Cited on pages 18, 22, 24, 26, 27, 28, 44, 115, 131, and 141.)

[107] J. Latt and B. Chopard. Lattice Boltzmann method with regularized non-equilibrium distribution functions. *arXiv preprint physics/0506157*, 2005. (Cited on pages 18, 43, and 98.)

[108] J. Latt and B. Chopard. Lattice Boltzmann method with regularized pre-collision distribution functions. *Math. Comput. Simul.*, 72(2-6):165–168, 2006. (Cited on pages 18, 42, 43, and 98.)

[109] R. Zhang, X. Shan, and H. Chen. Efficient kinetic method for fluid simulation beyond the Navier-Stokes equation. *Phys. Rev. E*, 74:046703, 2006. (Cited on pages 18, 74, 132, and 133.)

[110] X. B. Nie, X. Shan, and H. Chen. Galilean invariance of lattice Boltzmann models. *Europhys. Lett.*, 81(3):34005, 2008. (Cited on pages 18 and 28.)

[111] X. Nie, X. Shan, and H. Chen. A lattice-Boltzmann / finite-difference hybrid simulation of transonic flow. In *Aerospace Sciences Meetings*, volume 139. American Institute of Aeronautics and Astronautics, 2009. (Cited on page 18.)

[112] E. Fares, M. Wessels, R. Zhang, et al. Validation of a lattice-Boltzmann approach for transonic and supersonic flow simulations. *52nd AIAA Aerospace Sciences Meeting*, 0952, 2014. (Cited on page 19.)

[113] P.-T. Lew, P. Gopalakrishnan, D. Casalino, et al. An extended lattice Boltzmann methodology for high subsonic jet noise prediction. In *AIAA Aviation*, pages –. American Institute of Aeronautics and Astronautics, 2014. (Cited on page 19.)

[114] O. Malaspinas. *Lattice Boltzmann method for the simulation of viscoelastic fluid flows.* PhD thesis, STI, Lausanne, 2009. (Cited on pages 24 and 26.)

[115] X. Shan and H. Chen. A general multiple-relaxation-time boltzmann collision model. *Int. J. Mod. Phys. C*, 18(04):635–643, 2007. (Cited on pages 26, 126, and 151.)

[116] Z. Guo, C. Zheng, B. Shi, and T. S. Zhao. Thermal lattice Boltzmann equation for low Mach number flows: Decoupling model. *Phys. Rev. E*, 75:036704, 2007. (Cited on pages 27, 93, 119, 126, 128, and 129.)

[117] X. He, X. Shan, and G. D. Doolen. Discrete Boltzmann equation model for nonideal gases. *Phys. Rev. E*, 57:R13–R16, 1998. (Cited on page 29.)

[118] P. J. Dellar. Bulk and shear viscosities in lattice Boltzmann equations. *Phys. Rev. E*, 64:031203, 2001. (Cited on pages 29, 126, and 145.)

[119] P. C. Philippi, L. A. Hegele, L. O. E. dos Santos, and R. Surmas. From the continuous to the lattice Boltzmann equation: The discretization problem and thermal models. *Phys. Rev. E*, 73:056702, 2006. (Cited on pages 30, 32, 33, 35, 45, 51, 74, 115, 120, 131, and 132.)

[120] X. Shan. The mathematical structure of the lattices of the lattice Boltzmann method. *J. Comput. Sci.*, 17:475 – 481, 2016. (Cited on pages 30, 32, 33, 51, 74, 113, 114, 132, 133, 134, and 135.)

[121] E. M. Viggen. Acoustic equations of state for simple lattice Boltzmann velocity sets. *Phys. Rev. E*, 90:013310, 2014. (Cited on pages 30, 121, and 126.)

[122] I. Karlin and P. Asinari. Factorization symmetry in the lattice Boltzmann method. *Physica A*, 389(8):1530 – 1548, 2010. (Cited on pages 32 and 34.)

[123] L. Hegele Jr. *Equação de Boltzmann em rede para escoamentos térmicos.* PhD thesis, Universidade Federal de Santa Catarina, 2010. (Cited on page 33.)

[124] S. Succi. *The Lattice Boltzmann Equation for Fluid Dynamics and Beyond.* Oxford University Press, USA, 2001. (Cited on pages 38, 132, 134, and 135.)

[125] M. L. Minion and D. L. Brown. Performance of under-resolved two-dimensional incompressible flow simulations, II. *J. Comput. Phys.*, 138(2):734 – 765, 1997. (Cited on page 38.)

[126] D. Ricot, S. Marié, P. Sagaut, and C. Bailly. Lattice Boltzmann method with selective viscosity filter. *J. Comput. Phys.*, 228(12):4478 – 4490, 2009. (Cited on pages 39, 64, 93, 111, and 112.)

[127] S. Pirozzoli. Numerical methods for high-speed flows. *Annu. Rev. Fluid Mech*, 43(1):163–194, 2011. (Cited on pages 40 and 53.)

[128] P. Lallemand and L.-S. Luo. Theory of the lattice Boltzmann method: Dispersion, dissipation, isotropy, galilean invariance, and stability. *Phys. Rev. E*, 61:6546–6562, 2000. (Cited on pages 42, 63, 89, 91, 93, 108, 109, and 126.)

[129] M. Geier, M. Schonherr, A. Pasquali, and M. Krafczyk. The cumulant lattice Boltzmann equation in three dimensions: Theory and validation. *Comput. Math. Appl.*, 70(4):507 – 547, 2015. (Cited on page 42.)

[130] B. M. Boghosian, J. Yepez, P. V. Coveney, and A. Wager. Entropic lattice Boltzmann methods. *Proc. Royal Soc. A*, 457(2007):717–766, 2001. (Cited on page 42.)

[131] S. Ansumali, I. V. Karlin, and H. C. Öttinger. Minimal entropic kinetic models for hydrodynamics. *Europhys. Lett.*, 63(6):798–804, 2003. (Cited on page 42.)

[132] A. J. C. Ladd and R. Verberg. Lattice-Boltzmann simulations of particle-fluid suspensions. *J. Stat. Phys.*, 104(5):1191–1251, 2001. (Cited on page 42.)

[133] H. Chen, R. Zhang, I. Staroselsky, and M. Jhon. Recovery of full rotational invariance in lattice Boltzmann formulations for high Knudsen number flows. *Physica A*, 362(1):125–131, 2006. (Cited on pages 42 and 43.)

[134] O. Malaspinas. Increasing stability and accuracy of the lattice Boltzmann scheme: recursivity and regularization. *ArXiv e-prints*, 2015. (Cited on pages 42, 43, 44, 46, 74, 92, 134, and 145.)

[135] K. K. Mattila, L. A. Hegele, and P. C. Philippi. Investigation of an entropic stabilizer for the lattice-Boltzmann method. *Phys. Rev. E*, 91:063010, 2015. (Cited on page 47.)

[136] G. A. Sod. A survey of several finite difference methods for systems of nonlinear hyperbolic conservation laws. *J. Comput. Phys.*, 27(1):1 – 31, 1978. (Cited on page 51.)

[137] E. Garnier, M. Mossi, P. Sagaut, P. Comte, and M. Deville. On the use of shock-capturing schemes for large-eddy simulation. *J. Comput. Phys.*, 153(2):273 – 311, 1999. (Cited on page 53.)

[138] L. Landau and E. M. Lifshitz. *Fluid Mechanics. Landau and Lifshitz: Course of Theoretical Physics, Volume 6.* Butterworth-Heinemann Ltd, rev ed edition, 1987. (Cited on page 62.)

[139] F. Charru. *Hydrodynamic Instabilities.* Cambridge Texts in Applied Mathematics. Cambridge University Press, 2011. (Cited on page 62.)

[140] W. M. Orr. The stability or instability of the steady motions of a perfect liquid and of a viscous liquid. Part I: A perfect liquid. *Proc. Royal Ir. Acad. Sect. A Math.*, 27:9–68, 1907. (Cited on page 62.)

[141] W. M. Orr. The stability or instability of the steady motions of a perfect liquid and of a viscous liquid. Part II: A viscous liquid. *Proc. Royal Ir. Acad. Sect. A Math.*, 27:69–138, 1907. (Cited on page 62.)

[142] A. Sommerfeld. Ein beitrag zur hydrodynamischen erklaerung der turbulenten fluessigkeitsbewegungen. *Proc. 4th Int. Congr. Math. Rome III*, 4:116–124, 1908. (Cited on page 62.)

[143] O. Axelsson. *Iterative solution methods.* Cambridge university press, 1996. (Cited on page 62.)

[144] G. H. Golub and C. F. Van Loan. *Matrix computations*, volume 3. JHU Press, 2012. (Cited on page 62.)

[145] J. Crank and P. Nicolson. A practical method for numerical evaluation of solutions of partial differential equations of the heat-conduction type. In *Mathematical Proceedings of the Cambridge Philosophical Society*, volume 43, pages 50–67. Cambridge University Press, 1947. (Cited on page 62.)

[146] J. G. Charney, R. Fjörtoft, and J. v. Neumann. Numerical integration of the barotropic vorticity equation. *Tellus*, 2(4):237–254, 1950. (Cited on page 62.)

[147] J. D. Sterling and S. Chen. Stability analysis of lattice Boltzmann methods. *J. Comput. Phys.*, 123(1):196 – 206, 1996. (Cited on page 62.)

[148] R. A. Worthing, J. Mozer, and G. Seeley. Stability of lattice Boltzmann methods in hydrodynamic regimes. *Phys. Rev. E*, 56:2243–2253, 1997. (Cited on page 63.)

[149] P. Lallemand and L.-S. Luo. Theory of the lattice Boltzmann method: Acoustic and thermal properties in two and three dimensions. *Phys. Rev. E*, 68:036706, 2003. (Cited on pages 63 and 93.)

[150] I. Ginzburg, D. d'Humières, and A. Kuzmin. Optimal stability of advection-diffusion lattice Boltzmann models with two relaxation times for positive/negative equilibrium. *J. Stat. Phys.*, 139(6):1090–1143, 2010. (Cited on page 63.)

[151] R. Adhikari and S. Succi. Duality in matrix lattice Boltzmann models. *Phys. Rev. E*, 78:066701, 2008. (Cited on page 63.)

[152] F. Dubois, T. Février, and B. Graille. On the stability of a relative velocity lattice Boltzmann scheme for compressible Navier–Stokes equations. *Comptes Rendus Mécanique*, 343(10):599 – 610, 2015. (Cited on page 63.)

[153] S. Marié, D. Ricot, and P. Sagaut. Comparison between lattice Boltzmann method and Navier–Stokes high order schemes for computational aeroacoustics. *J. Comput. Phys.*, 228(4):1056 – 1070, 2009. (Cited on pages 63 and 73.)

[154] C. Bogey and C. Bailly. A family of low dispersive and low dissipative explicit schemes for flow and noise computations. *J. Comput. Phys.*, 194(1):194 – 214, 2004. (Cited on page 63.)

[155] H. Xu and P. Sagaut. Optimal low-dispersion low-dissipation LBM schemes for computational aeroacoustics. *J. Comput. Phys.*, 230(13):5353 – 5382, 2011. (Cited on page 64.)

[156] H. Xu, O. Malaspinas, and P. Sagaut. Sensitivity analysis and determination of free relaxation parameters for the weakly-compressible MRT–lbm schemes. *J. Comput. Phys.*, 231(21):7335 – 7367, 2012. (Cited on page 64.)

[157] H. N. W. Lekkerkerker and J. P. Boon. Hydrodynamic modes and light scattering near the convective instability. *Phys. Rev. A*, 10:1355–1360, 1974. (Cited on pages 67 and 68.)

[158] P. Sagaut. *Large eddy simulation for incompressible flows: an introduction.* Springer Science & Business Media, 2006. (Cited on page 111.)

[159] E. Lévêque, F. Toschi, L. Shao, and J.-P. Bertoglio. Shear-improved Smagorinsky model for large-eddy simulation of wall-bounded turbulent flows. *J. Fluid Mech.*, 570:491–502, 2007. (Cited on page 111.)

[160] N. Afzal. Wake layer in a turbulent boundary layer with pressure gradient: A new approach. In *IUTAM Symposium on Asymptotic Methods for Turbulent Shear Flows at High Reynolds Numbers*, pages 95–118. Bochum, Germany, 1996. (Cited on page 111.)

[161] F. Chevillotte and D. Ricot. Development and evaluation of non-reflective boundary conditions for lattice Boltzmann method. In *22nd AIAA/CEAS Aeroacoustics Conference*, page 2915, 2016. (Cited on page 111.)

[162] T. Gao, Y.-H. Tseng, and X.-Y. Lu. An improved hybrid cartesian/immersed boundary method for fluid–solid flows. *Int. J. Numer. Meth. Fluids*, 55(12):1189–1211, 2007. (Cited on page 111.)

[163] R. Zhang and H. Chen. Lattice Boltzmann method for simulations of liquid-vapor thermal flows. *Phys. Rev. E*, 67:066711, 2003. (Cited on page 113.)

[164] E. M. Shakhov. Generalization of the Krook kinetic relaxation equation. *Fluid Dyn.*, 3(5):95–96, 1968. (Cited on page 125.)

[165] L. H. Holway. New statistical models for kinetic theory: Methods of construction. *Phys. Fluids*, 9(9):1658–1673, 1966. (Cited on page 125.)

[166] J. Meng, Y. Zhang, N. G. Hadjiconstantinou, G. A. Radtke, and X. Shan. Lattice ellipsoidal statistical BGK model for thermal non-equilibrium flows. *J. Fluid Mech.*, 718:347–370, 2013. (Cited on page 125.)

[167] S. Ansumali, S. Arcidiacono, S. S. Chikatamarla, et al. Quasi-equilibrium lattice Boltzmann method. *Eur. Phys. J. B*, 56(2):135–139, 2007. (Cited on page 126.)

[168] X. He, S. Chen, and G. D. Doolen. A novel thermal model for the lattice Boltzmann method in incompressible limit. *J. Comput. Phys.*, 146(1):282 – 300, 1998. (Cited on pages 126 and 128.)

[169] Q. Li, K. H. Luo, Y. L. He, Y. J. Gao, and W. Q. Tao. Coupling lattice Boltzmann model for simulation of thermal flows on standard lattices. *Phys. Rev. E*, 85:016710, 2012. (Cited on pages 126 and 129.)

[170] J. Latt. *Hydrodynamic limit of lattice Boltzmann equations*. PhD thesis, University of Geneva, 2007. (Cited on page 126.)

[171] L. C. Woods. *An introduction to the kinetic theory of gases and magnetoplasmas.* Oxford, England, Oxford University Press., 1993. (Cited on page 128.)

[172] P. J. Dellar. Lattice Boltzmann algorithms without cubic defects in galilean invariance on standard lattices. *J. Comput. Phys.*, 259(0):270 – 283, 2014. (Cited on page 132.)

Résumé court

Ce manuscrit est consacré au développement et à la validation d'un nouveau modèle de collision destiné à améliorer la stabilité des modèles lattice Boltzmann (LB) d'ordre élevés lors de la simulation d'écoulements : (1) isothermes et faiblement compressibles à nombre de Reynolds élevés, ou (2) compressibles et comprenant des discontinuités telles que des ondes de choc.

Ce modèle de collision s'appuie sur une étape de régularisation améliorée. Cette dernière inclut désormais un calcul par récurrence des coefficients hors-équilibre du développement en polynômes d'Hermite. Ces formules de récurrence sont directement issues du développement de Chapman-Enskog, et permettent de correctement filtrer les contributions non-hydrodynamiques émergeant lors de l'utilisation de maillages sous-résolus. Cette approche est d'autant plus intéressante quelle est compatible avec un grand nombre de réseaux de vitesses discrètes.

Ce modèle LB d'ordre élevé est validé tout d'abord pour des écoulements isothermes à nombre de Reynolds élevé. Un couplage avec une technique de capture de choc permet ensuite d'étendre son domaine de validité aux écoulements compressibles incluant des ondes de choc. Ce travail se conclut avec une étude de stabilité linéaire des modèles considérés, le tout dans le cas d'écoulements isothermes. Ceci permet de quantifier de manière distincte l'impact des discrétisations en vitesse et numérique, sur le comportement spectrale du jeu d'équations associé. Cette étude permet au final de confirmer le gain en stabilité induit par le nouveau modèle de collision.

Short abstract

This thesis is dedicated to the derivation and the validation of a new collision model as a stabilization technique for high-order lattice Boltzmann methods (LBM). More specifically, it intends to stabilize simulations of: (1) isothermal and weakly compressible flows at high Reynolds numbers, and (2) fully compressible flows including discontinuities such as shock waves.

The new collision model relies on an enhanced regularization step. The latter includes a recursive computation of nonequilibrium Hermite polynomial coefficients. These recursive formulas directly derive from the Chapman-Enskog expansion, and allow to properly filter out second- (and higher-) order nonhydrodynamic contributions in underresolved conditions. This approach is even more interesting since it is compatible with a very large number of velocity sets.

This high-order LBM is first validated in the isothermal case, and for high-Reynolds number flows. The coupling with a shock-capturing technique allows to further extend its validity domain to the simulation of fully compressible flows including shockwaves. The present work ends with the linear stability analysis(LSA) of the new approach, in the isothermal case. This leads to a proper quantification of the impact induced by each discretization (velocity and numerical) on the spectral properties of the related set of equations. The LSA of the recursive regularized LBM finally confirms the drastic stability gain obtained with this new approach.